

Copyright
by
Seung-Hyun Chae
2010

**The Dissertation Committee for Seung-Hyun Chae Certifies that this is the
approved version of the following dissertation:**

**Electromigration and Thermomigration Reliability of
Lead-Free Solder Joints for Advanced Packaging Applications**

Committee:

Paul S. Ho, Supervisor

Desiderio Kovar

Rui Huang

Jang-hi Im

Kejun Zeng

**Electromigration and Thermomigration Reliability of
Lead-Free Solder Joints for Advanced Packaging Applications**

by

Seung-Hyun Chae, B.S.; M.S.E.

Dissertation

Presented to the Faculty of the Graduate School of

The University of Texas at Austin

in Partial Fulfillment

of the Requirements

for the Degree of

Doctor of Philosophy

The University of Texas at Austin

May 2010

Dedication

To my dear parents

Acknowledgements

First of all, I would like to express my sincere gratitude to Prof. Paul S. Ho for his guidance and support throughout my doctoral research. As a supervisor, he has been motivating and encouraging me with his deep insight into understanding research problems. His dedication to science and research, and profound knowledge has been a great inspiration to me.

I would also like to express my deep appreciation to Dr. Jang-hi Im for his invaluable advice and suggestions in this work. I have admired his prudence and insight with which he could point out what I overlooked. I also thank him for proofreading this dissertation.

I want to thank Texas Instruments, Inc. for my internship opportunity and fellowship support for the last two years. Special thanks go to Dr. Jie-Hua Zhao as a mentor. His passion and invaluable advice have motivated me to produce valuable results during my internship. I am also grateful to Mr. Darvin R. Edwards and other team members at TI for their encouragement and useful discussion.

I extend many thanks to my current and former colleagues in the Laboratory for Interconnect and Packaging for their friendship and helpful discussion. I am especially thankful to Kuan-Hsun Lu for helping my experiments while I was interning in Dallas. Special gratitude is given to Ms. Jo Ann Smith for her kind support for administrative works.

Great appreciation is also given to Mr. Trent Uehling and Freescale Semiconductor, Inc. for the partial support for this work and supplying test vehicles.

Also, I thank Prof. Desiderio Kovar, Prof. Rui Huang, and Dr. Kejun Zeng for serving as my doctoral committee members.

Last but not least, I wish to express my thanks to my parents and brothers from the bottom of my heart for their unconditional love and endless trust. They have been a solid support for me to accomplish my goal.

Electromigration and Thermomigration Reliability of Lead-Free Solder Joints for Advanced Packaging Applications

Publication No. _____

Seung-Hyun Chae, Ph.D.

The University of Texas at Austin, 2010

Supervisor: Paul S. Ho

Electromigration (EM) and thermomigration (TM) reliability of Pb-free solder joints are emerging as critical concerns in advanced packages. In this study, EM and TM phenomena in Sn-2.5Ag solder joints with thick Cu or thin Ni under-bump metallurgy (UBM) were investigated.

A series of EM tests were performed to obtain activation energy (Q) and current density exponent (n), and to understand failure mechanisms. Joule heating was also taken into account. Q and n values were determined as follows: for Cu UBM solders, $Q = 1.0$ eV and $n = 1.5$; for Ni UBM solders, $Q = 0.9$ and $n = 2.2$. Important factors limiting EM reliability of Pb-free solder joints were found to be UBM dissolution with extensive intermetallic compound (IMC) growth and current crowding.

IMC growth without current stressing was found to follow the parabolic growth law whereas linear growth law was observed for Cu_6Sn_5 and Ni_3Sn_4 under high current stressing. For Cu UBM solders, the apparent activation energy for IMC growth was consistent with the activation energy for EM, which supports that EM failure was closely

related to IMC growth. In contrast, for Ni UBM solders the apparent activation energy was higher than the EM activation energy. It was suggested that the EM failure in the Ni UBM solders could be associated with more than one mass transport mechanism.

The current crowding effect was analyzed with different thicknesses of Ni UBM. It was found that the maximum current density in solder could represent the current density term in Black's equation better than the average current density. FEM studies demonstrated that current crowding was mainly controlled by UBM thickness, metal trace design, and passivation opening diameter.

A large temperature gradient of the order of 10^3 °C/cm was generated across the sample to induce noticeable TM and to compare its effect against that of EM. TM-induced voiding was observed in Ni UBM solders while UBM dissolution with IMC formation occurred in Cu UBM solders. However, the relative effect of TM was found to be several times smaller than that of EM even at this large temperature gradient.

Table of Contents

List of Tables	xiii
List of Figures	xv
Chapter 1: Introduction	1
1.1 Background	2
1.2 Flip Chip Technology	5
1.2.1 Overview	5
1.2.2 Solder Bumping Processes	8
1.2.2.1 Evaporation	9
1.2.2.2 Electroplating	10
1.2.2.3 Stencil Printing	10
1.2.3 Under Bump Metallurgy (UBM)	12
1.2.4 Pb-Free Solder Alloys	12
1.2.5 Intermetallic Compounds (IMCs)	15
1.3 Electromigration and Thermomigration Phenomena in Solder Joints	17
1.3.1 Overview	17
1.3.2 Electromigration	18
1.3.2.1 Fundamentals of Electromigration (EM)	18
1.3.2.2 EM in Solder Joints	20
1.3.2.3 EM of Fast Diffusers in Solder Alloys [1.68]	24
1.3.2.4 EM-Enhanced IMC Growth	28
1.3.3 Thermomigration (TM)	31
1.3.3.1 Fundamentals of Thermomigration (TM)	31
1.3.3.2 TM in Solder Joints	34
1.4 Objectives and Overview	36
Chapter 2: Experimental Setup and Reliability Data Analysis	38
2.1 Test Vehicle	38
2.2 Wheatstone Bridge Method	41

2.3 Test System Configuration	43
2.4 General Test Procedure.....	53
2.5 Statistical Analysis for Electromigration Lifetime	56
2.5.1 Fundamentals of Lognormal Distribution and Weakest-Link Model.....	56
2.5.2 Extracting CDF Values Based on Weakest Link Model	59
Chapter 3: Electromigration Failure Characteristics of Pb-Free Solder Joints.....	64
3.1 Introduction.....	64
3.2 Experimental Details.....	66
3.3 Results and Discussion	69
3.3.1 Failure Criteria	69
3.3.1.1 Typical V_g Traces for Pb-Free Solder Joints	69
3.3.1.2 Open Failure Criterion vs. First Resistance Jump Criterion	74
3.3.2 Electromigration Lifetime.....	75
3.3.3 Joule Heating Characterization	82
3.3.3.1 Experimental Joule Heating Measurement	82
3.3.3.2 Coupled Electro-Thermal Finite Element Analysis.....	86
3.3.4 Determination of Electromigration Activation Energy (Q) and Current Density Exponent (n).....	89
3.3.5 Electromigration Damage Evolution	94
3.3.5.1 Solder Joints with Thick Cu UBM	94
3.3.5.2 Solder Joints with Thin Ni UBM.....	103
3.4 Summary	109
Chapter 4: Electromigration (EM)-Enhanced Intermetallic Compound Growth in Pb- Free Solder Joints and Its Effect on EM Reliability	110
4.1 Introduction.....	110
4.2 Experimental Details.....	111
4.3 Results and Discussion	113
4.3.1 IMC Growth during Thermal Aging Only.....	113
4.3.2 IMC Growth with Current Stressing.....	128
4.3.3 Effects of EM-Enhanced IMC Growth on EM Reliability	142
4.4 Summary	151

Chapter 5: Effects of Current Crowding on Electromigration Reliability of Solder Joints with Thin Ni UBM	152
5.1 Introduction.....	152
5.2 Experimental Details.....	154
5.3 Finite Element Modeling	156
5.4 Experimental Results	158
5.5 Discussion	162
5.5.1 Correlation between Current Crowding and EM Lifetime	162
5.5.2 Effects of Metal Trace Design on Current Crowding.....	167
5.5.3 Effects of Solder Joint Scaling on Current Density Distribution.....	171
5.6 Summary	174
Chapter 6: Electromigration versus Thermomigration in Pb-Free Solder Joint Reliability.....	176
6.1 Introduction.....	176
6.2 Experimental Details.....	178
6.3 Finite Element Modeling	182
6.4 Results and Discussion	190
6.5 Summary	203
Chapter 7: Conclusions and Future Work.....	205
7.1 Conclusions.....	205
7.2 Suggestions for Future Work.....	208
Appendix A: Thermal-Electric Analysis Using Finite Element Method.....	210
A.1 Introduction.....	210
A.2 Governing Equations.....	210
A.3 Element Description.....	212
A.4 Boundary Conditions and Load	213

Glossary	214
References.....	216
Vita	235
List of Publications	236

List of Tables

Table 1.1:	Sn-based Pb-free solder alloys [1.25].	14
Table 2.1:	Example of deducing CDF values through the deconvolution process. The data analysis follows the steps described in ref. [2.2].	61
Table 2.2:	Example of the deconvolution process taking into account “losses” of good samples. The major changes are marked in bold.	63
Table 3.1:	Chamber temperature set to achieve desired Si backside temperatures for each EM test condition.....	68
Table 3.2:	Summary of temperature dependent EM lifetime, based on two different failure criteria. The applied current was 1.01 A ($j = 5.16 \times 10^4$ A/cm ²).	76
Table 3.3:	Summary of current density dependent EM lifetime, based on two different failure criteria. The Si backside temperature was fixed at 140°C.	79
Table 3.4:	Summary of temperature dependent EM lifetime, after the solder temperature correction. The applied current was 1.01 A ($j = 5.16 \times 10^4$ A/cm ²).	91
Table 3.5:	Summary of current density dependent EM lifetime extrapolated to the arbitrarily fixed solder temperature of 140°C, after the solder temperature correction was made.	93
Table 4.1:	Physical properties of Cu, Ni, Sn and their intermetallics at room temperature, excerpted from [4.10].	111
Table 4.2:	Solder temperatures calculated by using FEM for various test conditions.	112
Table 4.3:	IMC growth rate constant, k (in nm/h ^{1/2}), without current stressing.....	120
Table 4.4:	Apparent activation energy for the Cu-Sn IMC growth.	126

Table 4.5:	Apparent activation energy for the Ni_3Sn_4 growth.	127
Table 4.6:	IMC growth rate constant, w (in nm/h), with current stressing.	136
Table 4.7:	Summary of activation energies for Cu-Sn and Ni-Sn systems obtained from different experiments.	141
Table 4.8:	Material properties used in FEM.	144
Table 4.9:	Thickness changes of each layer in Cu UBM solders at 155°C with 1.0 A, interpolated from data shown in Fig. 4.10.	145
Table 4.10:	Thickness changes of each layer in Ni UBM solders at 155°C with 1.0 A, interpolated from data shown in Fig. 4.10.	146
Table 5.1:	Electrical conductivity of the materials used in FEM.	158
Table 5.2:	Average and maximum current density and current crowding factor (j_{\max} $/j_{\text{avg}}$) in each layer.	163
Table 5.3:	Variations in metal trace design simulated by FEM.	167
Table 5.4:	Solder joint scaling matrix for FEM analyses (unit: μm).	172
Table 6.1:	Summary of TM and EM test conditions.	180
Table 6.2:	Solder joint temperatures determined by FEM.	188
Table 6.3:	Summary of TM and EM test results.	190

List of Figures

Figure 1.1: Package roadmap by ASE. (Source: http://www.asejp.aseglobal.com)	1
Figure 1.2: Plot of CPU transistor counts against dates of introduction, showing the number of transistors to double every two years [1.1].....	3
Figure 1.3: Flip-chip area array pitch projected by ITRS in 2007.	4
Figure 1.4: First-level (chip-to-package) interconnection techniques [1.8].	6
Figure 1.5: Examples of (a) wire bonding [1.11], (b) TAB [1.12], (c) flip-chip solder bumps [1.13], and (d) flip-chip package (Intel 32 nm processor) [1.14].....	7
Figure 1.6: Three common solder bumping process flows [1.18]. Electroplated solder bumps are either (a) plated over the resist edge (mushroom), or (b) fully plated in-via. With electroplating, the UBM is always etched after solder deposition. (c) With stencil printing, the UBM etch is done before solder deposition. Unlike electroplated, printed solder bumps are reflowed before resist stripping.	11
Figure 1.7: Phase diagram for Ag-Sn system [1.27].	14
Figure 1.8: Phase diagram for (a) Cu-Sn system, and (b) Ni-Sn system [1.27].	16
Figure 1.9: Cross-sectional SEM images of the current stressed eutectic Sn-Pb solder bumps at 150°C for 6 h, taken from [1.62]. Electrons flowed (a) from the substrate side to the chip side, and (b) from the chip side to the substrate side.	22
Figure 1.10: SEM images of cathode side of composite (97Pb-3Sn on the die side and 63Sn-37Pb on the substrate side) bumps after current stressing of 2.25×10^4 A/cm ² at 155°C. (a) Before current stressing, (b) after 3 h, (c) after 12 h, (d) after 18 h, and (e) after 20 h [1.64].	23

Figure 1.11: Schematic illustration depicting the cross-section of a solder joint with pancake-type void formation and propagation in eutectic Sn-Pb solder [1.55].	24
Figure 1.12: Concentration profile near a phase boundary [1.74].	30
Figure 1.13: Simulated EM-enhanced IMC growth [1.74].	31
Figure 1.14: Simulated vacancy flux as a function of current stressing time [1.74]. The negative sign indicates that the vacancy flux is moving in the direction from the Sn solder to the Cu UBM.	31
Figure 1.15: Composite (97Pb-3Sn with eutectic Sn-Pb) solder joints (a) before testing, and (b) after TM [1.77].	35
Figure 2.1: Flip-chip test vehicle.	38
Figure 2.2: (a) X-ray microscope image of a test vehicle. The viewing direction is from the top of Si die to the bottom of substrate (top view). (b) Top view of an array of 579 solder bumps between a Si die and a substrate. The red boxes indicate two pairs of bumps for EM tests.	39
Figure 2.3: Schematic diagram of the cross-section of a test vehicle. Only bumps under test are shown. The image is not scaled.	40
Figure 2.4: Schematic diagram of a Wheatstone bridge circuit in the solder EM test system designed for detecting small resistance changes of solder bumps.	42
Figure 2.5: Schematic diagram of the test system configuration designed for solder EM.	45
Figure 2.6: HP 6031A system power supply.	46
Figure 2.7: 6 constant current controlling boards with each board having 10 channels.	47
Figure 2.8: Wheatstone bridge circuit board.	48

Figure 2.9: Schematic diagram of a potentiometer.	48
Figure 2.10: Sigma M42 temperature chamber.	50
Figure 2.11: Schematic diagram of a test configuration inside a temperature chamber. Thermal compound (not shown) is applied between the test vehicle and Cu plate. The image is not scaled.	50
Figure 2.12: Keithley 7001 switch system. Three switch mainframes are shown and 5 out of 6 card slots are in use.	51
Figure 2.13: Keithley 196 system DMM.	52
Figure 2.14: Data acquisition system.	52
Figure 2.15: Soldered and insulated test vehicle.	53
Figure 2.16: 30 test vehicles attached on a Cu plate inside a temperature chamber.	54
Figure 2.17: Trends of CDF plots with respect to N based on the weakest link model. In the plot, the single-link ($N = 1$) system was assumed to obey the lognormal distribution. [2.3]	59
Figure 2.18: A CDF plot from Table 2.1. The failure data of samples consisting of two anode joints were deconvoluted to obtain the CDF values for samples with a single anode joint.	62
Figure 3.1: Schematic diagrams of flip-chip solder joints with (a) Cu UBM (18 μm), and (b) Ni UBM (2 μm).	66
Figure 3.2: Typical V_g traces for solder joints with Cu UBM.	70
Figure 3.3: Typical V_g traces for solder joints with Ni UBM.	72
Figure 3.3: (<i>cont'd</i>) Typical V_g traces for solder joints with Ni UBM.	73
Figure 3.4: Calculated off-balance voltage V_g with respect to the fraction of voided area (ratio of void to interfacial area).	75

Figure 3.5: Temperature dependence of deconvoluted failure distributions based on the open failure criterion for solder joints with (a) Cu UBM, and (b) Ni UBM. Current density was fixed at 5.16×10^4 A/cm ² . Temperatures shown represent the Si backside temperatures.....	77
Figure 3.6: Temperature dependence of deconvoluted failure distributions based on the first resistance jump criterion for solder joints with (a) Cu UBM, and (b) Ni UBM. Current density was fixed at 5.16×10^4 A/cm ² . Temperatures shown represent the Si backside temperatures.....	78
Figure 3.7: Current density dependence of deconvoluted failure distributions based on the open failure criterion for solder joints with (a) Cu UBM, and (b) Ni UBM. The Si backside temperature was fixed at 140°C.	80
Figure 3.8: Current density dependence of deconvoluted failure distributions based on the first resistance jump criterion for solder joints with (a) Cu UBM, and (b) Ni UBM. The Si backside temperature was fixed at 140°C.....	81
Figure 3.9: Plot of R/R_r with temperature for the TCR measurement.	83
Figure 3.10: Plot of the resistance increase as a function of the applied current when the chamber temperature was set to 120°C.....	85
Figure 3.11: Simulated temperature (in K) of the anode solder joints with Cu UBM under current stressing of (a) 0.81 A, (b) 1.01 A, and (c) 1.11 A. Top – die side; bottom – substrate side.	88
Figure 3.12: EM activation energies after taking into account the Joule heating effect under current stressing of 1.01A, based on (a) the open failure criterion, and (b) the first resistance jump criterion.	90

Figure 3.13: Refined current density exponent after taking into account the Joule heating, based on (a) the open failure criterion, and (b) the first resistance jump criterion.	92
Figure 3.14: SEM micrographs of solder joints with Cu UBM. (a) A joint in a pristine sample, (b) a joint without current stressing at 140°C for 263 hrs, (c) a cathode joint and (d) an anode joint with 1.01 A current stressing. (b)-(d) are from the same sample.	97
Figure 3.14: (<i>cont'd</i>) SEM micrographs of solder joints with Cu UBM. (a) A joint in a pristine sample, (b) a joint without current stressing at 140°C for 263 hrs, (c) a cathode joint and (d) an anode joint with 1.01 A current stressing. (b)-(d) are from the same sample.	98
Figure 3.15: EM damage evolution in the anode joint with Cu UBM. (a) Initial stage of Cu depletion, (b) void initiation prior to the resistance jump, (c) crack propagation subsequent to the resistance jump, and (d) final open failure.	101
Figure 3.15: (<i>cont'd</i>) EM damage evolution in the anode joint with Cu UBM. (a) Initial stage of Cu depletion, (b) void initiation prior to the resistance jump, (c) crack propagation subsequent to the resistance jump, and (d) final open failure.	102
Figure 3.16: SEM micrographs of solder joints with Ni UBM. (a) A joint without current stressing at 130°C for 150 hrs, (b) a magnified view of (a), (c) a cathode joint and (d) an anode joint with 1.01 A current stressing. (a)-(d) are from the same sample.	104

Figure 3.16: (<i>cont'd</i>) SEM micrographs of solder joints with Ni UBM. (a) A joint without current stressing at 130°C for 150 hrs, (b) a magnified view of (a), (c) a cathode joint and (d) an anode joint with 1.01 A current stressing. (a)-(d) are from the same sample.	105
Figure 3.17: EM damage evolution in the anode joint with Ni UBM. (a) Ni depletion and void formation, (b) void propagation along the IMC/solder interface, (c) further IMC and void formation, and (d) a nearly opened solder.	107
Figure 3.17: (<i>cont'd</i>) EM damage evolution in the anode joint with Ni UBM. (a) Ni depletion and void formation, (b) void propagation along the IMC/solder interface, (c) further IMC and void formation, and (d) a nearly opened solder.	108
Figure 4.1: IMC growth in Cu UBM solders at 150°C. (a) After 117 hours, and (b) after 1594 hours.	114
Figure 4.2: IMC growth in Ni UBM solders at 150°C. (a) After 71 hours, and (b) after 430 hours.	115
Figure 4.3: Schematic illustration of microstructural evolution at the interface between solder and Cu: (a) after reflow; (b) after aging. The vertical arrows in (a) indicate the diffusion of Cu atoms, while those in (b) indicate the moving directions of the boundaries during aging [4.11].	116
Figure 4.4: IMC thickness as a function of aging time without current stressing. (a) Cu ₃ Sn, (b) Cu ₆ Sn ₅ , (c) total Cu-Sn IMCs, and (d) Ni ₃ Sn ₄	118
Figure 4.4: (<i>cont'd</i>) IMC thickness as a function of aging time without current stressing. (a) Cu ₃ Sn, (b) Cu ₆ Sn ₅ , (c) total Cu-Sn IMCs, and (d) Ni ₃ Sn ₄	119
Figure 4.5: Thickness increase of the Cu ₃ Sn layer during thermal aging at intermediate temperatures (125-150°C).....	122

Figure 4.6: Arrhenius plot for the growth rates of Cu-Sn and Ni-Sn IMCs.	123
Figure 4.7: IMC growth in anode joints with Cu UBM under 1.01 A of current stressing for (a) 30 hours at 145°C, and (b) 1536 hours at 130°C.	130
Figure 4.8: Schematic diagram of IMC growth under a non-uniform current stressing condition. An arbitrary current density (j) profile is shown above. The dotted arrows indicate atomic migration or diffusion paths for the formation of IMCs at interfaces, and the solid arrows indicate the resulting interfacial movements.	131
Figure 4.9: IMC growth in Ni UBM solders under 1.01 A of current stressing for (a) 88 hours at 155°C, and (b) 121 hours at 155°C.	132
Figure 4.10: IMC thickness as a function of aging time with current stressing. (a) Cu ₃ Sn, (b) Cu ₆ Sn ₅ , (c) total Cu-Sn IMCs, and (d) Ni ₃ Sn ₄	134
Figure 4.10: (<i>cont'd</i>) IMC thickness as a function of aging time with current stressing. (a) Cu ₃ Sn, (b) Cu ₆ Sn ₅ , (c) total Cu-Sn IMCs, and (d) Ni ₃ Sn ₄	135
Figure 4.11: Cu ₆ Sn ₅ growth under various current stressing conditions simulated by H.-L. Chao [4.70].	137
Figure 4.12: EM-enhanced IMC growth with current density of 5.16×10^4 A/cm ² simulated by H.-L. Chao. (a) Cu ₃ Sn, and (b) Cu ₆ Sn ₅ [4.70].	138
Figure 4.13: Arrhenius plot of wT/j where w is the EM drift velocity and growth rate of Cu ₆ Sn ₅ , (Cu ₃ Sn + Cu ₆ Sn ₅), and Ni ₃ Sn ₄ under current stressing.	140
Figure 4.14: Geometry of axisymmetric FEM model for solder joints with (a) Cu UBM, and (b) Ni UBM.	144
Figure 4.15: Stress-strain curves for Sn-3.5Ag solder (at 155°C) [4.73], Cu at (155°C) [4.74], and Ni (at 200°C) [4.75].	145

Figure 4.16: Hydrostatic pressure contour in a Cu UBM solder at 155°C with 1.0 μm of Cu_3Sn and 9.8 μm of Cu_6Sn_5 (at time = 83 h).	149
Figure 4.17: Maximum hydrostatic stress evolution in Cu UBM solders with IMC growth at 155°C.	149
Figure 4.18: Hydrostatic pressure contour in a Ni UBM solder at 155°C with 4.0 μm of Ni_3Sn_4 (at time = 133 h).	150
Figure 4.19: Maximum hydrostatic stress evolution in Ni UBM solders with IMC growth at 155°C.	150
Figure 5.1: SEM images of upper part of pristine solder joints with (a) 1 μm , (b) 2 μm , and (c) 3 μm of Ni UBM. Diameters of passivation opening, Al pad, and UBM are marked.	155
Figure 5.2: Diameters of solder bump and substrate pad.	156
Figure 5.3: (a) Solid model of a pair of solder joint with 2 μm UBM, and (b) finite element mesh. The cross-sectional plane is the symmetry plane.	157
Figure 5.4: Example of resistance traces for (a) 1 μm , (b) 2 μm , and (c) 3 μm of Ni UBM.	159
Figure 5.5: Log-normal CDF plot of EM lifetime of solder joints with Ni UBM of 1, 2, and 3 μm in thickness.	160
Figure 5.6: SEM images of Sn-2.5Ag solder joints with 3 μm Ni UBM at 1.0 A of current stressing. (a) EM voiding initiated at a current crowding region and propagated through the IMC/solder interface ($\Delta R \sim 10 \text{ m}\Omega$). (b) Failed solder based on the first resistance jump criterion ($\Delta R \sim 160 \text{ m}\Omega$). UBM was almost depleted.	161

Figure 5.7: Current density contour for a solder joint with 2 μm Ni UBM at an applied current of 1 A. (a) shows the entire solder joint system, and (b) shows the solder bump only (rotated from (a) for better illustration of the area of interest).	164
Figure 5.8: Maximum current density in each layer as a function of UBM thickness at an applied current of 1 A.....	166
Figure 5.9: Log-log plot of t_{50} vs. $j_{\text{max, solder}}$ for different UBM thicknesses.	166
Figure 5.10: Current density distribution for various metal trace designs. (a) Design A, (b) Design B, (c) Design C, (d) Design D, and (e) Design E.....	169
Figure 5.10: (<i>cont'd</i>) Current density distribution for various metal trace designs. (a) Design A, (b) Design B, (c) Design C, (d) Design D, and (e) Design E.	170
Figure 5.11: Maximum current density in each layer with different metal trace designs at an applied current of 1 A. For Design C, D, and E, the local maximum at the entrance of passivation opening was chosen as j_{max} in the metal trace.	171
Figure 5.12: Effects of solder joint scaling on maximum current density. The applied current was fixed at 1 A.	174
Figure 6.1: Schematic diagram of the experimental setup (not to scale). Thermal compound (not shown) was applied between the Cu plate and the test module and between the test module and the cooler base.	180
Figure 6.2: Pristine solder joint with (a) Ni UBM (1 μm), and (b) Cu UBM (18 μm).	181

Figure 6.3:	X-ray microscope image of solder bump arrays (shown as black solid circles) in a test module. Resistance of two pairs of solder joints (4th, 5th, 8th, and 9th from left in the bottom first row) was monitored during test. 31 solder joints in the bottom first row were cross-sectioned after test. The cross-sectioned plane is marked as a dotted line in red.	182
Figure 6.4:	Finite element model. (a) Geometry and mesh of test module, and (b) geometry of a bump array and substrate traces.....	184
Figure 6.5:	Comparison of initial resistances from measurement and FEM as a model validation.....	185
Figure 6.6:	Contour plots of Sample B subject to 0.5 A of current stressing. (a)-(c) Temperature contour (in K), and (d) z-component of temperature gradient contour (in K/mm). (a) Package (quarter model), (b) solder joint pair, and (c)-(d) cross-sectioned solder bump pair.	186
Figure 6.6:	(<i>cont'd</i>) Contour plots of Sample B subject to 0.5 A of current stressing. (a)-(c) Temperature contour (in K), and (d) z-component of temperature gradient contour (in K/mm). (a) Package (quarter model), (b) solder joint pair, and (c)-(d) cross-sectioned solder bump pair.	187
Figure 6.7:	FEM results of (a) temperature, and (b) average temperature gradient in a solder bump.....	189
Figure 6.8:	Backscattered electron micrograph of a solder joint with Ni UBM in Sample A after 139 days of thermal aging.....	192
Figure 6.9:	Solder joints with Ni UBM subject to a current stressing of 0.5 A in Sample B. (a) 4th, (b) 5th, (c) 8th, and (d) 9th solder joint.	192

Figure 6.10: Solder joints with Ni UBM in Sample B after 138 days of TM stressing. (a)-(f) show 6 solder joints with voids. The other 21 solder joints under TM stressing only had no voids as shown in (g).	193
Figure 6.11: Solder joints with Ni UBM under current stressing of 0.8 A in Sample C. (a) 4th, (b) 5th, (c) 8th, and (d) 9th solder joint.	195
Figure 6.12: Solder joints with Ni UBM in Sample C after 69 days of TM stressing. (a)-(g) show 7 solder joints with voids. The other 20 solder joints without current stressing had no voids as shown in (h).	196
Figure 6.13: Solder joints with Cu UBM (a)-(d) under current stressing of 0.8 A for 12 days, and (e) under TM stressing for 48 days, in Sample D. (a) 4th, (b) 5th, (c) 8th, and (d) 9th solder joint.	199
Figure 6.14: Solder joints with Cu UBM in Sample E after TM stressing of 48 days. (a)-(d) show 4 solder joints with UBM dissolution. The other 27 solder joints had no noticeable UBM dissolution as shown in (e).	200
Figure 6.15: Estimated atomic flux driven by EM and TM, and the ratio of corresponding driving forces as a function of temperature for solder joints.....	203

Chapter 1: Introduction

Trends in semiconductor devices and packages are toward higher performance, multi-functionality, smaller form factor, and eco-friendliness as shown in Fig. 1.1. This leads to demands for higher I/O (input/output) and power density, finer interconnection pitch, and implementation of new materials such as Pb-free solder. To fulfill these demands it is necessary to address reliability concerns associated with them. In this chapter, a brief overview for flip chip technologies, reliability issues including electromigration (EM) and thermomigration (TM) in solder joints are reviewed, and research objectives for this dissertation are discussed.

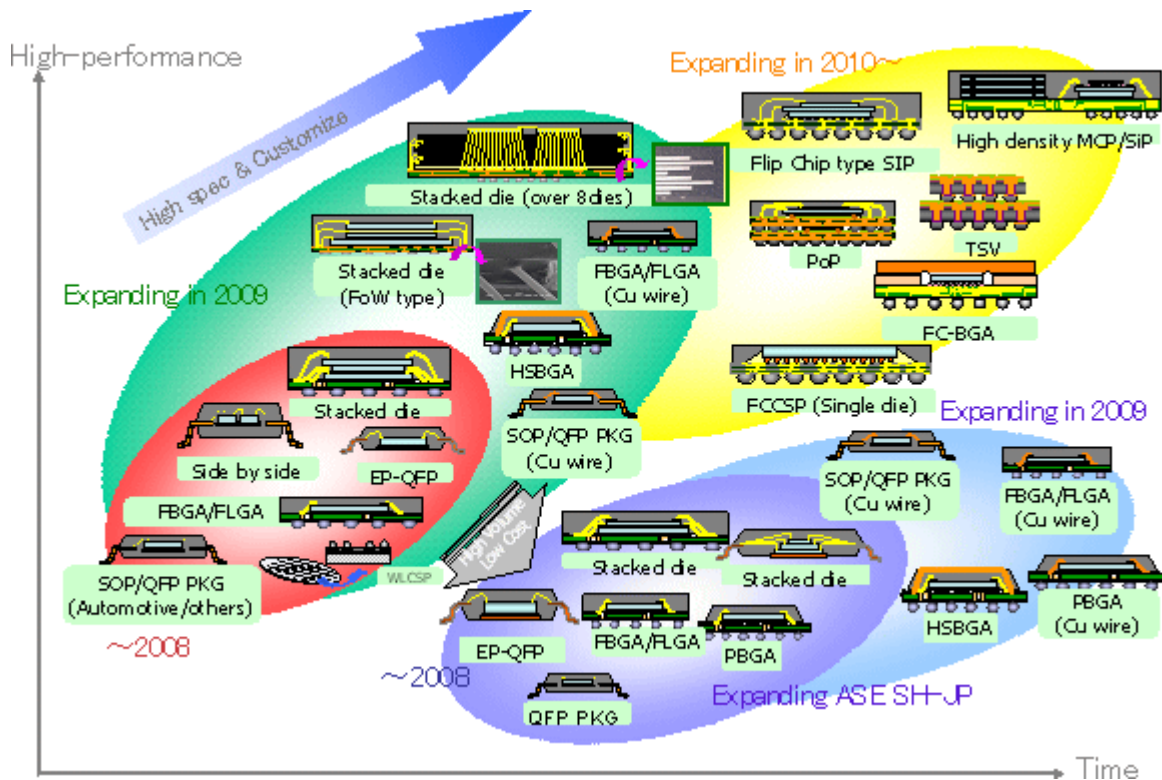


Figure 1.1: Package roadmap by ASE. (Source: <http://www.asejp.aseglobal.com>)

1.1 BACKGROUND

Assembly and packaging is the final manufacturing process transforming semiconductor devices into functional products for end users. Packaging provides electrical connection for signal and power, thermal dissipation paths, and mechanical/environmental protection. Packaging technologies have been developed in parallel with semiconductor device technologies. Moore's law, stating the number of transistors doubles every two years, has proven to be accurate for nearly 40 years (see Fig. 1.2) and served as a main driver for semiconductor technology innovations. The transistor count increased from 2,300 in 1971 to 2,300,000,000 in 2010 [1.1]. Over the same period, the microprocessor die size has grown approximately 7% annually, which has been accompanied by doubling the frequency every two years, and power has increased at an exponential rate [1.2]. These trends have also a significant impact on packaging technology. As the transistor count and frequency increase, the required number of interconnects between the die and package has to increase to accommodate increased signal counts as well as to support the increased demand for power and ground. According to Rent's Rule, the number of terminal pins, T , follows a power-law relation $T = tg^p$, where g is the number of logic gates, t and p are constants ($p < 1.0$, and generally $0.5 < p < 0.8$) [1.3]. This has changed the first-level interconnect technology from peripheral wire bonding to area array flip-chip bumping. The flip-chip solder pitch is projected to continuously decrease to meet these requirements according to International Technology Roadmap for Semiconductors (ITRS) [1.4], as seen in Fig. 1.3.

Transistor count

Curve shows "Moore's Law": transistor count doubling every two years

Date of introduction

Processor	Approx. Date of Introduction	Approx. Transistor Count
Intel 4004	1971	2,300
Intel 8008	1972	6,000
Intel 8080	1974	60,000
Intel 286	1982	290,000
Intel 386	1985	2.75 million
Intel 486	1989	12 million
Intel Pentium	1993	3.1 million
Intel K5	1995	5.5 million
Intel K6	1997	5 million
Intel P5	1997	5.5 million
Intel P6	1999	9.5 million
Intel K7	2000	9.5 million
Intel K8	2002	29 million
Intel K9	2004	73 million
Intel K10	2006	310 million
Core 2 Duo	2006	291 million
Core i7	2008	731 million
Core i9	2008	731 million

3

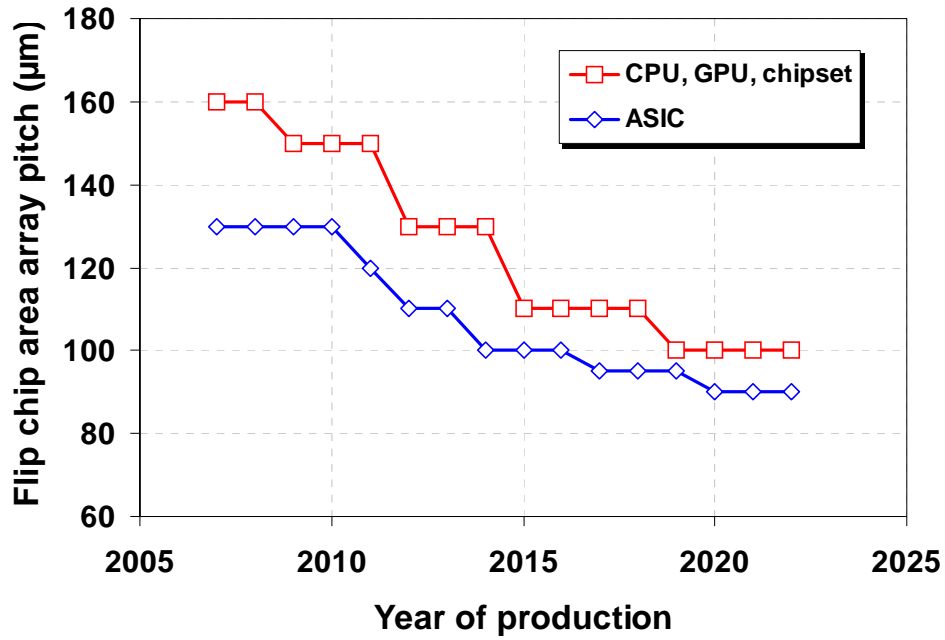


Figure 1.3: Flip-chip area array pitch projected by ITRS in 2007.

Meanwhile, the microelectronics industry is approaching the limit of traditional CMOS (complementary metal–oxide–semiconductor) scaling [1.4]. The continued growth of the industry, driven by a continuous reduction in cost per function, will require new device types and materials. There will be a gap between the time when CMOS scaling can no longer follow the Moore’s law and the time when a new generation of device architectures and materials is developed to support the continuous drop in cost per function. As the traditional Moore’s law scaling becomes more difficult to attain, assembly and packaging offers another route to improve in both cost and performance for microelectronic systems. As a result, the industry is putting more efforts on packaging technology innovations to fill this gap. Recent advances in system-in-package (SiP) and 3D integration using through-silicon-via (TSV) are a few examples [1.4]. In these new

types of packages, solder bumping technology can also be a viable solution for die-to-die or die-to-interposer interconnection.

Traditionally, lead-tin (Pb-Sn) alloys have been widely used as solder alloys in microelectronics. However, due to the potential hazards associated with the toxicity of Pb, regulations to ban the use of Pb in electronics have been established by the European Union (EU) through the Waste Electrical and Electronic Equipment (WEEE) Directive and Restriction of Hazardous Substances (RoHS) Directive. The RoHS directive took effect on July 1, 2006, with some exceptions [1.5]. Although Pb in solders used for flip chip packages are currently exempt from the RoHS directive [1.6], the electronic industry is pushing ahead toward complete elimination of Pb in all products [1.7].

1.2 FLIP CHIP TECHNOLOGY

1.2.1 Overview

Flip chip is one of the advanced methods of the first-level interconnection – electrically connecting the chip (die) to the package carrier. Other, more conventional methods include wire bonding and tape automated bonding (TAB). Schematic diagrams of these three interconnection methods are illustrated in Fig. 1.4.

Wire bonding is a technique where fine metal wires (typically Au or Al) are individually connected between the I/O pads on a chip and the substrate pads. This technology originated from AT&T's beam lead bonding in the 1950's [1.8]. This is the oldest and most widely used technology in the first-level interconnection. By virtue of its flexibility derived from the point-to-point process and high reliability, wire bonding accounts for approximately 90% of all the chip-to-package interconnections [1.9]. Cu bonding wires are currently being developed to prevent bonding failure due to the

formation of the brittle Au-Al intermetallic compounds and to save manufacturing cost while achieving superior electrical, thermal, and mechanical performance [1.10]. However, the maximum number of I/O is limited because only the periphery of the chip can be used for wiring as shown in Fig. 1.5(a). Also, due to its long wire loops, the resistance and inductance are relatively high, which can degrade electrical performance.

TAB, which was invented in mid 1960's, involves mounting and interconnecting integrated circuits (ICs) on metallized flexible polymer tapes (Fig. 1.5(b)). The interconnection between the chip and the tape lead is accomplished through gold or solder bumps which are placed either on the chip or on the tape. Subsequently, the tape lead is bonded to a substrate or package [1.9]. Although TAB can handle slightly higher I/O counts than wire bonding, the maximum number is still limited since only the periphery is used for interconnection in most cases. Other shortcomings include limited production infrastructure, process inflexibility, and high cost [1.8].

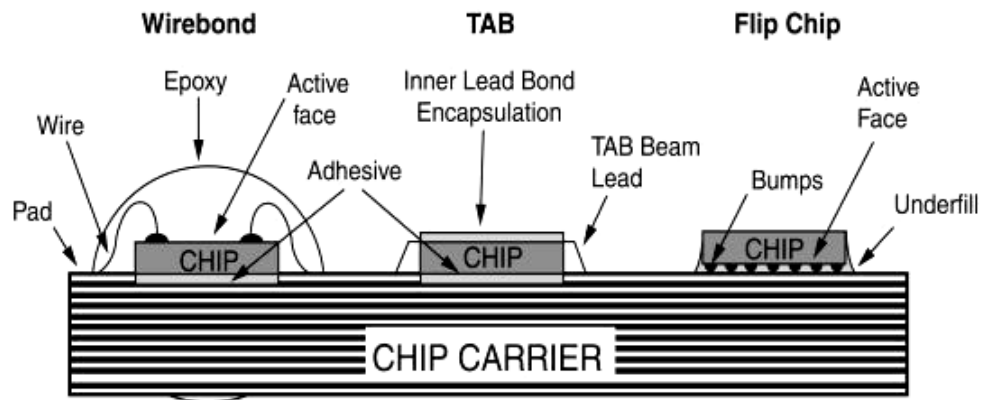
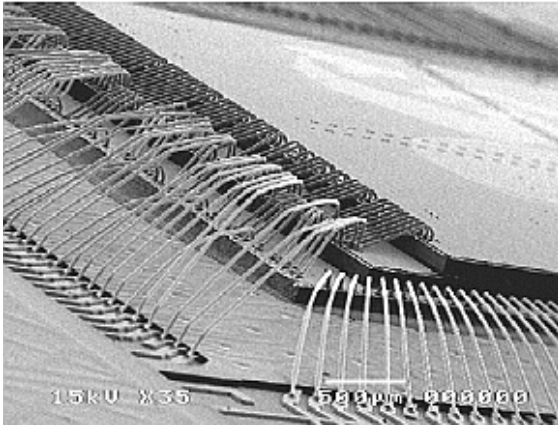
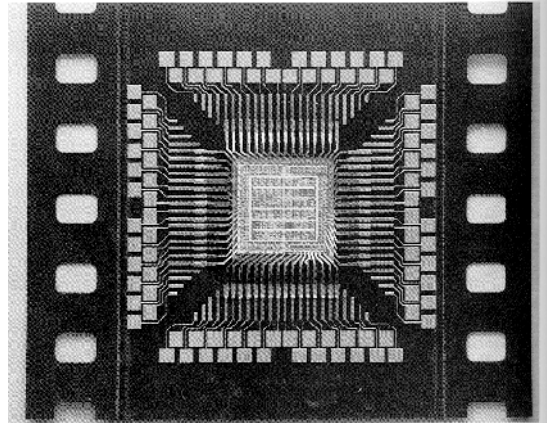


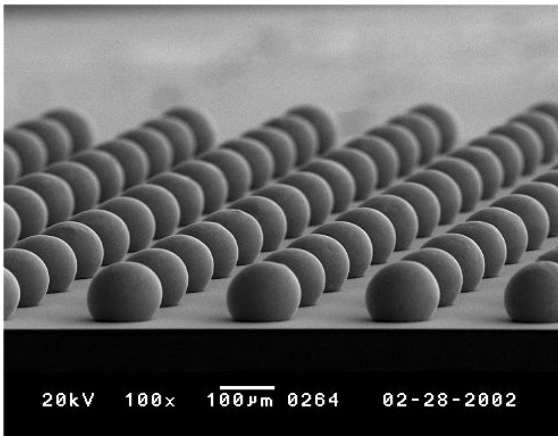
Figure 1.4: First-level (chip-to-package) interconnection techniques [1.8].



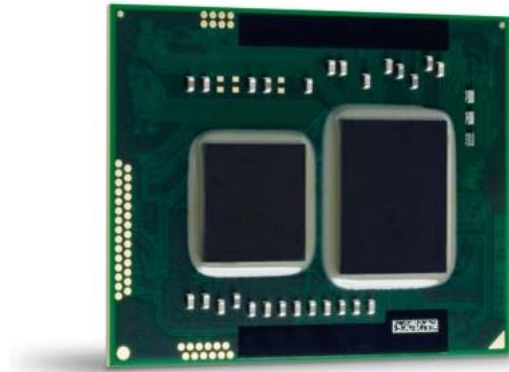
(a)



(b)



(c)



(d)

Figure 1.5: Examples of (a) wire bonding [1.11], (b) TAB [1.12], (c) flip-chip solder bumps [1.13], and (d) flip-chip package (Intel 32 nm processor) [1.14].

In contrast to wire bonding and TAB, flip chip can utilize the entire area of a chip to achieve the chip-to-package interconnection, usually through an area-array bump structure. This process was first introduced by IBM in 1964 for ceramic substrates as the Solid Logic Technology [1.15], which was converted to the Controlled Collapse Chip Connection (C4) in 1969 [1.16]. In this process, semiconductor chips are “flipped over” with their active face down, and bonded directly to a printed circuit board or chip carrier

substrate. The most common method of flip chip interconnection is by reflowing solder bumps. Another method is thermocompression bonding of non-solder bumps with polymer-based electrically conductive adhesives (ECAs) [1.17]. Non-solder bumps include Au or Cu stud bumps, Au plating bumps, and electroless Ni/Au bumps. Isotropic conductive adhesives (ICAs) or anisotropic conductive adhesives (ACAs) are used as ECAs. Although the second method holds advantages including low processing temperature and fine pitch application, it is not adequate for high-end applications due to its high bonding pressure and inferior current carrying capability. In this regard, discussion of flip-chip process and technology will be only on the first method hereafter. Figures 1.5(c) and (d) show an example of a flip chip package. Although flip chip technology has been in manufacturing for nearly 40 years, it is gaining momentum only recently to accommodate for ever-increasing demand for improving I/O density, pin counts and electrical performance [1.18]. The maximum capability for I/O count in 2010 is expected to be 1000 for wire bonding, 2000 for TAB, and 10000 for flip chip [1.8]. In addition, flip chip provides a superior electrical performance including extremely low resistance, capacitance, and inductance per joint. This allows the chip to operate at very high frequencies (up to 100 GHz) [1.9]. Therefore, flip chip has emerged as the most viable solution for high-end devices such as MPUs, graphics processors, and high performance application-specific integrated circuits (ASICs).

1.2.2 Solder Bumping Processes

Flip chip bonding typically involves the electrical and mechanical interconnections by solder bumps between the chip and the carrier substrate. Figure 1.6 illustrates the most common solder bumping processes including electroplating and solder paste printing (stencil printing). The solder joints used in this study were

electroplated Sn-2.5Ag solders with electroplated Cu or Ni under-bump metallurgy (UBM). The general process flow for solder bumping by electroplating is as follows:

1. Sputter TiW/Cu or Ti/Cu seed layers;
2. Spin-coat photo-resist layer, followed by baking;
3. Expose and develop desired pattern over the Al or Cu bond pads;
4. Electroplate Cu or Ni;
5. Strip photo-resist pattern;
6. Selectively etch Cu seed layer followed by TiW or Ti layer;
7. Reflow solder bumps;
8. Flux clean.

1.2.2.1 Evaporation

Evaporated bumps were the original flip chip approach pioneered by IBM 40 years ago with high-lead solder. However, the geometry of evaporators, directing a stream of material in straight lines from a small source to an entire wafer, can not be readily scaled up to accommodate larger wafers. In addition, many of the proposed Pb-free alloys have greater than 90 wt.% Sn content. The extremely low vapor pressure of Sn makes it evaporate more slowly than Pb. This requires a longer deposition time, which reduces the manufacturing throughput and increases operating costs. Generally, evaporators waste more material than is deposited. This is wasteful since Sn is more expensive than Pb. As a result, evaporating Pb-free bumps onto 300mm wafers appears to be infeasible although evaporation will remain important for smaller wafers for many specialty applications [1.17, 1.19, 1.20].

1.2.2.2 Electroplating

Electroplating has long been the preferred method to produce excellent quality, fine pitch solder bumps. However, some proposed Pb-free alloys will make electroplating difficult. The large electrochemical potential difference between Sn and Ag in these alloys requires special handling. Electroplating of ternary and quaternary lead-free alloys will further increase the process complexity and cost since the difficulties in controlling the bath chemistry and avoiding contamination increase with the number of baths required. Larger wafers also increase the difficulty of maintaining uniform plating bath concentrations and current densities across the entire wafer. Non-uniformities cause plating thickness and deposition rate variations, raising bumping costs and lowering bump quality [1.17].

1.2.2.3 Stencil Printing

Stencil printing of solder paste is easily adapted to Pb-free solders since the paste is available in a wide range of alloys. However, stencil printing is limited to bump pitches greater than 150 μm . Printed solder paste shrinks during reflow, requiring a starting paste print area substantially larger than the resulting bump. The molten spheres must be well separated during reflow to avoid solder bridging. The printing process, forcing paste through stencil holes, may introduce voids within the bumps. Variations in the volume of deposited paste cause bump height variations. Maintaining precise stencil alignments across the wafer becomes more difficult for larger wafers, affecting cost, quality, or both [1.17].

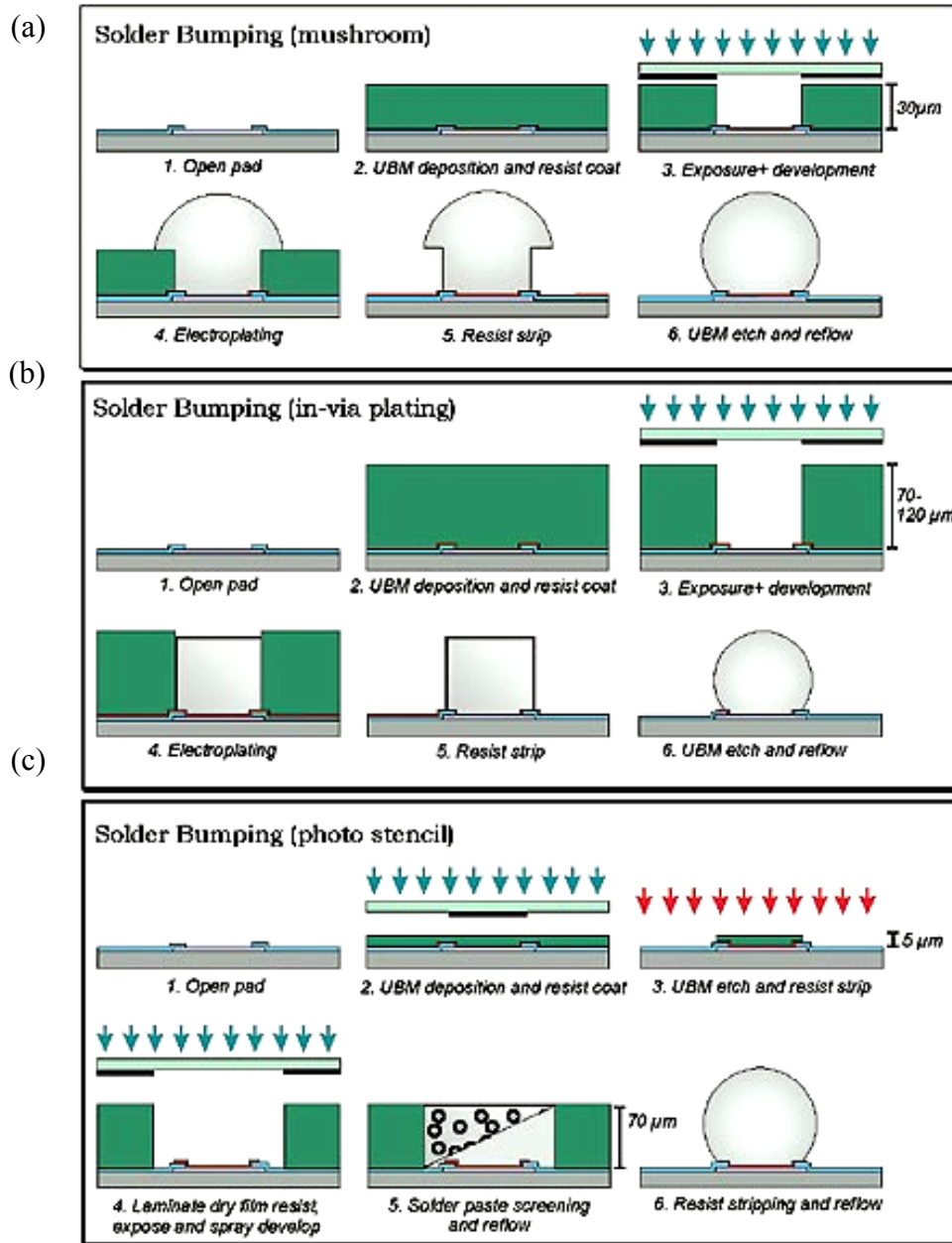


Figure 1.6: Three common solder bumping process flows [1.18]. Electroplated solder bumps are either (a) plated over the resist edge (mushroom), or (b) fully plated in-via. With electroplating, the UBM is always etched after solder deposition. (c) With stencil printing, the UBM etch is done before solder deposition. Unlike electroplated, printed solder bumps are reflowed before resist stripping.

1.2.3 Under Bump Metallurgy (UBM)

Flip chip processes require UBM deposition prior to solder bumping. UBM provides a critical interface between metal pads of the IC chip and solder bumps. It should satisfy the following requirements [1.18, 1.21]:

- Good adhesion to the wafer passivation and the final metal pad (Al or Cu);
- Protection of the final metal pad from the environment;
- Low contact resistance between the metal pad and the bump;
- Effective barrier to solder diffusion into the metal pad;
- Seed layer for solder wettability.

UBM usually consists of a multi-layer metal stack to fulfill the above functions. Ti and TiW are most common adhesion/barrier layers in UBM stacks. Cr was used in the past, but has been eliminated due to environmental issues associated with etching of Cr [1.21]. Cu has been widely used as a solderable layer that reacts with Sn to form intermetallic compounds (IMCs). However, a thick layer of Cu is necessary with Pb-free solders because the high Sn content in Pb-free solders results in rapid consumption of Cu. Alternatively, Ni can be used as a solderable layer as well as a barrier layer because of its much slower reaction rate with Sn. However, the thickness of Ni needs to be controlled since the residual stress of the Ni film is typically high [1.21, 1.22]

1.2.4 Pb-Free Solder Alloys

At present, nearly all Pb-free solders are Sn-based alloys. These include eutectic Sn-3.5Ag with alloying elements of Bi, Cu, Sb, In, or Zn. Other alloys based on the Sn-Cu, Sn-In, Sn-Sb, Sn-Bi, and Sn-Zn systems have also been proposed. Table 1.1 listed the potential Pb-free solder candidates. Also, a narrow two-phase region (temperature

difference between liquidus and solidus) is desired because it prevents the joint from moving and becoming disturbed during solidification. Binary or ternary near-eutectic alloys are also desired because these simpler alloys reduce the potential for compositional variations that affect the behavior of the solder joint. Based on these criteria, Sn-3.5Ag, Sn-0.7Cu, and Sn-3.8Ag-0.7Cu are among the promising flip-chip solder alloys [1.23]. Eutectic Sn-Bi and eutectic Sn-In have low melting points. Due to relative poor high temperature mechanical strength, lack of ductility (for Sn-Bi alloys), high cost (for Sn-In alloys) and limited resource, these alloys are finding very limited applications in the industry [1.24]. Sn-Zn or Sn-Zn-Bi alloys have significant processing difficulties due to the rapid oxidation behavior of Zn in the molten state and corrosion susceptibility of the alloy after solidification [1.23, 1.24]. Sn-Sb alloy has a wide two phase region and the liquidus temperature is too high for chip attachment to organic substrates. Sn-Ag-Bi alloy also has a wide two-phase region. Sn-Ag-Cu-Sb would damage the die in flip-chip applications due to the high strength of the alloy [1.23].

Below eutectic temperatures, equilibrium phases of Sn-Ag, Sn-Cu, and Sn-Ag-Cu alloys consist of a Sn-rich phase and an IMC. For example, the Sn-rich phase is in equilibrium with Ag_3Sn in the eutectic Sn-Ag alloy below 221°C as shown in Fig. 1.7. Since metallic Sn (white tin or β -Sn) has the body-centered tetragonal lattice structure and tends to deform by twinning, its mechanical and electrical properties are anisotropic. Sn-based solder alloys are expected to have anisotropic properties, too. Thus the dispersion of the IMC may lead to inhomogeneous microstructures, such as large plate-type Ag_3Sn . To avoid the formation of such large plate-like IMC which can make the solder more brittle, the Ag concentration in the solder should be less than 3% [1.26]. A plate-type Ag_3Sn phase was not observed in Sn-2.5Ag investigated in this study.

Table 1.1: Sn-based Pb-free solder alloys [1.25].

Alloy system	Composition (wt.%)	Melting point or range (°C)
Sn-Bi	Sn-58Bi (eutectic)	138
Sn-In	Sn-52In (eutectic)	118
	Sn-50In	118-125
Sn-Zn	Sn-9Zn (eutectic)	198.5
Sn-Bi-Zn	Sn-8Zn-3Bi	189-199
Sn-Cu	Sn-0.7Cu (eutectic)	227
Sn-Ag	Sn-3.5Ag (eutectic)	221
	Sn-2Ag	221-226
Sn-Ag-Bi	Sn-3.5Ag-3Bi	206-213
	Sn-7.5Bi-2Ag	207-212
Sn-Ag-Cu	Sn-3.8Ag-0.7Cu (eutectic)	217
	Sn-3.0Ag-0.5Cu	218
Sn-Ag-Cu-Sb	Sn-2Ag-0.8Cu-0.5Sb	216-222
Sn-Sb	Sn-5Sb	232-240
Sn-Au	Au-20Sn	280

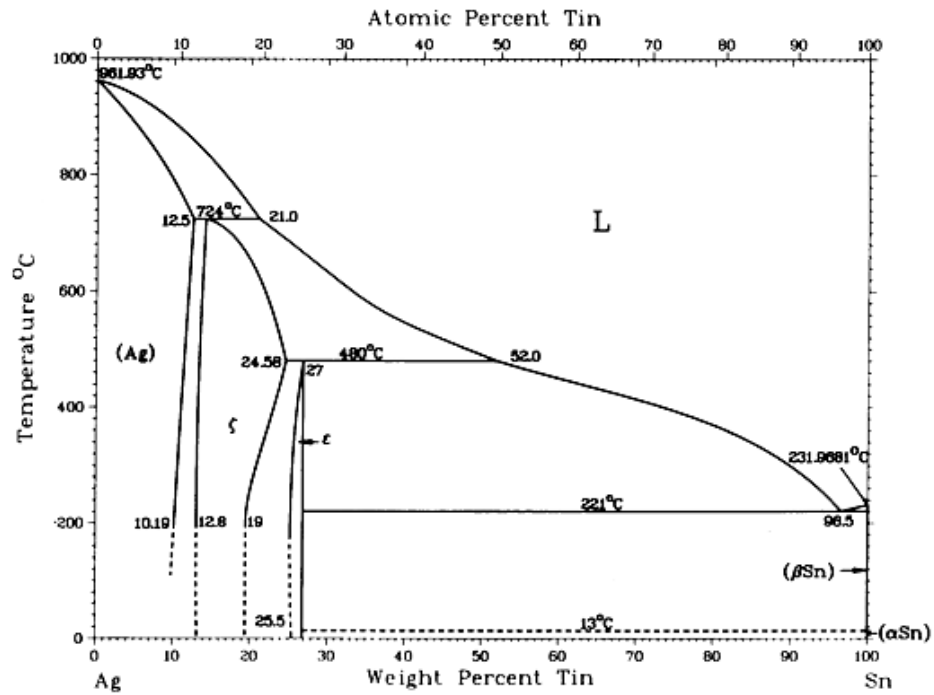


Figure 1.7: Phase diagram for Ag-Sn system [1.27].

1.2.5 Intermetallic Compounds (IMCs)

Upon solder reflow, IMC layers form at the interface between the molten solder and metal substrate (or UBM). For the Cu-Sn reaction, Cu_3Sn and Cu_6Sn_5 are stable phases according to the phase diagram shown in Fig. 1.8(a). However, it has been reported that the Cu_3Sn phase did not appear immediately but appeared after a certain amount of reflow time or solid-state annealing time [1.24, 1.28-1.30]. The Cu_3Sn phase has been shown to grow at the expense of the Cu_6Sn_5 phase. As the Cu_3Sn phase expanded, Kirkendall voids were found in the Cu_3Sn phase near the Cu/ Cu_3Sn interface [1.31]. According to Yang and Messler, Kirkendall voiding is only observed with electroplated Cu because the Kirkendall void formation is facilitated by hydrogen entrapment in the electroplated Cu deposit [1.32]. The morphology of the Cu_6Sn_5 phase changes from scallop-type to layer-type with aging time [1.30, 1.33].

In the Ni-Sn system, Ni_3Sn_4 has been observed to grow at the Ni/Sn interface [1.34-1.41] while there are three thermodynamically stable IMCs, Ni_3Sn , Ni_3Sn_2 , and Ni_3Sn_4 , according to the phase diagram shown in Fig. 1.8(b). The initial morphology of the Ni_3Sn_4 phase is scallop-like or needle-like [1.37, 1.40-1.42]. It is interesting to note that if solder alloys containing Cu, such as Sn-Ag-Cu alloys, react with Ni, $(\text{Cu,Ni})_6\text{Sn}_5$ forms and grows at the solder/Ni interface [1.43]. During thermal aging, the growth of both Cu-Sn and Ni-Sn IMCs were found to follow the parabolic growth law ($t^{1/2}$ dependence), indicating that the growth is diffusion-controlled [1.5, 1.24, 1.28-42].

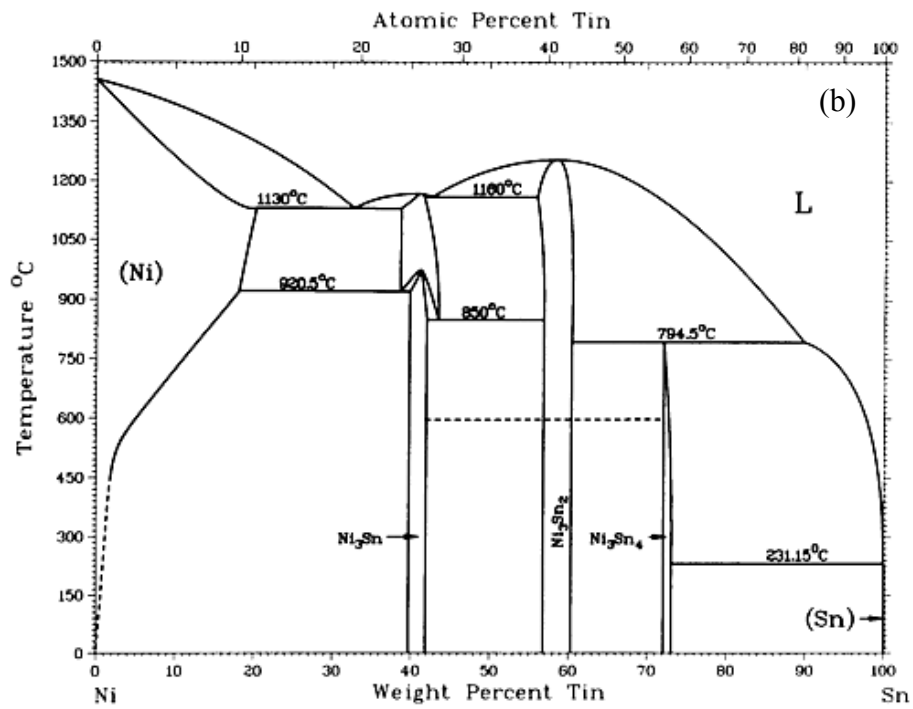
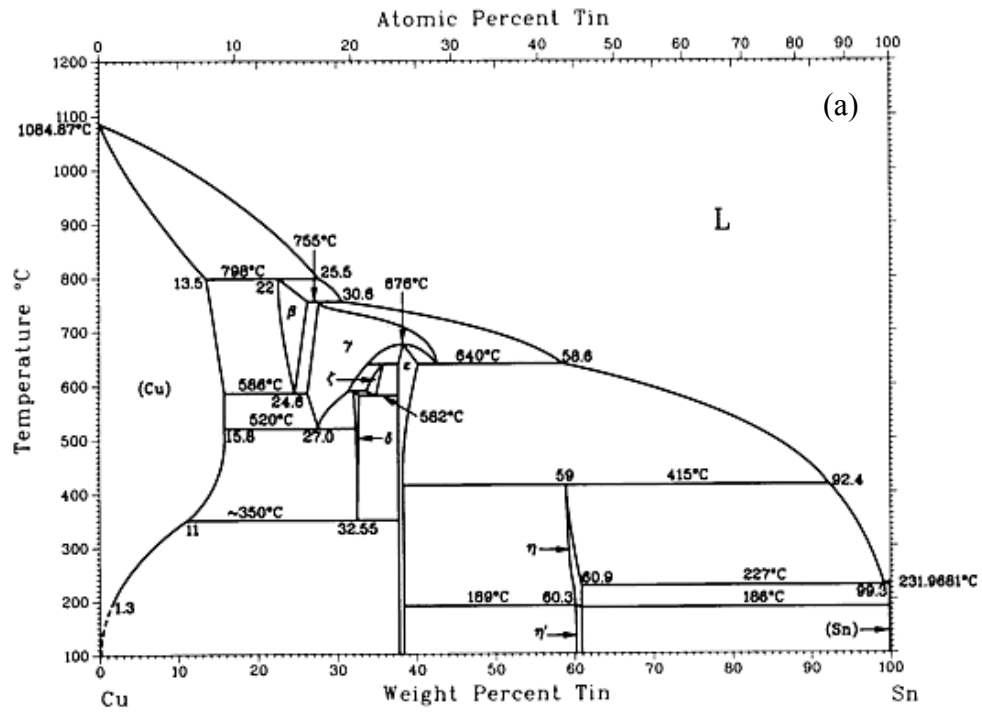


Figure 1.8: Phase diagram for (a) Cu-Sn system, and (b) Ni-Sn system [1.27].

1.3 ELECTROMIGRATION AND THERMOMIGRATION PHENOMENA IN SOLDER JOINTS

1.3.1 Overview

As seen in Fig. 1.3, the solder bump pitch in flip chip packages is expected to be reduced by ~30% in the next 10 years. Assuming that the current applied to a solder joint remains the same, the current density will increase by a factor of 2. In today's circuit design, each power bump may carry 0.2 A [1.44]. Under this condition, the average current density in a 50 μm solder bump will reach 10^4 A/cm^2 , while the current density at the passivation opening (contact area between a bond pad and UBM) will be even larger. This current density level is about two orders of magnitude lower than that for Al or Cu interconnects in BEOL (back-end-of-the-line). However, electromigration (EM) can still be a serious reliability concern in flip-chip solder joints at such low current density because solder alloys have a low melting point, high diffusivity, and a large effective charge number [1.44, 1.45]. Furthermore, IMC growth is enhanced by current stressing. This is more prominent in Sn-based Pb-free solders. Not only this can accelerate voiding by flux imbalance, but also degrade the mechanical reliability and electrical performance of solder joints due to the brittle, highly stressed, and highly electrically resistive nature of IMCs.

As the device feature size decreases and power density increases, local hot spots can be created. Heat dissipation from die to package substrate would be less efficient due to the smaller size of solder bumps. Thus, the temperature gradient in solder joints can increase to induce thermomigration (TM) [1.46]. TM or the Soret effect is a forced-diffusion driven by a temperature gradient. During EM testing metal traces on the die are major Joule heat sources [1.47]. This could cause the die side to be hotter than the substrate side. When the temperature gradient in a solder joint is large enough, the effect

of TM may occur along with EM. Hence, it is important to understand EM and TM together for Pb-free solder joints in flip chip packages.

1.3.2 Electromigration

1.3.2.1 Fundamentals of Electromigration (EM)

EM is defined as a mass transport phenomenon in metals due to momentum transfer between conducting electrons and diffusing metal atoms under an applied electric field. The driving force for EM consists of two parts: (1) the interaction of the inherent charge of each metal ion with the electric field (electrostatic force, F_{el}), and (2) the momentum transfer of electrons onto the metal ions (“electron wind” force, F_{wd}). Combining both effects, the effective driving force is expressed as [1.48]:

$$F_{EM} = F_{el} + F_{wd} = (Z_{el} + Z_{wd})eE = Z^*eE = Z^*e\rho j, \quad (1.1)$$

where Z_{el} is the nominal valence of the metal ion, Z_{wd} is the assumed charge number accounting for the momentum exchange effect, e is the electron charge, E is the electric field, Z^* is called the effective charge number, ρ is the resistivity, and j is the current density. Z^* represents the net force exerting to a metal ion by electrons. Z_{el} is positive while Z_{wd} is usually negative. Typical Z^* values for pure metals were found to be of the order of -10^{-1} to -10^{-2} [1.49] The drift velocity, v_d , of the moving ions under EM is described by using the Nernst-Einstein relationship as

$$v_d = \mu F_{EM} = \frac{D}{kT} Z^* e \rho j, \quad (1.2)$$

where μ is the mobility of metal ions, D is the diffusivity, k is the Boltzmann's constant, T is the absolute temperature. The atomic flux driven by EM, J_{EM} , is then given by

$$J_{\text{EM}} = C v_d = C \frac{D}{kT} Z^* e \rho j, \quad (1.3)$$

where C is the concentration of atoms per unit volume. From Eqs. (1.2) and (1.3), it can be found that the DZ^* product at a given condition (temperature and current density) is a key parameter determining the EM reliability.

While the equations described above provide a general description of EM in bulk materials as well as in thin films, they need to be modified to account for the effect of stress-induced backflow in interconnect lines observed by Blech [1.50]. Under EM, the electron wind pushes metal ions toward the anode end while vacancies migrate toward the cathode end. Thus, hydrostatic tensile and compressive stresses are gradually built up at the cathode end and anode end, respectively. The resulting stress gradient drives metal atoms back towards the cathode end resulting in mass transport against the direction of electron wind force. This phenomenon is called the ‘‘Blech effect’’. The driving force for the backflow, F_σ , can be written as:

$$F_\sigma = -\Omega \frac{d\sigma}{dx}, \quad (1.4)$$

where Ω is the atomic volume, σ is the hydrostatic stress in the metal. Consequently, the net atomic flux and the drift velocity are expressed as

$$J = J_{\text{EM}} + J_{\sigma} = C \frac{D}{kT} Z^* e \rho j - C \frac{D}{kT} \frac{\Omega d\sigma}{dx}, \quad (1.5)$$

$$v_d = \frac{D}{kT} (Z^* e \rho j - \Omega \frac{d\sigma}{dx}). \quad (1.6)$$

If one takes $J = 0$ or $v_d = 0$ with approximating $d\sigma/dx$ to $\Delta\sigma/\Delta x$ and replacing Δx by the interconnect line length, L , a threshold value or critical product, $(jL)_c$, is obtained as:

$$(jL)_c = \frac{\Omega \Delta\sigma}{Z^* e \rho}, \quad (1.7)$$

below which the net mass transport vanishes. Therefore, at a given current density EM damage in interconnect lines can be minimized by choosing the line length below the critical value, L_c . Also, the EM reliability can improve by increasing $\Delta\sigma$. This is accomplished by optimizing the design and material to enhance the confinement effect [1.51].

1.3.2.2 EM in Solder Joints

EM in solder joints are differentiated from that in BEOL Al or Cu interconnects for several reasons. First, solder alloys usually consist of at least two components, rather than one as in interconnects. For solder materials, lattice diffusion is the dominant diffusion mechanism because of their low melting point [1.44]. Second, typical UBM materials such as Cu and Ni are noble or near-noble metals, which are fast diffusing species in Pb and Sn by an interstitial diffusion mechanism [1.45, 1.52-1.54]. Third, the EM-driven diffusion encounters multiple phases including UBM, IMCs, and solder. IMC

growth is enhanced by EM, which could govern the mass transport. Fourth, the cross-sectional area changes abruptly when a current passes from a metal trace line on the die to a solder bump. This leads to non-uniform distribution of current density in solder joints, which causes the current crowding at the inner corner of the passivation opening area. This has been known as a critical factor controlling EM reliability [1.55]. Also, since the electric power is proportional to I^2R (I : electric current, R : resistance), significant Joule heat can be generated during EM testing with a high applied current, mainly from the thin metal trace on the die [1.56]. This makes it difficult to determine the solder temperature accurately, which could affect parameters deduced from EM test results.

EM failure in Pb-alloy solders can be classified in two ways: (1) the mass transport of major constituents of solder alloys such as Pb and Sn; (2) the mass transport of minor constituents such as fast diffusers from UBM or substrate. EM of Pb or Sn can lead to voids or extrusions, which eventually cause open or short circuits [1.57-1.60]. Fast diffusion of Cu or Ni in UBM can induce the dissolution of UBM and the formation of interfacial IMC layers. This can lead to circuit failures by dewetting of the solder from the contact or by interfacial fracture [1.61].

Phase separation was observed in eutectic Sn-Pb solder joints under EM [1.26, 1.58, 1.60, 1.62]. Figure 1.9 shows the microstructure of eutectic Sn-Pb solder bumps after current stressing of 2.25×10^4 A/cm² at 150°C. A Pb-rich phase accumulated at the anode side while a Sn-rich phase accumulated at the cathode side. This is because the diffusivities of the two components are different. It has been reported that under current stressing, Pb was found to be the dominant diffusion species at temperatures above 100°C, while Sn was dominant at temperatures below 100°C [1.63].

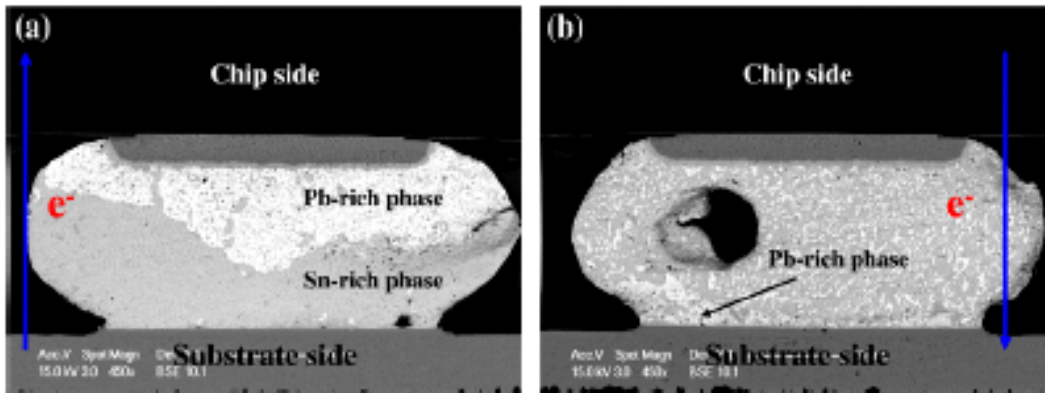


Figure 1.9: Cross-sectional SEM images of the current stressed eutectic Sn-Pb solder bumps at 150°C for 6 h, taken from [1.62]. Electrons flowed (a) from the substrate side to the chip side, and (b) from the chip side to the substrate side.

Figure 1.10 shows composite solder joints (high Pb solder on the die side and eutectic Sn-Pb solder on the substrate side) with 5 μm Cu UBM, under current stressing [1.64]. At the upper left corner of the UBM, IMC grew and UBM depleted, followed by void formation. This was due to the current crowding that occurred where the metal trace with a small cross-section meets the solder joint with a large cross-section. This led to a “pancake-type” void propagation as illustrated in Fig. 1.11. As voids form, the current crowding region moves toward the void front, where the subsequent void propagation takes place. In this way, voids propagate through the interface tracking the current crowding. This is a common failure mode by EM especially when UBM is relatively thin [1.55, 1.64-1.67]. The current density at the current crowding region was found to be about one order of magnitude higher than the average current density at the interface. This makes EM in solder joints more serious. The current crowding can also cause the EM failure rate to be different depending on the current polarity. Typically, solder joints

with electrons passing toward the substrate side fail much faster than those with electrons moving toward the die side.

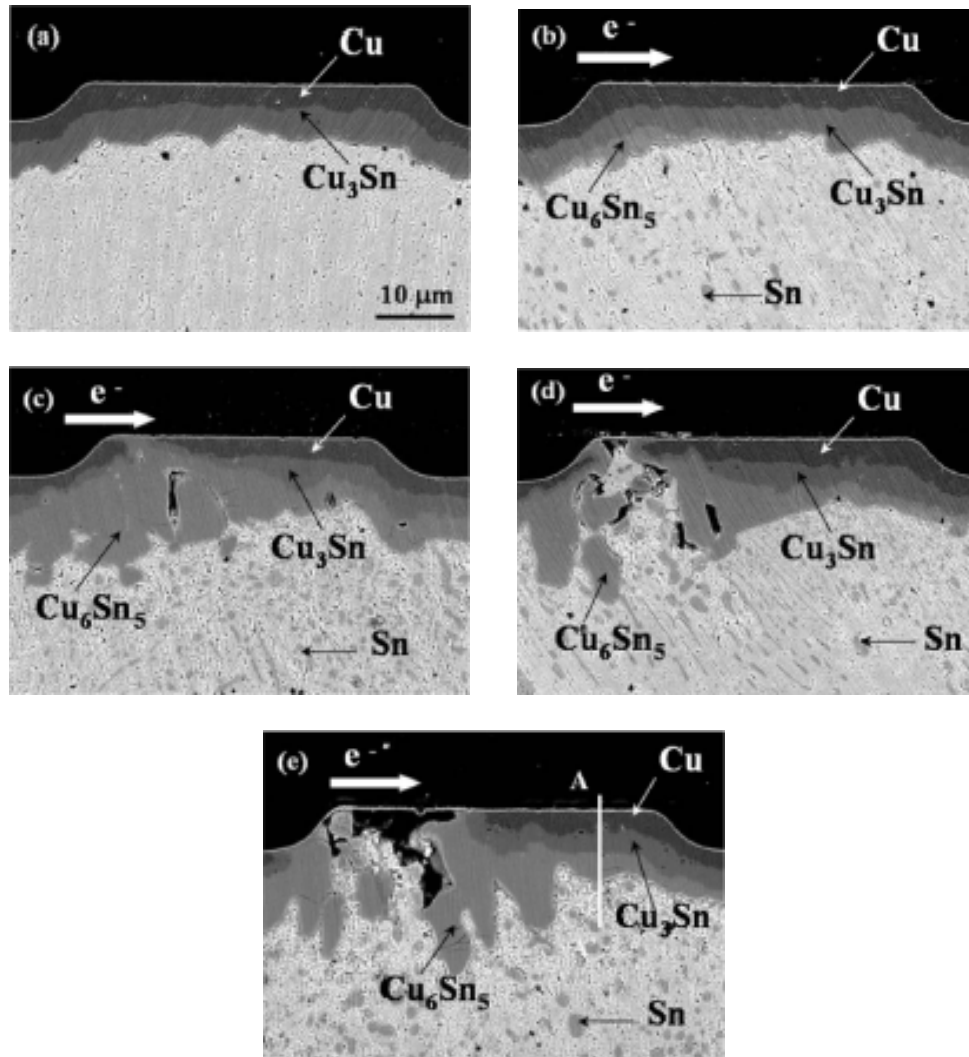


Figure 1.10: SEM images of cathode side of composite (97Pb-3Sn on the die side and 63Sn-37Pb on the substrate side) bumps after current stressing of 2.25×10^4 A/cm² at 155°C. (a) Before current stressing, (b) after 3 h, (c) after 12 h, (d) after 18 h, and (e) after 20 h [1.64].

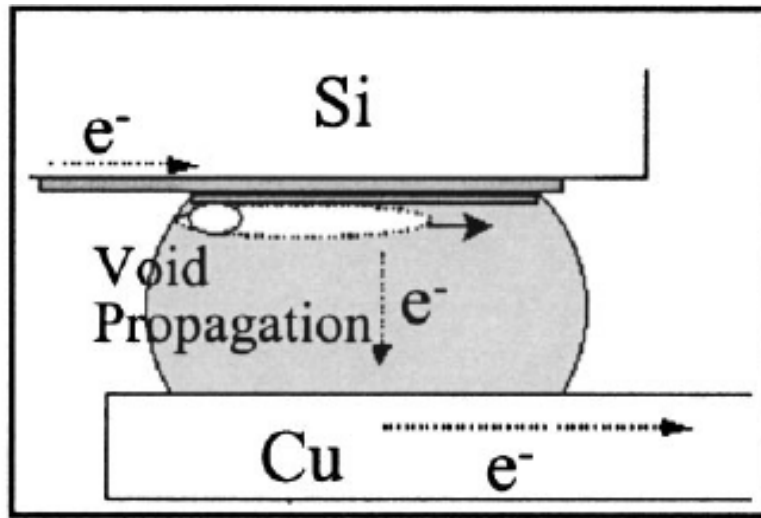


Figure 1.11: Schematic illustration depicting the cross-section of a solder joint with pancake-type void formation and propagation in eutectic Sn-Pb solder [1.55].

1.3.2.3 EM of Fast Diffusers in Solder Alloys [1.68]

The noble and near-noble elements such as Cu, Ag, Au, and Ni are known as “fast diffusers” in Pb and Sn that diffuse interstitially. They play an important role in solder joint reliability since they do not only diffuse extremely fast compared to other elements, but also form IMCs with solder constituents. Pb has a close-packed face centered cubic (FCC) lattice, while metallic Sn has a body centered tetragonal (BCT) lattice. Both of these structures contain relatively large interstitial sites that can accommodate the smaller fast diffuser atoms without significant strain. Because interstitial diffusion does not require a vacancy for the diffusing atom to jump into, the vacancy formation term is absent in the diffusivity equation. Instead, the diffusing atoms need to be small enough to fit into the interstices of the host metal lattice. Diffusion of Ni is 10^4 - 10^5 faster than Au and Ag in Sn because the atomic radius of Ni (1.246 Å) is

smaller than those of Au (1.442 Å) and Ag (1.445 Å). However, atomic radius is not the only determining factor. With Pb, chemical affinity or valence effects are also important factors. Also, the size effect is more prominent in Sn than Pb.

There is a strong inverse correlation between diffusivity and solubility. Sn has a substantial solubility in Pb, and the diffusivity of Sn in Pb is 5 orders of magnitude lower than Cu at 100°C. The solubility of Cu in Pb is estimated in the parts-per-million (ppm) range. The fastest solid state diffusion known is Ni in Sn, where the solubility is almost unmeasurable 10 parts per billion (ppb). This low solubility may limit mass transport. Instead, IMCs tend to form with fast diffuser elements in Pb and Sn. Therefore, EM-induced metallurgical changes could impact the reliability of solder joints. For example, the appearance of a Au_3Sn layer due to EM at an interface may generate cracking. The low solubility is more than compensated by the very high diffusivity in defining the mass flux of the mobile components in solder interconnects.

A. EM of Fast Diffusers in Pb and Pb-Based Alloys

Noble metals exhibit rather weak EM characteristics ($Z^* \sim 1$) in Pb alloys and can be directed toward the anode or the cathode. Ni appears to be more susceptible to EM than the noble metals, exhibiting a higher value of Z^* . In all cases, the diffusion rates are exceedingly fast.

Behavior of Ag

In pure Pb and dilute Pb-Sn alloys, Ag is pushed toward the cathode under EM. As the Sn concentration increases beyond 12%, the direction of migration reverses toward the anode. The absolute Z_{Ag}^* was found to be on the order of 1 or less, either positive or negative. In Pb-In alloys, Z_{Ag}^* was observed to decrease with the addition of

In, but a reversal of the direction of migration was not observed [1.69]. The diffusivity of Ag increases with the addition of Sn as well as In. The increased diffusivity of Ag with the addition of In is remarkable, being over 60 times greater for a 30% In alloy than pure Pb in 200°C. The activation energy for diffusion also decreased from 0.63 to 0.38 eV as the In content increased from 0 to 45%.

Behavior of Cu

In pure Pb, Z_{Cu}^* was positive ($\sim +1$) moving toward the cathode, like Ag [1.70]. However, there was no measurable temperature effect, unlike Ag. Cu exhibits the highest diffusivity and the lowest solubility in Pb among the noble metals. In both Pb-Sn and Pb-In, Z_{Cu}^* remains essentially unchanged with increases in alloying element. The diffusivity of Cu decreases sharply with increasing Sn or In. The binding energy of Cu with Sn is estimated at 0.3 eV.

Behavior of Ni

In pure Pb, Ni was observed to migrate toward the anode, but Z_{Ni}^* values (~ -5) were substantially higher than any of the noble and semi-noble metals [1.71]. In addition, there was a marked increase in Z_{Ni}^* at low temperatures with increasing Ni from 0.1 to 3 ppm.

In Pb alloys as well, EM of Ni was toward the anode. Correspondingly, Z_{Ni}^* was found to be much higher at lower temperatures than high temperatures, with the absolute values at least 1 order of magnitude larger for the noble metals. The behavior of Ni with additions of Sn or In to the Pb matrix was found to be very different. Sn additions reduced Z_{Ni}^* , whereas In additions increased Z_{Ni}^* . The diffusivity of Ni was observed to be considerably retarded by Sn and In in Pb-Sn and Pb-In alloys. The Ni-to-Sn and Ni-to-

In binding energies were estimated at 1.25 and 1.1 eV, respectively. It has been suggested that EM failure in eutectic Sn-Pb alloys is attributed to Ni migration and EM-induced IMC dissolution at interfaces [1.61].

B. EM of Fast Diffusers in Sn and Sn-Based Alloys

It is well known that Sn acts very much like Pb as a host for fast diffusers. However, an important difference stems from the different lattice structure. Diffusivity in Pb is independent of the orientation because Pb is FCC. In contrast, in metallic Sn which is BCT, the diffusivity is remarkably different between parallel and perpendicular direction to the c -axis of the Sn lattice. This is also true for self-diffusion. For fast diffusers, the ratio of the diffusivity typically varies by a factor of 30-40 at 200°C. Because of the effects of the anisotropic lattice structure, EM studies for fast diffusers in Sn have been performed with single crystals.

Behavior of Ag and Au

EM of Ag parallel to the c -axis was observed to exhibit Z_{Ag}^* of about -2 independent of temperature. For Au, Z_{Au}^* was also insensitive to temperature, which was approximately -9. However, Z_{Au}^* perpendicular to the c -axis was observed to be about half of this value [1.72].

Behavior of Ni

Ni is the most interesting fast diffuser in Sn. Perpendicular to the c -axis, Ni diffusion in Sn was found to be fast with an activation energy of 0.5 eV. This is not very different from the other fast diffusers. In contrast, parallel to the c -axis, Ni diffuses extraordinarily fast, with extremely low activation energy of less than 0.2 eV [1.73]. In

fact, the solid state diffusion of Ni in Sn at 100°C is faster than diffusion of noble metals in liquid Sn at more than 232°C. The ratio of diffusion parallel and perpendicular to the c -axis is more than 10^5 at 120°C, which is the greatest directional dependency known. EM of Ni in Sn is unusually high, similar to the case in Pb. Z_{Ni}^* perpendicular to the c -axis was found to be -36 at 203°C and to rise to -67 at 166°C, which exhibits a significant temperature dependence. The fast diffusion of Ni in Sn and the unusually high Z_{Ni}^* could cause reliability problems.

1.3.2.4 EM-Enhanced IMC Growth

In order to calculate the mass transport in solder joints, the flux driven by concentration gradient also needs to be taken into account, and Eq. (1.5) should be modified to

$$J = J_{EM} + J_{chem} + J_{\sigma} = C \frac{D}{kT} Z^* e \rho j - D \frac{dC}{dx} - C \frac{D}{kT} \frac{\Omega d\sigma}{dx}, \quad (1.8)$$

where J_{chem} denotes the atomic flux driven by a concentration gradient. Equation (1.8) needs to be solved in each phase if there exist multiple phases, to calculate the vacancy flux and IMC growth.

Recently, Chao addressed this problem for a Cu-Sn diffusion couple by using a numerical method [1.74]. The last term in Eq. (1.8) was ignored in his analysis since the interstitial diffusion of Cu in Sn was not expected to generate a significant back-stress. By assumption, diffusion processes in every phase were through substitutional mechanism. Figure 1.12 describes the concentrations of two adjacent phases near their respective interfaces. The velocity of the interfacial movement is derived as:

$$\begin{aligned}
v &= \frac{dx}{dt} = v_{\text{chem}} + v_{\text{EM}} \\
&= \frac{1}{C_{\alpha\beta} - C_{\beta\alpha}} \left\{ \left(\tilde{D}_{\beta} \frac{\partial C_{\beta}}{\partial x} - \tilde{D}_{\alpha} \frac{\partial C_{\alpha}}{\partial x} \right) + j \left[\frac{C_{\beta\alpha} (C_{0,\beta} - C_{\beta\alpha})}{C_{0,\beta}} \tilde{\phi}_{\beta} - \frac{C_{\alpha\beta} (C_{0,\alpha} - C_{\alpha\beta})}{C_{0,\alpha}} \tilde{\phi}_{\alpha} \right] \right\} \quad (1.9)
\end{aligned}$$

where α and β represent the two adjacent phases separated by the interface of interest, $C_{\alpha\beta}$ and $C_{\beta\alpha}$ represent the composition of the two phases at this interface. The two relevant parameters, interdiffusion coefficient, \tilde{D} , and effective interdiffusion electromigration coefficient, $\tilde{\phi}$, are defined as follows:

$$\tilde{D}_i = X_{\text{Cu},i} D_{\text{Sn},i} + X_{\text{Sn},i} D_{\text{Cu},i} \quad (1.10)$$

$$\tilde{\phi}_i = D_{\text{Sn},i} \phi_{\text{Sn},i} - D_{\text{Cu},i} \phi_{\text{Cu},i} \quad (1.11)$$

where ϕ is the electromigration factor defined as $\phi = \frac{Z^*}{kT} e\rho$. And the rate of local vacancy concentration change, $R(x)$, is given by

$$R(x) = -\frac{\partial J_v}{\partial x} = -(D_{\text{Cu}} - D_{\text{Sn}}) \frac{\partial^2 C}{\partial x^2} - \tilde{\phi} j \frac{\partial C}{\partial x} \quad (1.12)$$

where J_v is the vacancy flux.

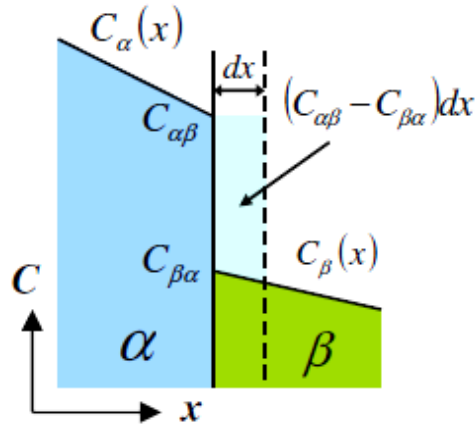


Figure 1.12: Concentration profile near a phase boundary [1.74].

Equations (1.9)-(1.12) were solved by using a finite difference method. Some selected results are shown in Figs. 1.13 and 1.14. The effect of EM on IMC growth was found to be significant especially for Cu_6Sn_5 . The growth kinetics nearly followed the linear time dependence under current stressing whereas the parabolic growth law typically governed thermal aging cases. It is also noted from Fig. 1.14 that vacancies tended to move toward the Cu UBM from the Sn solder. This analysis suggests that IMC growth can be an important factor controlling the EM reliability of Sn-based Pb-free solder joints.

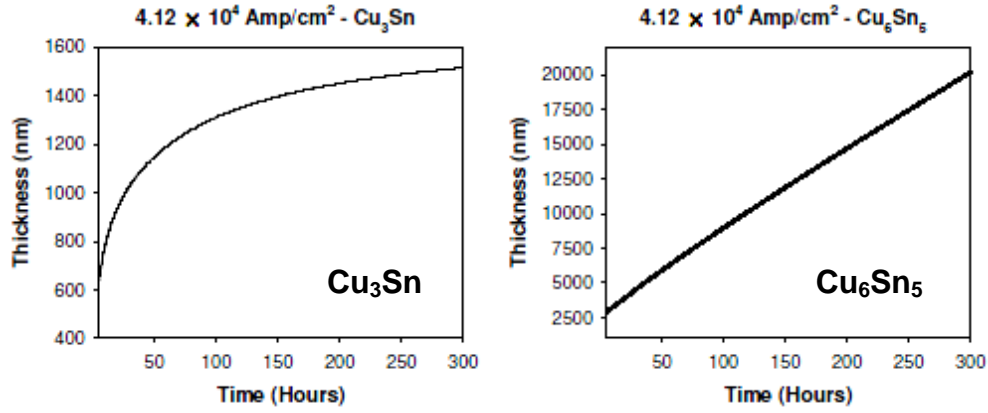


Figure 1.13: Simulated EM-enhanced IMC growth [1.74].

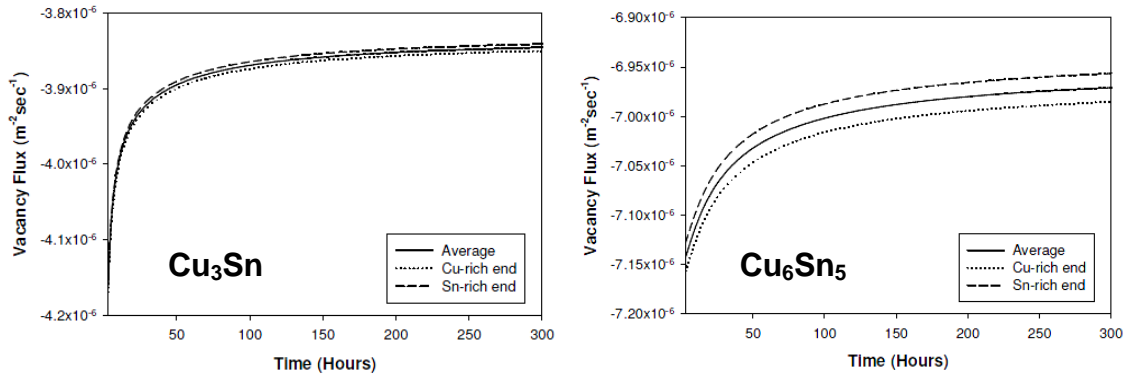


Figure 1.14: Simulated vacancy flux as a function of current stressing time [1.74]. The negative sign indicates that the vacancy flux is moving in the direction from the Sn solder to the Cu UBM.

1.3.3 Thermomigration (TM)

1.3.3.1 Fundamentals of Thermomigration (TM)

TM, also known as the Ludwig-Soret effect or Soret effect, is mass transport driven by a temperature gradient. This can make a homogeneous alloy inhomogeneous under a temperature gradient. TM can also take place in pure metals. Although the

physical basis behind TM is not well established, the most accepted theory is analogous to EM, in that momentum exchange occurs from collision of diffusing atoms and conducting electrons. The energy and momentum of electrons at higher temperatures is greater than at lower temperatures. The gradient in the momentum exchange produces a driving force for mass transport [1.68]. The driving force for TM is represented as:

$$F_{\text{TM}} = -\frac{Q^*}{T} \frac{dT}{dx}, \quad (1.13)$$

where Q^* is defined as heat of transport, and T is the absolute temperature. Q^* has a unit of (heat) energy, and thus can be interpreted as the difference between the heat carried by the migrating atom and the heat of the atom at the initial state (the hot end or the cold end) [1.26]. Q^* can be positive or negative depending on the direction of migration, similar to Z^* . For $Q^* > 0$, the flux is from the hot end to the cold end; for $Q^* < 0$, the flux is from the cold end to the hot end. For metals with a high Z^* , Q^* should be correspondingly high as well [1.68]. The flux equation of TM is then expressed as:

$$J_{\text{TM}} = -C \frac{D}{kT} \frac{Q^*}{T} \frac{dT}{dx}. \quad (1.14)$$

The jump mechanism or mean jump frequency is not changed by the temperature gradient at any given temperature. However, the temperature gradient biases the direction of jumps.

TM can cause a uniform single-phase solid solution (e.g. interstitial alloys) to become nonuniform. This creates a concentration gradient, which acts as opposing TM. Thus the flux equation is modified to:

$$J = J_{\text{TM}} + J_{\text{chem}} = -C \frac{D}{kT} \frac{Q^*}{T} \frac{dT}{dx} - D \frac{dC}{dx}. \quad (1.15)$$

When a steady state is reached, i.e. $J = 0$, the net effect of TM will vanish and a constant concentration gradient will be maintained. In this condition,

$$\frac{d \ln C}{dx} = - \frac{Q^*}{kT^2} \frac{dT}{dx}. \quad (1.16)$$

Using Eq. (1.16), Q^* can be determined from a concentration profile of solute atoms at a given temperature gradient.

If a diffusion occurs through a vacancy mechanism, the effect of stress-induced backflow can also exist, similar to that of EM. Then

$$J = J_{\text{TM}} + J_{\sigma} = -C \frac{D}{kT} \frac{Q^*}{T} \frac{dT}{dx} - C \frac{D}{kT} \frac{\Omega d\sigma}{dx}. \quad (1.17)$$

Subsequently, at $J = 0$,

$$\left[L \left(\frac{dT}{dx} \right) \right]_c = \frac{\Omega \Delta \sigma}{Q^*} T, \quad (1.18)$$

where the specimen length, L , replaced Δx . Equation (1.18) is a critical product below which no net effect of TM exists [1.26].

If all possible driving forces for atomic migration are concurrent, the net flux will be governed by

$$\begin{aligned}
J &= J_{\text{EM}} + J_{\text{TM}} + J_{\text{chem}} + J_{\sigma} \\
&= C \frac{D}{kT} Z^* e \rho j - C \frac{D}{kT} \frac{Q^*}{T} \frac{dT}{dx} - D \frac{dC}{dx} - C \frac{D}{kT} \frac{\Omega d\sigma}{dx} .
\end{aligned} \tag{1.19}$$

1.3.3.2 TM in Solder Joints

In most solids except refractory and transition metals, Q^* is rather small, and TM has generally a negligible effect [1.75]. For typical good conductors used as interconnect lines, the ratio of the driving force for TM to that for EM is in the order of 10^{-3} . In contrast, this ratio is about 0.5 for solder joints, taking ρ to be $10^{-7} \Omega\text{m}$; j , 10^4 A/cm^2 ; Z^* , 10; T , 400K; dT/dx , 10^3 K/cm ; Q^* , 0.2 eV. The value of Q^* was estimated for Cu in Pb by Lloyd using Eq. (1.16) [1.68]. Therefore, the effect of TM in solder joints could be quite comparable to that of EM in cases where a high temperature gradient is present.

TM in flip chip solder joints was first discussed by Ye *et al.* [1.76]. They found voids on the die side in eutectic Sn-Pb solder joints in which electrons flowed from the substrate side to the die side. This could not be explained by EM, and they reported it was because TM accompanied EM. The major heat source which makes the die side of solder joints hotter than the substrate side is known to be the thin metal trace on the die carrying an electric current. Also, due to the current crowding, the current density distribution in solder joints is not uniform. This can also play a role in setting up the temperature gradient in the solder. Using a finite element method (FEM), Ye estimated the temperature gradient in the solder to be $\sim 1500 \text{ }^\circ\text{C/cm}$.

Because Si is a good thermal conductor, the unpowered solder joints adjacent to powered solder joints can experience a similar thermal effect. Figure 1.15 shows a damaged unpowered bump due to TM at an ambient temperature of 150°C . The adjacent powered solder joints were under 1 A of current stressing. The redistribution of Pb-rich

and Sn-rich phases occurred such that the Pb-rich phase moved toward the cold end while the Sn-rich phases moved toward the hot end.

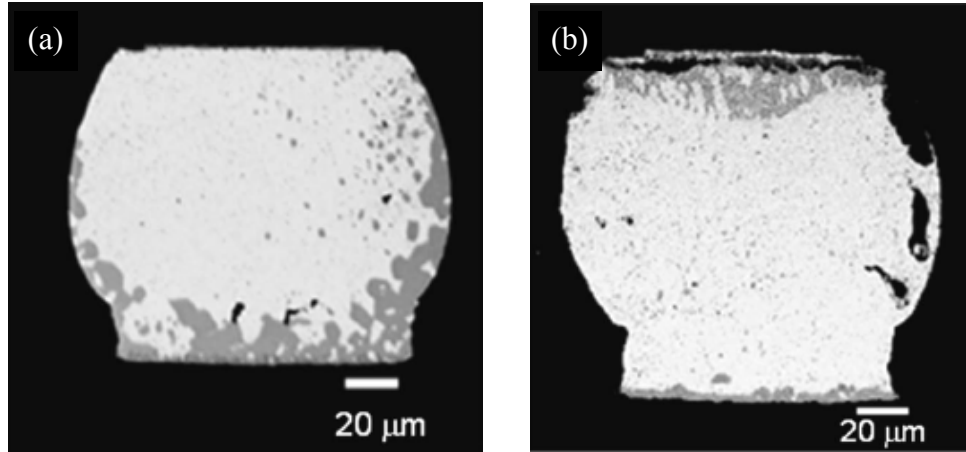


Figure 1.15: Composite (97Pb-3Sn with eutectic Sn-Pb) solder joints (a) before testing, and (b) after TM [1.77].

In a recent study on a bulk eutectic SnPb solder without current stressing, the Pb phase was found to deplete from the hot end under the constant temperature gradient of 1000 °C/cm although voiding was not observed [1.78]. The heat of transport was estimated to be 22.16 kJ/mol, which is equivalent to 0.23 eV.

TM was also studied by using an alternating current at 45 Hz [1.79]. The same amount of Joule heating was expected to be created with retarded EM-induced damage. The temperature gradient in eutectic SnPb solder joints was measured directly to be 2143 °C/cm at 100°C by infrared microscopy. The flux by TM was calculated by the marker motion, and the heat of transport was obtained to be 26.8 kJ/mol or 0.28 eV.

TM in solder joints has not attracted much attention yet because creating a large temperature gradient and measuring it directly are not easy, and in most cases, the failure rate is still relatively slow compared to EM. Nevertheless, it should be interesting to

study the effects of TM on the Pb-free solder joint reliability since little information is available yet on this topic. It is very important that the temperature gradient in solder joints should be small enough to suppress TM during EM reliability testing. Otherwise, the reliability data cannot be used for predicting the field life of the solder joints.

1.4 OBJECTIVES AND OVERVIEW

This study is focused on EM and TM reliability of Pb-free solder joints used in advanced packaging applications including flip chip packages and system-in-packages (SiPs). Two types of UBM designs, thick electroplated Cu UBM and thin electroplated Ni UBM, are studied in parallel and their differences are compared.

Experimental details and reliability data analysis procedures are described in Chapter 2. The Wheatstone bridge method is utilized to reduce electrical noise and obtain greater sensitivity for resistance measurements.

The first objective of this dissertation research is to obtain statistical lifetime data and to identify failure mechanisms for Pb-free solder joints under EM. The resistance changes of solder joints are closely monitored and a reasonable failure criterion is introduced. The EM lifetime data will be analyzed in order to determine its temperature and current density dependence. Because Joule heating is significant in solder EM testing, the solder temperature will be confirmed with FEM. In this study, the EM activation energy and the current density exponent will be determined. The failure modes and damage evolution processes for Cu UBM and Ni UBM solders will be compared. These will be covered in Chapter 3.

The second objective is to characterize the IMC growth enhanced by EM. Because extensive amount of IMCs can be formed in Sn-rich Pb-free solders under current stressing, it is important to assess the kinetics of the enhanced IMC growth. In

Chapter 4, the IMC growth with and without current stressing will be compared where the apparent activation energies for IMC formation will be determined. The IMC activation energies will be compared with those determined in Chapter 3 for further understanding of the EM failure mechanisms for Pb-free solder joints. IMC formation also accompanies a volumetric shrinkage, which produces stresses. Since EM voiding is closely related to stresses, the IMC-induced stresses will be simulated using FEM to predict its effect on the EM reliability in Chapter 4.

The third objective is to correlate the current crowding effect with EM lifetime quantitatively. The experimental results of different thicknesses of Ni UBM will be discussed and supplemented by FEM for the current density distribution in Chapter 5. A modification of Black's equation will be suggested. Then the effect of metal trace design on current density distribution will be investigated using FEM in an attempt to enhance the EM reliability. FEM will be also carried out to estimate the impact of solder joint scaling.

The last objective of this study is to investigate the TM reliability of Pb-free solder joints. A special experimental setup is used to create very large temperature gradient without current stressing in Chapter 6. Corresponding temperature gradient will be determined by FEM simulations. Morphology changes by TM will be compared with those by EM. Thermally-aged solder joints with very small temperature gradient will also be compared as a control. The relative effect of TM compared to EM will be also examined.

Finally, Chapter 7 will conclude this study and provide suggestions for future work.

Chapter 2: Experimental Setup and Reliability Data Analysis

This chapter covers experimental details of electromigration (EM) reliability tests for solder joints. The test vehicle was configured to test two pairs of flip chip solder joints. The resistance changes of solder joints were monitored using the Wheatstone bridge method as well as 4-point probe method. The Wheatstone bridge method provides great sensitivity in detecting small resistance changes. The description of the test equipment incorporating Wheatstone bridge circuits follows. Lastly, general test procedures are presented.

2.1 TEST VEHICLE

The test vehicle used in this study is shown in Fig. 2.1. It is a flip chip plastic ball grid array (FC-PBGA) module with 360 BGA pads. The dimensions of the organic substrate and the Si die were $25\text{ mm} \times 25\text{ mm} \times 0.72\text{ mm}$ and $9.2\text{ mm} \times 6.8\text{ mm} \times 1.1\text{ mm}$, respectively. The die-substrate interconnection was accomplished through 579 solder bumps as shown in Fig. 2.2. After a die was assembled with a substrate by flip-chip processes, the gap between the die and the substrate was filled with an underfill.

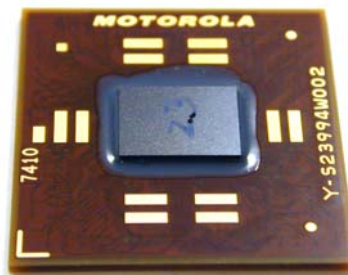
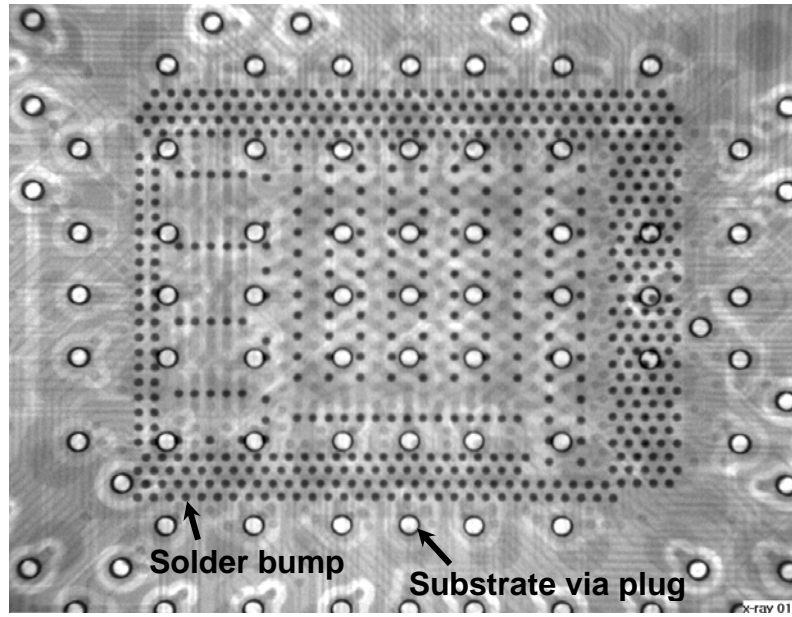
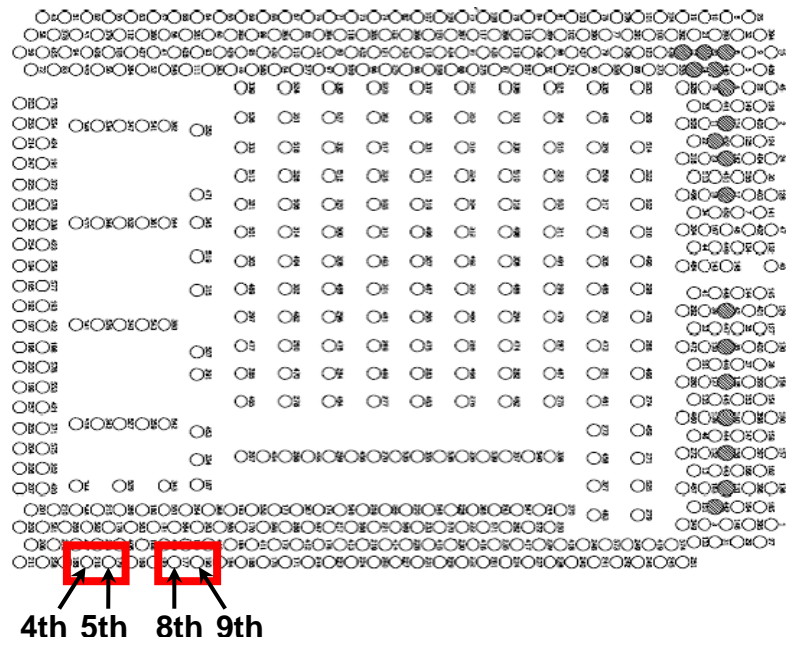


Figure 2.1: Flip-chip test vehicle.



(a)



(b)

Figure 2.2: (a) X-ray microscope image of a test vehicle. The viewing direction is from the top of Si die to the bottom of substrate (top view). (b) Top view of an array of 579 solder bumps between a Si die and a substrate. The red boxes indicate two pairs of bumps for EM tests.

In this test vehicle, two pairs of solder joints (four solder joints in total) were configured for EM tests, which were located in the first row as shown in Fig. 2.2(b). The locations of these four bumps are denoted by red boxes. These four bumps were connected in series in a daisy-chain fashion. The 4th and 5th bumps, and the 8th and 9th bumps (from left) are connected through thin metal traces on the die side, respectively. The metal trace was made of Cu with dimensions of $300\text{ }\mu\text{m}$ (length) \times $75\text{ }\mu\text{m}$ (width) \times $1\text{ }\mu\text{m}$ (thickness). The 5th and 8th bumps were linked through substrate traces. The trace width was $\sim 50\text{ }\mu\text{m}$, and the thickness was $16\text{--}18\text{ }\mu\text{m}$. One BGA pad was connected to the 4th bump, and another to 9th bump for a current supply. The electric current path for EM tests was as follows: substrate BGA pad \rightarrow substrate trace \rightarrow 9th bump \rightarrow metal (die) trace \rightarrow 8th bump \rightarrow substrate trace \rightarrow 5th bump \rightarrow metal (die) trace \rightarrow 4th bump \rightarrow substrate trace \rightarrow substrate BGA pad. As a result, electrons flowed in the opposite direction. The total length of the substrate traces in the above current path was $\sim 33.3\text{ mm}$. The schematic of the cross-section of a test vehicle is shown in Fig. 2.3.

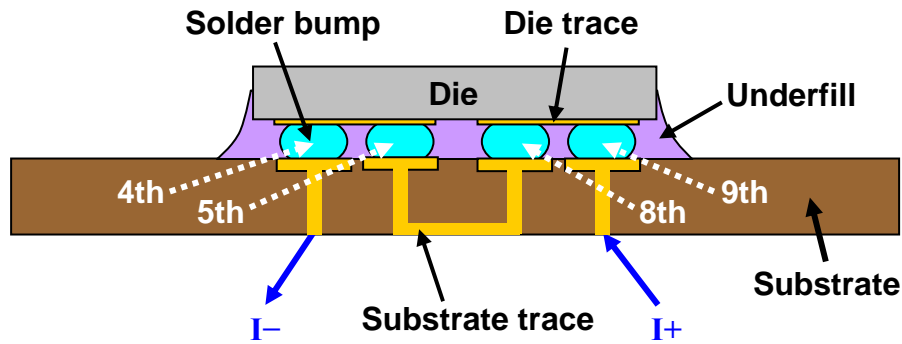


Figure 2.3: Schematic diagram of the cross-section of a test vehicle. Only bumps under test are shown. The image is not scaled.

2.2 WHEATSTONE BRIDGE METHOD

The resistance of an individual solder bump is typically a few $\text{m}\Omega$, while that of a metal trace on the die side and substrate traces are in the order of $10^2 \text{ m}\Omega$ and $10^3 \text{ m}\Omega$, respectively. Therefore, it was difficult to detect resistance changes of a solder bump with high accuracy and sensitivity. Consequently, Wheatstone bridge circuits were implemented since this method is a well-known technique for detecting very small resistance changes [2.1].

Figure 2.4 shows a schematic of a Wheatstone bridge designed for solder electromigration experiments. Three BGA pads were wired for each test vehicle. Two of them were for electrical in and out, and one of them was used as a midpoint connection for off-balance voltage (V_g) measurements in a Wheatstone bridge circuit. Four solder joints in each test vehicle were divided into two groups (i.e. two solder joints in each group). Each group served as a resistor unit (R_1 or R_2) in one leg of a Wheatstone bridge. For the test structure used in this study, both R_1 and R_2 consisted of two solder joints: a cathode and an anode joint. Here, the cathode joint refers to a solder joint where electrons flow from the substrate side to the die side and the anode joint refers to one where electrons flow in the opposite direction. Hence, the 4th and 8th solder bumps from the left (see Fig. 2.2) correspond to cathode joints; the 5th and 9th solder bumps are anode joints. The other leg consisted of two large (in the order of $\text{k}\Omega$) resistors, R_3 and R_4 . Thus current flowed primarily through the test vehicle. Before each EM test began, V_g was set to 0 (zero) by adjusting the variable resistor (or potentiometer, R_4).

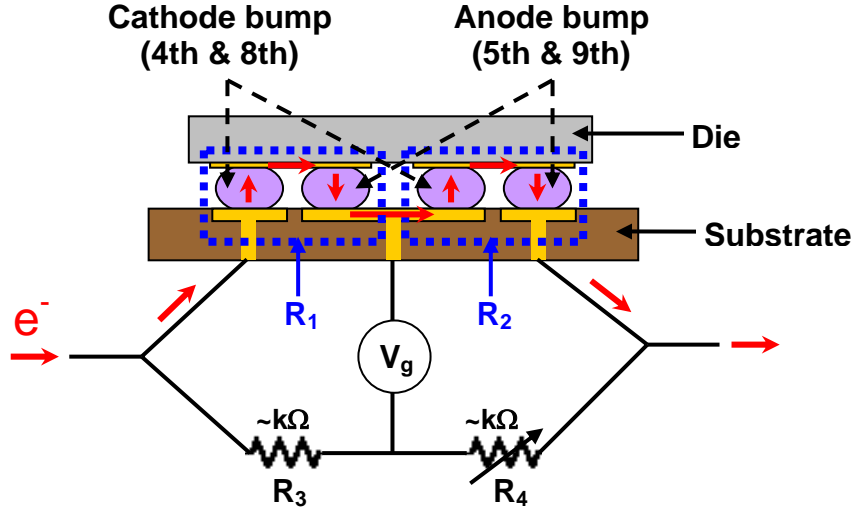


Figure 2.4: Schematic diagram of a Wheatstone bridge circuit in the solder EM test system designed for detecting small resistance changes of solder bumps.

R_3 and R_4 are fixed during electromigration experiments, thus V_g is directly correlated with net changes of R_1 and R_2 . Following Kirchhoff's laws,

$$V_g = V_s \left(\frac{R_1}{R_1 + R_2} - \frac{R_4}{R_3 + R_4} \right) = IR \left(\frac{R_1}{R_1 + R_2} - \frac{R_4}{R_3 + R_4} \right), \quad (2.1)$$

where V_s is the voltage drop across a Wheatstone bridge, I is the applied current and R is the net resistance of R_1 , R_2 , R_3 and R_4 (i.e. $R = \frac{(R_1 + R_2)(R_3 + R_4)}{R_1 + R_2 + R_3 + R_4}$). R can be simplified to $R \approx R_1 + R_2$ because $R_3, R_4 \gg R_1, R_2$. Then Eq. (2.1) is reduced to:

$$V_g \cong I \left(R_1 - \frac{(R_1 + R_2)R_4}{R_3 + R_4} \right). \quad (2.2)$$

In case of $R_1 = R_2$ prior to applying current (subsequently, $R_3 = R_4$ as well), Eq. (2.2) can be further simplified, during the current application, to [2.1]:

$$V_g \cong 0.5I(R_1 - R_2) . \quad (2.3)$$

Since only solder bumps are expected to fail by electromigration damage, the resistance of the other parts, except solder bumps, would remain constant throughout the electromigration test. Therefore, V_g reflects the net resistance changes of solder bumps only, which should now be large enough to be easily detectable for a slight change of resistance.

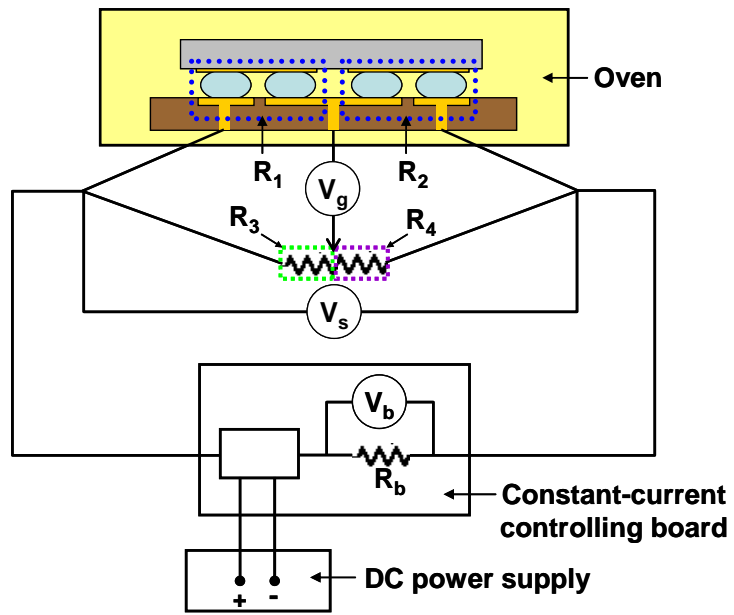
2.3 TEST SYSTEM CONFIGURATION

Figure 2.5 shows the configuration of the solder EM test system. This system was designed and built in our laboratory to control the applied current precisely and to detect resistance changes of solder joints with high sensitivity. The system is equipped with a power supply, constant current controlling boards, Wheatstone bridge circuit boards, temperature chambers, switch controllers, a digital multimeter (DMM), and a PC.

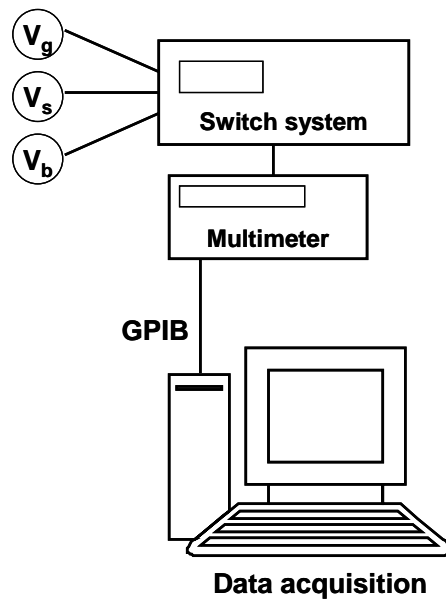
Instead of using two individual resistors (a fixed resistor R_3 and a variable resistor R_4 in Fig. 2.4) in a Wheatstone bridge, one potentiometer (three-terminal resistor) was used. A potentiometer is divided into resistors by the middle terminal which is connected to the digital multimeter (DMM) through the switch system for V_g measurements. Thus basically, the function of one potentiometer serves to replace two individual resistors illustrated previously.

In addition to the off-balance voltage V_g , V_s was measured as a voltage drop across a test vehicle. Then its resistance was simultaneously calculated based on Ohm's law and recorded in a PC by a LabVIEW program. As a result, the overall resistance changes were monitored throughout EM tests together with V_g changes. Another voltage drop measured was V_b . This was used to monitor the applied current which was being generated on constant current controlling boards. A known resistor (0.33Ω) per channel was incorporated on the board as an ammeter so that the current level could be monitored by V_b . Conversion of V_b to the applied current was performed by the LabVIEW program as soon as it was measured.

The aforementioned three voltage values per each test vehicle were monitored in turn by a switch system (Keithley 7001) and a digital multimeter (Keithley 196 System DMM). Then voltage measurements proceeded to the next module in the same manner. These processes were controlled and recorded by the automated LabView control in the PC through the GPIB interface until an experiment was terminated. This enabled real-time measurements and recording of the voltages and current levels.



(a)



(b)

Figure 2.5: Schematic diagram of the test system configuration designed for solder EM.

Each component of the test system is elaborated below.

DC power supply

The power supply is shown in Fig. 2.6. The maximum voltage and current levels the unit can support are 20 V and 120 A, respectively. Before every experiment, a supply voltage should be set to an appropriate level so that the applied current could be interrupted as soon as a solder joint fails. If a supply voltage is too high, it may cause a solder bump to melt or the test vehicle to burn due to the overloading and excessive Joule heating. If it is too low, the stability of the applied current could be low or the current could be interrupted prior to the electrical open of a solder bump. Generally, it is set between 4 and 5 V depending on the applied current level, the resistance of a test structure, and the number of test vehicles under test.



Figure 2.6: HP 6031A system power supply.

Constant current controlling board

Custom-made constant current controlling boards (Fig. 2.7) regulate the applied current with high stability. This high stability of the applied current is one of the most crucial conditions in electromigration experiments. This board is designed for the high

current supply specified for solder EM experiments. Six boards are in use and each board has 10 channels. An applied current of each channel can be set independently by adjusting potentiometers. Thus 60 test vehicles can be tested simultaneously with each test vehicle subject to a desired current level. The current supplied from each channel is continuously monitored by an ammeter in each channel. This ammeter basically measures the voltage drop across a known resistor ($0.33\ \Omega$). Due to its characteristic of high current application, the boards are always cooled by cooling fans installed above the board frame.

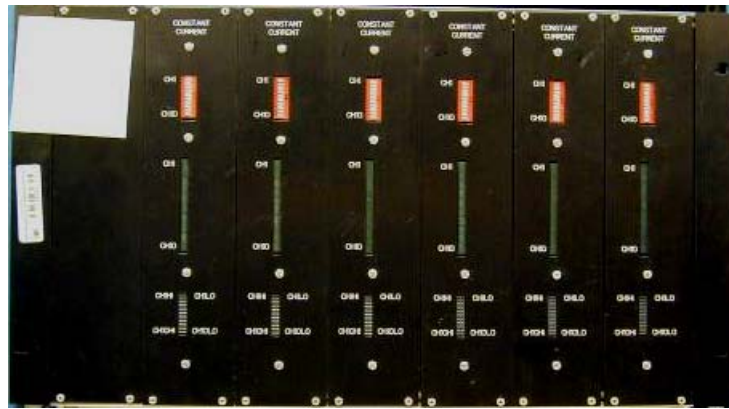


Figure 2.7: 6 constant current controlling boards with each board having 10 channels.

Wheatstone bridge circuit board

Figure 2.8 shows a Wheatstone bridge circuit board containing 20 potentiometers. Basically, one potentiometer functions as two series resistors, R_3 and R_4 , as shown in Fig. 2.5. In a potentiometer, R_3 and R_4 are adjusted simultaneously by rotating a screw shown in Fig. 2.10. The total resistance ($R_3 + R_4$) of a potentiometer is fixed. To make sure that electric current should flow primarily through the test vehicle side of the circuit,

potentiometers of as large as 5 k Ω are used. As shown in Fig. 2.9, two end-terminals are for the current in and out; the middle terminal is for the midpoint connection in a Wheatstone bridge circuit. This middle terminal is connected to the digital multimeter through the switch system for V_g measurements. Prior to every electromigration test, potentiometers are adjusted to set initial V_g values to zero.

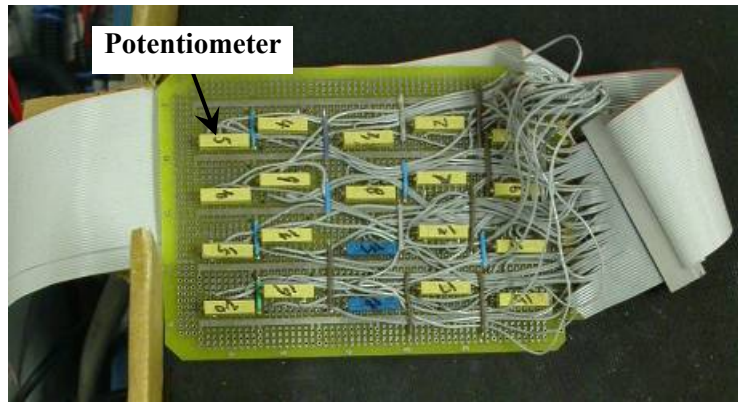


Figure 2.8: Wheatstone bridge circuit board.

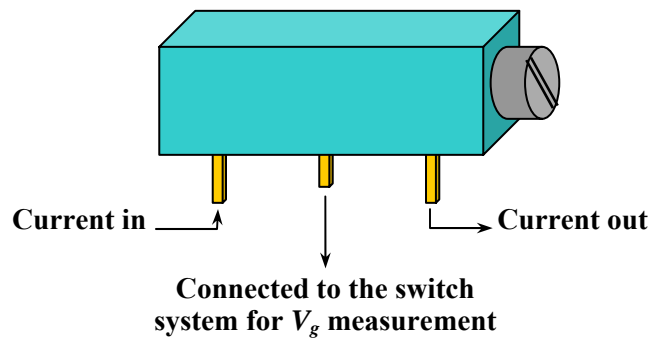


Figure 2.9: Schematic diagram of a potentiometer.

Temperature chamber

Two identical temperature chambers (Fig. 2.10) are used for solder EM experiments. They are forced-convection ovens where the air is continuously circulated and mixed. During EM tests, the temperature inside a chamber is maintained constant and uniform. Inside a chamber, a Cu plate (H-shaped in Fig. 2.10) on a supporting block is used for loading test vehicles. Up to 30 test modules can be arranged on the Cu plate in a way that the Si backside of each package is attached to the Cu plate using thermal compound as schematically shown in Fig. 2.11. This Cu plate helps to maintain a uniform temperature distribution among test vehicles because Cu is a good thermal conductor. More importantly, it also serves as a heat sink. Since relatively large current (~ 1 A) is applied in solder EM experiments, a large amount of Joule heat is generated from test vehicles, making actual solder temperature higher than the chamber temperature. As EM damage progresses in solder joints, the Joule heating effect can go worse. This may cause thermal runaway failures, which makes it difficult to determine EM lifetime data. This side-effect can be minimized by using a heat sink.

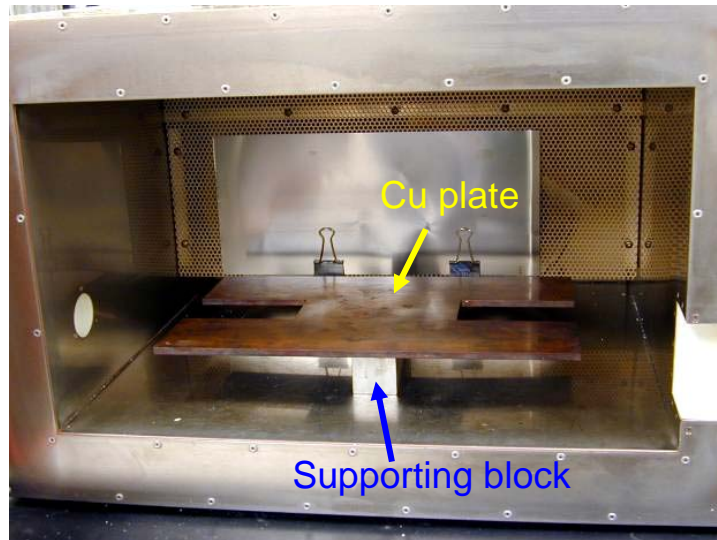


Figure 2.10: Sigma M42 temperature chamber.

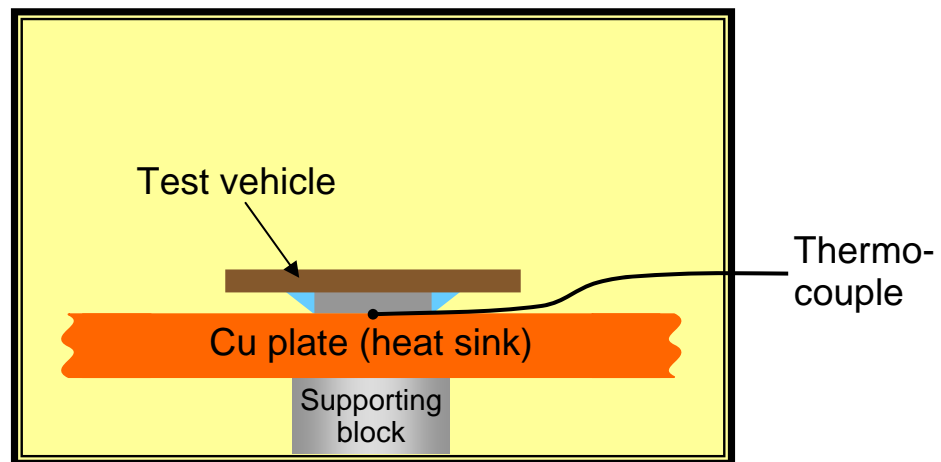


Figure 2.11: Schematic diagram of a test configuration inside a temperature chamber. Thermal compound (not shown) is applied between the test vehicle and Cu plate. The image is not scaled.

Switch system

Three switch mainframes are shown in Fig. 2.12. Each mainframe has two card slots. Five out of 6 switch cards are installed and each switch card has 40 available channels. As each channel can be assigned to detect either V_b , V_g or V_s , three channels should be allocated to each test vehicle. As a result, maximum 180 channels (3 channels/test vehicle \times 60 test vehicles) are in use out of 200 available channels.



Figure 2.12: Keithley 7001 switch system. Three switch mainframes are shown and 5 out of 6 card slots are in use.

Digital multimeter (DMM)

A Keithley 196 system DMM (Fig. 2.13) is connected with the switch system as well as a PC via GPIB cables in order to read V_b , V_g and V_s values. With GPIB connection, the PC can control the switch system and record DMM readings. The DMM has a resolution of 100 nV.



Figure 2.13: Keithley 196 system DMM.

PC for instrument control and data acquisition

Figure 2.14 shows a PC for switch system control and data acquisition. A GPIB card in the PC is connected with the switch system and the DMM through GPIB cables. They are controlled by a National Instruments LabVIEW program. It sends the switch system commands to switch in a preset order and receives real-time DMM readings simultaneously. Elapsed time, applied current (I), off-balance voltage (V_g) and overall module resistance (V_s) data for each test vehicle are also saved automatically. In this way, real-time damage evolution in every test vehicle can be monitored.

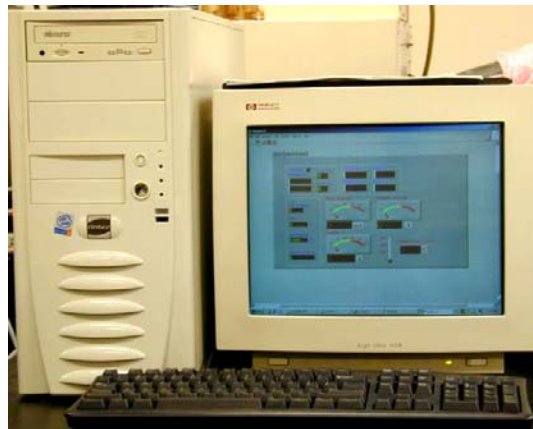


Figure 2.14: Data acquisition system.

2.4 GENERAL TEST PROCEDURE

The following describes general steps for a solder EM experiment.

- A. Test sample preparation
 - a) Two wires are soldered on two BGA pads separately for the electric current in and out. This makes an electric current flow into the 9th bump and out of the 4th bump (see Figs. 2.2 and 2.3). Another wire is soldered on two adjacent I/O pads. This allows a connection between the 5th and the 8th bumps as well as a midpoint connection for V_g in a Wheatstone bridge.
 - b) The soldered area was covered for insulation with a mixture of Aremco Ceramabond 571 liquid and powder. Then it was cured at $\sim 70\text{-}80^\circ\text{C}$ for ~ 1 hour. An insulated test vehicle after curing is shown in Fig. 2.15.

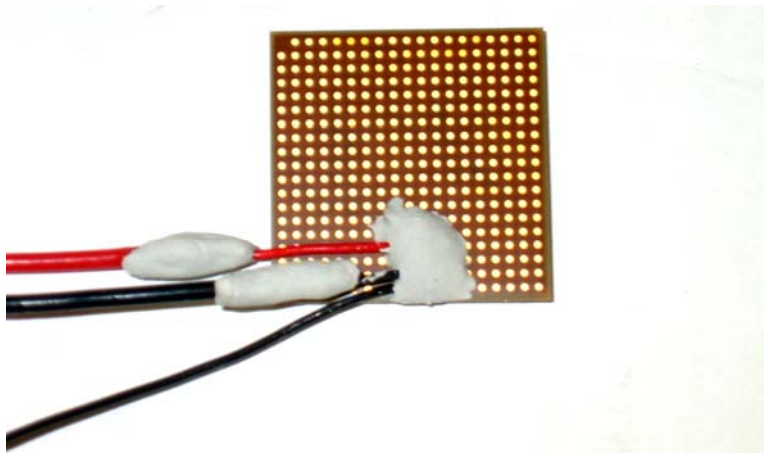


Figure 2.15: Soldered and insulated test vehicle.

B. Sample installation

- c) For efficient heat dissipation, heat sink compound with high thermal conductivity is applied on the backside of the Si die.
- d) Test vehicles are attached on the Cu plate. Thermocouples are sandwiched between the Si dies and the Cu plate. Thermocouples are positioned as close to the solder bumps under test as possible.
- e) Test vehicles and the Cu plate are clipped firmly to ensure a good thermal contact as shown in Fig. 2.16.
- f) Wires are connected to the current sources or the DMM (through the switch system).

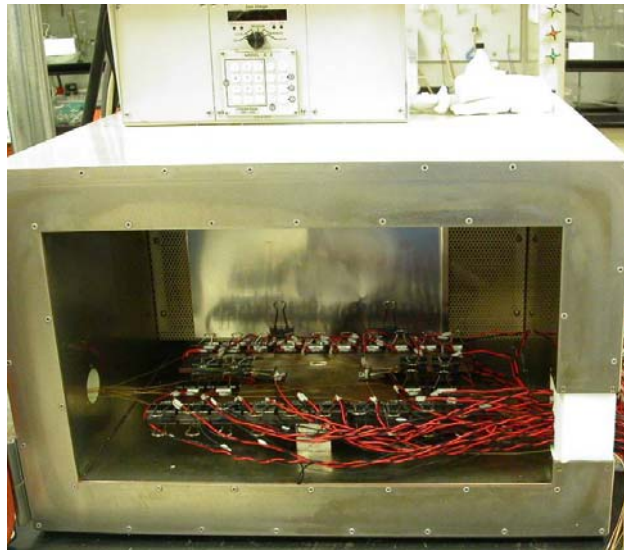


Figure 2.16: 30 test vehicles attached on a Cu plate inside a temperature chamber.

C. EM testing

- g) The applied current of each channel in the constant current controlling boards is adjusted to a desired level.
- h) The off-balance voltage V_g is set to zero by adjusting a potentiometer on the Wheatstone bridge circuit board.
- i) Every channel of the current boards is turned off after the steps g) and h) to avoid any damage before a test begins.
- j) Temperature of the chamber is set to a target temperature.
- k) When the chamber temperature reaches the target temperature, all the current channels connected to test vehicles are turned on.
- l) The LabVIEW program is launched. Then it starts to control the switch system to receive DMM readings for each test vehicle.
- m) Temperature of the Si backside is frequently monitored. This temperature (not the chamber temperature) is kept constant during the EM test. Because the failure of test vehicles usually causes the Si backside temperature of active test vehicles to drop, the sample temperature is needed to be compensated by increasing the chamber temperature whenever failures occur.
- n) Some of failed samples are taken out of the chamber in the middle of the experiment, in order to prevent post-failure intermetallic compounds growth. To do this, the LabVIEW program is paused first. Then the failed sample is taken out as quickly as possible. Meanwhile, the Si backside temperature is monitored. When it reaches the initial temperature again, the LabVIEW program is resumed.
- o) The applied current can sometimes be interrupted on purpose for certain samples in order to examine damage evolution of solder joints prior to an electrical open.

D. Failure analysis

- p) Samples are encapsulated in epoxy or acrylic mounting compounds.
- q) Mounted samples are ground and polished for cross-sectional inspection.
- r) Cross-sectioned solder joints are examined under scanning electron microscopy (SEM) and energy-dispersive X-ray spectroscopy (EDS).

2.5 STATISTICAL ANALYSIS FOR ELECTROMIGRATION LIFETIME

For Al or Cu interconnects in back-end-of-line (BEOL), their EM failure distribution has been known to obey the lognormal distribution. For interconnects, multi-link (or series chain) structures have been implemented into test structure and the results evaluated using a statistical approach [2.2, 2.3]. This approach has a key advantage in reducing the overall test time and improving the sensitivity to detect early failure. Due to the characteristics of the lognormal distribution that do not scale with the number of links [2.4], failure data from multi-link structure should be analyzed using the deconvolution procedure [2.2] or by Monte Carlo simulation [2.3] to deduce EM lifetime parameters. For solder EM investigated in this study, experimental EM failure data were analyzed using a similar approach. The failure distribution was deconvoluted using the Kaplan-Meier method [2.5, 2.6] and failure data were plotted based on the lognormal distribution. EM failure distribution for solder joints also closely followed the lognormal distribution.

2.5.1 Fundamentals of Lognormal Distribution and Weakest-Link Model

Generally, EM failure data have traditionally been treated with the lognormal distribution, where the logarithms of the failure times are normally distributed [2.2, 2.3,

2.5]. The probability density function (PDF), $f(t)$, for the lognormal distribution is given by

$$f(t) = \frac{1}{\sqrt{2\pi}\sigma t} \exp\left[-\frac{(\ln t - \ln t_{50})^2}{2\sigma^2}\right], \quad (2.4)$$

where t is the time, σ is the standard deviation in units of logarithmic time or the shape parameter for the lognormal distribution, and t_{50} is the median time to fail (MTTF). The cumulative distribution function (CDF), $F(t)$, is the integral of the PDF over t :

$$F(t) = \int_0^t f(t) dt. \quad (2.5)$$

$F(t)$ is also called the unreliability function and represents the fraction of all units in the population which fail within the time window t . It is also thought of as the probability that a random unit drawn from the population fails within the time window t [2.5]. The reliability function (survival function), $R(t)$, is then defined by

$$R(t) = 1 - F(t). \quad (2.6)$$

The reliability function is interpreted as either the fraction of all units in the population which will survive at least for time t or the probability that a random unit drawn from the population will still be in operation after time t .

If a system is made up of N independent components and all must operate for the system to function properly, the system fails when any of the components fails first. This

is called the weakest link model or series system model. According to this model, the system reliability function $R_s(t)$ is obtained as follows:

$$R_s(t) = \prod_{i=1}^N R_i(t) = R_1(t) \times R_2(t) \times \cdots \times R_N(t), \quad (2.7)$$

where $R_i(t)$ is the reliability function of the i th component. In terms of the CDF functions,

$$F_s(t) = 1 - \prod_{i=1}^N [1 - F_i(t)], \quad (2.8)$$

where $F_s(t)$ is the system CDF. If all the components are identical, i.e. $R_1(t) = R_2(t) = \cdots = R_N(t) = R(t)$ and $F_1(t) = F_2(t) = \cdots = F_N(t) = F(t)$, then

$$R_s(t) = [R(t)]^N, \quad (2.9)$$

$$F_s(t) = 1 - [1 - F(t)]^N. \quad (2.10)$$

Eq. (2.10) is depicted in Fig. 2.17. With increasing N , it is clear that the lifetime reduces and the lifetime spread becomes smaller. Thus using multi-link systems is beneficial in reducing the test time. It is important to note that the lognormal distribution does not scale with the number of components (links) in a system [2.4]. In other words, even if a single component obeys the lognormal distribution, the multi-link system consisting of N components does not follow the lognormal behavior as shown in Fig. 2.17.

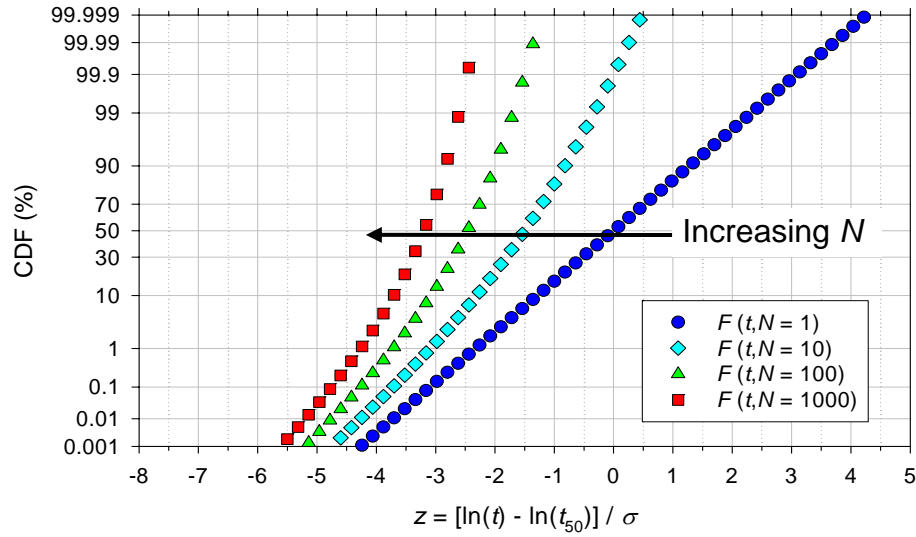


Figure 2.17: Trends of CDF plots with respect to N based on the weakest link model. In the plot, the single-link ($N = 1$) system was assumed to obey the lognormal distribution. [2.3]

2.5.2 Extracting CDF Values Based on Weakest Link Model

In the test module, four solder joints were subjected to current stressing. Two of them were cathode joints and the other two were anode joints according to the current polarity (see Fig 2.4). Among them, only the anode joints developed EM-induced fatal damage and failure due to the current crowding which was much severer in anode joints than cathode joints, as will be discussed in Chapter 3. This means that the failure rate of anode joints was much faster than that of cathode joints. As a result, two out of four solder joints were treated as components (links) which would potentially fail. This is to say that the test structure was a 2-link ($N = 2$) system. In case where 15 modules were under test, 60 solder joints were subject to current stressing but 30 of the anode joints would be vulnerable to EM failure.

Since the lognormal distribution does not scale with the number of links, the multi-link failure distribution data must be deconvoluted. Through the statistical deconvolution process, the lognormal distribution parameters, t_{50} and σ , for the single-link system were deduced from the EM lifetime data of the 2-link system. The Kaplan-Meier method [2.5, 2.6] was used to extract CDF values for the single-link system. For example, consider 15 samples under test, each consisting of 2 components. Therefore, there are 30 components at the beginning of the test. Suppose that one failure occurs at t_1 and another failure at t_2 . Assuming that the event where two components fail at the same time is rare, the probability that the components survive until time t_1 is 29/30. The probability that the components survive from t_1 to t_2 is 27/28 because the other anode (component) in the same sample is also out of test whenever one sample fails. Then the probability of surviving from time zero to t_2 is calculated by $(29/30) \times (27/28)$. Consequently, the CDF values at t_1 and t_2 are obtained by subtracting the survival values from 1: $F(t_1) = 1 - (29/30)$ and $F(t_2) = 1 - [(29/30) \times (27/28)]$. Similarly, the CDF values for all the failure data are determined. This can be generalized by the following formula [2.7]:

$$F(t_i) = 1 - \prod_{j=1}^i \frac{n_j - d_j}{n_j}, \quad i = 1, 2, \dots, m \quad (2.11)$$

where m is the total number of samples (systems), n_j is the total number of components “at risk” just prior to time t_j , d_j is the number of deaths at time t_j . In the aforementioned example, $m = 15$, $n_j = (m + 1 - j) \times 2$, and $d_j = 1$.

CDF values can be readily calculated using a spreadsheet based on Eq. (2.11). Table 2.1 represents an example of the deconvolution process. The first column is the number of failures by time t_i . The second column represents the time to fail for the i th

Table 2.1: Example of deducing CDF values through the deconvolution process. The data analysis follows the steps described in ref. [2.2].

i	t_i (hrs)	n_i	$1/n_i$	$R'(t_i) = 1 - 1/n_i$	$R(t_i) = R(t_{i-1}) \times R'(t_i)$	$F(t_i) = 1 - R(t_i)$
# failure	Time to fail of the i th sample	# operating links at t_{i-1}	Prob. of failure between t_{i-1} and t_i	Conditional reliability function (prob. of survival between t_{i-1} and t_i)	Reliability function	CDF
1	81.6	30	0.03333	0.96667	0.96667	0.03333
2	85.1	28	0.03571	0.96429	0.93214	0.06786
3	97.7	26	0.03846	0.96154	0.89629	0.10371
4	106.4	24	0.04167	0.95833	0.85895	0.14105
5	112.1	22	0.04545	0.95455	0.81990	0.18010
6	118.2	20	0.05000	0.95000	0.77891	0.22109
7	122.4	18	0.05556	0.94444	0.73563	0.26437
8	136.2	16	0.06250	0.93750	0.68966	0.31034
9	138.8	14	0.07143	0.92857	0.64040	0.35960
10	176.2	12	0.08333	0.91667	0.58703	0.41297
11	184.8	10	0.10000	0.90000	0.52833	0.47167
12	219.7	8	0.12500	0.87500	0.46229	0.53771
13	237.1	6	0.16667	0.83333	0.38524	0.61476
14	262.5	4	0.25000	0.75000	0.28893	0.71107
15	346.8	2	0.50000	0.50000	0.14446	0.85554

failed sample, which should be experimentally determined. The third column is the total number of components under operation or “at risk” just prior to time t_i . This decreases by 2 (the number of links in each sample, N) whenever a failure occurs. The fourth column gives the probability of failure between t_{i-1} and t_i . This is simply the reciprocal of the value in the third column because only one fails from t_{i-1} to t_i . The fifth column gives the conditional reliability function or probability of survival between t_{i-1} and t_i . This is calculated by subtracting the value in the fourth column from 1. The sixth column is the reliability function for the single component, meaning the fraction of all components in

population which will survive by time t_i . The last column yields the CDF, which represents the fraction of all components in the population which will fail by time t_i . The CDF plot for data in Table 2.1 is exemplified in Fig. 2.18.

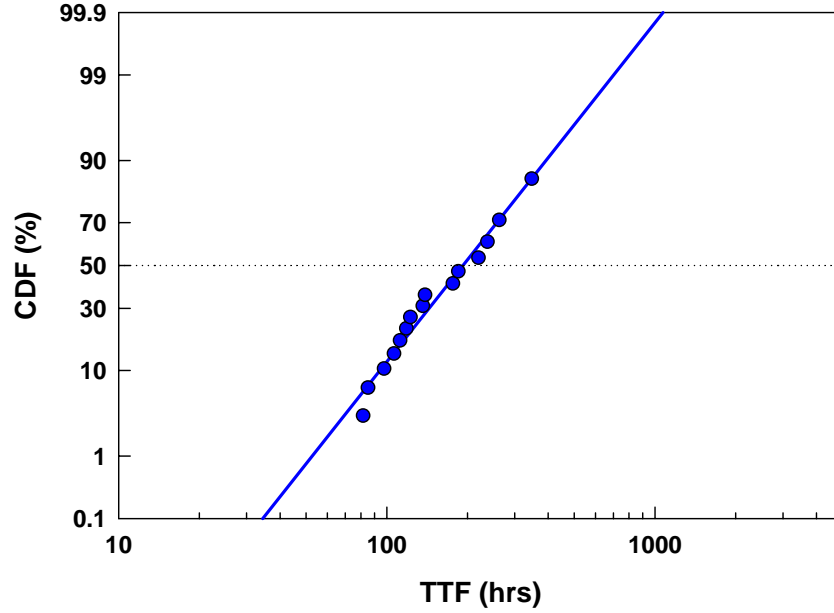


Figure 2.18: A CDF plot from Table 2.1. The failure data of samples consisting of two anode joints were deconvoluted to obtain the CDF values for samples with a single anode joint.

An important advantage of the Kaplan-Meier method is that this method can take into account "censored" samples – losses from the samples before failures occurred. Some of the samples which were still running were sometimes removed from the chamber for cross-sectional examination. In this case, the number of components “at risk,” n_j , in Eq. (2.11) is changed, which must be properly accounted for in calculating the CDF. As an example, suppose two good samples are removed from the test, one between t_1 and t_2 and the other between t_5 and t_6 , respectively. Assume also that the other

preconditions are the same as the aforementioned example. Then the probability that the components survive from t_1 to t_2 is $25/26$ due to the loss of 2 components from a good sample. Accordingly, the reliability function $R(t_2)$ is changed to $(29/30) \times (25/26)$, and the $R(t_i)$ thereafter should be different from those in Table 2.1. In a similar manner, $R(t_6)$ is calculated and $R(t_i)$ thereafter are modified accordingly. The modified values resulting from two losses are listed in Table 2.2.

Table 2.2: Example of the deconvolution process taking into account “losses” of good samples. The major changes are marked in bold.

i	t_i (hrs)	n_i	$1/n_i$	$R'(t_i) = 1 - 1/n_i$	$R(t_i) = R(t_{i-1}) \times R'(t_i)$	$F(t_i) = 1 - R(t_i)$
1	81.6	30	0.03333	0.96667	0.96667	0.03333
2	85.1	26	0.03846	0.96154	0.92949	0.07051
3	97.7	24	0.04167	0.95833	0.89076	0.10924
4	106.4	22	0.04545	0.95455	0.85027	0.14973
5	112.1	20	0.05000	0.95000	0.80776	0.19224
6	118.2	16	0.06250	0.93750	0.75727	0.24273
7	122.4	14	0.07143	0.92857	0.70318	0.29682
8	136.2	12	0.08333	0.91667	0.64458	0.35542
9	138.8	10	0.10000	0.90000	0.58012	0.41988
10	176.2	8	0.12500	0.87500	0.50761	0.49239
11	184.8	6	0.16667	0.83333	0.42301	0.57699
12	219.7	4	0.25000	0.75000	0.31726	0.68274
13	237.1	2	0.50000	0.50000	0.15863	0.84137

Chapter 3: Electromigration Failure Characteristics of Pb-Free Solder Joints

A series of electromigration tests were performed as a function of temperature and current density on Pb-free flip-chip solder joints to investigate lifetime statistics and failure characteristics. Thick Cu and thin Ni under-bump-metallization (UBM) systems were compared. Based on the overall shape of resistance traces, a conservative failure criterion for time-to-failure (TTF) was introduced. These results were compared with those based on the conventional open-failure criterion. The Joule heating effect was quantified based on the experimental data and finite element analysis. The temperature of the solder joints was determined to be approximately 15°C higher than that at the Si die surface when 1 A of current was passed. With the appropriate temperature estimation for solder joints, the activation energies and the current density exponents were determined. The failure mechanisms were different depending on the type of UBM. For solders with Cu UBM, voids were formed initially at the Cu₆Sn₅/solder interface while the final open failure occurred at the Cu₃Sn/Cu₆Sn₅ interface. For Ni UBM, voids were formed initially at the Ni₃Sn₄/solder interface, through which voids propagated.

3.1 INTRODUCTION

With continuing demands to increase I/O density and power requirement, electromigration (EM) failure of solder joints raises increasing reliability concern for flip-chip packages. It is anticipated that flip-chip solder joints will be subject to a current density in the order of 10^4 A/cm² in the near future [3.1]. Although this current density level is still about two orders of magnitude lower than that for Cu interconnects, EM

damage for solder joints still causes a serious concern due to their low current carrying capability [3.2]. In solder joints, the formation of intermetallic compounds (IMCs) at the interface between the solder and the under-bump-metallization (UBM) plays an important role in controlling EM reliability. Noble or near-noble metals such as Cu or Ni in the UBM can diffuse rapidly in Pb or Sn by an interstitial diffusion mechanism [3.3-3.5], and react at a fast rate with Sn to form IMCs [3.6]. The implementation of eco-friendly Pb-free solders generates further interest in studying the effect of UBM on EM reliability of solder joints. This effect is expected to be more significant for Sn-based Pb-free solders. Since Sn is a major constituent of the IMCs, its inexhaustible supply from such Pb-free solders can greatly enhance the IMC formation to degrade EM reliability [3.6, 3.7].

The study was undertaken to investigate the effect of UBM selection on EM reliability for Sn-2.5Ag flip chip solder joints on organic substrate. The Cu UBM was compared with the Ni UBM. Due to the rapid reaction rate of Cu with Sn [3.7], the thick Cu stud in the UBM was of interest. For Ni UBM, the thin Ni film in the UBM was of primary interest due to the slower reaction rate of Ni with Sn [3.8]. Samples were tested under various temperature and current conditions to obtain EM statistical data. The results were compared based on the conventional open-failure criterion and a more conservative criterion. The latter was introduced in this study based on the resistance traces and damage evolution. In accelerated solder EM tests, approximately 1 A current is usually applied [3.6, 3.7, 3.9], which can cause substantial Joule heating. Moreover, heat dissipation in flip chip packages with organic substrate is much less efficient than those with ceramic substrate. Thus the Joule heating effect was taken into account to deduce EM statistics by combining experiments and simulations. EM damage evolution and failure mechanisms were investigated by cross-sectional microscopy of solder joints, with emphasis on the morphology changes of solder joints with IMC growth.

3.2 EXPERIMENTAL DETAILS

Figure 3.1 shows schematic diagrams of the two types of solder joint structures tested in this study. The Pb-free solder material was Sn-2.5Ag solder alloy. The eutectic temperature of Sn-Ag system is 221°C. Figure 3.1(a) shows the TiW (0.25 μm)/Cu (18 μm) UBM structure, and Fig. 3.1(b) represents the Ti (0.1 μm)/Ni (2 μm) UBM structure. The TiW and Ti layer served as a layer for seed layer deposition as well as a barrier layer preventing wicking of UBM material to Si die. Both Cu and Ni UBM were electroplated after sputter deposition of the seed layers. Thickness variations of Cu and Ni UBM were $\pm 4 \mu\text{m}$ and $\pm 0.5 \mu\text{m}$, respectively. The passivation opening of the UBM was 50 μm in diameter. On the substrate side, a 5 μm -Ni(P) was plated electrolessly as a substrate finish layer on the substrate Cu pad. The solder bump had a nominal diameter of 130 μm . The stand-off height (distance between UBM and substrate finish layer) of the solder bump was $\sim 40 \mu\text{m}$ for Cu UBM and $\sim 56 \mu\text{m}$ for Ni UBM, respectively.

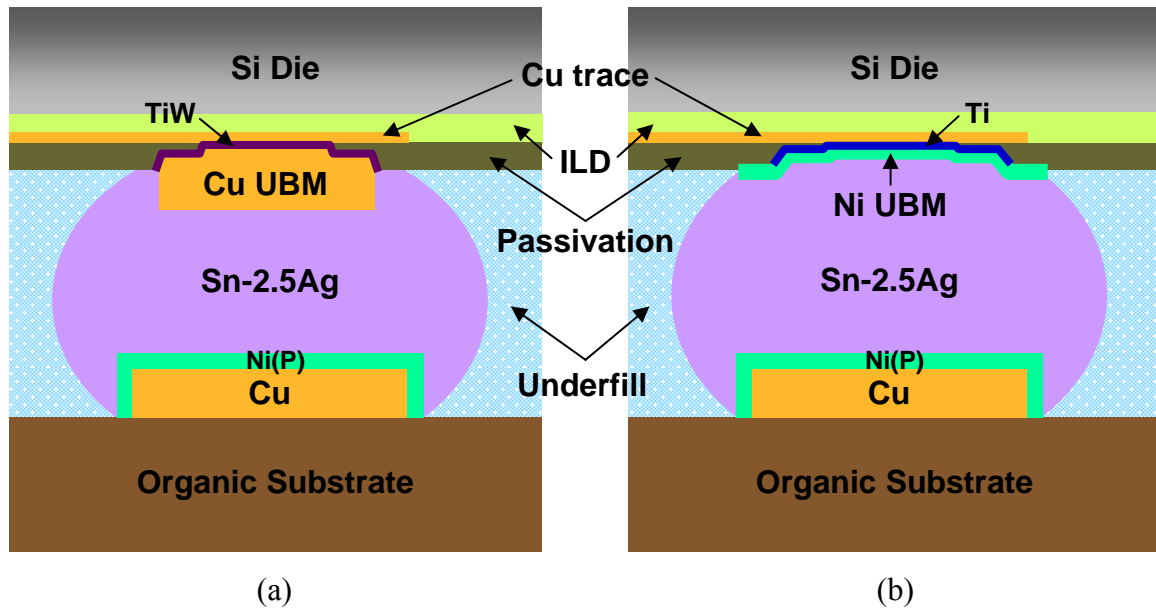


Figure 3.1: Schematic diagrams of flip-chip solder joints with (a) Cu UBM (18 μm), and (b) Ni UBM (2 μm).

In the EM test oven, a set of samples were arranged such that the Si backside of the samples was brought into contact with a Cu plate. To enhance the thermal contact, a thermal compound was applied between the Si die and the Cu plate. In this manner, the temperature deviation from one sample to another was minimized and Joule heat in the test sample was able to be dissipated efficiently. Thermocouples were sandwiched between the backside of dies and the Cu plate to monitor the Si backside temperature, which was generally higher than the oven temperature by 7-20°C depending on the applied current.

Six EM runs were conducted on test modules with a 2-link chain structure. Two UBM types were tested altogether in a chamber to ensure the same test conditions to be applied. 12-15 samples (i.e. 24-30 pairs of solder joints) of each UBM structure were loaded under each run. Test temperatures were chosen based on the Si backside temperature. Then the chamber temperature was adjusted such that the Si backside temperature matched this pre-determined temperature. Due to Joule heating, the chamber temperature was set to about 7.5 to 20°C lower than the pre-determined Si backside temperature. Several thermocouples sandwiched between the Si backside and the Cu plate were monitored throughout experiments. The average thermocouple reading was taken to represent the Si backside temperature. The maximum temperature difference between the thermocouple readings was usually less than ~2°C.

Four runs were carried out at different temperatures with a fixed applied current to investigate the temperature dependence of the EM lifetime. Two additional runs were conducted at a fixed temperature with different applied currents to determine the current density dependence. The applied currents of 0.81, 1.01, and 1.11 A corresponded to current densities of 4.12, 5.16, and 5.67 in 10^4 A/cm^2 , respectively, based on the area of the passivation opening. Table 3.1 summarizes the chamber temperature setting for each

EM test. Whenever a sample failed, the Si backside temperatures of other samples were also decreased by $\sim 0.2\text{-}0.5^{\circ}\text{C}$ because a Joule heat source was removed and the Cu plate in contact with the Si backside quickly equilibrated to the new temperature. Accordingly, the chamber temperature was adjusted to bring the Si backside temperature back to the set point, whenever failure occurred.

Table 3.1: Chamber temperature set to achieve desired Si backside temperatures for each EM test condition.

Chamber temp. ($^{\circ}\text{C}$)	Applied current (A)	Si backside temp. ($^{\circ}\text{C}$)	Total # samples
103.0	1.01	115	29
118.0	1.01	130	25
126.1	1.01	140	30
138.0	1.01	150	28
132.5	0.81	140	28
120.4	1.11	140	29

To investigate damage evolution and failure mechanisms for Pb-free solder EM, 66 test modules (264 solder joints) which had been subject to current stressing were cross-sectioned and examined with SEM/EDS. A backscattered electron detector was used to clearly distinguish the different materials in solder joints. The applied current to a test module was sometimes interrupted when it became necessary to investigate initial void formation and void propagation (or growth) with respect to the resistance rise.

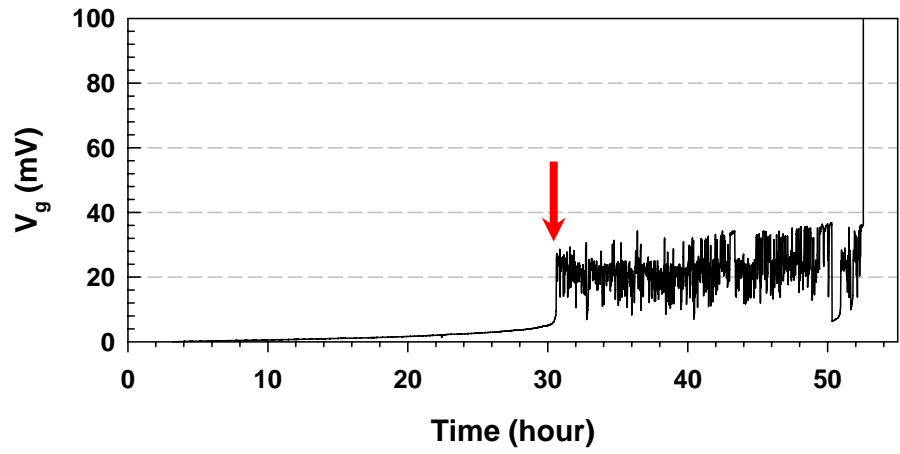
3.3 RESULTS AND DISCUSSION

3.3.1 Failure Criteria

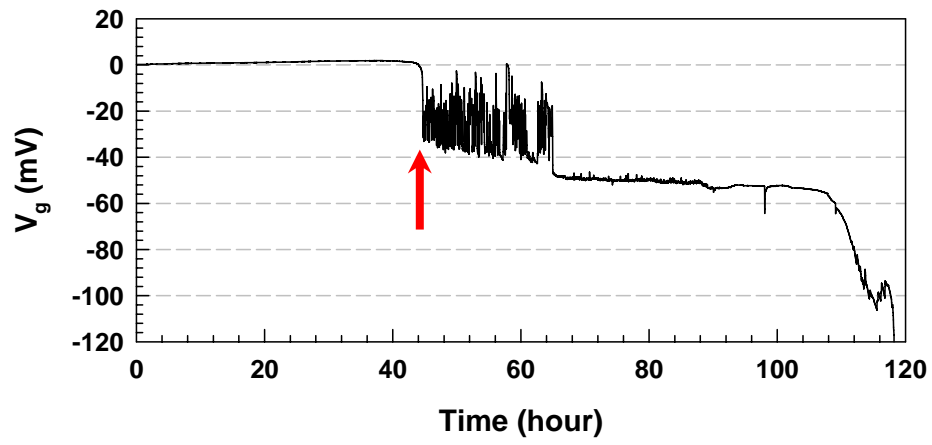
During and after EM experiments, off-balance voltage (V_g) and resistance (R converted from V_s) traces for test modules were inspected to monitor the structural damage, such as IMC growth and voiding, caused by EM. Because of the high sensitivity of the Wheatstone bridge method, resistance changes of solder joints were monitored primarily with V_g traces while R (or V_s) traces were monitored for reference purposes. Resistance traces in solder EM experiments showed distinctive characteristics. A resistance jump preceded well before a solder joint became electrically open. Moreover, this jump was usually followed by unstable resistance fluctuation. Based on this observation, a new failure criterion, named first resistance jump, was suggested and applied to determine EM lifetimes.

3.3.1.1 Typical V_g Traces for Pb-Free Solder Joints

Figures 3.2 and 3.3 represent typical V_g traces of Sn-2.5Ag solder joints with Cu and Ni UBM, respectively. Initially, V_g increased slowly. Then an abrupt jump in V_g occurred, which was followed by unstable fluctuations. The V_g increase was more abrupt in Cu UBM than Ni UBM. The resistance fluctuations were attributed to simultaneous damage evolution and recovery process in solder joints, which eventually led to an electrical open failure [3.10]. At this stage, the solder joints became unstable and vulnerable to failure. The period of unstable fluctuations lasted usually longer for solder joints with Cu UBM than with Ni UBM in this study, which could be related to their thickness difference.

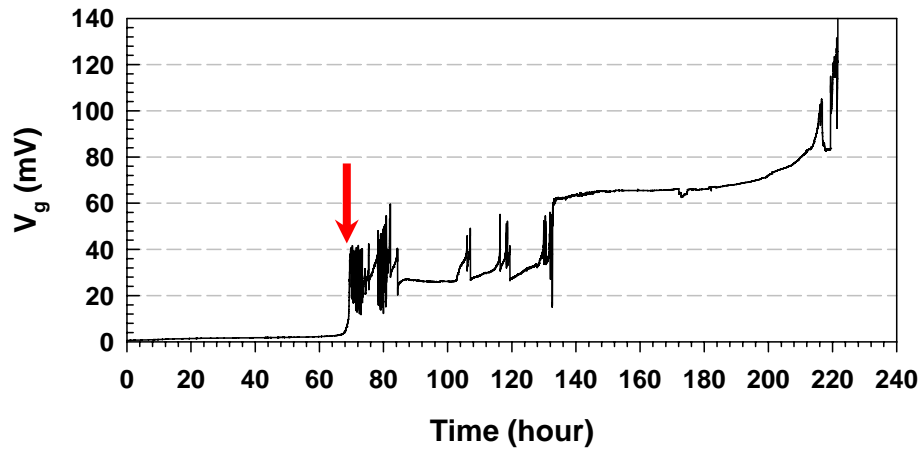


(a)

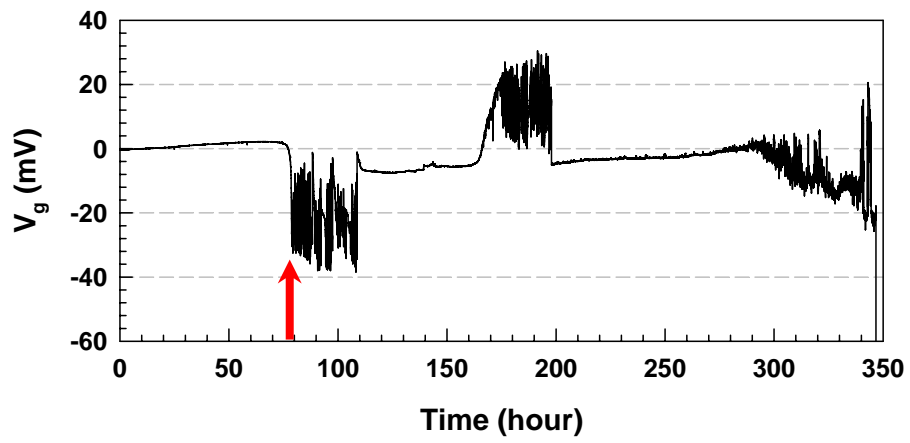


(b)

Figure 3.2: Typical V_g traces for solder joints with Cu UBM.

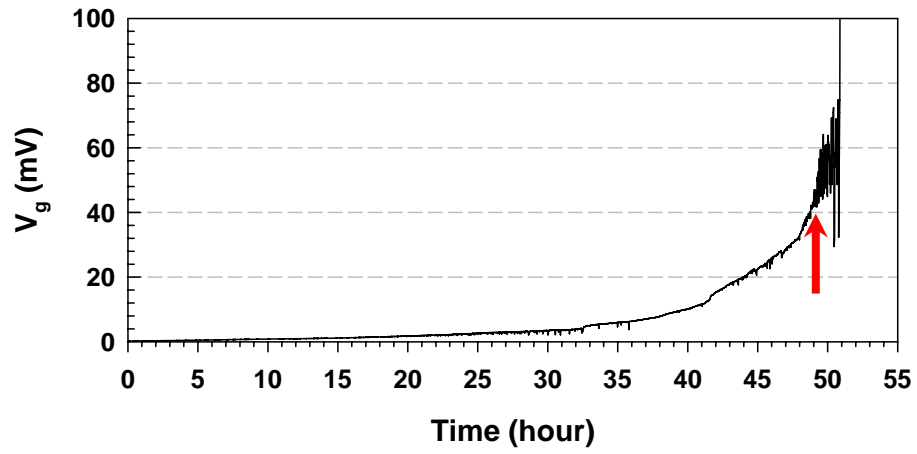


(c)

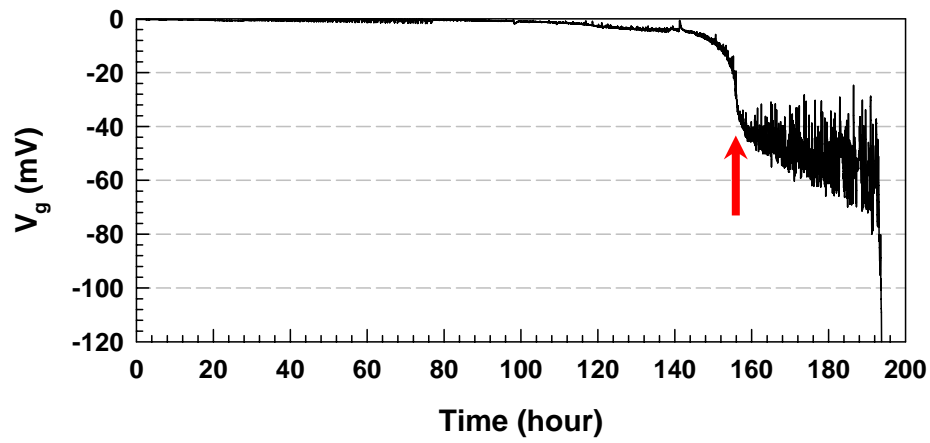


(d)

Figure 3.2: (cont'd) Typical V_g traces for solder joints with Cu UBM.

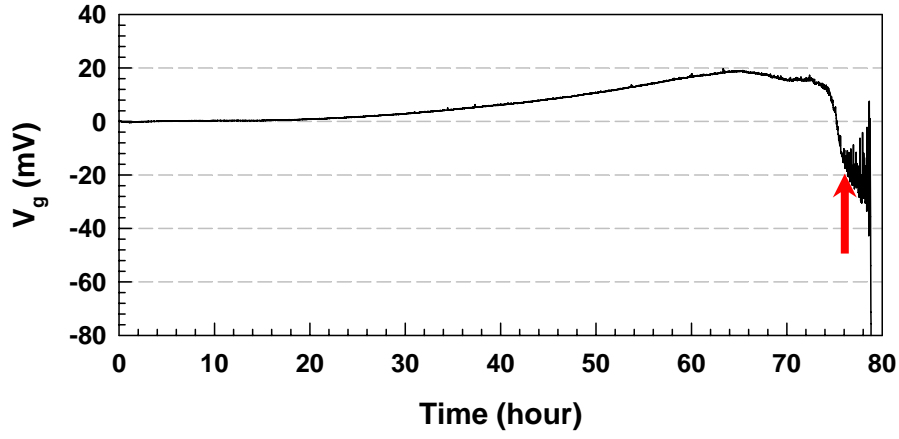


(a)



(b)

Figure 3.3: Typical V_g traces for solder joints with Ni UBM.



(c)

Figure 3.3: (cont'd) Typical V_g traces for solder joints with Ni UBM.

For solder joints with Cu UBM, the resistance jump occurred with a sharp transition from a few mV to $\sim 30\text{-}40$ mV in V_g . This corresponded to a $\sim 50\text{-}100\text{m}\Omega$ increase in resistance of a single solder joint. The resistance fluctuations usually lasted for a prolonged time. Figure 3.2(a) shows a jittering period occupying about half the total lifetime. According to Eq. (2.3), the failing or failed solder joint was identified from the sign of V_g . Thus Fig. 3.2(a) indicates the failure occurred in the first pair of solder joints (4th or 5th joint from the left). Because EM failures always occurred in anode joints as will be discussed later, the 5th joint was the one that failed. In contrast, when the 9th solder joint failed, V_g increased in the opposite way, that is, with a negative sign as shown in Fig. 3.2(b). A plateau region is seen subsequent to the resistance fluctuations. As shown in Fig. 3.2(c), a state of lull sometimes existed between jitters. Figure 3.2(d) shows another example of a resistance trace for solder joints with Cu UBM. The first jittering took place with a negative sign and then came to a momentary lull. What

followed was the second resistance jump with a positive sign. With this kind of resistance trace, it was expected that serious EM damage was developed in both the 5th and 9th solder joints.

Figure 3.3 shows V_g traces for solder joints with Ni UBM. Typically, the resistance rise was more gradual and the jittering period was much shorter compared with Cu UBM solders as shown in Fig. 3.3(a). Still, the onset of resistance fluctuation occurred at ~40 mV. Figure 3.3(b) shows a relatively long jittering period for Ni UBM solders. Also, the amplitude of jittering grew larger with time. This was followed directly by the final open. Unlike Cu UBM solders, a state of lull during jittering was rarely observed in Ni UBM. Figure 3.3(c) shows that the initial EM damage in the 4th joint was developing faster than in the 9th joint but the latter failed first. This may indicate that void growth is a more critical factor than void initiation (or nucleation) in controlling EM lifetime of solder joints.

3.3.1.2 Open Failure Criterion vs. First Resistance Jump Criterion

Resistance traces in solder EM experiments had a distinctive characteristic of the resistance jump. In order to estimate the extent of voiding at this stage, V_g was calculated with respect to the fraction of open (voiding area/interfacial contact area) using MATLAB. According to the result as shown in Fig. 3.4, a 30-40 mV change in V_g corresponded to >90% opening of the solder joint. This was also confirmed by cross-sectional SEM observations and will be discussed in the following section. After a resistance jump, the solder joint became almost open with fatal EM damage including extensive IMC formation and voiding. Moreover, significant additional Joule heat could be generated at this stage. In this regard, jittering represents the instability of this stage. Therefore, the first resistance jump or the onset of jittering is suggested as an alternate

failure criterion in this study to supplement the conventional open failure criterion to evaluate EM lifetime. Arrows in Figs. 3.2 and 3.3 indicate where the first resistance jump criterion regards as failure of a solder joint.

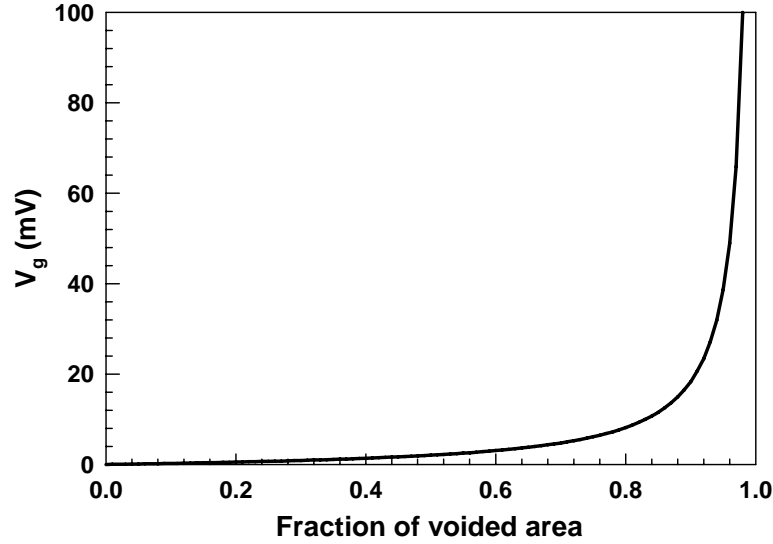


Figure 3.4: Calculated off-balance voltage V_g with respect to the fraction of voided area (ratio of void to interfacial area).

3.3.2 Electromigration Lifetime

Temperature dependence of EM lifetime was investigated with the current density fixed at 5.16×10^4 A/cm². EM runs were performed at 115, 130, 140 and 150°C of the Si backside temperature with 1.01A. Since two pairs of solder joints were connected in series, cumulative distribution function (CDF) was deconvoluted based on the weakest link model described in Section 2.5 to deduce statistical EM parameters, t_{50} and σ , pertaining to a single solder joint. The deconvoluted CDF plots for solder joints with Cu and Ni UBM are depicted in Figs. 3.5 and 3.6 based on the lognormal distribution. The time to fail (TTF) of each sample was determined by both the open failure criterion (Fig.

3.5) and the first resistance jump criterion (Fig. 3.6). For Cu UBM solders, the data of 130°C and 140°C show unusual behavior. Although the reason was not clearly understood, it was hypothesized to the initial resistance deviation and/or temperature deviation between samples. The results of t_{50} and σ are summarized in Table 3.2.

Based on the open failure criterion, the MTTF of solder joints with Cu UBM was 1.5 to 4 times longer than that Ni UBM. In contrast, when the first resistance jump criterion was applied, the MTTFs of solder joints with Cu and Ni UBM became comparable. This is attributed to the fact that the period of resistance fluctuation in Cu UBM solders amounted to a large portion, as much as 49 % on the average, of the total lifetime whereas the jittering period in Ni UBM solders amounted to only 12 % on the average.

Table 3.2: Summary of temperature dependent EM lifetime, based on two different failure criteria. The applied current was 1.01 A ($j = 5.16 \times 10^4$ A/cm²).

Si backside temperature (°C)	Open failure criterion				First resistance jump criterion			
	Cu UBM		Ni UBM		Cu UBM		Ni UBM	
	t_{50} (hrs)	σ	t_{50} (hrs)	σ	t_{50} (hrs)	σ	t_{50} (hrs)	σ
115	1570	1.1	410	1.0	460	0.6	380	1.0
130	690	1.3	290	1.4	440	1.3	240	1.3
140	190	0.6	130	1.3	93	0.8	96	1.1
150	140	1.0	56	1.2	49	0.7	45	1.0

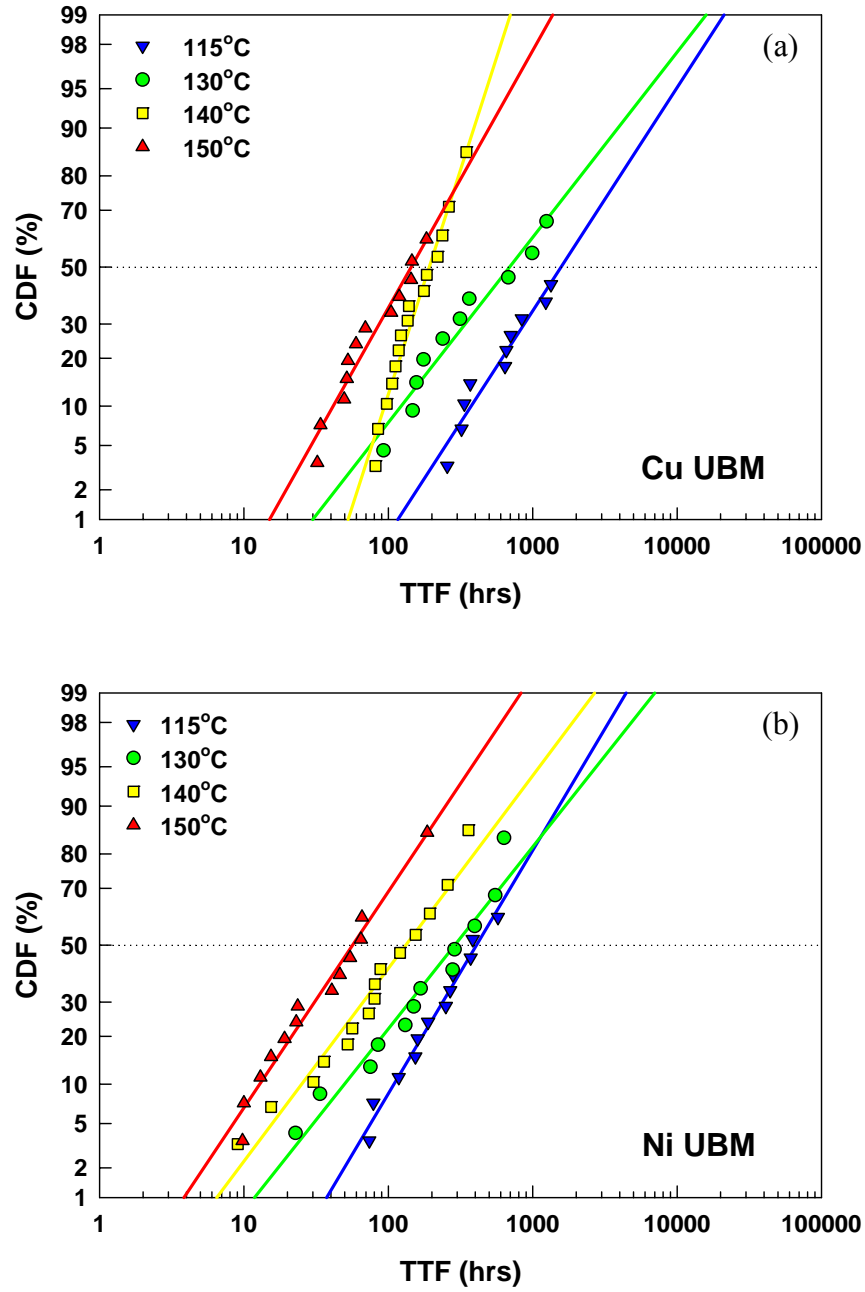


Figure 3.5: Temperature dependence of deconvoluted failure distributions based on the open failure criterion for solder joints with (a) Cu UBM, and (b) Ni UBM. Current density was fixed at 5.16×10^4 A/cm². Temperatures shown represent the Si backside temperatures.

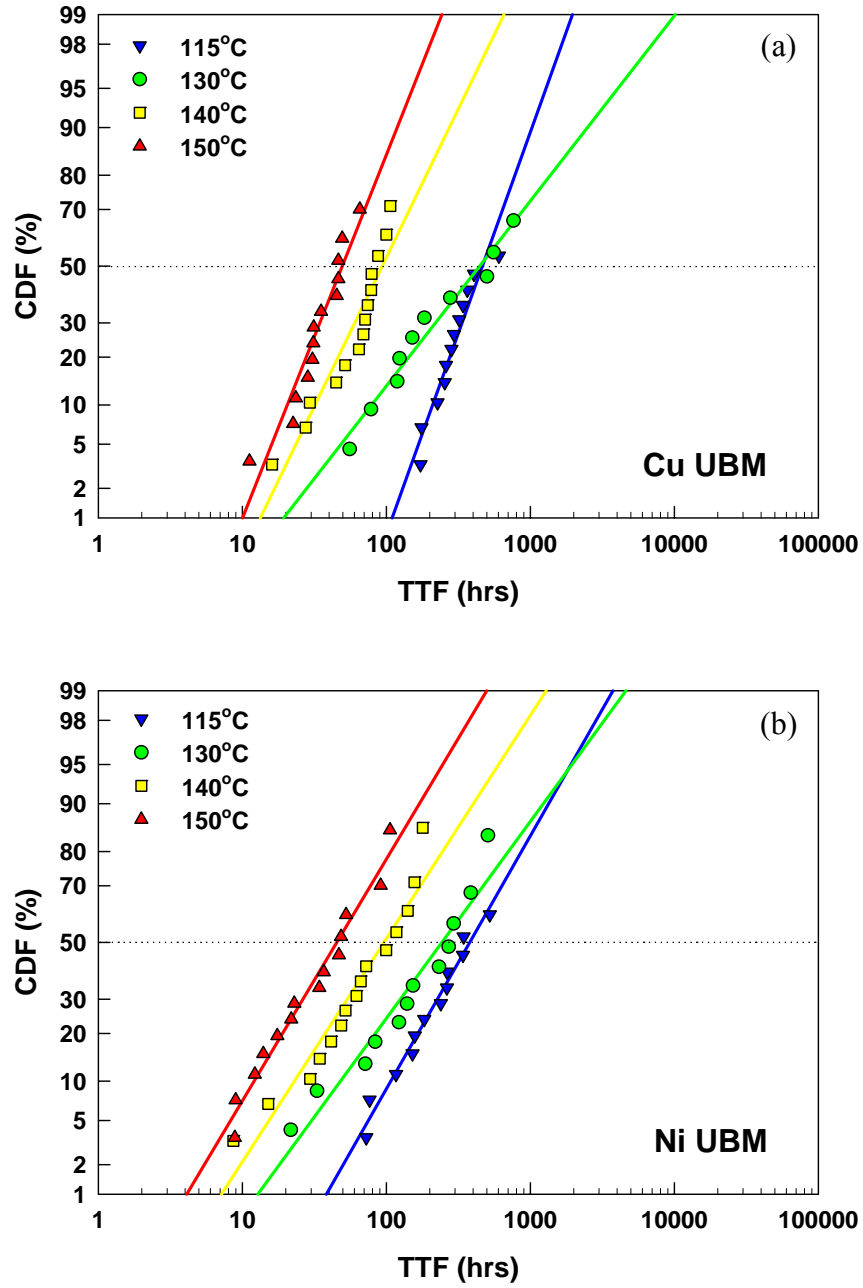


Figure 3.6: Temperature dependence of deconvoluted failure distributions based on the first resistance jump criterion for solder joints with (a) Cu UBM, and (b) Ni UBM. Current density was fixed at 5.16×10^4 A/cm². Temperatures shown represent the Si backside temperatures.

Current density dependence of EM lifetime was examined with the Si backside temperature fixed at 140°C. Three different current levels, 0.81, 1.01 and 1.11 A, were applied, which corresponded to 4.12, 5.16 and 5.67×10^4 A/cm², respectively. The current density was calculated based on the passivation opening (50 µm in diameter). The failure distributions deconvoluted for a single anode joint were plotted in Figs. 3.7 and 3.8. The resulting t_{50} and σ are listed in Table 3.3.

The MTTF of solder joints with Cu UBM was 1.5-3 times longer than that with Ni UBM based on the open failure criterion, but under the first resistance jump criterion both MTTFs were comparable for the same reason discussed above. It was also found that the fraction of resistance fluctuations over the whole lifetime for Cu UBM solders became longer when current density was small. At $j = 4.12 \times 10^4$ A/cm², the MTTF of Cu UBM solders was reduced by a factor of 4 when the first resistance jump criterion was applied. Considering that the onset of resistance fluctuation already corresponds to significant damage of a solder joint as discussed in the previous section, it is important to select a proper failure criterion to evaluate solder reliability, particularly for a thick Cu UBM.

Table 3.3: Summary of current density dependent EM lifetime, based on two different failure criteria. The Si backside temperature was fixed at 140°C.

Applied current (A)	Current density (10^4 A/cm ²)	Open failure criterion				First resistance jump criterion			
		Cu UBM		Ni UBM		Cu UBM		Ni UBM	
		t_{50} (hrs)	σ	t_{50} (hrs)	σ	t_{50} (hrs)	σ	t_{50} (hrs)	σ
0.81	4.12	910	1.3	310	1.4	230	0.8	260	1.3
1.01	5.16	190	0.6	130	1.3	93	0.8	96	1.1
1.11	5.67	200	0.6	110	1.3	98	0.9	92	1.2

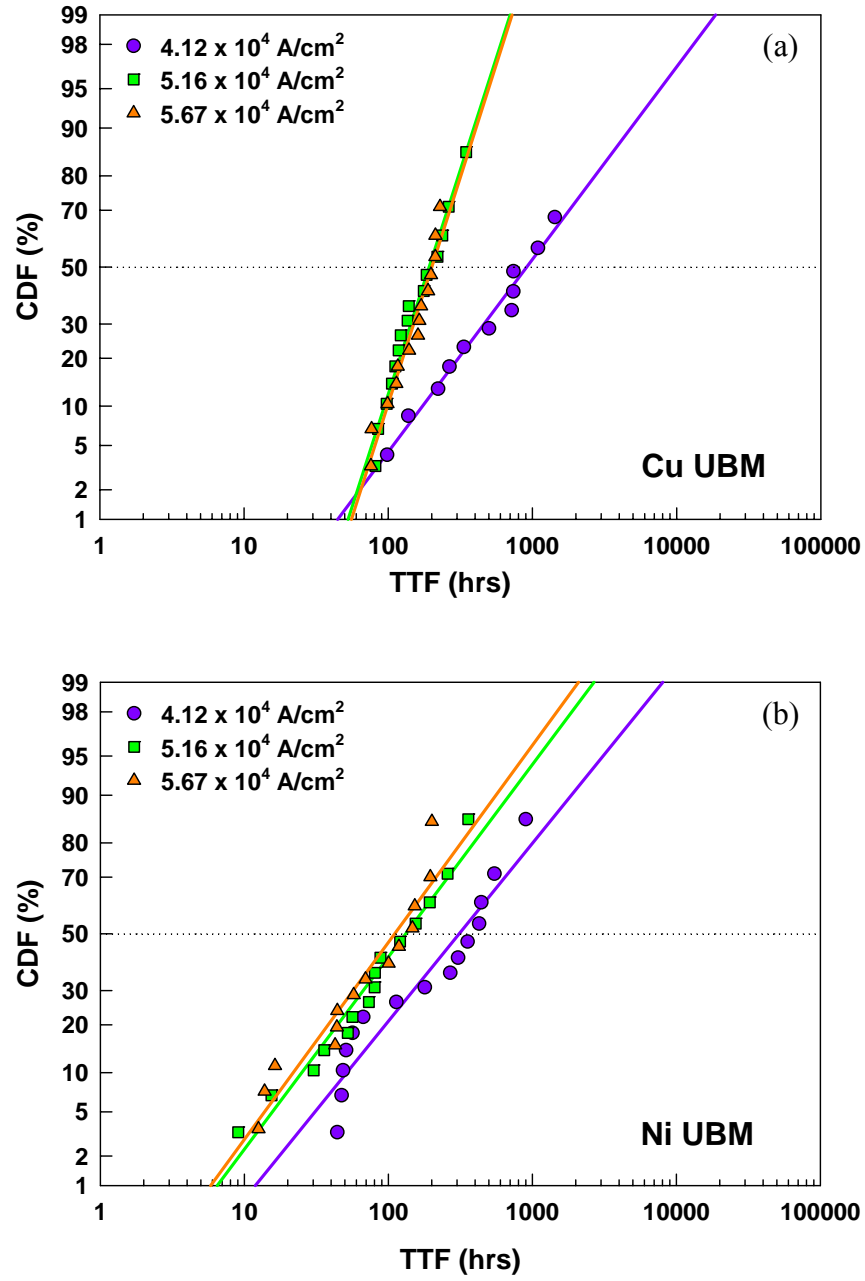


Figure 3.7: Current density dependence of deconvoluted failure distributions based on the open failure criterion for solder joints with (a) Cu UBM, and (b) Ni UBM. The Si backside temperature was fixed at 140°C.

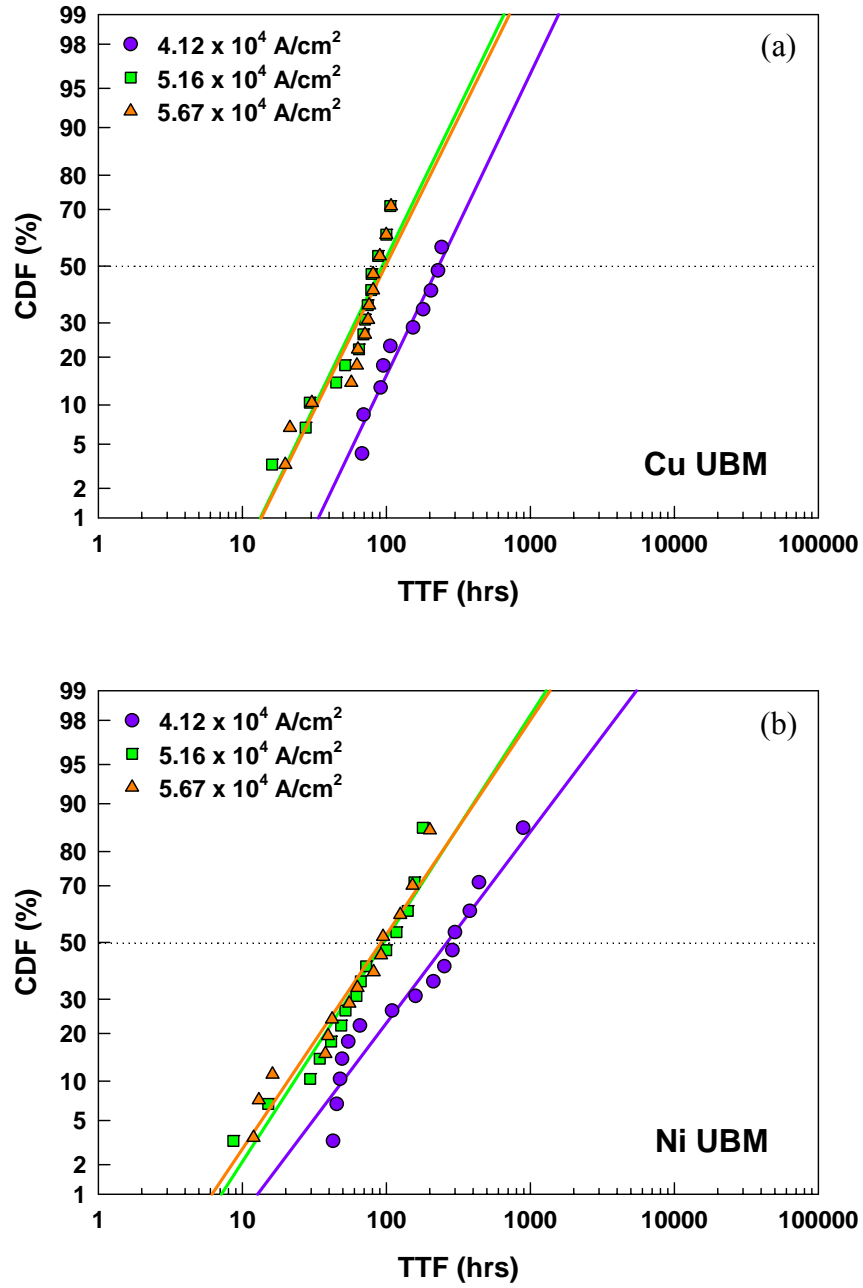


Figure 3.8: Current density dependence of deconvoluted failure distributions based on the first resistance jump criterion for solder joints with (a) Cu UBM, and (b) Ni UBM. The Si backside temperature was fixed at 140°C.

3.3.3 Joule Heating Characterization

Due to the large applied current (~ 1 A), the Joule heating effect should be present, causing the temperature of the solder joints to increase. This can make the solder temperature different from the temperature at the backside of the Si die although the former was often assumed to be the same as the latter [3.11, 3.12]. To determine the Joule heating effect, the resistance changes were measured as a function of temperature and then applied current. Subsequently, these experimental results were supplemented with finite element analysis (FEA).

3.3.3.1 Experimental Joule Heating Measurement

A two-step procedure was employed for experimental Joule heating measurements. First, the temperature coefficient of resistance (TCR) of the test structure was determined by measuring the resistance with increasing temperature. TCR is defined as the slope of the fractional resistance deviation ($\Delta R/R$). For this measurement, resistance values of 9 samples were recorded, ranging from room temperature ($\sim 25^\circ\text{C}$) to the target temperature (140°C). Every time the chamber temperature was changed to the next set temperature, the corresponding resistances were measured after about 1 hour so that thermal equilibrium condition could be attained between the samples, the Cu plate, and the ambient air in the chamber. The applied current was minimal (< 50 mA) to avoid unintentional Joule heating effect. TCR was calculated from the measurement results according to the following equation [3.13]:

$$R = R_r[1 + \alpha(T - T_r)], \quad (3.1)$$

where R is the resistance at the chamber temperature T , R_r is the resistance at a reference temperature (usually room temperature) T_r , and α is the temperature coefficient of resistance (TCR). It was confirmed by thermocouple measurements that the Si backside temperature was the same as the chamber temperature at this low current level. Under this condition, the temperature of solder joints was assumed to be the same as the chamber temperature. As shown in Fig. 3.9, the TCR was found to be $3.57 \times 10^{-3} (\text{°C})^{-1}$. This value is plausible considering the TCR of bulk Cu is $3.9 \times 10^{-3} (\text{°C})^{-1}$ and that of $0.5 \mu\text{m}$ wide Cu interconnects is $3.3 \times 10^{-3} (\text{°C})^{-1}$ [3.13], because the major part of the current path was through the Cu trace while the portion of the path through solder and UBM was almost negligible.

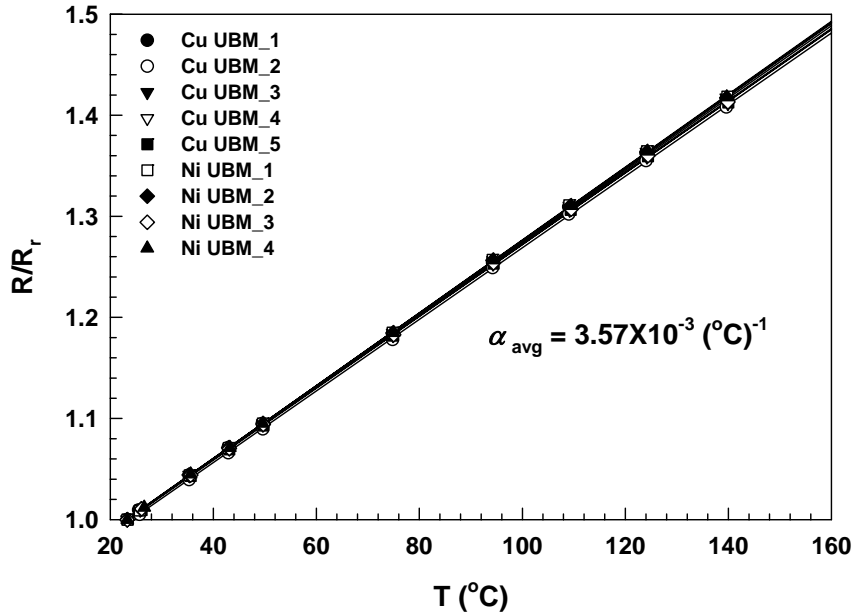


Figure 3.9: Plot of R/R_r with temperature for the TCR measurement.

In the next step, the chamber temperature was set to 120 °C, and resistance changes were measured while the applied current was raised from the minimum current to 1.1 A. From Eq. (3.1),

$$\Delta R = R(i) - R_0 = \alpha R_0 (T - T_0) = \alpha R_0 \Delta T , \quad (3.2)$$

where $R(i)$ is the resistance as a function of the applied current, R_0 is the baseline resistance at T_0 , and T_0 is the test (chamber) temperature. Therefore, R_0 is the resistance without the Joule heating effect and $R(i)$ is the resistance affected by the Joule heating. The temperature rise by Joule heating is proportional to the electrical power according to the following relationship:

$$\Delta T = R_{th} P = R_{th} i^2 R , \quad (3.3)$$

where R_{th} is the thermal resistance (°C/W), P is the electrical power, and i is the applied current. Combining Eqs. (3.2) and (3.3) gives

$$\frac{\Delta R}{R_0} = \alpha \Delta T = \alpha R_{th} i^2 R . \quad (3.4)$$

Because R in Eqs. (3.3) and (3.4) is a temperature-dependent term, it is also a function of i . This is because the Joule heating due to the applied current increases the temperature of the material, and in turn increases its resistance. Subsequently, this may cause a temperature rise again. This recurring process will be equilibrated when the system reaches the thermal equilibrium by dissipating heat to the surroundings in a steady state fashion. As a result, the $\Delta R/R_0$ vs. i relationship after thermal equilibrium can have an

exponent higher than 2. The current dependency of $\Delta R/R_0$ was deduced from the log-log plot of $\Delta R/R_0$ and i as shown in Fig. 3.10, leading to

$$\Delta R/R_0 = 0.158 \cdot i^{2.166}. \quad (3.5)$$

A similar result was obtained when the chamber temperature was set to 140°C:

$$\Delta R/R_0 = 0.157 \cdot i^{2.162}. \quad (3.6)$$

As seen in Fig. 3.10, the electrical behavior of solder joints with Cu and Ni UBM did not show any noticeable difference.

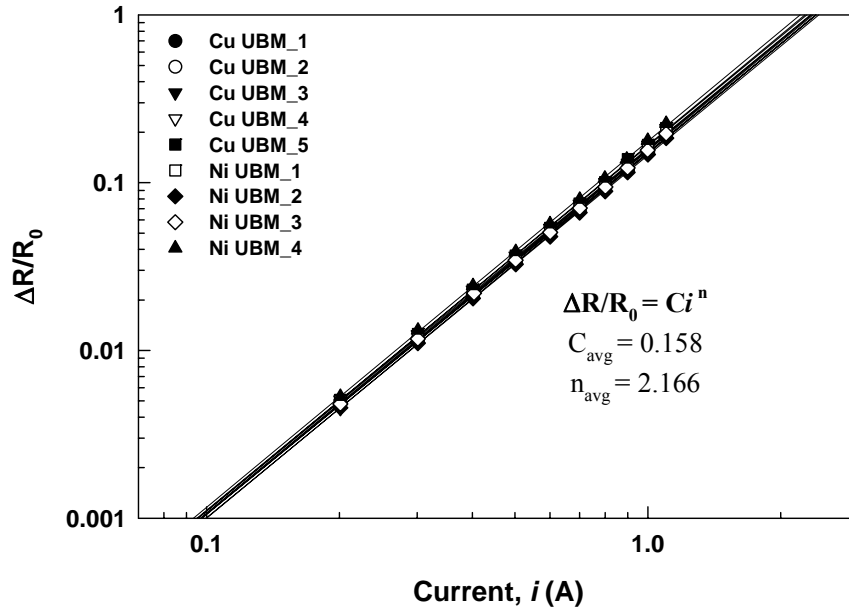


Figure 3.10: Plot of the resistance increase as a function of the applied current when the chamber temperature was set to 120°C.

The $\Delta R/R_0$ relationship experimentally obtained was then substituted to Eq. (3.2) to determine ΔT . At the applied current of 0.81, 1.01 and 1.11 A, ΔT (i.e. temperature difference between the test structure and the chamber) was found to be ~28, 45 and 55.5°C. Considering the temperature difference between the Si backside and the chamber as shown in Table 3.1, this indicated that the temperature of the test structure was ~20, 33 and 36°C higher than the Si backside temperature, respectively. However, this would be valid only when the temperature gradient along the current path was negligible. Since the temperature gradient was expected to exist inside the test structure (including solder joints, die traces and substrate traces), the ΔT obtained above would only represent an averaged temperature rise in the test structure. Therefore, a supplemental analysis should be performed in order to determine the temperature at a specific region such as solder joints.

3.3.3.2 Coupled Electro-Thermal Finite Element Analysis

To supplement the experimental Joule heating results, the temperature distribution inside the test structure was modeled using a coupled electro-thermal finite element method (FEM). A detailed description of the FEM simulation is provided in Appendix A. FEM was conducted on the Cu UBM structure only because the TCR and Joule heating experiments showed no distinguishable difference between the Cu and the Ni UBM structure. The resistance values for the current path from FEM results agreed well with the experimental result. At 0.81, 1.01 and 1.11 A of the applied current, the solder joint temperature turned out to be higher than that at the Si backside by 10, 15 and 17°C, respectively as depicted in Fig. 3.11. The maximum temperature in the current path was observed in the substrate Cu trace, the length of which was ~33 mm. Although the very thin die traces were also a major source of Joule heat, their temperature was lower than

the substrate trace temperature. This was because the Joule heat from die traces could be dissipated effectively through Si die which is a good thermal conductor. As a result, the temperature difference within the solder was less than 3°C, being slightly higher at the substrate side than the die side. The thermal gradient was about 375 °C/cm. Because thermomigration (TM) was reported in Pb-In solder alloys at a thermal gradient of 1200 °C/cm [3.14] and in Pb-Sn at >1000 °C/cm [3.15, 3.16], TM was not a factor affecting the mass transport in this study with the relatively low thermal gradient.

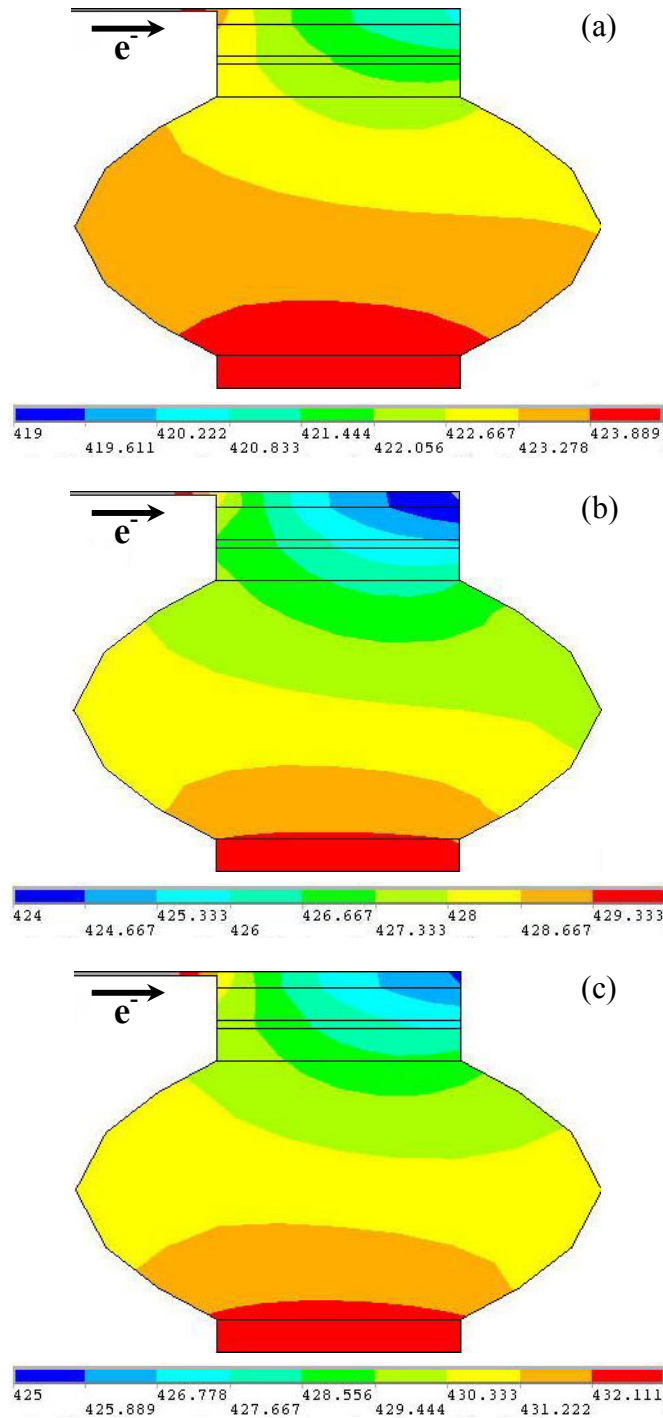


Figure 3.11: Simulated temperature (in K) of the anode solder joints with Cu UBM under current stressing of (a) 0.81 A, (b) 1.01 A, and (c) 1.11 A. Top – die side; bottom – substrate side.

3.3.4 Determination of Electromigration Activation Energy (Q) and Current Density Exponent (n)

From the EM lifetime data, the EM activation energy and the current density exponent for solder joints were calculated using the Black's equation [3.17]:

$$t_{50} = Aj^{-n} \exp\left(\frac{Q}{kT}\right), \quad (3.7)$$

where t_{50} is the median time to fail (MTTF), A is a constant, j is the current density, n is the current density exponent, Q is the activation energy, k is the Boltzmann constant, and T is the absolute temperature. First, activation energies for EM were determined with the corrected solder temperatures under the current stressing of 1.01 A. The corrected solder temperatures from various Si backside temperatures were obtained by FEM and the results are summarized in Table 3.4. Figure 3.12 depicts Arrhenius plots to obtain activation energies. The EM activation energies were found to be little dependent on the failure criteria applied for each type of UBM. The activation energies for Sn-2.5Ag solder joints with Cu UBM and Ni UBM were determined to be 1.0 ± 0.3 eV and 0.9 ± 0.2 eV, respectively, based on the first resistance jump criterion. These values were in good agreement with those from Cu-Sn and Ni-Sn IMC growth experiments in the literature, respectively [3.18-3.22]. This suggests that IMC growth due to the interdiffusion between the UBM material and the Sn-based solder plays a significant role in solder EM reliability. Further discussion on the activation energy will be given in Chapter 4.

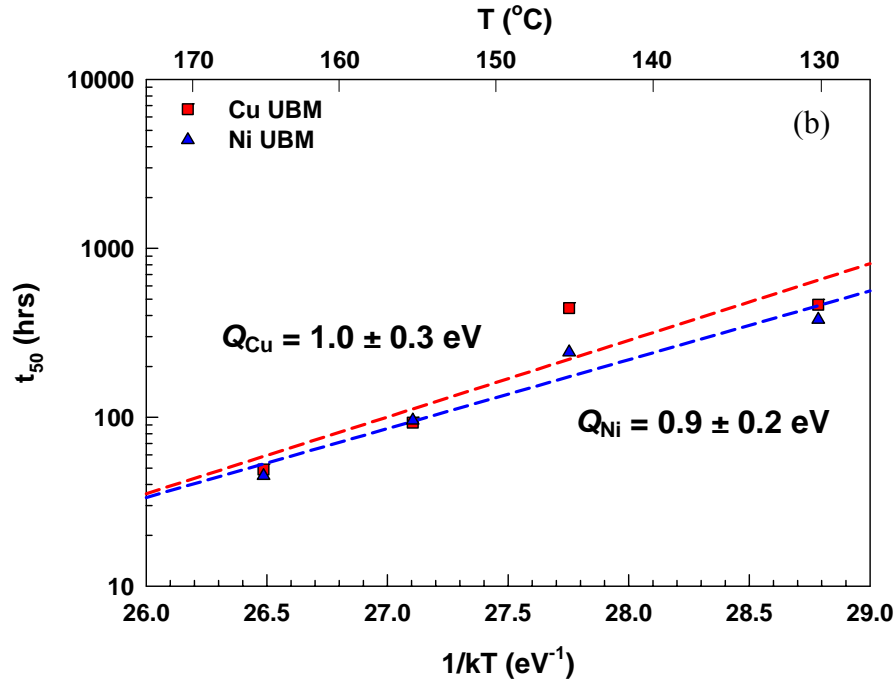
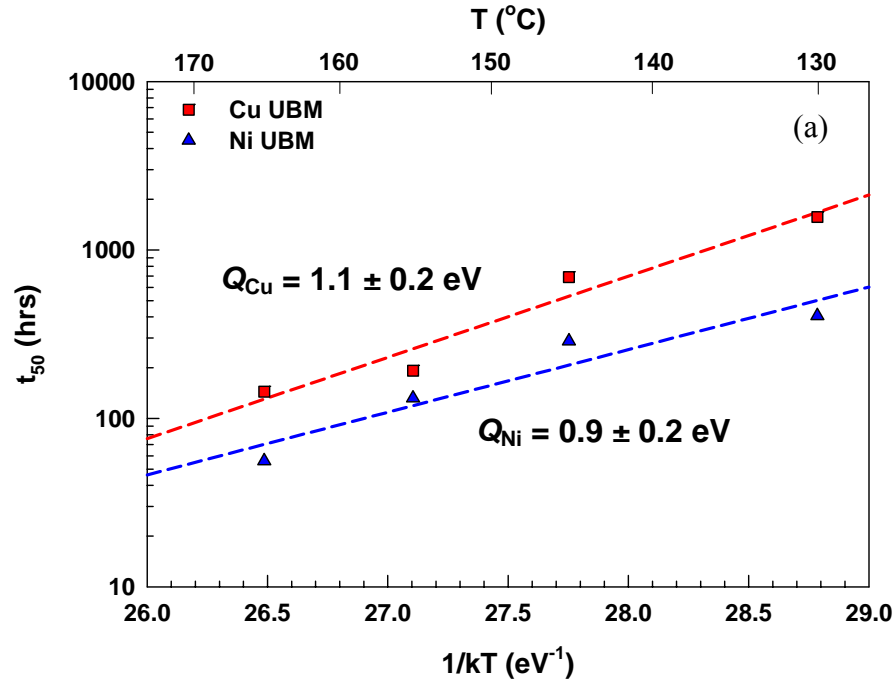


Figure 3.12: EM activation energies after taking into account the Joule heating effect under current stressing of 1.01A, based on (a) the open failure criterion, and (b) the first resistance jump criterion.

Table 3.4: Summary of temperature dependent EM lifetime, after the solder temperature correction. The applied current was 1.01 A ($j = 5.16 \times 10^4$ A/cm²).

Si backside temperature (°C)	Simulated solder temp. (°C)	t_{50} (hrs)			
		Open failure criterion		First resistance jump criterion	
		Cu UBM	Ni UBM	Cu UBM	Ni UBM
115	130	1570	407	464	379
130	145	690	288	444	243
140	155	192	132	93	96
150	165	144	56	49	45

Current density exponents were also deduced using Eq. (3.7). However, this was not as straightforward as the activation energy calculation. Although the experiments to study the current density dependence were done with the Si backside temperature fixed, the solder temperature under each current density condition was found to be different due to the difference in Joule heating as shown in Table 3.5. Thus an extrapolation of the MTTFs obtained from different solder temperatures, 150, 155 and 157°C, was performed to deduce MTTFs which corresponded to a fixed reference temperature. 140°C was chosen as the reference temperature. Several different reference temperatures were also tried, but the choice of the reference temperature had a negligible effect on the final result. Extrapolation was done using the Black's equation and the activation energies obtained above. The MTTFs at 140°C after extrapolation are summarized in Table 3.5. With these lifetime data, the current density exponents were determined as shown in Fig. 3.13.

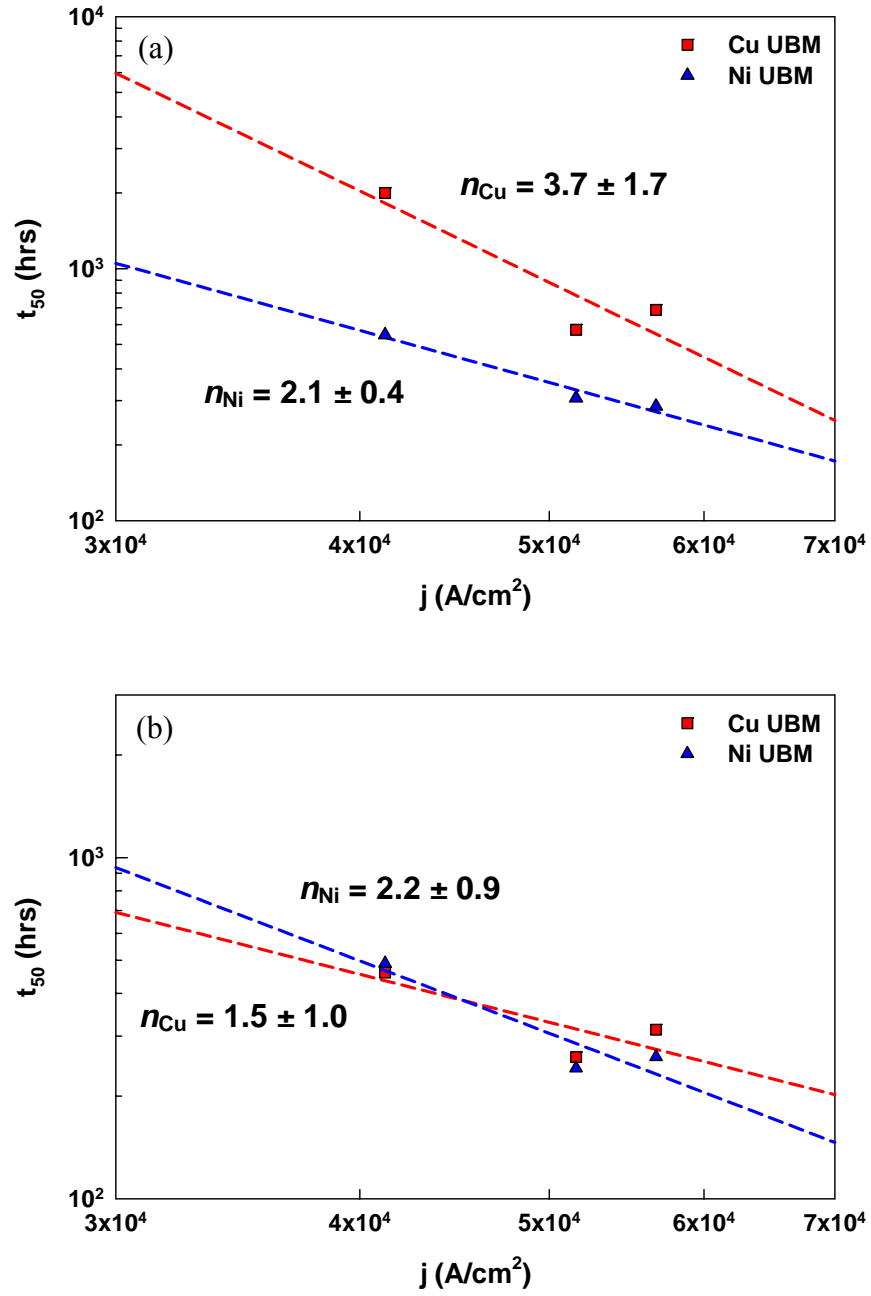


Figure 3.13: Refined current density exponent after taking into account the Joule heating, based on (a) the open failure criterion, and (b) the first resistance jump criterion.

Table 3.5: Summary of current density dependent EM lifetime extrapolated to the arbitrarily fixed solder temperature of 140°C, after the solder temperature correction was made.

Applied current (A)	Simulated solder temp. (°C)	Extrapolated t_{50} (hrs) at the solder temp. of 140°C			
		Open failure criterion		First resistance jump criterion	
		Cu UBM	Ni UBM	Cu UBM	Ni UBM
0.81	150	1995	545	461	490
1.01	155	572	306	260	242
1.11	157	686	284	313	261

For reference, the current density exponents without the Joule heat consideration were 5.1 (Cu UBM) and 3.3 (Ni UBM) based on the open failure criterion, and 3.5 (Cu UBM) and 2.9 (Ni UBM) based on the first resistance jump criterion. Larger n values typically indicate that significant Joule heat is generated. Therefore, a current density exponent for solder joints would be overestimated without appropriate Joule heat treatment. This can lead to a significant error in reliability prediction at field conditions. Note that the current density exponent of Cu UBM solders was strongly dependent on the failure criteria. This reflects that the resistance fluctuation period for solders with Cu UBM became substantially longer when the current density was small as seen in Table 3.5. Thus the EM lifetime of solder joints with Cu UBM reduced more at a lower current density when the first resistance jump criterion was applied. This resulted in a smaller n value based on the first resistance jump criterion for Cu UBM solders. Considering that extrinsic factors such as severe Joule heating or solder melting may play a role after the onset of jittering, the n values obtained based on the first resistance jump criterion could be more reasonable.

3.3.5 Electromigration Damage Evolution

Because the die trace was thin (0.8-1.0 μm thick) compared with the substrate trace (16-18 μm thick), current crowding mainly occurred in anode joints at the region where electrons flowed in from the die trace. As a result, EM failures always occurred in anode joints since the failure rate in there was much faster than in cathode joints. In cathode joints, EM voids were rarely observed although significant IMC growth was often observed.

3.3.5.1 Solder Joints with Thick Cu UBM

Due to the current crowding effect, EM failures were always observed in anode joints where the electron flux flowed from the die side to the substrate side, consistent with the results reported in other studies [3.11, 3.24, 3.25]. Figures 3.14(b)-(d) show morphological changes in solder joints during thermal aging or EM test for 263 hrs at 140°C (Si backside temperature). For comparison, a pristine solder joint in the as-received condition was included in Fig. 3.14(a). A small number of Kirkendall voids were formed during solder reflow as can be seen in the figure between Cu UBM and Cu_6Sn_5 . The Cu_3Sn phase should be present between Cu UBM and Cu_6Sn_5 [3.26] although this layer was too thin to be identified in Fig. 3.14(a).

Although fatal EM damage was developed only in the anode joint (Fig. 3.14(d)), some microstructural changes were still observed in the joint without current stressing and in the cathode joint. Without current passing (Fig. 3.14(b)), the number of Kirkendall voids increased and the scallop-shaped Cu_6Sn_5 phase became flattened during thermal aging. This is because Cu was the dominant diffusing species and the valleys in the scallop-shaped Cu_6Sn_5 phase were the faster diffusion path for Cu atoms [3.26]. The

increase of Kirkendall voids and the Cu_6Sn_5 flattening process progressed further with a longer aging time and increasing temperature.

When electric current was applied, additional microstructural changes were observed. In the cathode joint (Fig. 3.14(c)), $(\text{Cu},\text{Ni})_6\text{Sn}_5$ migrated from the substrate pad or top-surface-metallization (TSM) on the substrate side toward the die side as a result of Cu and Ni migration. Cu atoms migrated from the initial $(\text{Cu},\text{Ni})_6\text{Sn}_5$ phase formed on the Ni(P) substrate finish layer during solder reflow. Ni atoms migrated from both the initial $(\text{Cu},\text{Ni})_6\text{Sn}_5$ phase and the substrate finish layer. This led to a decrease of Ni concentration with distance from TSM to IMC. Meanwhile, the Cu_3Sn layer grew thicker between UBM and Cu_6Sn_5 under current stressing. The density of Kirkendall voids also increased but the density difference with and without current stressing was not distinctive. At this point, most of the Kirkendall voids were still located in the Cu_3Sn layer near the UBM/ Cu_3Sn interface while the Cu UBM continued to be depleted in the process of IMC growth as shown in Fig. 3.14(c). This indicates that Sn atoms were driven by current through the IMC layers to react with Cu atoms, while Cu atoms diffused into solder in the direction opposite to the electron flow. Without Sn diffusion, the additional depletion of Cu UBM cannot be explained as compared with the case without current stressing (Fig. 3.14(b)). Without Cu diffusion, on the other hand, Kirkendall voids would have moved toward the substrate side away from the Cu UBM/ Cu_3Sn interface. Thus both Cu and Sn atoms interdiffused in the cathode joint, but the diffusion of Cu atoms might be somewhat suppressed as its direction is opposite to the electron wind force.

In the anode joint (Fig. 3.14(d)), a significant amount of IMC formation and damage evolution was observed. Most of the Cu UBM dissolved into solder to form IMCs. A large domain of Cu_6Sn_5 , enhanced by the electron flow, was formed to develop an extended morphology in concert with the electron flux. In contrast, the Cu_3Sn layer

maintained its parallel interfaces, i.e. the Cu UBM/Cu₃Sn interface and the Cu₃Sn/Cu₆Sn₅ interface were almost parallel to each other during Cu₃Sn growth as shown in Fig. 3.14(d). The amount and location of Kirkendall voids in the anode joint were similar to those in the cathode joint. Interestingly, the Kirkendall voids in the Cu₃Sn layer had very little to do with EM-induced voids which led to gross failure as shown in Fig. 3.14(d). Nevertheless, the formation of Kirkendall voids during thermal aging or under current stressing can raise other reliability concerns since they weaken the mechanical strength of solder joints [3.26].

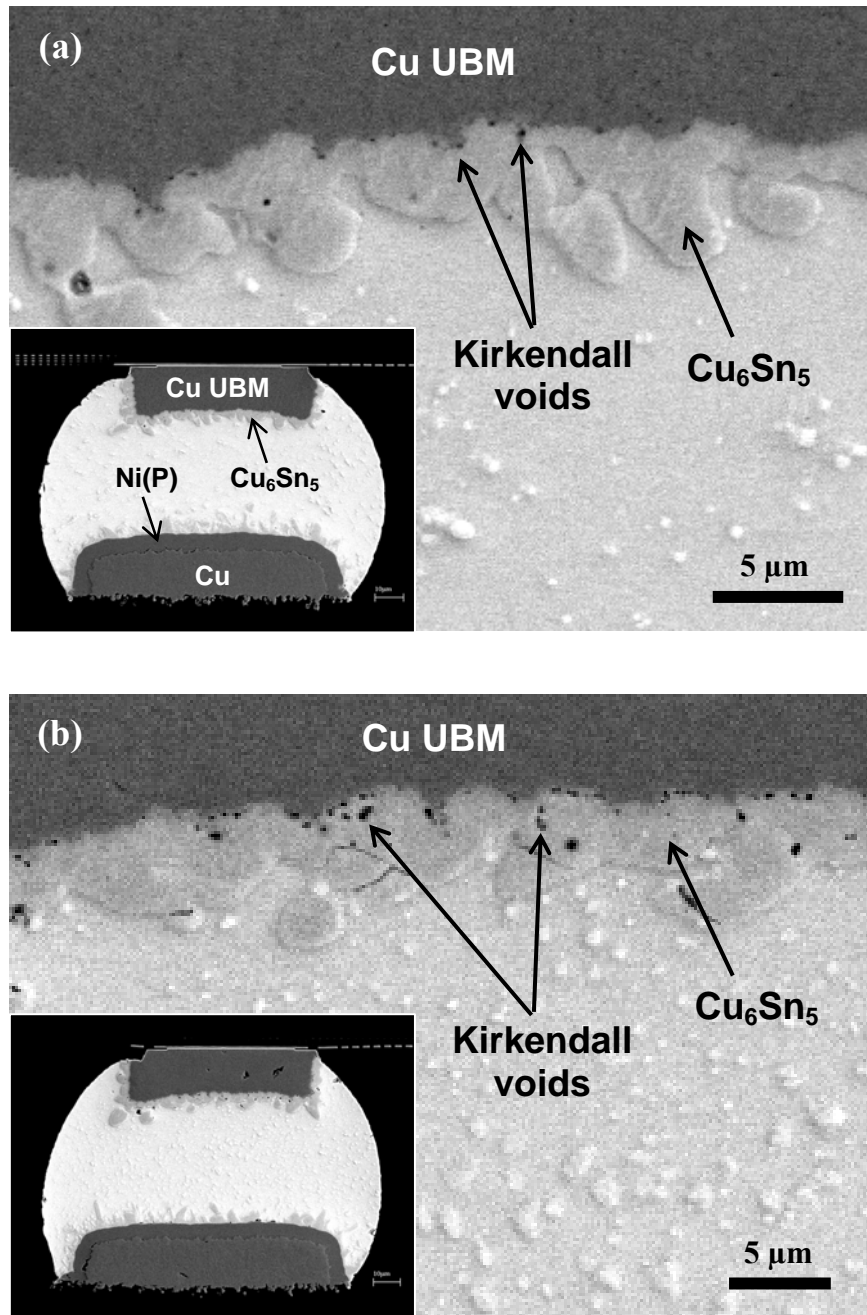


Figure 3.14: SEM micrographs of solder joints with Cu UBM. (a) A joint in a pristine sample, (b) a joint without current stressing at 140°C for 263 hrs, (c) a cathode joint and (d) an anode joint with 1.01 A current stressing. (b)-(d) are from the same sample.

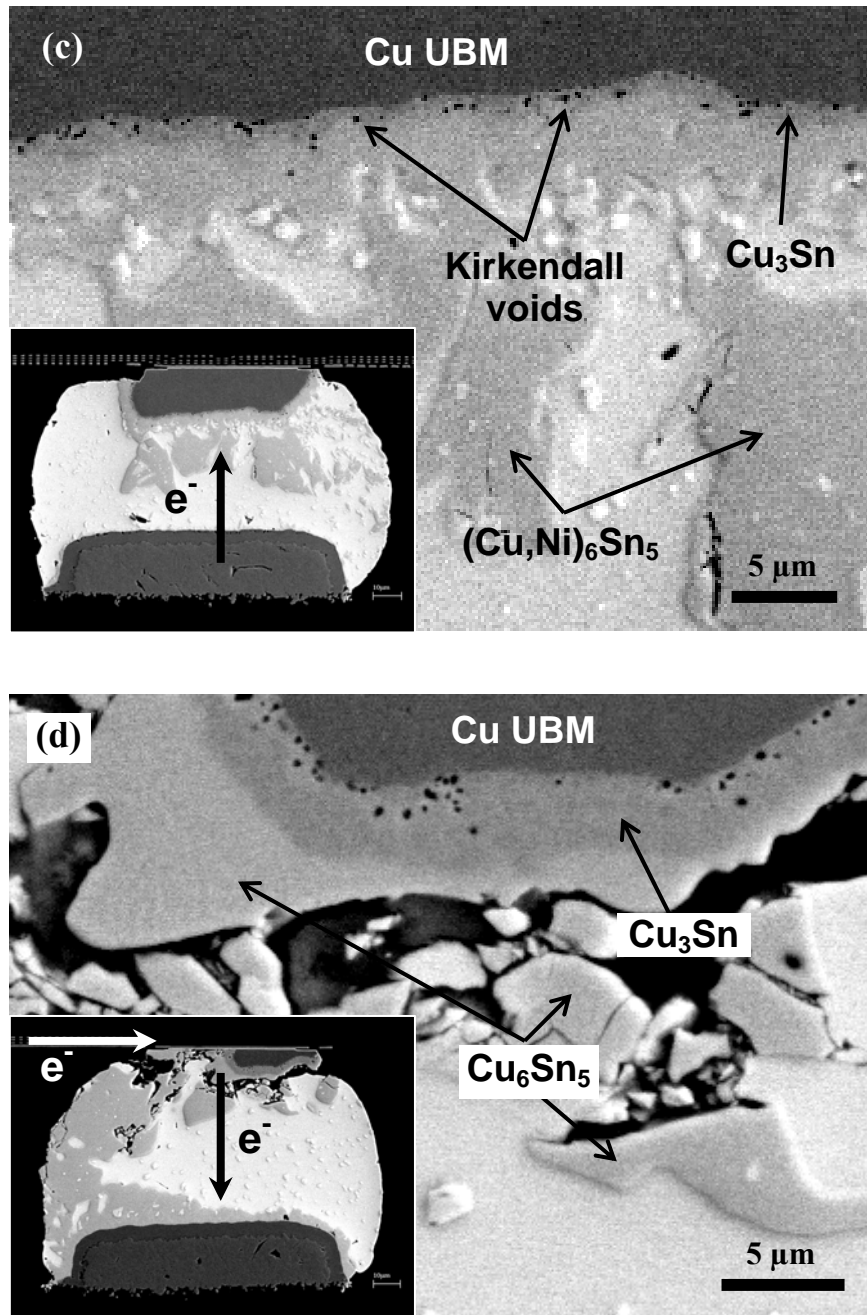


Figure 3.14: (cont'd) SEM micrographs of solder joints with Cu UBM. (a) A joint in a pristine sample, (b) a joint without current stressing at 140°C for 263 hrs, (c) a cathode joint and (d) an anode joint with 1.01 A current stressing. (b)-(d) are from the same sample.

Since EM failure was observed only in anode joints in this study, the voiding process in anode joints was extensively investigated. Figure 3.15 displays EM damage evolution in the anode joint with Cu UBM. At an early stage, IMC layers grew by consuming Cu UBM (Fig 3.15(a)). The V_g increase was negligible in this stage. Next, EM-induced voids were initiated at the Cu_6Sn_5 /solder interface as shown in Fig. 3.15(b). These voids grew independent of Kirkendall voids observed in the Cu_3Sn layer after solder reflow. At this point, V_g was still only a few mV but gradually increasing, corresponding to an increase of several $\text{m}\Omega$ in resistance. The current crowding effect on UBM consumption and void initiation was found to be weak owing to the thick Cu UBM structure. Crowded electrons at the corner of Cu UBM could be relaxed or spread out through the thick UBM before they reached the IMC/solder interface. Figure 3.15(c) depicts a solder joint after an abrupt jump to ~ 40 mV in V_g . At this stage, substantial Cu_6Sn_5 growth was observed, and EM voids were widespread in the Cu_6Sn_5 layer near the $\text{Cu}_3\text{Sn}/\text{Cu}_6\text{Sn}_5$ interface. Note that the voiding location moved from the Cu_6Sn_5 /solder interface to the vicinity of the $\text{Cu}_3\text{Sn}/\text{Cu}_6\text{Sn}_5$ interface. Before discrete voids were connected to each other (Fig. 3.15(b)), the ligament between the voids had a high current density, which further enhanced Cu_6Sn_5 growth with simultaneous void enlargement. Simultaneously, vacancies were driven toward the die side to compensate for the flux imbalance. Chao *et al.* developed a 1-D vacancy transport model using a finite difference method and showed that vacancies were accumulated in the Cu_6Sn_5 layer near the $\text{Cu}_3\text{Sn}/\text{Cu}_6\text{Sn}_5$ interface in a Cu-Sn diffusion couple under current stressing [3.27]. This was partly attributed to the fact that the diffusivity (D) and the effective charge number (Z^*) of Cu in the Cu_6Sn_5 layer was found to be larger than those in the Cu_3Sn layer. The resistance increased abruptly when the discrete voids became connected to form a global crack, the process of which could have been aided by tensile stress developed during

IMC formation. The solder joint was almost open at this stage as shown in Fig. 3.15(c), which is consistent with what was expected in Fig. 3.4. At this stage, Cu_6Sn_5 grew preferentially through the limited region where solder was still connected. Increased local current density at this region could result in fast IMC growth until failure. When an open failure finally occurred, an extensive formation of Cu_6Sn_5 was observed spanning out from the IMC on the die side to the substrate side as shown in Fig. 3.15(d). The void size increased further while the Cu_3Sn layer grew but at a lower growth rate compared with Cu_6Sn_5 . This eventually led to crack that propagated through the Cu_6Sn_5 phase near the $\text{Cu}_3\text{Sn}/\text{Cu}_6\text{Sn}_5$ interface.

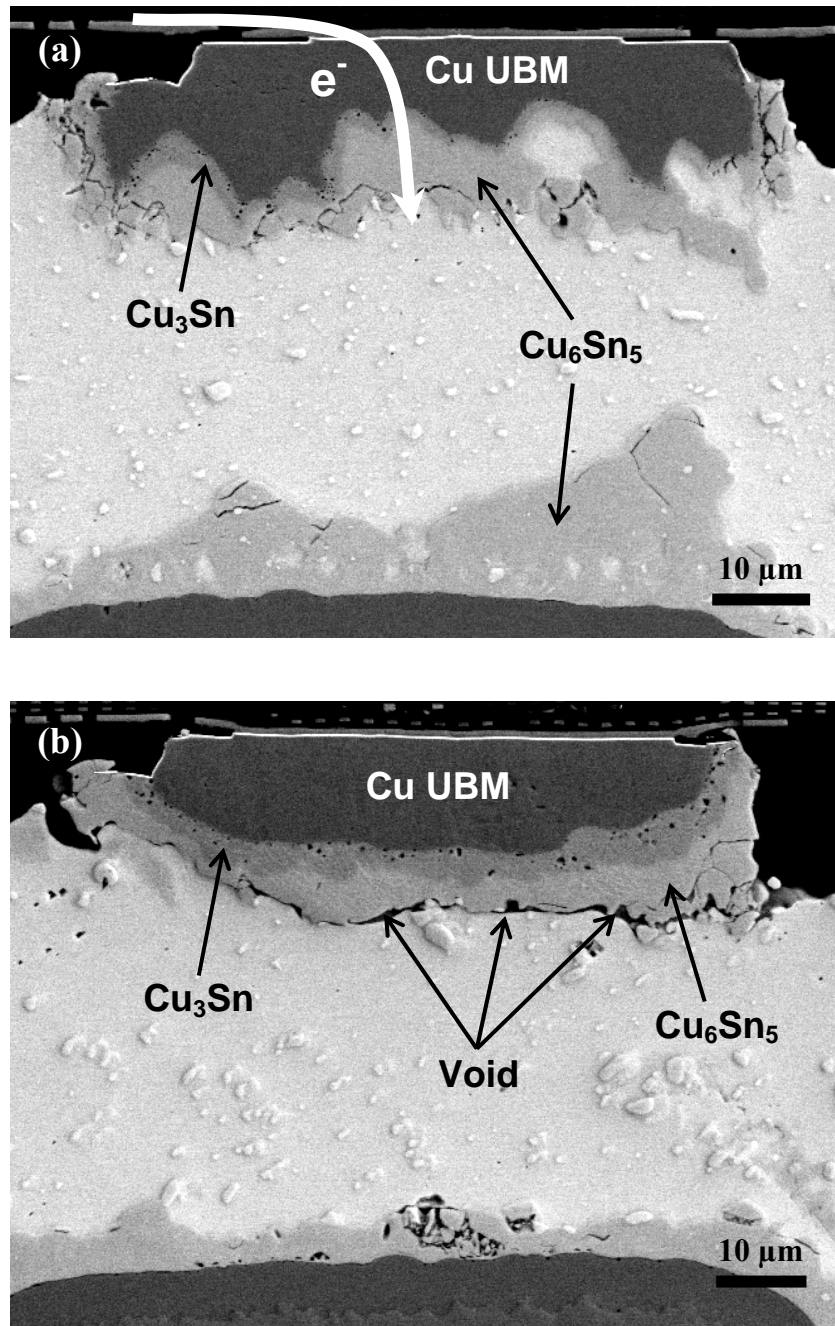


Figure 3.15: EM damage evolution in the anode joint with Cu UBM. (a) Initial stage of Cu depletion, (b) void initiation prior to the resistance jump, (c) crack propagation subsequent to the resistance jump, and (d) final open failure.

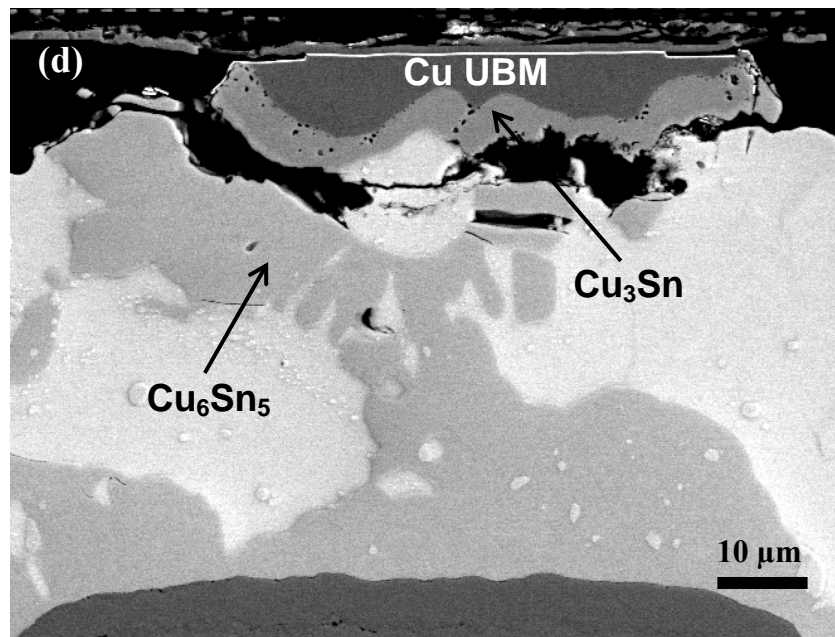
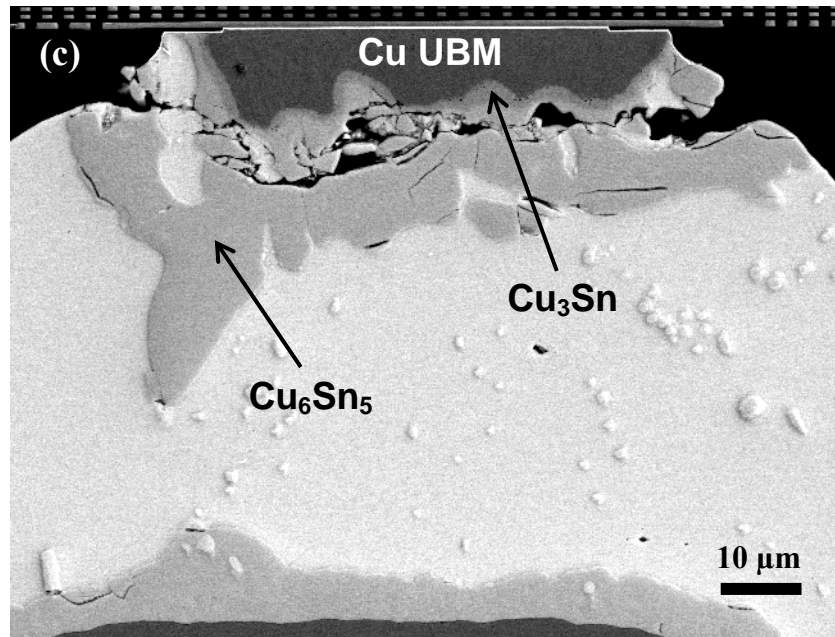


Figure 3.15: (*cont'd*) EM damage evolution in the anode joint with Cu UBM. (a) Initial stage of Cu depletion, (b) void initiation prior to the resistance jump, (c) crack propagation subsequent to the resistance jump, and (d) final open failure.

3.3.5.2 Solder Joints with Thin Ni UBM

Figure 3.16 shows the morphology of cross-sectioned solder joints with Ni UBM after 150 hrs of an EM test at 130°C (Si backside temperature) with 1.01 A. For the control sample without current stressing, a thin Ni_3Sn_4 layer had been formed between the Ni UBM and the solder during solder reflow, otherwise little change occurred in the solder (Figs. 3.16(a) and (b)). In the cathode joint with current stressing (Fig. 3.16(c)), Ni atoms from the substrate finish layer migrated through the solder toward the die side to form Ni_3Sn_4 to sustain the growth of Ni_3Sn_4 on the die side. In contrast, Ni_3Sn_4 growth on the substrate side was enhanced at the beginning but subsequently retarded as Ni in the substrate finish layer was depleted. When Ni was sufficiently depleted, needle-like fissures were found in the Ni(P) finish layer as shown in Fig. 3.16(c). This may degrade mechanical strength of the cathode solder joints. This also indicates that electromigration of Ni is faster than Sn although Chen *et al.* considered Sn to be the dominant diffusing species in the Sn/Ni/Sn reaction couple with current stressing [3.28]. In the anode joint (Fig. 3.16(d)), EM-induced voids formed at the Ni_3Sn_4 /solder interface as a result of enhanced growth of Ni_3Sn_4 by the current flow. The growth of Ni_3Sn_4 was slower than Cu_6Sn_5 , resulting in a slower dissolution of Ni UBM than that of Cu UBM.

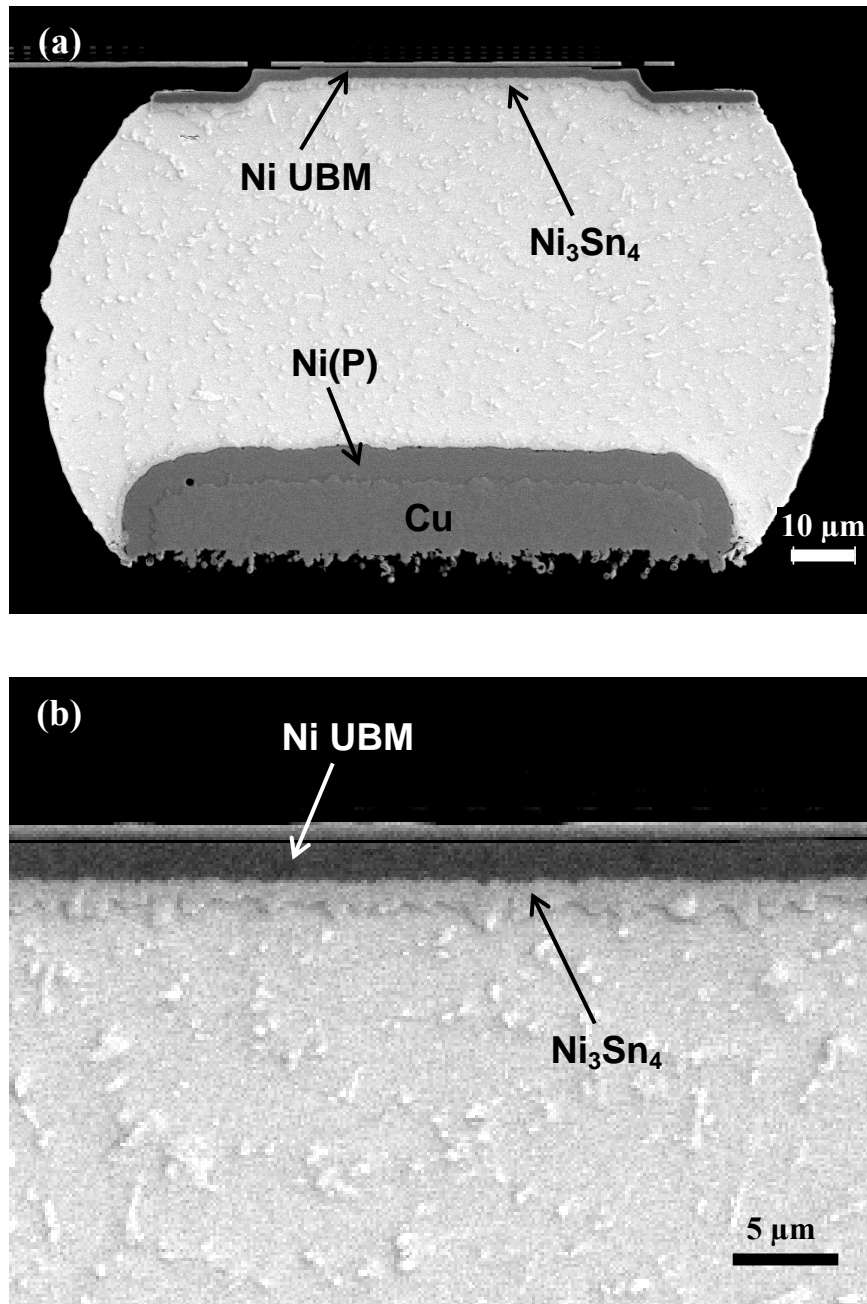


Figure 3.16: SEM micrographs of solder joints with Ni UBM. (a) A joint without current stressing at 130°C for 150 hrs, (b) a magnified view of (a), (c) a cathode joint and (d) an anode joint with 1.01 A current stressing. (a)-(d) are from the same sample.

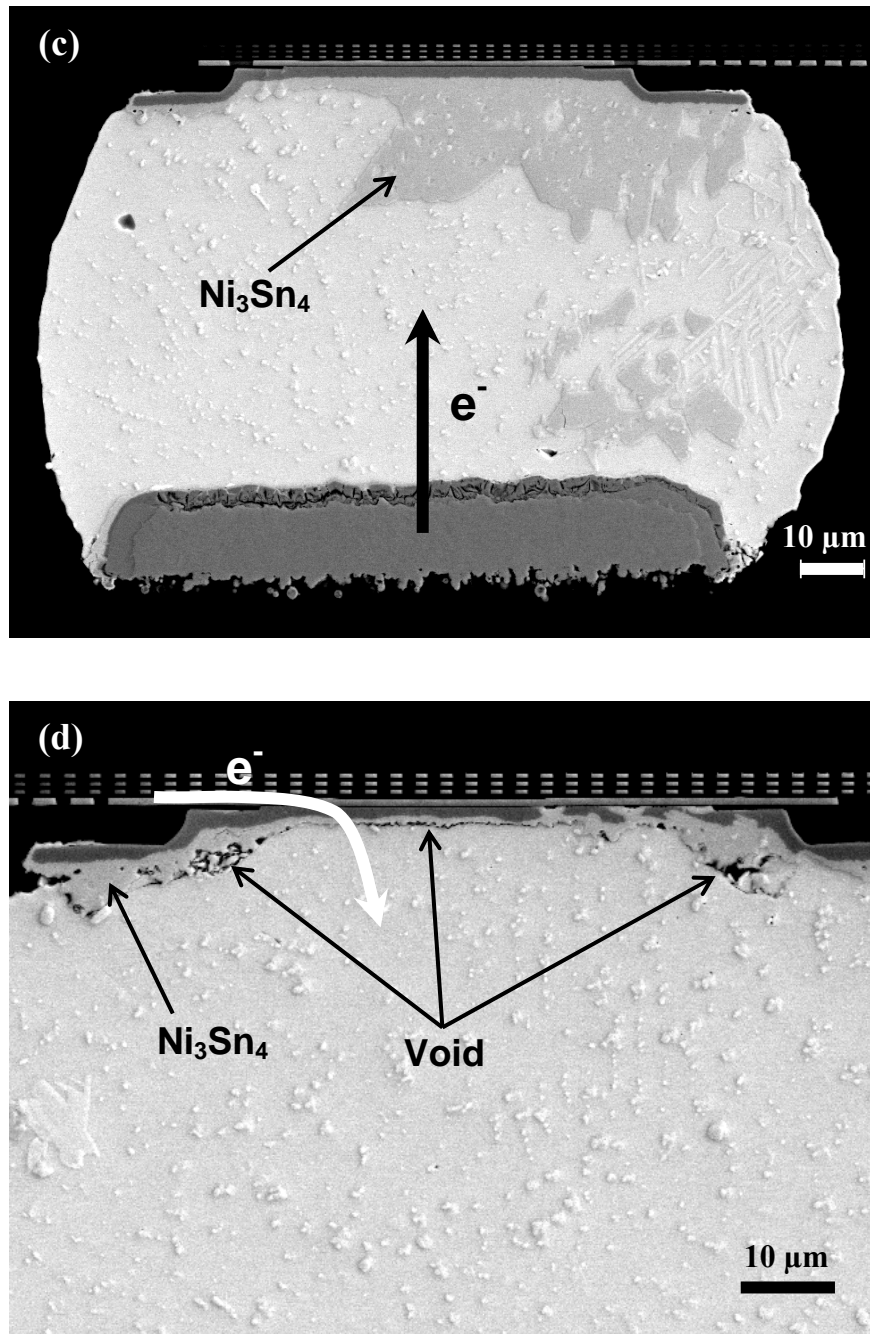


Figure 3.16: (*cont'd*) SEM micrographs of solder joints with Ni UBM. (a) A joint without current stressing at 130°C for 150 hrs, (b) a magnified view of (a), (c) a cathode joint and (d) an anode joint with 1.01 A current stressing. (a)-(d) are from the same sample.

Damage evolution in the anode joint with Ni UBM is depicted in Fig. 3.17. At an early stage where the change in V_g was negligible, initial voids were found at the current crowding location as shown in Fig. 3.17(a). Some part of Ni UBM was dissolved into solder to form Ni_3Sn_4 . Continued testing led to the growth of voids, which propagated through the Ni_3Sn_4 /solder interface (Fig. 3.17(b)). At this point, the IMC growth was not substantial and had a relatively small volume of void formation. Although voids occupied well over a half of the interface, V_g was only a few mV. Compared with Cu UBM, Ni UBM showed void growth in more regular fashion through the Ni_3Sn_4 /solder interface. This could account for the more gradual increase of V_g as seen in Fig. 3.3. Further void growth increased the local current density, leading to accelerated IMC and void growth. In Fig. 3.17(c), void volume became much larger and the amount of Ni_3Sn_4 increased in the region where solder was still connected. This stage corresponded to ~ 10 mV of V_g where voids occupied nearly 70 % of the IMC/solder interface. Figure 3.17(d) shows the EM damage state of a solder joint in the middle of unstable resistance fluctuation. At this stage, the solder joint became almost open with a large amount of IMC accumulated on the substrate side. Some solder joints were melted after this stage due to the substantial increase of Joule heat prior to the final open failure.

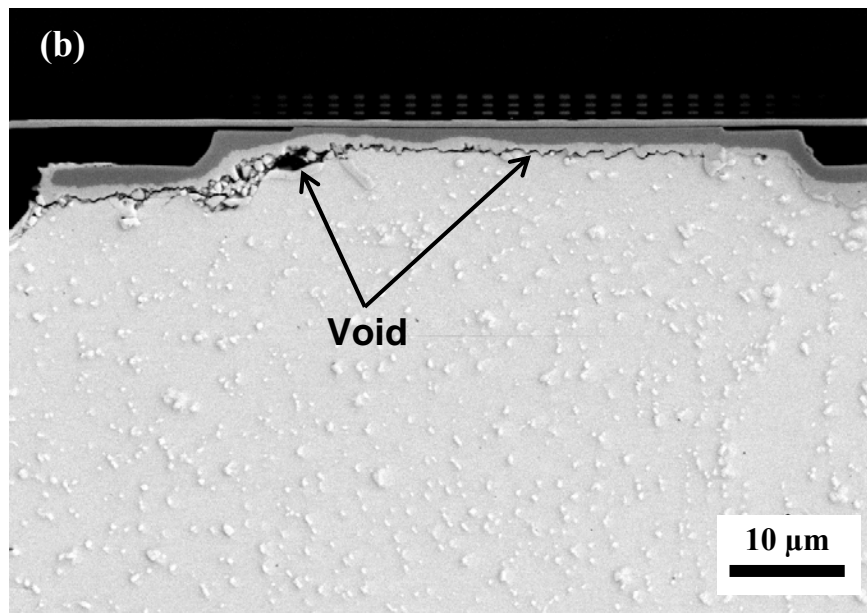
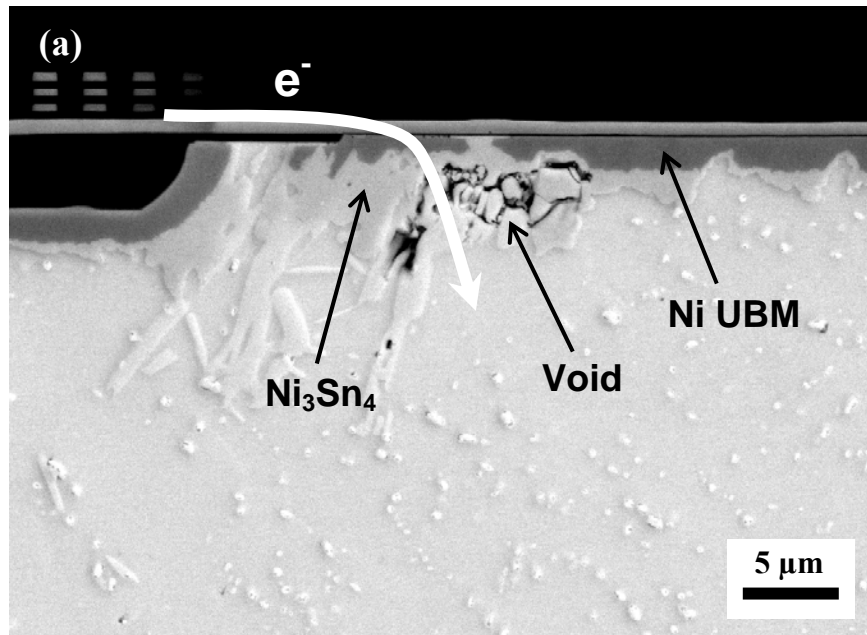


Figure 3.17: EM damage evolution in the anode joint with Ni UBM. (a) Ni depletion and void formation, (b) void propagation along the IMC/solder interface, (c) further IMC and void formation, and (d) a nearly opened solder.

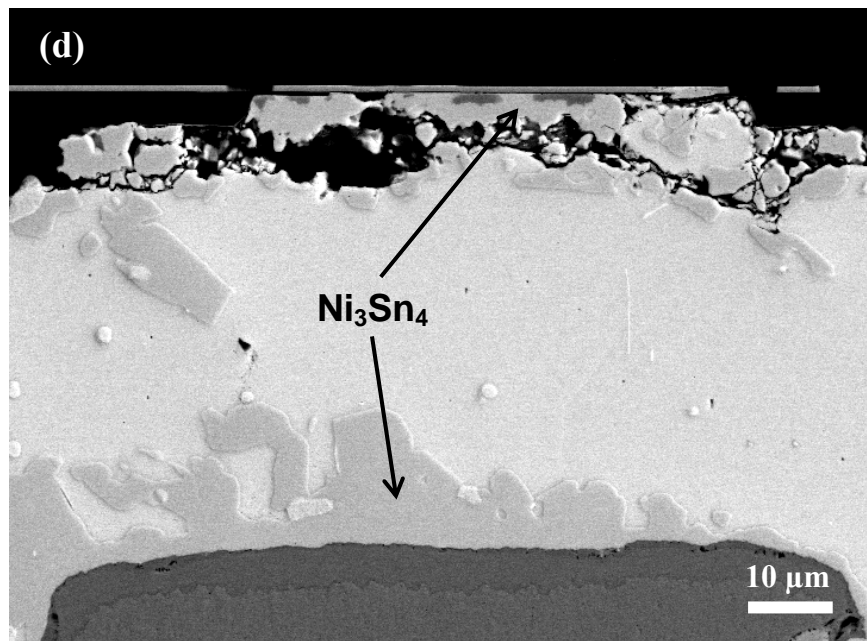
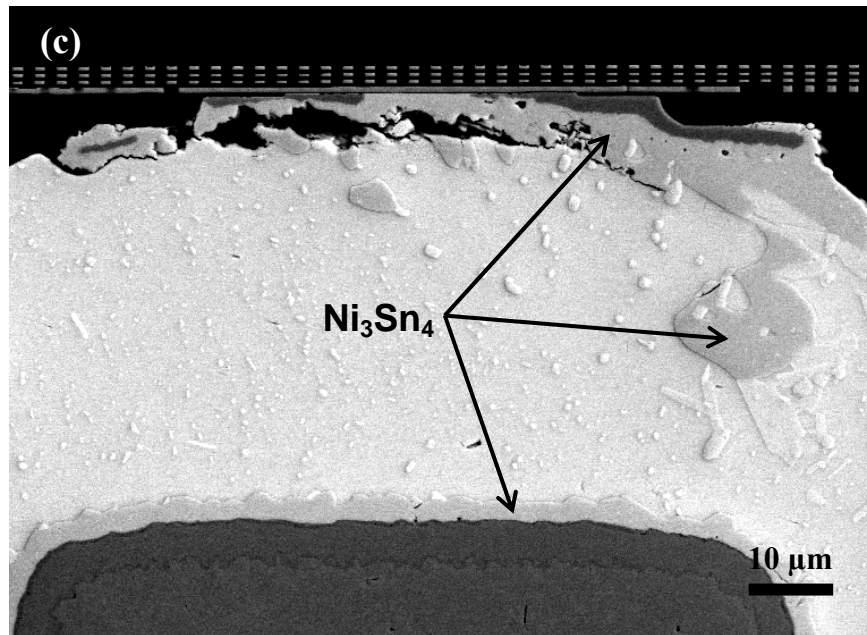


Figure 3.17: (*cont'd*) EM damage evolution in the anode joint with Ni UBM. (a) Ni depletion and void formation, (b) void propagation along the IMC/solder interface, (c) further IMC and void formation, and (d) a nearly opened solder.

3.4 SUMMARY

EM studies were conducted on Pb-free Sn-2.5Ag solder joints with Cu and Ni UBM in organic flip-chip packages. Si backside temperatures of 115, 130, 140 and 150°C were chosen for tests with 1.01 A current stressing. Two more tests at 140°C were performed with 0.81 and 1.11 A in order to determine the current density exponent. To supplement the open-failure criterion, a first resistance jump failure criterion was used to analyze EM lifetime results. Solder joints with thick Cu UBM had a longer lifetime than those with thin Ni UBM, based on the open-failure criterion; however, the lifetime of Ni UBM solders was comparable if the first resistance jump criterion was applied. This was due to the longer resistance fluctuation period of solder joints with thick Cu UBM. Numerical analysis of V_g in combination with failure analysis showed that solder was almost open after the onset of unstable resistance fluctuations. Experiments and finite element analysis were conducted to determine the temperature of solder joints under current stressing. After the Joule heating effect was taken into account EM activation energies (Q) and current density exponents (n) were determined. $Q = 1.0$ eV for Cu UBM solders and $Q = 0.9$ eV for Ni UBM solders. $n = 1.5$ for Cu UBM solders and $n = 2.1$ for Ni UBM solders, based on the first resistance jump criterion. In solder joints with Cu UBM, EM voids initiated at the Cu_6Sn_5 /solder interface but the voiding location moved near the $\text{Cu}_3\text{Sn}/\text{Cu}_6\text{Sn}_5$ interface as IMCs and voids grew. The EM-induced voids evolved independently of the initial Kirkendall voids in the Cu_3Sn layer. In solder joints with Ni UBM, initial EM voiding was observed at the current crowding location and failure occurred at the Ni_3Sn_4 /solder interface where voids initially formed.

Chapter 4: Electromigration (EM)-Enhanced Intermetallic Compound Growth in Pb-Free Solder Joints and Its Effect on EM Reliability

In the previous chapter, morphology changes in Pb-free solder joints were discussed under current stressing conditions. One of the key differences which distinguish Pb-free solders from Pb-based solders in electromigration (EM)-induced damage, is the extensive intermetallic compound (IMC) formation in the Pb-free solders. In this chapter, EM-enhanced IMC growth is studied and compared with IMC growth without current stressing. It was found that the IMC growth in thermally aged solders followed a parabolic growth law. In contrast, when current was applied, the IMC growth showed a linear dependence on time. Furthermore, finite element method (FEM) results of IMC-induced stress indicated that IMC growth could accelerate the EM damage.

4.1 INTRODUCTION

Since its inception nearly 40 years ago, the flip chip technology has gained momentum over the past decade to meet the ever-increasing demand for high I/O density and pin count as well as superior electrical performance and a small form factor [4.1, 4.2]. Historically, Pb-Sn has been the dominant alloy used as solder bumps for flip-chip packages. However, worldwide regulations including RoHS and WEEE to ban hazardous Pb due to environmental concerns have driven the industry to switch to Pb-free solders [4.3, 4.4]. In Pb-Sn solders, Sn is the primary element reacting with the under-bump metallurgy (UBM) such as Cu or Ni to form IMCs, while Pb remains inactive [4.5, 4.6]. In Sn-based Pb-free solder joints, the IMC growth was found to be substantially enhanced by EM by virtue of virtually inexhaustible supply of Sn from the solder [4.7-4.9].

IMC formation is accompanied by volume changes. Table 4.1 summarizes molar volumes of Cu, Ni, Sn, and their IMCs. When Cu and Ni atoms react with Sn atoms to form Cu_3Sn , Cu_6Sn_5 , and Ni_3Sn_4 , the overall volumes decrease by 7.7 %, 5.1 %, and 11.4 %, respectively. This could induce tensile stress within the solder joint, which may further degrade EM reliability when combined with void formation due to the current enhanced IMC formation. Moreover, excessive IMC formation can raise mechanical reliability concerns of solder joints since IMCs are more brittle and have higher Young's modulus than the solder as shown in Table 6.1. Therefore, it was useful to investigate the current-enhanced IMC growth in Sn-based Pb-free solder joints. Then, the effects of extensive IMC growth on tensile stress evolution and EM reliability in solder joints were further analyzed using FEM in combination with experimental data.

Table 4.1: Physical properties of Cu, Ni, Sn and their intermetallics at room temperature, excerpted from [4.10].

Parameter	Cu	Ni	Sn	Cu_6Sn_5	Cu_3Sn	Ni_3Sn_4
Young's Modulus (GPa)	124	214	42	85.6	108.3	133.3
Molar volume (cm^3/mol)	7.11	6.59	16.30	117.8	34.7	75.3

4.2 EXPERIMENTAL DETAILS

Sn-2.5Ag flip chip solder joints with Cu (18 μm) or Ni (2 μm) UBM were used for this study. The test structure was the same as shown in Fig. 3.1. Two pairs of solder joints were subject to a current stressing at elevated temperatures. The remaining solder joints were thus under thermal aging only. Thermocouples were sandwiched between the backside of Si die and the Cu plate to monitor the temperature. This temperature was kept

constant throughout the given experiment. Experiments were conducted at various Si backside temperatures with current stressing of 1.0 A or 0.8 A. The corresponding average current density at the passivation opening was $5.16 \times 10^4 \text{ A/cm}^2$ and $4.12 \times 10^4 \text{ A/cm}^2$, respectively. As an electric current was applied to test modules, the temperature of solder joints increased due to Joule heating. As discussed in the previous chapter, the temperature of solder bumps was about 10 and 15°C higher than the Si backside temperature when the solder bumps were subject to 0.8 A and 1.0 A of current stressing, respectively. The temperature of solder bumps without current stressing was about 5°C lower than that with current stressing. The simulated solder temperatures for various test conditions are summarized in Table 4.2.

Table 4.2: Solder temperatures calculated by using FEM for various test conditions.

Applied current (A)	Si backside temperature (°C)	Simulated solder temperature (°C)	
		Current stressing	No current stressing
1.0	115	130	125
1.0	130	145	140
0.8	140	150	145
1.0	140	155	150
1.0	150	165	160

To measure the IMC thickness, the samples were taken out to cross-section them before they failed by EM. For solder joints under EM, only anode joints where electrons flowed from the die side to the substrate side were investigated. The measurements were conducted at several locations and then averaged. In case that the IMC morphology was irregular, especially for solder joints under current stressing, the area of an IMC phase

was calculated using image processing software and then it was divided by the initial width of UBM to obtain the nominal thickness. In the current-stressed solders, the electron current drove atoms of UBM toward substrate side leading to IMC growth at the solder/substrate finish layer as well. In addition, IMCs from the UBM side and the substrate side were sometimes bridged when extensive IMC growth occurred by EM. In that case, IMC thicknesses at the UBM side and at the substrate side were added, followed by subtraction of the initial IMC thickness on the substrate side.

4.3 RESULTS AND DISCUSSION

4.3.1 IMC Growth during Thermal Aging Only

Figures 4.1 and 4.2 show IMC growth and the accompanying morphology changes during thermal aging in Cu and Ni UBM solders, respectively. IMC growth is driven by the concentration gradient – more precisely, chemical potential gradient. The mass flux is governed by Fick's first law:

$$J = -D \frac{\partial C}{\partial x}, \quad (4.1)$$

where D is the diffusivity, and C is the concentration. The scallop-shaped morphology of Cu_6Sn_5 and Ni_3Sn_4 became flattened as they were thickened. This is because Cu atoms can diffuse faster into and react with Sn through the region where Cu_6Sn_5 is thinner as illustrated in Fig. 4.3 [4.11]. The flattening of Ni_3Sn_4 can be understood with the same explanation. This flattening process is also controlled by thermodynamics because the surface energy of the IMC grains to the solid solder is higher than that to the liquid solder [4.11, 4.12]. The layer-type Cu_3Sn also grew with aging time. Meanwhile, the number

and the size of Kirkendall voids in the Cu_3Sn layer increased due to the diffusion of Cu into Sn. For Ni-Sn diffusion couples, however, Kirkendall voids were not observed.

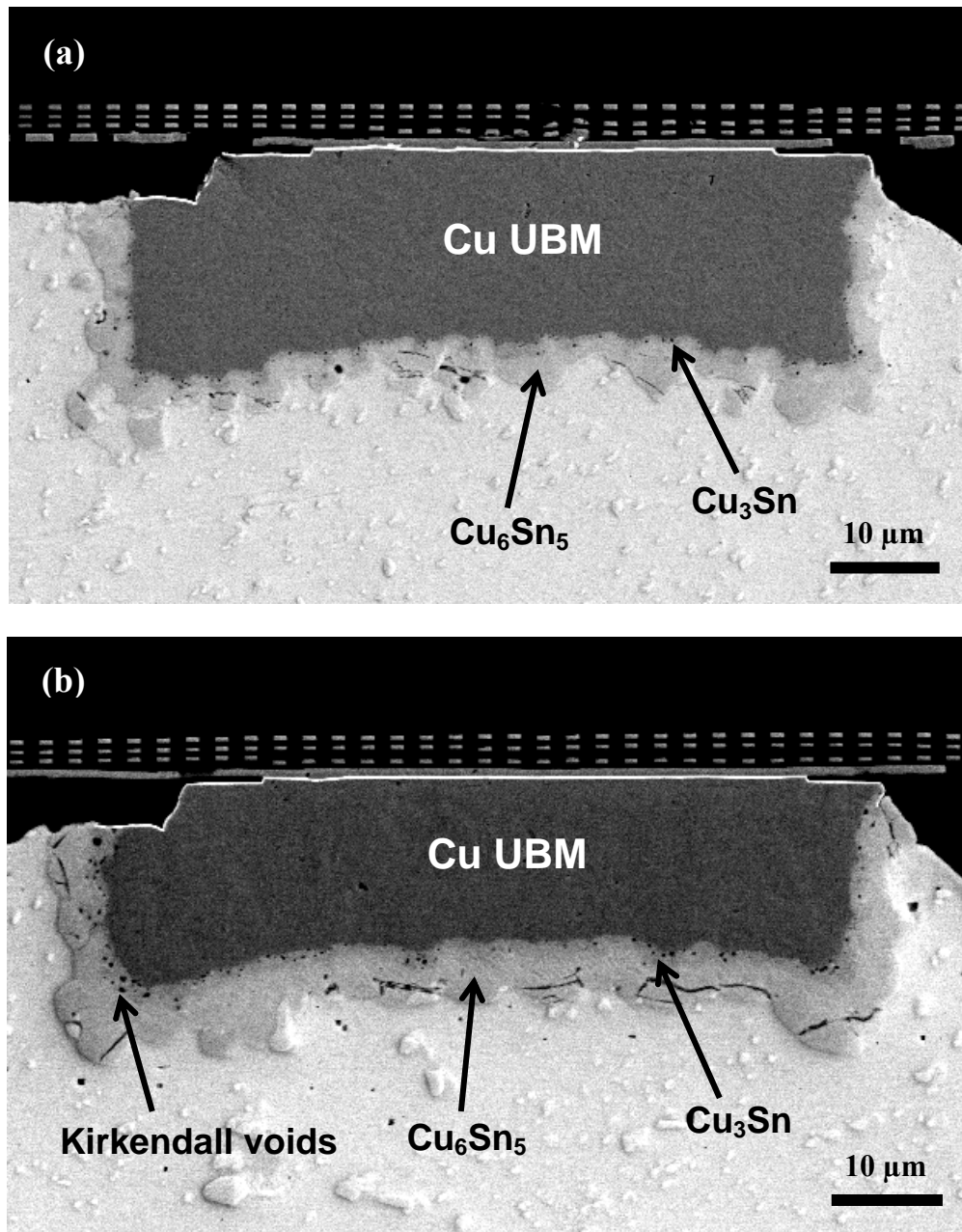


Figure 4.1: IMC growth in Cu UBM solders at 150°C. (a) After 117 hours, and (b) after 1594 hours.

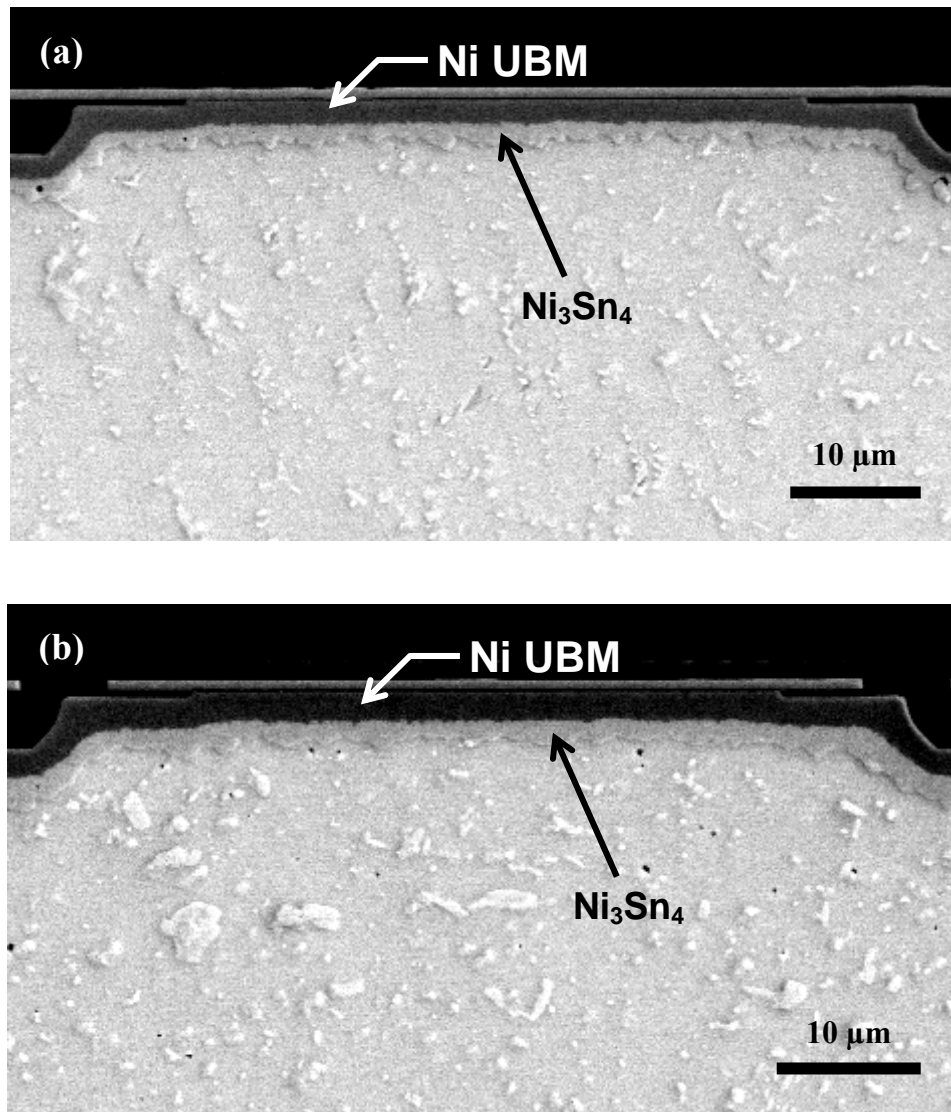


Figure 4.2: IMC growth in Ni UBM solders at 150°C. (a) After 71 hours, and (b) after 430 hours.

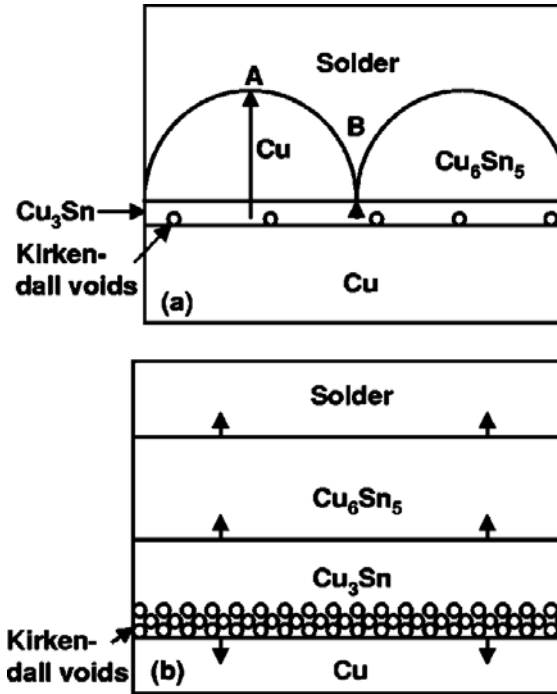


Figure 4.3: Schematic illustration of microstructural evolution at the interface between solder and Cu: (a) after reflow; (b) after aging. The vertical arrows in (a) indicate the diffusion of Cu atoms, while those in (b) indicate the moving directions of the boundaries during aging [4.11].

The IMC layer growth can be expressed by an equation of the usual form [4.13]:

$$x = x_0 + kt^n \quad (4.2)$$

where x is the thickness at time t , x_0 is the initial thickness at $t = 0$, k is the growth rate constant, and n is the time exponent indicative of the IMC growth mechanism. The exponent, n , is 0.5 if bulk (lattice) diffusion is the rate-controlling mechanism, while $n = 1$ if the growth is controlled by interfacial reaction. Other n values ranging from 0.21 to 0.37 have been reported for interfacial solid-liquid reactions [4.14-4.20]. Schaefer *et al.*

observed a $t^{1/4}$ dependence of the IMC growth between Cu and liquid Sn-Pb solder, and proposed a grain boundary diffusion controlled mechanism for thin IMC layers with the predicted $n = 1/3$ [4.21]. They explained that the discrepancy could be due to the transition of the predominant transport mechanism from grain boundary diffusion to slower volume diffusion. For $n = 1/3$, a mechanism similar to grain coarsening was also proposed [4.18]. Vianco *et al.* found that $n = 0.5$ for lower temperatures (70°C, 100°C, and 135°C) and $n = 0.42$ for higher temperatures (170°C and 205°C) from their study on IMC growth of pure Sn, Sn-3.5Ag, and Sn-5Sb solders.

Figure 4.4 shows the thickness changes of each IMC as a function of $\sqrt{\text{time}}$ at different temperatures. Relatively large error bars for Cu_6Sn_5 and Ni_3Sn_4 were attributed to the large variance of thickness over the irregular scallop morphology. Obviously, the growth rate increased with increasing temperature. The thickness was found to be a linear function of $t^{1/2}$, confirming that the growth kinetics of the IMCs followed the parabolic diffusion-controlled growth law under thermal aging. As the IMC layer becomes thicker, the atomic diffusion through IMC layers takes a longer time leading to slower IMC growth. Cu_6Sn_5 showed the fastest growth rate and Cu_3Sn the slowest of three IMCs. The growth rate constant, k , is summarized in Table 4.3.

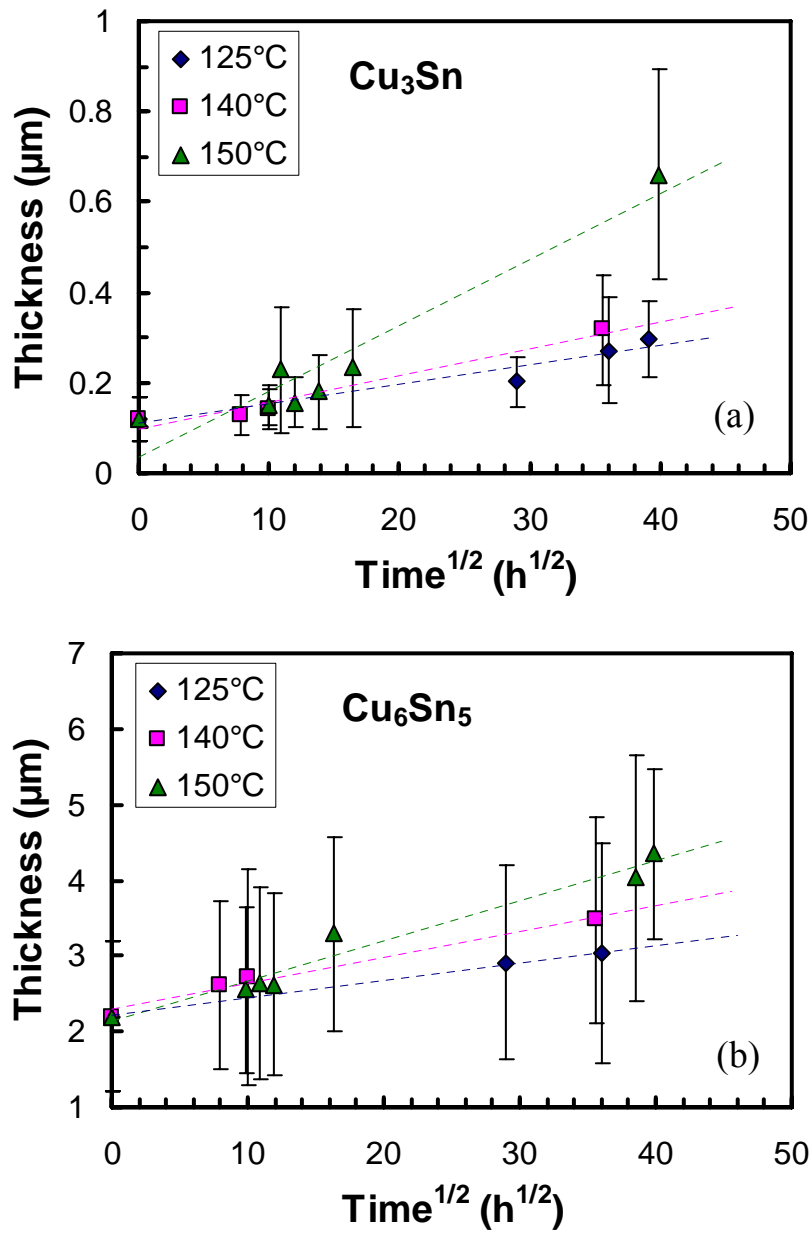


Figure 4.4: IMC thickness as a function of aging time without current stressing. (a) Cu_3Sn , (b) Cu_6Sn_5 , (c) total Cu-Sn IMCs, and (d) Ni_3Sn_4 .

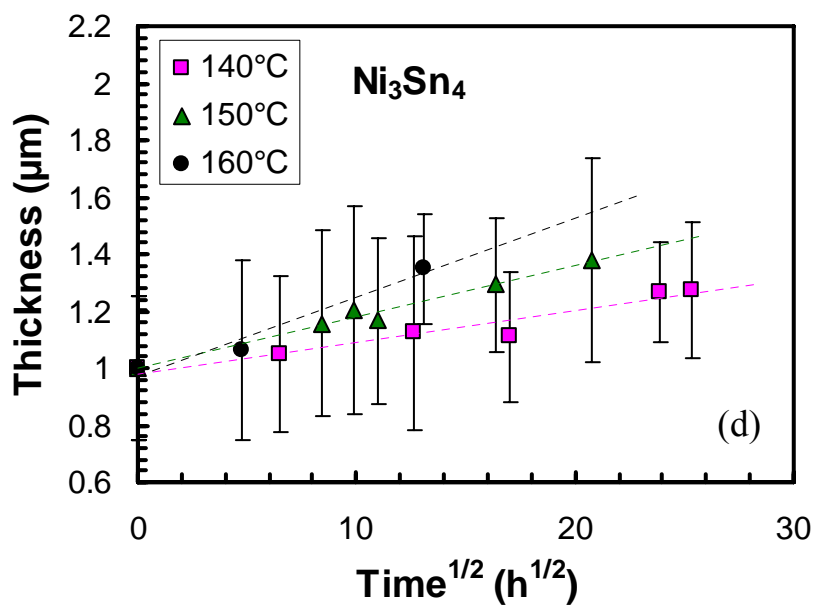
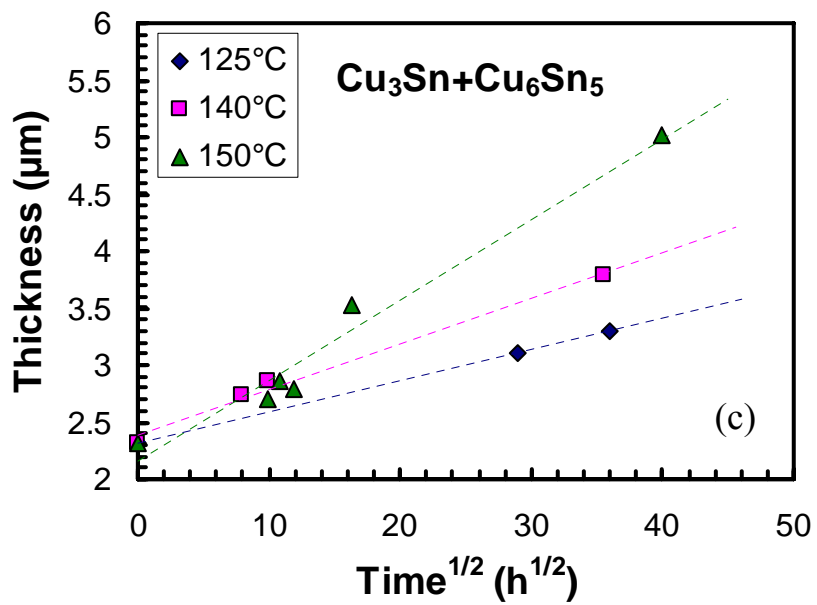


Figure 4.4: (cont'd) IMC thickness as a function of aging time without current stressing. (a) Cu_3Sn , (b) Cu_6Sn_5 , (c) total Cu-Sn IMCs, and (d) Ni_3Sn_4 .

Table 4.3: IMC growth rate constant, k (in nm/h^{1/2}), without current stressing.

Solder temperature (°C)	Cu ₃ Sn	Cu ₆ Sn ₅	Total Cu-Sn IMCs	Ni ₃ Sn ₄
125	4	23	27	-
140	6	34	40	11
150	15	53	71	18
160	-	-	-	28

The ratio of k for the ε -phase (Cu₃Sn) to the η -phase (Cu₆Sn₅) increased with aging temperature as can be seen in Table 4.3. This was also predicted by Mei et al. in their multiphase diffusion model for Cu-Sn diffusion couples [4.32]. The effect of isothermal aging on Cu-Sn diffusion couples can be analyzed in three temperature ranges: low ($T < 70^\circ\text{C}$), intermediate ($70^\circ\text{C} < T < 170^\circ\text{C}$), and high ($T > 170^\circ\text{C}$) temperatures. It has been observed that, upon thermal aging of a Cu-solder diffusion couple with η -phase layer at the interface at low temperatures, the η -phase grew in thickness without forming the ε -phase [4.33-4.36], while at high temperatures the ε -phase formed immediately [4.33-4.35, 4.37]. For annealing at intermediate temperatures, the ε -phase started to form after an incubation time [4.34, 4.37, 4.38]. This incubation time decreased with increasing temperature. The ε -phase has been shown to grow at the expense of the η -phase and has a higher activation energy of formation. Thus, the growth of the ε -phase becomes more prominent at higher temperatures [4.35, 4.36]. The absence of ε -phase at low temperatures and the presence of the incubation time at intermediate temperatures were also explained with Cu-Sn equilibrium phase diagram [4.42]. The η -phase is in equilibrium with Sn saturated with Cu, while the ε -phase is in equilibrium with Cu saturated with Sn. During solder reflow, Cu may not have a chance to be saturated with

Sn even at the reflow temperature because Cu dissolves into the molten solder. This means the initial phase formed at the interface is likely to be the η -phase. Moreover, the diffusivity of Sn in Cu ($\sim 10^{-24}$ m²/s at 220°C) is very low compared with that of Cu in Sn ($\sim 10^{-11}$ m²/s at 220°C). Therefore, during an annealing process the ε -phase would not appear until Cu becomes saturated with Sn. Harrison *et al.* found both η - and ε -phases when Sn0.7Cu solder was reflowed on Cu-Sn metallization whereas they found only η -phase when the metallization was pure Cu [4.43].

Also, IMC growth characteristics are influenced by the interdiffusion mechanism of Cu and Sn. Previous studies [4.22, 4.36, 4.39-4.41] suggest that interstitial diffusion of Cu is dominant at lower temperatures ($< 170^\circ\text{C}$), while vacancy diffusion of Sn becomes predominant at higher temperatures ($> 170^\circ\text{C}$). Inert markers in a Cu-Sn diffusion couple moved toward the Cu side at low temperature ($< 170^\circ\text{C}$) [4.36], but toward the Sn side at high temperature ($> 170^\circ\text{C}$) [4.22, 4.40, 4.41].

Figure 4.5 plots the thickness increase of the Cu₃Sn layer. The incubation time was also observed in this study at the intermediate temperature range although it was not very straightforward to determine the incubation times with those limited data points.

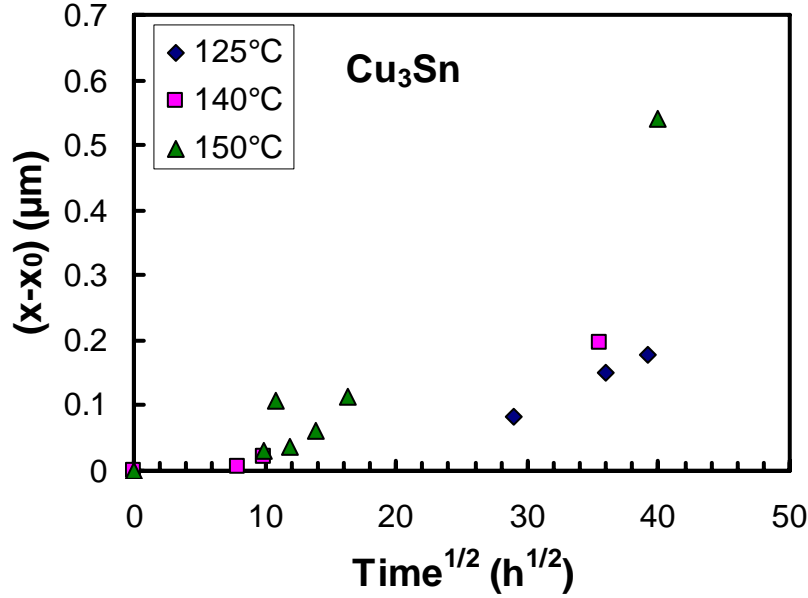


Figure 4.5: Thickness increase of the Cu₃Sn layer during thermal aging at intermediate temperatures (125-150°C).

From the temperature dependent growth rate constants the apparent activation energy for IMC growth can be calculated. In case of $n = 0.5$ in Eq. (4.2), k^2 has the same unit, m²/s, as the diffusivity. The apparent activation energy for IMC growth can be determined by the following Arrhenius equation [4.22-4.31]:

$$k^2 = k_0^2 \exp\left(-\frac{Q}{RT}\right), \quad (4.3)$$

where k^2 is the square of the growth rate constant, k_0^2 is the pre-exponential factor, Q is the apparent activation energy, R is the gas constant, and T is the aging temperature. The activation energy is obtained from the slope of the Arrhenius plot. Figure 4.6 plots $\ln k^2$ vs. $1/T$ for Cu-Sn and Ni-Sn IMCs. The apparent activation energies were determined to

be 1.1 ± 0.3 eV for $(\text{Cu}_3\text{Sn} + \text{Cu}_6\text{Sn}_5)$, 1.3 ± 0.6 eV for Cu_3Sn , 0.9 ± 0.2 eV for Cu_6Sn_5 , and 1.41 ± 0.04 eV for Ni_3Sn_4 . Here, the upper and lower bound in the activation energy were expressed using the standard error. As discussed above, the activation energy for the ε -phase was larger than that for the η -phase. The apparent activation energy for the growth of the total Cu-Sn IMCs is in good agreement with the EM activation energy for Cu UBM solders (1.0 ± 0.3 eV) discussed in the previous chapter (see Fig. 3.12(b)). This indicates that the Cu-Sn IMC growth plays a critical role in controlling the EM reliability. For the Ni_3Sn_4 growth, the apparent activation energy is higher than the EM activation energy for Ni UBM solders (0.9 ± 0.2 eV as in Fig. 3.12(b)). This will be discussed further later on.

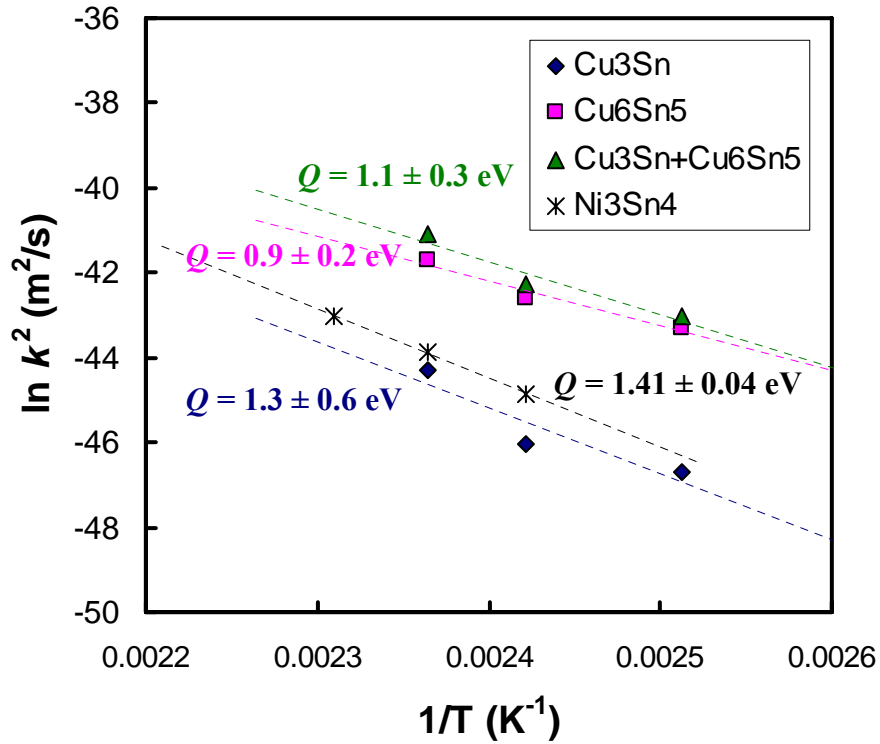


Figure 4.6: Arrhenius plot for the growth rates of Cu-Sn and Ni-Sn IMCs.

Tables 4.4 and 4.5 summarize apparent activation energies reported by various researchers for the growth of Cu-Sn IMCs and Ni_3Sn_4 , respectively. Temperature dependency of the activation energy was also studied in [4.30, 4.34, 4.49, 4.50, 4.59], which suggested different interdiffusion characteristics of Cu and Sn, or Ni and Sn, as discussed earlier. Overall, the apparent activation energies vary significantly between the experiments. They have been ascribed to the differences in the microstructure of the metallization (UBM or substrate) layer as well as IMC layers due to the differences in processing of the diffusion couples. The different grain size and the morphology of the layers can have a substantial effect on the IMC growth kinetics [4.42].

Addition of minor elements can also change the growth kinetics. Pinizzotto *et al.* added 4.5 wt.% of Ni particles in eutectic SnPb solder on Cu substrate and found that the resulting activation energies increased from 0.8 eV to 2.17 eV for the η -phase [4.65]. Choi *et al.* added 20 vol.% η -phase particles to eutectic SnPb and eutectic SnAg solders and found that Q for the ε -phase growth increased from 1.15 eV to 1.67 eV (eutectic SnPb) and 1.20 eV to 2.10 eV (eutectic SnAg) [4.25]. For the test module used in this work, Ni atoms from the Ni-P substrate finish layer was expected to saturate the molten solder during the second solder reflow. Therefore, relatively high activation energies for the Cu-Sn and Ni-Sn reactions in this work are not surprising.

Another way commonly used to obtain apparent activation energies is using an empirical power law equation [4.12, 4.34, 4.37, 4.42, 4.50, 4.61, 4.64, 4.66]:

$$x = x_0 + A \exp\left(-\frac{Q}{RT}\right) t^n, \quad (4.4)$$

where A is a constant. Comparing Eq. (4.4) with Eqs. (4.2)-(4.3), it is clear that the

apparent activation energy calculated from the former is equal to half that from the latter. This is also responsible for the large variation in the activation energy. A consensus needs to be made on which equation to be used. Equations (4.2)-(4.3) seems a better choice when the IMC growth is controlled by lattice diffusion (parabolic growth law; $n = 0.5$), because k^2 is closely related to the diffusivity as seen in Eq. (4.3). For this reason, Eqs. (4.2)-(4.3) were used throughout this study. Regardless of the choice, the fitting quality (i.e. the R^2 value) remained the same.

Table 4.4: Apparent activation energy for the Cu-Sn IMC growth.

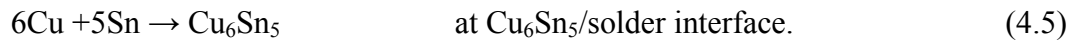
Solder alloy	Soldering method	Metallization	Temperature range (°C)	Apparent activation energy (eV)			Ref.
				Cu ₃ Sn	Cu ₆ Sn ₅	Total	
Sn		Cu	180-210	1.34	1.39	-	[4.44]
60Sn-40Pb	Hot dipping	Cu	100-175	-	-	0.25	[4.45]
Sn	Electroplating	Cu	70-170	-	-	0.29	[4.46],
60Sn-40Pb	Electroplating	Cu	70-170	-	-	0.34	[4.47]
Sn		Cu	190-220	0.63	0.55	0.60	[4.22]
Sn	Electroplating	Rolled Cu	70-170	-	-	0.30	[4.48]
Sn	Electroplating	Phosphor bronze	22-140	-	-	0.27	[4.49]
			140-220	-	-	0.51	
Sn	Hot dipping	Cu tab	70-205	0.45	-	0.68	[4.34]
			70-135	-	-	1.09	
			170-205	-	-	0.26	
63Sn-37Pb	Hot dipping	Cu tab	70-170	0.22	-	0.47	
Sn-3.5Ag	Hot dipping	Cu tab	70-205	0.52	-	0.61	[4.50]
			70-135	-	-	1.05	
			170-205	-	-	0.44	
Sn-5Sb	Hot dipping	Cu tab	70-205	0.52	-	0.63	[4.50]
			70-135	-	-	0.83	
			170-205	-	-	0.40	
63Sn-37Pb	Reflow	Cu pad	70-170	-	-	1.09	[4.51]
63Sn-37Pb	Reflow	Cu strip	50-150	-	1.15	-	[4.25]
Composite 63Sn-37Pb	Reflow	Cu strip	50-150	-	1.67	-	
Sn-3.5Ag	Reflow	Cu strip	70-180	-	1.20	-	
Composite Sn-3.5Ag	Reflow	Cu strip	70-180	-	2.10	-	
Sn-1.2 at.% Cu	Hot dipping	Cu (3.5 at.% Sn)	100-170	0.87	0.59	0.80	[4.37]
63Sn-37Pb	Reflow	Electroless Cu/Au	80-160	-	-	0.31	[4.35]
63Sn-37Pb	Electroplating	Sputtered Cu	85-150	-	-	0.78-1.14	[4.26]
63Sn-37Pb	Reflow	Electroplated Cu	125-170	-	-	1.25	[4.52]
Sn-3.5Ag	Reflow	Electroplated Cu	125-170	-	-	1.19	
Sn-3.8Ag-0.7Cu	Reflow	Electroplated Cu	125-170	-	-	0.94	
Sn-0.7Cu	Reflow	Electroplated Cu	125-170	-	-	1.00	
Sn-3.2Ag-0.8Cu			70-150	-	-	0.74	[4.53]
Sn-3.5Ag	Reflow	Cu pad	70-170	0.92	0.50	0.67	[4.54]
Sn-58Bi	Reflow	Cu sheet	70-120	-	1.33	-	[4.55]
Sn-58Bi	Reflow	Cu sheet	70-200	0.94	1.02	1.11	[4.56]
Sn-3.5Ag	Reflow	Cu sheet	70-200	0.78	0.57	0.68	[4.57]
Sn-3.5Ag-0.75Cu	Reflow	Cu sheet	100-200	0.83	0.51	0.65	[4.58]
Sn-3.5Ag	Hot dipping	Cu coupon	70-170	-	0.61	0.78	[4.29]
Sn	Electroplating	Electroplated Cu	100-150	-	-	0.66	[4.30]
			150-175	-	-	1.43	
Sn	Reflow	Electroplated Cu	125-180	-	-	0.57	[4.31]

Table 4.5: Apparent activation energy for the Ni_3Sn_4 growth.

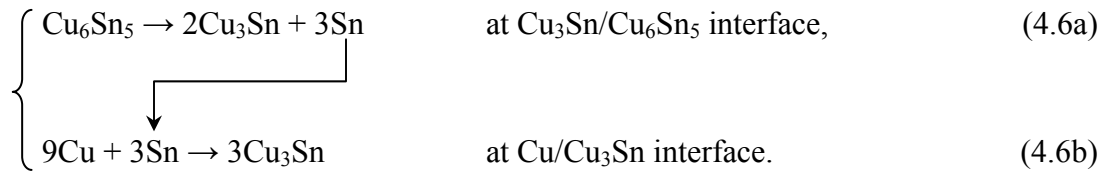
Solder alloy	Soldering method	Metallization	Temperature range (°C)	Apparent activation energy (eV)	Ref.
Sn	Electroplating	Electroplated Ni	100-150	0.60	[4.59]
			150-175	0.94	
Sn		Electroless Ni	75-160	0.31	[4.24]
		Electroless Ni/Au	75-160	0.19	
		Electroless Ni/Pd	75-160	0.25	
Sn-3.5Ag		Electroless Ni	75-160	0.13	
		Electroless Ni/Au	75-160	0.55	
		Electroless Ni/Pd	75-160	0.07	
63Sn-37Pb		Electroless Ni	75-160	0.29	
		Electroless Ni/Au	75-160	0.41	
		Electroless Ni/Pd	75-160	0.19	
Sn-58Bi	Hot dipping	Ni slab	85-120	0.93	[4.60]
63Sn-37Pb	Reflow	Electroplated Ni/Au	80-160	0.47	[4.61]
SnPbAg	Reflow	Electroplated Ni/Au	125-175	1.62	[4.62]
SnAg	Reflow	Electroplated Ni/Au	125-175	1.61	
Sn-3.5Ag	Reflow	Electroless Ni-P/Au	70-170	0.75	[4.54]
Sn-58Bi	Reflow	Electroless Ni-P	70-120	0.85	[4.55]
Sn-3.5Ag-5Bi	Reflow	Electroless Ni-P	100-170	0.55	[4.63]
Sn-3.5Ag	Reflow	Electroless Ni-P	100-170	0.51	[4.28]
Sn-37Pb	Reflow	Electroless Ni-P	130-190	1.46	[4.64]
Sn-3.5Ag	Reflow	Electroless Ni-P	130-190	1.14	[4.27]
		Sputtered Ni	130-190	0.94	
Sn-3.5Ag	Reflow	Electroplated Ni/Au	150-200	0.17	[4.12]
Sn	Electroplating	Electroplated Ni	100-150	0.60	[4.30]
			150-175	0.94	

4.3.2 IMC Growth with Current Stressing

Figure 4.7 shows cross-sectional SEM images of IMC growth in Cu UBM solders under current stressing. The effect of the electric current on IMC formation was found to be very significant. The enhanced growth of the η -phase (Cu_6Sn_5) was especially apparent during an extended time period of current stressing. Gan and Tu observed a polarity effect in solder joints where the IMC growth was enhanced on the anode side while it was retarded on the cathode side [4.8]. In this study, the IMC growth on both sides was enhanced under current stressing as seen in Fig. 4.7. The η -phase grew in a non-uniform fashion representing the electron flow direction. It was often observed that the extensively grown η -phase from the UBM side was bridged to the substrate finish layer as shown in Fig. 4.7(b). Figure 4.7(b) also shows that the ε -phase (Cu_3Sn) became apparent after an extended period of current stressing. Nevertheless, the ε -phase maintained its layer-type morphology, meaning that the layer was quite conformal. This finding supports that the ε -phase grows at the expense of the η -phase [4.35, 4.36, 4.67]. Therefore, an IMC reaction mechanism under current stressing is proposed as follows. For the η -phase growth,



Cu atoms primarily driven by the electron current migrate to the $\text{Cu}_6\text{Sn}_5/\text{solder interface}$ to react with Sn. And for the ε -phase,



First, Cu_6Sn_5 at the $\text{Cu}_3\text{Sn}/\text{Cu}_6\text{Sn}_5$ interface is dissociated into Cu_3Sn and Sn. Then Sn diffuses to the $\text{Cu}/\text{Cu}_3\text{Sn}$ interface driven by the concentration gradient to react with Cu. In this way, the Cu_3Sn layer grows at both interfaces and can preserve its conformality. The above processes, under a non-uniform current stressing condition, are illustrated in Fig. 4.8, where the local growth rate of Cu_6Sn_5 is assumed to increase only with local current density. In reality, however, the local growth rate is not a function of current density only, as seen in Fig. 4.7(b). It can be also dependent on phase boundary mobility, grain orientation of Sn matrix, and possibly others. Further research on this area can help in-depth understanding of the IMC growth kinetics and morphology evolution under EM, which is beyond the scope of this dissertation.

The current-enhanced Ni_3Sn_4 growth is shown in Fig. 4.9. It was not as aggressive as the Cu_6Sn_5 growth. In addition to the slower growth of Ni_3Sn_4 , its growth could be limited by the volume of the thin Ni UBM.

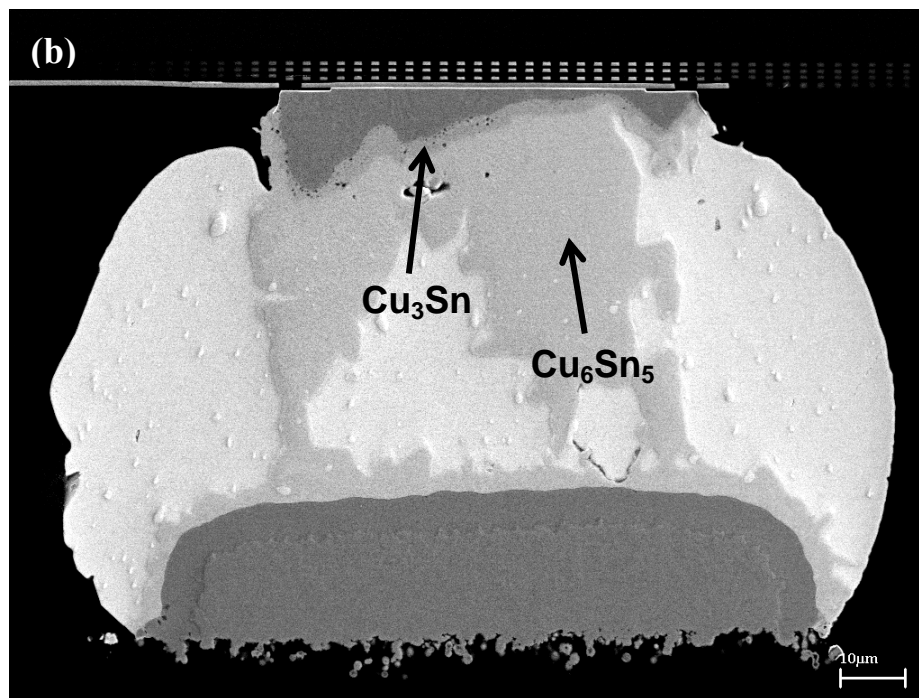
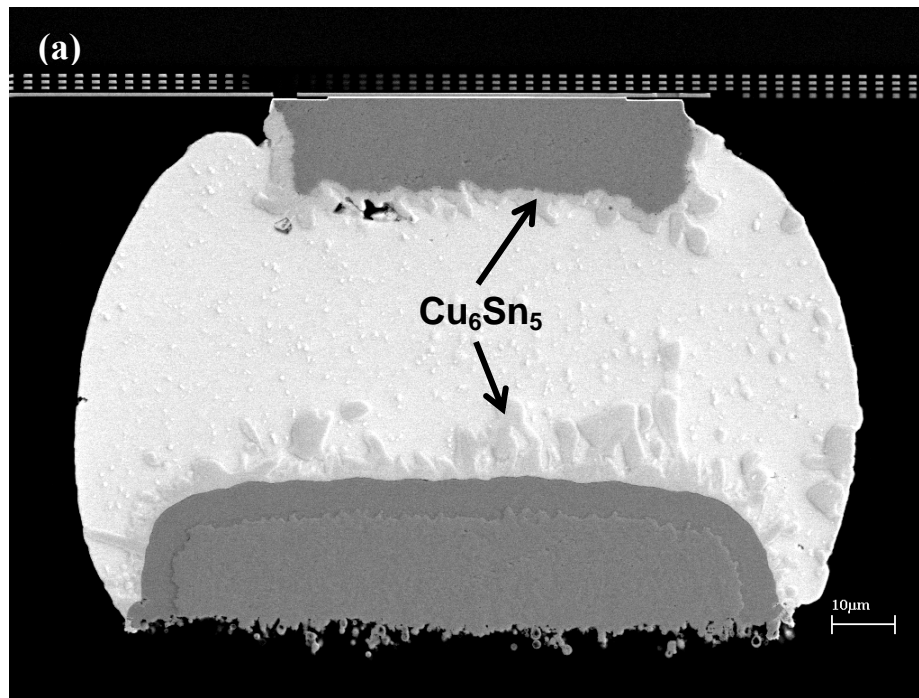


Figure 4.7: IMC growth in anode joints with Cu UBM under 1.01 A of current stressing for (a) 30 hours at 145°C, and (b) 1536 hours at 130°C.

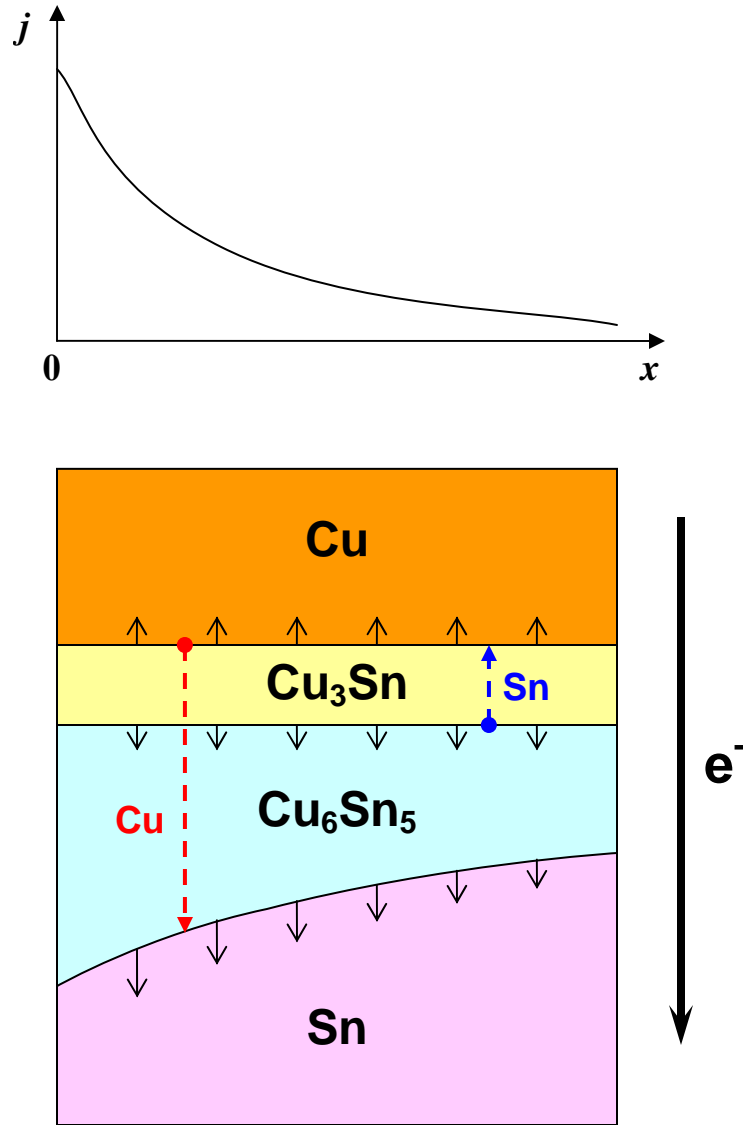


Figure 4.8: Schematic diagram of IMC growth under a non-uniform current stressing condition. An arbitrary current density (j) profile is shown above. The dotted arrows indicate atomic migration or diffusion paths for the formation of IMCs at interfaces, and the solid arrows indicate the resulting interfacial movements.

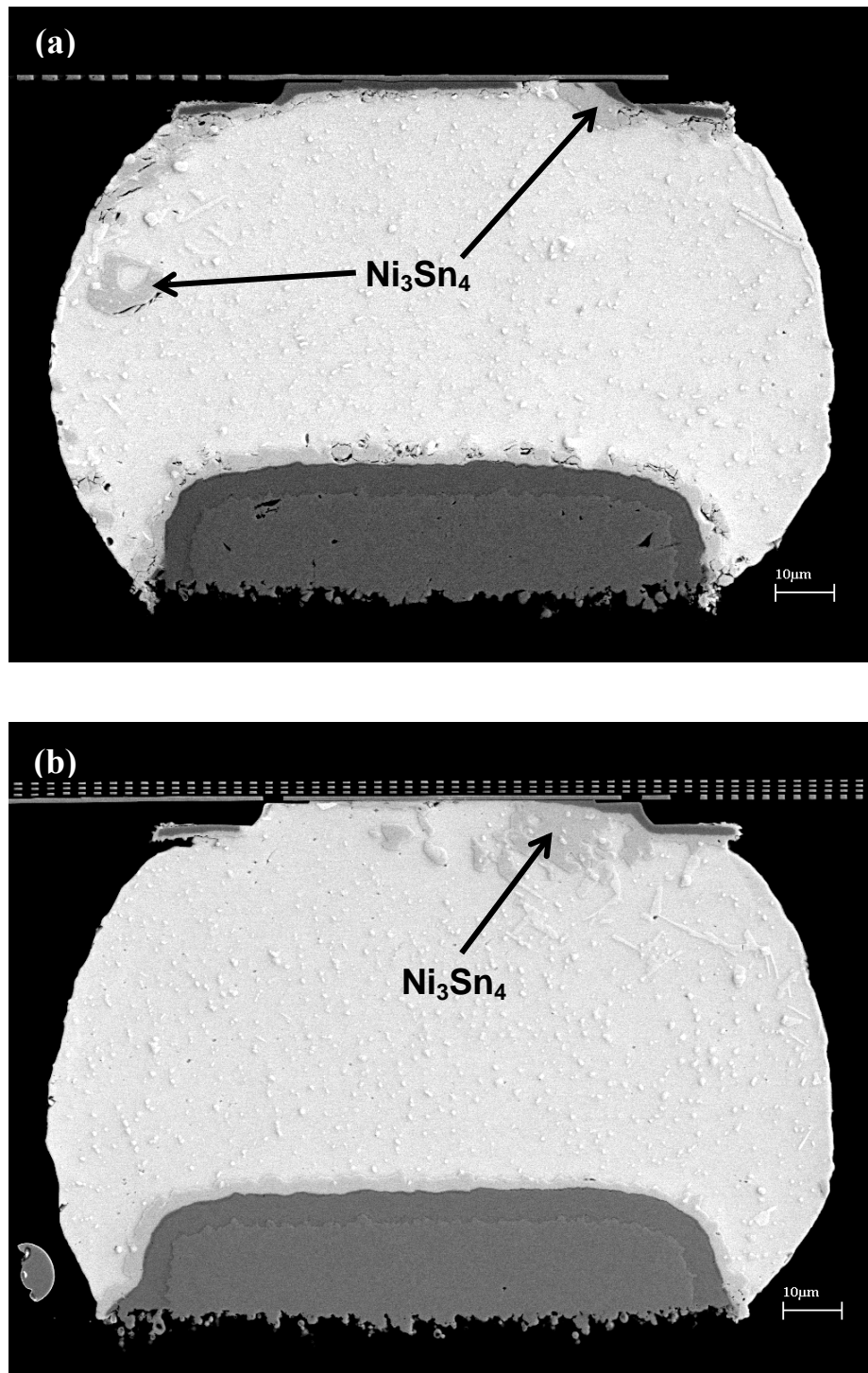


Figure 4.9: IMC growth in Ni UBM solders under 1.01 A of current stressing for (a) 88 hours at 155°C, and (b) 121 hours at 155°C.

The nominal thickness changes of the IMCs in the anode solder joints are shown in Fig. 4.10. With the passage of an electric current, Gan *et al.* reported parabolic growth kinetics for IMC growth [4.8]. In this study, however, the current-enhanced IMC growth was found to follow linear growth kinetics except for the ε -phase. Figure 4.10(a) plots the thickness of the Cu_3Sn layer as a function of $\sqrt{\text{time}}$. The growth of Cu_3Sn was more likely to follow the parabolic growth law under the EM condition although its temperature dependence was not readily understood. This suggests the Cu_3Sn growth was a diffusion-controlled process. Yet the growth rate constant, k , was more than 10 times larger than without current stressing. Figures 4.10(b)-(d) plot the other IMC thicknesses versus time. The growth of both Cu_6Sn_5 and Ni_3Sn_4 were well described by the linear time dependence. The total Cu-Sn IMC thickness also closely followed the t -dependence because Cu_6Sn_5 was the dominant phase in the IMC growth. The IMC growth rate constants for the case of $n = 1$, w , are summarized in Table 4.6.

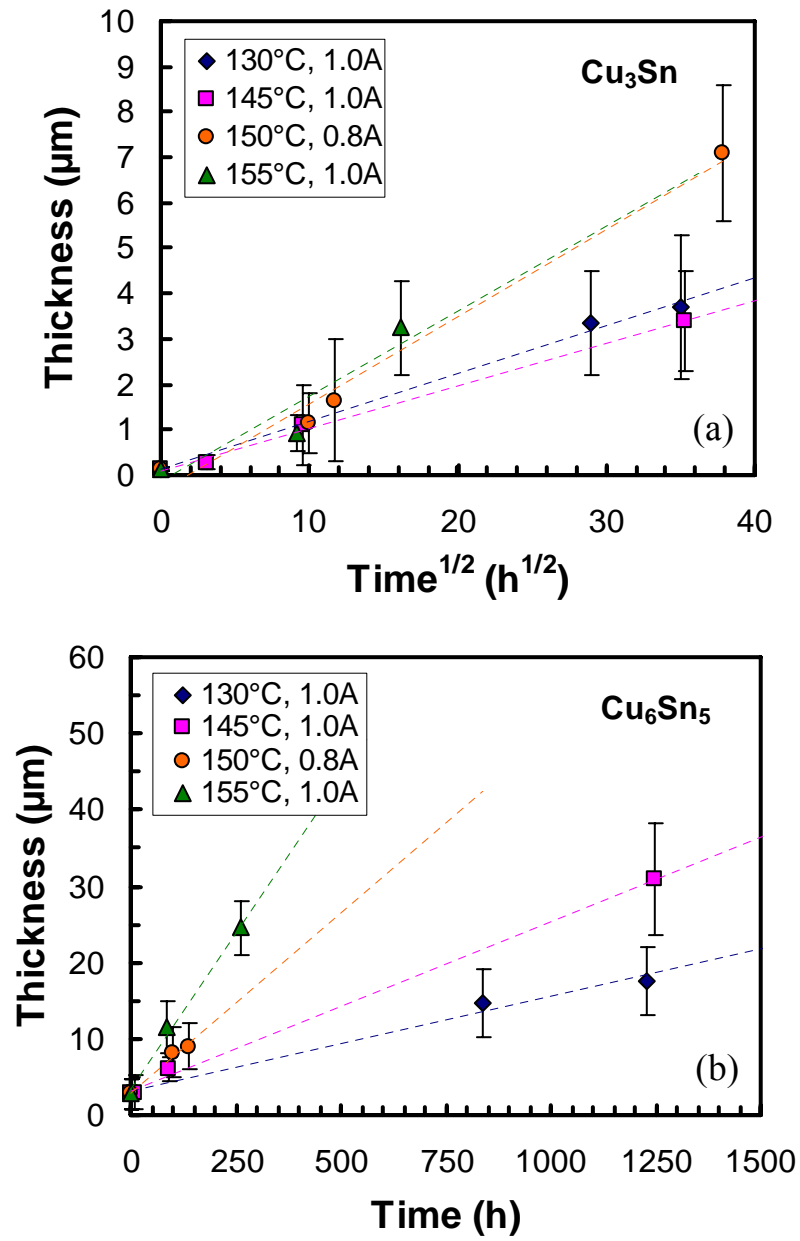


Figure 4.10: IMC thickness as a function of aging time with current stressing. (a) Cu_3Sn , (b) Cu_6Sn_5 , (c) total Cu-Sn IMCs, and (d) Ni_3Sn_4 .

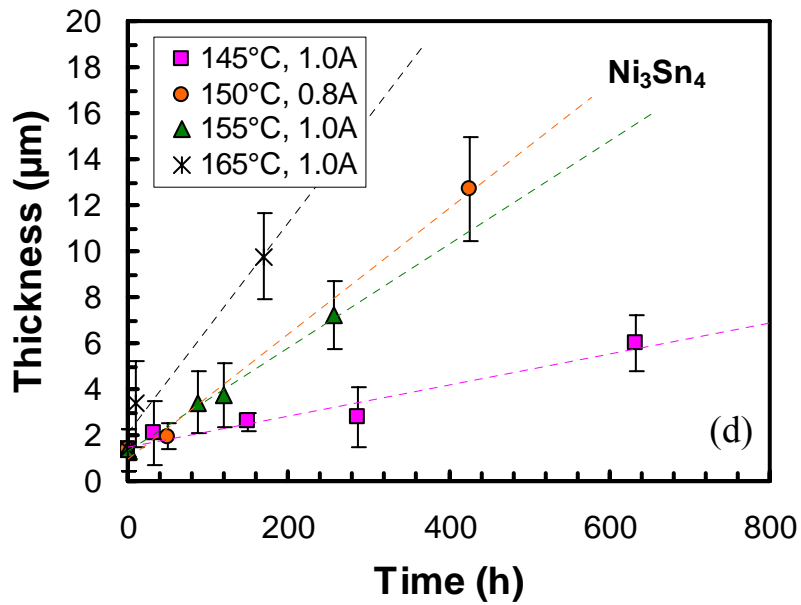
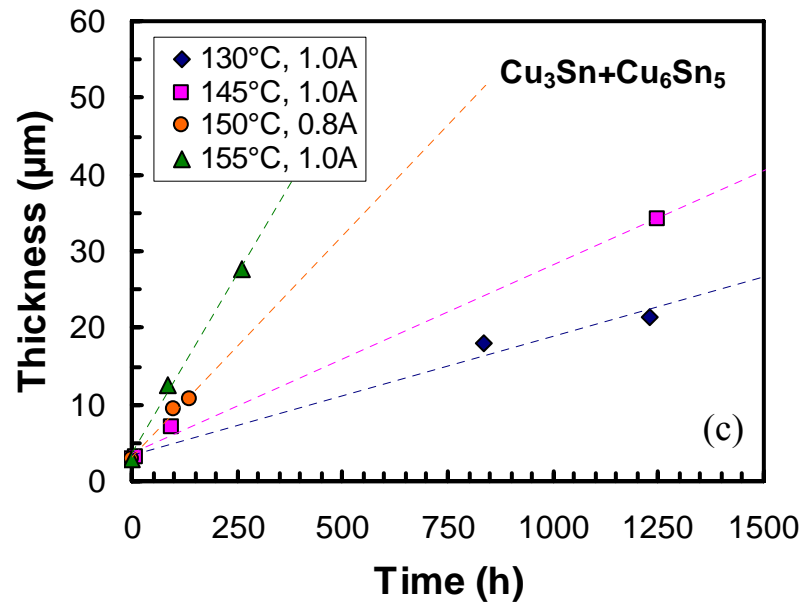


Figure 4.10: (cont'd) IMC thickness as a function of aging time with current stressing. (a) Cu_3Sn , (b) Cu_6Sn_5 , (c) total Cu-Sn IMCs, and (d) Ni_3Sn_4 .

Table 4.6: IMC growth rate constant, w (in nm/h), with current stressing.

Solder temperature (°C)	Applied current (A)	Cu ₆ Sn ₅	Total Cu-Sn IMCs	Ni ₃ Sn ₄
130	1.0	12	16	-
145	1.0	22	25	6.8
150	0.8	47	58	27
155	1.0	81	93	23
165	1.0	-	-	46

To understand the IMC growth phenomena under current stressing it is important to solve the flux equation. Under current stressing conditions, both the chemical potential gradient and the electron momentum transfer contribute to the diffusion of atoms. The mass transport can be expressed by a general form:

$$J = J_{\text{chem}} + J_{\text{EM}} = -D \frac{\partial C}{\partial x} + C \frac{D}{kT} Z^* e \rho j, \quad (4.7)$$

where J_{chem} is the mass flux driven by chemical potential gradient, J_{EM} is the mass flux driven by the electron momentum transfer, D is the diffusivity, C is the concentration, k is the Boltzmann constant, T is the temperature, Z^* is the effective charge number, e is the electron charge, ρ is the resistivity, and j is the current density. Obtaining a general solution of Eq. (4.7) for Cu-Sn diffusion couples is not trivial because Eq. (4.7) needs to be applied to each of four phases (that is, Cu, Cu₃Sn, Cu₆Sn₅, and Sn) and there are three moving phase boundaries. Furthermore, the critical material properties such as D and Z^* have never been reported for Cu and Sn in the IMC phases. H.-L. Chao recently developed a multiphase diffusion model for a Cu-Sn diffusion couple under current

stressing, and deduced unknown material properties in the IMC phases from the experimental data shown in Figs. 4.4 and 4.10 using the finite difference method and simulated annealing technique [4.68-4.70]. He predicted the growth kinetics of Cu_6Sn_5 changed from parabolic to linear as the current density increased as shown in Fig. 4.11. This is because the second term on the right side of Eq. (4.7) becomes dominant at a high current density condition. Figure 4.12 depicts the simulated growth of Cu_3Sn and Cu_6Sn_5 under $5.16 \times 10^4 \text{ A/cm}^2$ of current stressing. This current density was equivalent to an average at the passivation opening when 1.0 A of current was applied. The growth of Cu_6Sn_5 clearly shows the linear time dependence. However, the simulated growth rate of Cu_3Sn decays faster than the parabolic growth law.

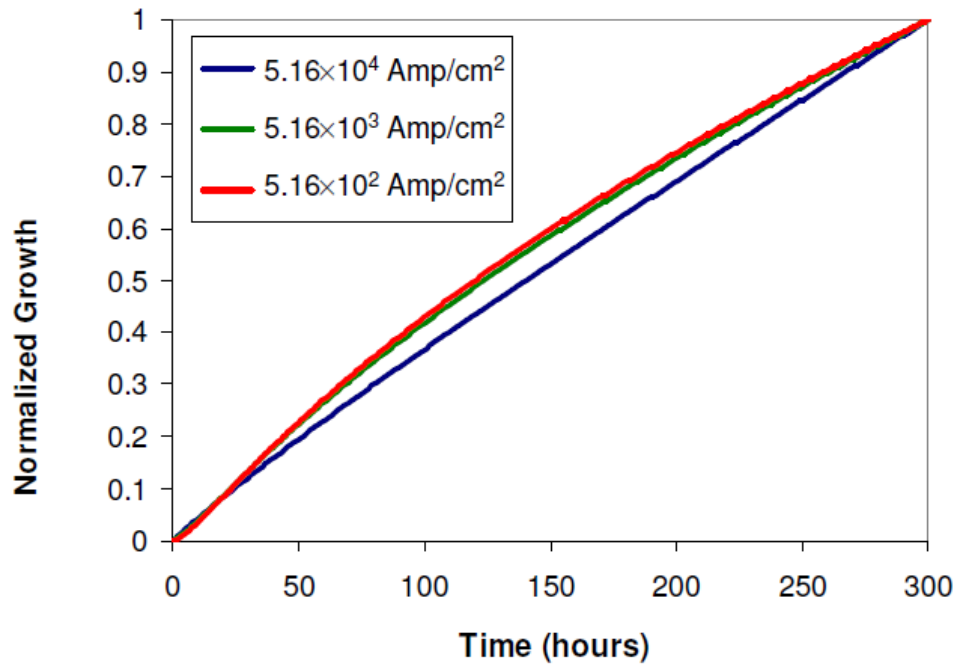


Figure 4.11: Cu_6Sn_5 growth under various current stressing conditions simulated by H.-L. Chao [4.70].

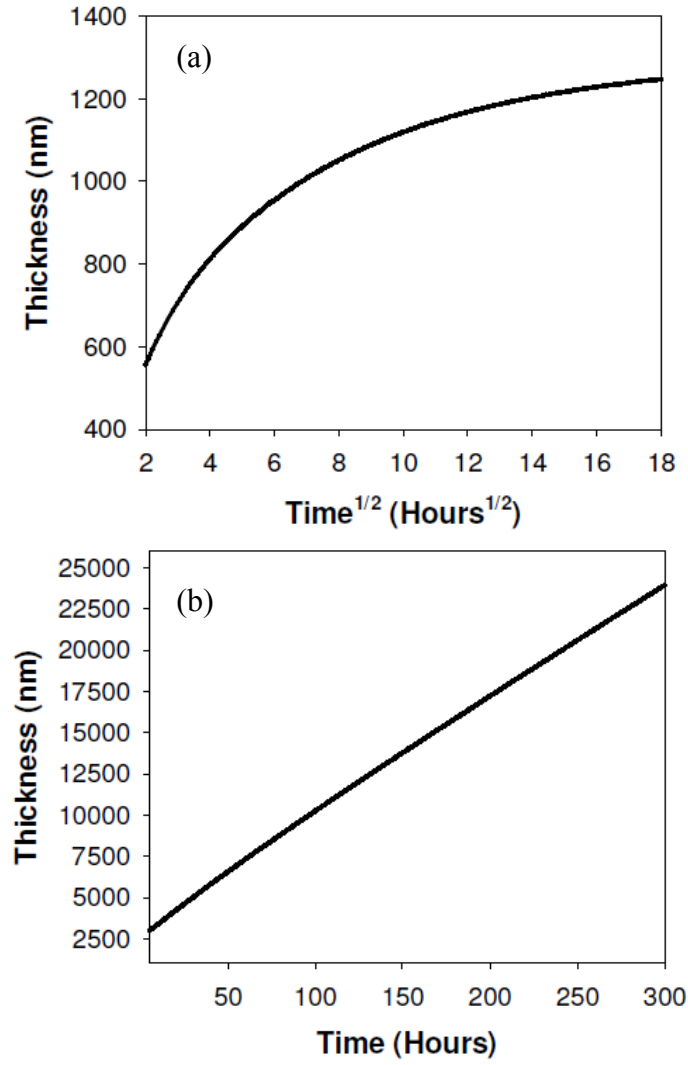


Figure 4.12: EM-enhanced IMC growth with current density of $5.16 \times 10^4 \text{ A/cm}^2$ simulated by H.-L. Chao. (a) Cu_3Sn , and (b) Cu_6Sn_5 [4.70].

When the second term on the right side of Eq. (4.7) is dominant, the EM-enhanced IMC growth follows the linear time dependence. In order to analyze the temperature dependency of the EM-enhanced IMC growth in this condition, Eq. (4.2) can be applied with $n = 1$:

$$x = x_0 + wt, \quad (4.8)$$

where the growth rate constant k in Eq. (4.2) is replaced by w to avoid confusion with the previous analysis on the thermal aging case. It is straightforward to find that w has units of velocity. Since the IMC growth is accomplished by atomic migration to a phase boundary, the IMC growth rate is proportional to the velocity of the net atomic movement, which is called the EM drift velocity [4.71]. From Eq. (4.7), the drift velocity is defined as

$$v_d = \frac{D}{kT} Z^* e \rho j = \frac{D_0}{kT} \exp\left(-\frac{Q}{kT}\right) Z^* e \rho j. \quad (4.9)$$

Therefore, the temperature dependence or apparent activation energy can be determined from an Arrhenius plot of $v_d T/j$. Figure 4.13 plots wT/j as a function of temperature for Cu_6Sn_5 , $(\text{Cu}_3\text{Sn} + \text{Cu}_6\text{Sn}_5)$, and Ni_3Sn_4 . The activation energies were found to be 1.2 ± 0.3 eV, 1.1 ± 0.3 eV, and 1.3 ± 0.7 eV, respectively. The values for the Cu-Sn IMCs were slightly larger than those determined from the thermal aging experiments, while that for Ni_3Sn_4 was smaller. Although the differences were not statistically significant, the errors could be attributed to the outliers in Fig. 4.13. In fact, although the cross-sectioning of solder joints was conducted before they failed, EM voids were already developed in some solder joints under current stressing. This could increase the local current density distribution subsequently leading to the change in the growth rate.

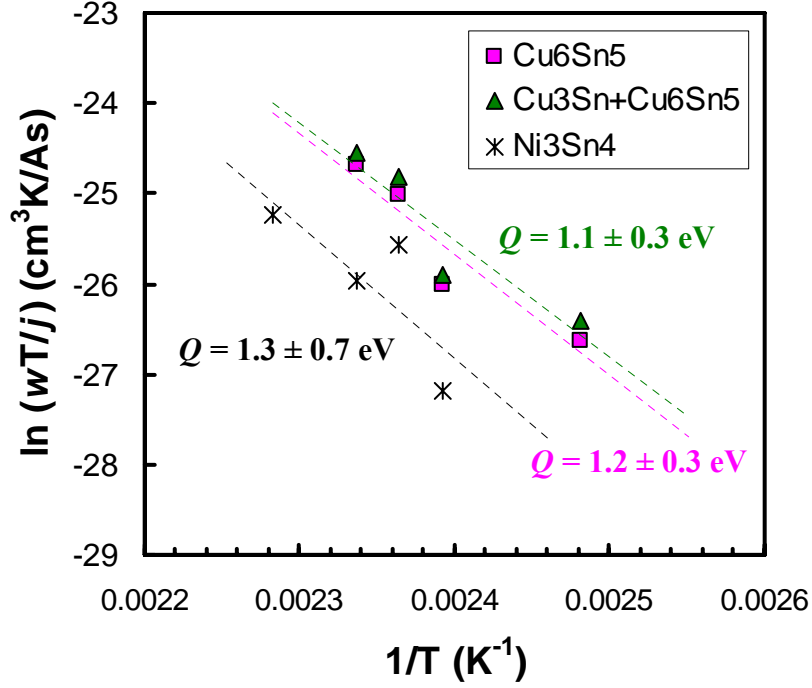


Figure 4.13: Arrhenius plot of wT/j where w is the EM drift velocity and growth rate of Cu_6Sn_5 , $(\text{Cu}_3\text{Sn} + \text{Cu}_6\text{Sn}_5)$, and Ni_3Sn_4 under current stressing.

The activation energies determined from different experiments in this study are summarized in Table 4.7. As discussed in the previous section, the EM reliability of solder joints with Cu UBM was found to be closely related to the IMC growth. The fact that the activation energies determined from three different measurements were in good agreement supports this finding. For Ni UBM solders, the activation energy for EM is lower than those associated with the IMC growth. Possible reasons are given as follows although a concrete conclusion cannot be made at present. First, Sn grain orientation was reported to have a significant effect on the EM failure mode or damage evolution in Ni UBM solders because the diffusivity of Ni along the c -axis of Sn is $\sim 10^5$ times faster than along the a -axis. According to Lu *et al.*, when the Ni diffusion path was aligned with the

c-axis of Sn, Ni UBM dissolved fast without significant IMC growth under EM [4.72]. Under this circumstance, the mass transport should be dominated by interstitial diffusion of Ni in Sn matrix, not by interdiffusion-driven IMC growth. Thus, this could have an effect on the difference in the activation energies determined from EM and IMC growth, although the Sn grain orientation in the solder joints is expected to be random. Second, in addition to EM of Ni atoms, EM of Sn atoms at the IMC/solder interface toward the substrate side is expected to be more prominent in the thin UBM structure than in the thick UBM structure due to the current crowding effect. This will contribute to EM damage evolution whereas it is not accounted for in the IMC growth measurements. Third, the thickness variation of the Ni UBM used in this study was $\pm 0.5 \mu\text{m}$. The UBM may deplete faster in a region where the UBM thickness is thinner than other regions. Then the EM failure kinetics would be described differently from the interdiffusion-driven IMC growth kinetics.

Table 4.7: Summary of activation energies for Cu-Sn and Ni-Sn systems obtained from different experiments.

Solder joint	IMC	Type of measurement		
		EM failure lifetime	IMC growth w/o current stressing	IMC growth w/ current stressing
Cu UBM solder	Cu_3Sn	$1.0 \pm 0.3 \text{ eV}$	$1.3 \pm 0.6 \text{ eV}$	-
	Cu_6Sn_5		$0.9 \pm 0.2 \text{ eV}$	$1.2 \pm 0.3 \text{ eV}$
	Total Cu-Sn IMCs		$1.1 \pm 0.3 \text{ eV}$	$1.1 \pm 0.3 \text{ eV}$
Ni UBM solder	Ni_3Sn_4	$0.9 \pm 0.2 \text{ eV}$	$1.41 \pm 0.04 \text{ eV}$	$1.3 \pm 0.7 \text{ eV}$

4.3.3 Effects of EM-Enhanced IMC Growth on EM Reliability

For the solid-state reaction between Cu and Sn, and Ni and Sn, the following reactions lead to the IMC formation:



At the solder joint temperature of 155°C, the molar volumes of Cu, Ni, Sn, Cu₃Sn, Cu₆Sn₅, and Ni₃Sn₄ were 7.16, 6.63, 16.43, 35.01, 118.72, and 75.68 cm³/mol, respectively. Therefore, IMC growth results in a net volume change of -4.4%, -5.1%, and -11.6% for Cu₃Sn, Cu₆Sn₅, and Ni₃Sn₄, respectively. If there is a negative volume change due to IMC growth, the IMC should be subjected to tensile hydrostatic stress due to confinement effect. Since the linear growth kinetics was observed for the IMC growth under high current stressing conditions, this volume change can have a significant effect on the reliability of solder joints. Finite element analyses were performed to investigate the stress evolution arisen by an extensive IMC growth.

Figure 4.14 shows the model geometry for Cu and Ni UBM structures. An axisymmetric analysis was conducted for this study. The solder radius was 63 µm and the gap height between the Si die and the organic substrate was 80 µm. Cu UBM had a radius of 38 µm and an initial thickness of 17 µm. For Ni UBM, its radius and initial thickness were 49 µm and 2 µm, respectively. The thickness of the interlayer dielectric (ILD; SiO₂) was 5 µm. Flat and uniform interfaces were assumed for UBMs and IMCs. In the Cu UBM structure, no IMC was assumed to be present on the vertical sidewall of Cu UBM for simplicity. The top surface of the Si die, the bottom surface of the substrate, and the

right-side surface of the model in Fig. 4.14 were constrained as boundary conditions. Material properties used in the analysis are summarized in Table 4.8. The properties at the experimental test condition were used if available. The plasticity of Sn-3.5Ag solder, Cu, and Ni was taken into account. Either a constitutive equation or strain-hardening parameters for these materials were taken from the literature [4.73-4.75]. Stress-strain curves for Sn-3.5Ag solder, Cu, and Ni are depicted in Figure 4.15. The stress evolution was investigated as a function of the IMC growth using FEM. The volumetric shrinkage during the IMC growth was modeled by utilizing a fictitious thermal load and a coefficient of thermal expansion (CTE). The experimental data at 155°C with 1.0 A shown in Fig. 4.10 were interpolated as listed in Tables 4.9 and 4.10. The FEM simulation was performed based on these IMC growth data.

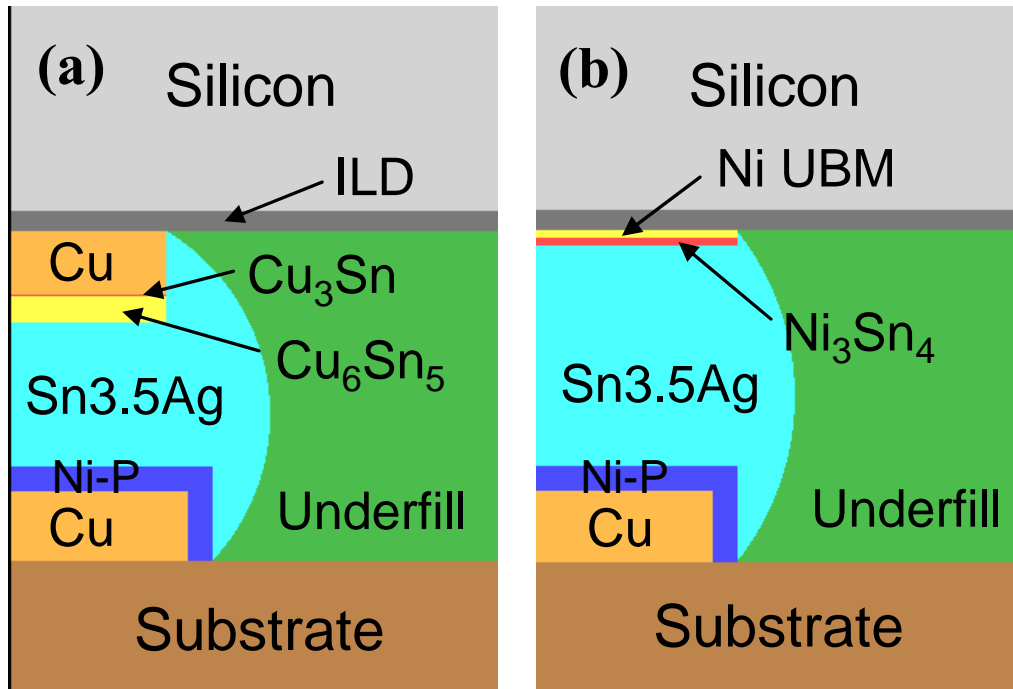


Figure 4.14: Geometry of axisymmetric FEM model for solder joints with (a) Cu UBM, and (b) Ni UBM.

Table 4.8: Material properties used in FEM.

	Temp. (°C)	E (GPa)	ν	σ_y (MPa)	Ref.
Sn-3.5Ag	155	38.4	0.4	8.9	[4.73]
Cu	155	83	0.34	130	[4.74]
Ni	200	137	0.28	323	[4.75]
Cu_3Sn^*	155	92	0.3	950	[4.76]
Cu_6Sn_5^*	155	73	0.31	1050	[4.76]
Ni_3Sn_4^*	155	113	0.33	1010	[4.76]
Ni(P)	25	50	0.3	-	[4.77]
Underfill	155	0.9	0.35	7	[4.78, 4.79]
ILD (SiO_2)	25	70	0.2	-	
Si	140	130	0.27	-	
Substrate (BT)	140	15	0.2	-	[4.80]

*The properties at 155 °C were linear-extrapolated from the room temperature data in [4.76], based on the temperature dependence of the properties of Cu and Ni.

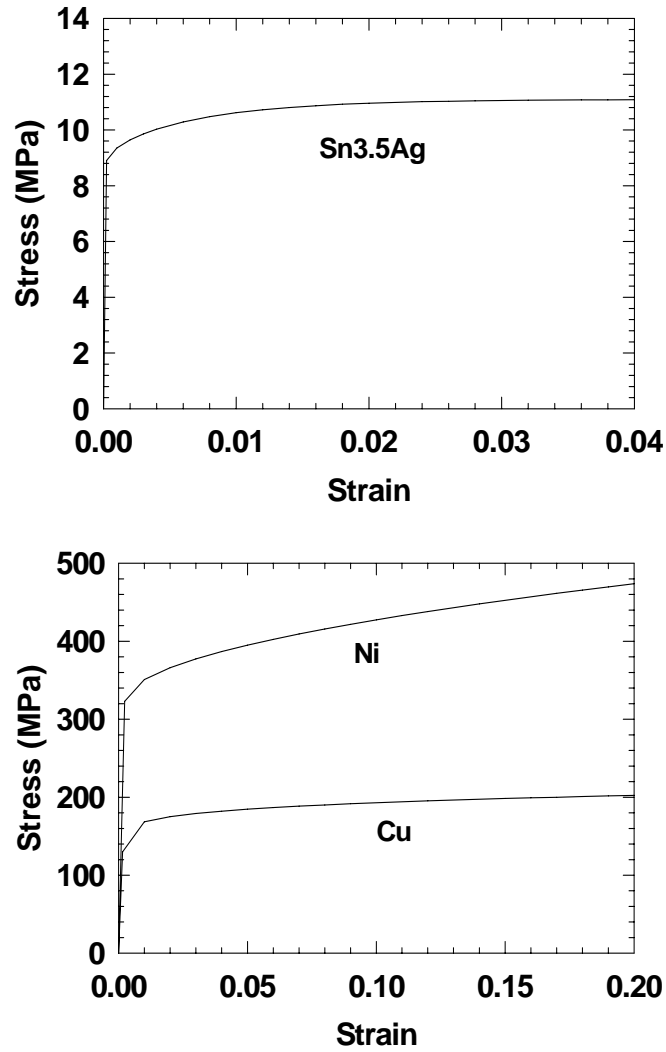


Figure 4.15: Stress-strain curves for Sn-3.5Ag solder (at 155°C) [4.73], Cu at (155°C) [4.74], and Ni (at 200°C) [4.75].

Table 4.9: Thickness changes of each layer in Cu UBM solders at 155°C with 1.0 A, interpolated from data shown in Fig. 4.10.

Time (h)	0	42	83	125	167	208
Cu UBM thickness (μm)	17	15.5	13.9	12.4	10.9	9.3
Cu_3Sn thickness (μm)	0	0.5	1.0	1.5	2.0	2.5
Cu_6Sn_5 thickness (μm)	3	6.4	9.8	13.1	16.5	19.9

Table 4.10: Thickness changes of each layer in Ni UBM solders at 155°C with 1.0 A, interpolated from data shown in Fig. 4.10.

Time (h)	0	44	89	133	178
Ni UBM thickness (μm)	2	1.7	1.5	1.2	0.9
Ni ₃ Sn ₄ thickness (μm)	1	2	3	4	5

During IMC formation, the negative net volume changes should cause tensile stresses. According to the Nabarro-Herring model of equilibrium vacancy concentration in a stressed solid, the tension region has more and the compressive region has less vacancies than the unstressed region so as to relieve stresses. The vacancy concentration in equilibrium under stressed conditions is expressed as [4.81]:

$$C_v = C_{v_0} \exp\left(\frac{\Omega\sigma}{kT}\right), \quad (4.13)$$

where C_v is the vacancy concentration, C_{v_0} is the equilibrium vacancy concentration in an unstressed condition at temperature T (in K), Ω is the atomic volume, σ is the stress, and kT is the thermal energy. Grain boundaries were assumed to be an effective source and sink to maintain a steady-state concentration of vacancies: C_{v_0} which is given by [4.82]:

$$C_{v_0} \cong 3 \exp\left(-\frac{\Delta H_v}{RT}\right), \quad (4.14)$$

where C_{v_0} is the equilibrium vacancy concentration at temperature T (in K), ΔH_v is the enthalpy of vacancy formation, and R is the gas constant. Typical values for C_{v_0} at melting temperature and ΔH_v are $\sim 10^{-4}$ - 10^{-3} and ~ 0.5 - 1.0 eV, respectively. The stress

induced by chemical reactions shown in Eqs. (4.10)-(4.12) was calculated based on the $\Delta V/V_0$ for each reaction. The resulting values of C_v were approximately 0.2% for the Cu-Sn IMCs and 2.4% for the Ni_3Sn_4 at 155°C. It was assumed that the equilibrium molar volumes of the IMC phases under the stressed condition increased by these vacancy concentrations and induce a volumetric strain as the FEM input.

Figure 4.16 shows a hydrostatic pressure (negative hydrostatic stress) contour for the thick Cu UBM structure with 1.0 μm of Cu_3Sn and 9.8 μm of Cu_6Sn_5 . Cu UBM was subject to a hydrostatic compressive stress (positive hydrostatic pressure in the figure) while IMCs were under a hydrostatic tensile stress (negative hydrostatic pressure). The maximum hydrostatic stress was found in the Cu_6Sn_5 layer near the $\text{Cu}_3\text{Sn}/\text{Cu}_6\text{Sn}_5$ interface. The stress gradient also existed through the thickness of the IMC layers. A part of the Cu UBM and solder was found to undergo plastic deformation. Figure 4.17 depicts the maximum hydrostatic stress evolution in Cu UBM solders at 155°C as a function of time for IMC growth. As the thickness of the IMC layers increased and that of the UBM layer decreased, the confinement effect by the thick Cu UBM was reduced. At the same time, plastic deformation occurred in more volume of the Cu UBM and solder. Thus, the maximum stress in the Cu_6Sn_5 layer decreased with IMC growth. Figure 4.18 shows a hydrostatic pressure contour for the thin Ni UBM structure with 4.0 μm of Ni_3Sn_4 . The IMC layer was also under tension and the maximum stress was found near the $\text{Ni}_3\text{Sn}_4/\text{solder}$ interface. The hydrostatic tensile stress was higher than that in the Cu UBM solder although the IMC thickness was much thinner. This was attributed to the fact that the formation of Ni_3Sn_4 involved more than $2\times$ volume shrinkage compared to the Cu-Sn IMCs. In the Ni_3Sn_4 layer and solder, plastic deformation occurred. The maximum stress evolution in Ni UBM solders as a function of the current stressing time is plotted in Fig. 4.19. Because the Ni UBM was thin the confinement effect by Si should

be more significant than that by the UBM. This led to the stress in the IMC layer increasing with the growth of Ni_3Sn_4 . Yet the stress increment over time decreased due to the plastic deformation of the IMC layer.

A large hydrostatic tensile stress can increase the equilibrium vacancy concentration and may trigger void nucleation. However, it was found that, for metal interconnect lines, homogeneous void nucleation by vacancy condensation required very high hydrostatic stress of the order of >5 GPa, and the rate of nucleation on a grain boundary was also very slow [4.81, 4.83]. This could also be true for the IMCs, with some exceptions. As discussed in Chapter 3, voiding was not observed in cathode joints except the interdiffusion-driven Kirkendall voids (in case of Cu UBM solders) even though the extensively-grown IMCs were often found there. Also, the stress gradient can drive an atomic flux, described as [4.84]:

$$J = \frac{D}{kT} \frac{\partial \sigma}{\partial x}. \quad (4.15)$$

Again, any evidence of this effect was not observed in cathode joints. However, when a flaw or void is present in the region of high hydrostatic tension, the resulting stress gradient causes metal atoms to diffuse away from the void to relax the stress [4.85]. In anode joints, EM-driven voids were observed in the IMC layer or at the IMC/solder interface. Therefore, once the initial void was formed in the high tensile stress region the void growth could be accelerated. In other words, the EM-driven vacancy flux and EM-enhanced IMC growth can have a synergistic effect on the EM damage evolution in solder joints.

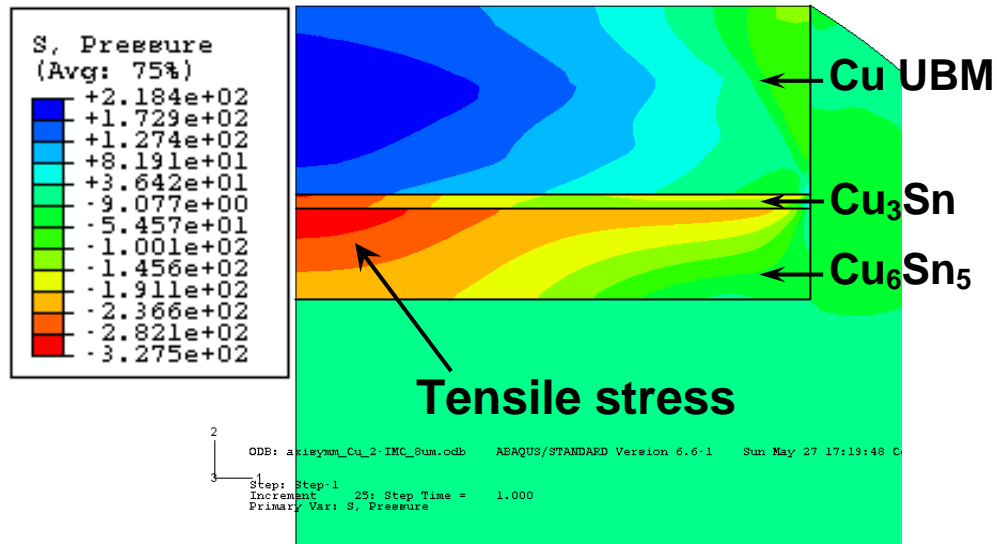


Figure 4.16: Hydrostatic pressure contour in a Cu UBM solder at 155°C with 1.0 μm of Cu_3Sn and 9.8 μm of Cu_6Sn_5 (at time = 83 h).

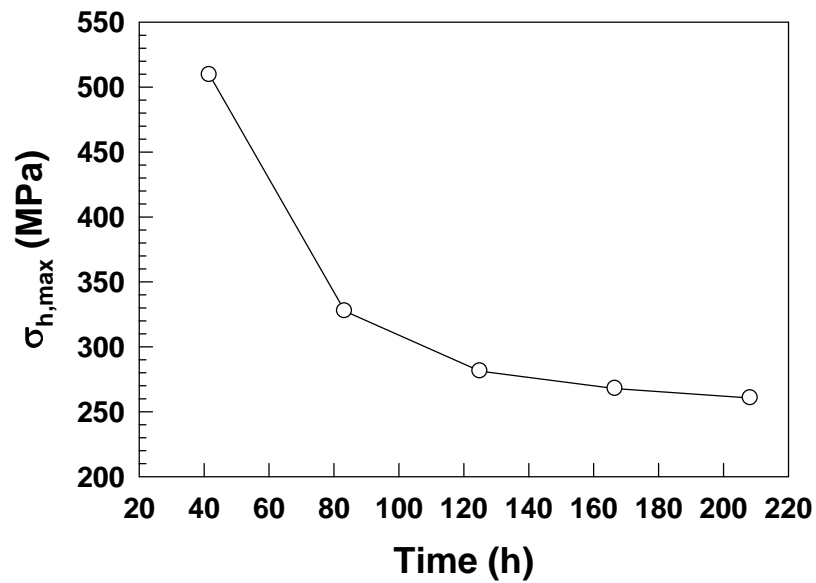


Figure 4.17: Maximum hydrostatic stress evolution in Cu UBM solders with IMC growth at 155°C.

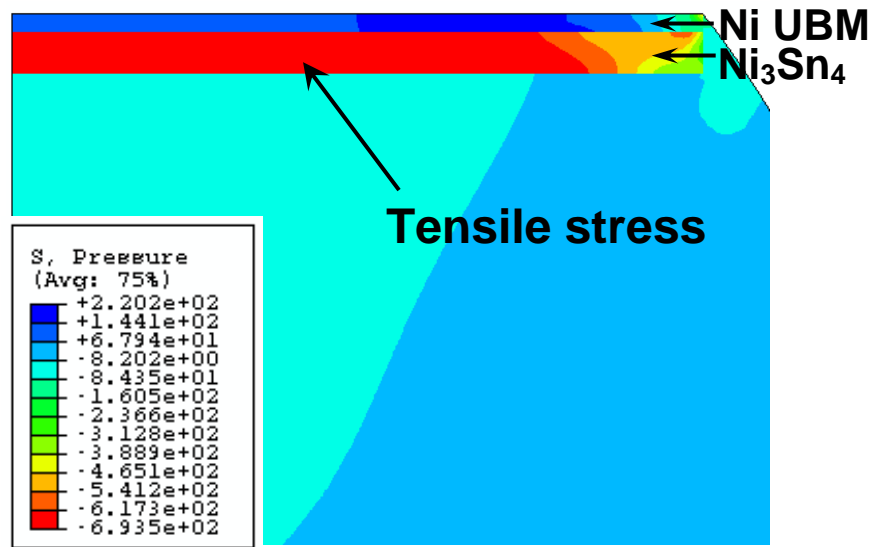


Figure 4.18: Hydrostatic pressure contour in a Ni UBM solder at 155°C with 4.0 μm of Ni_3Sn_4 (at time = 133 h).

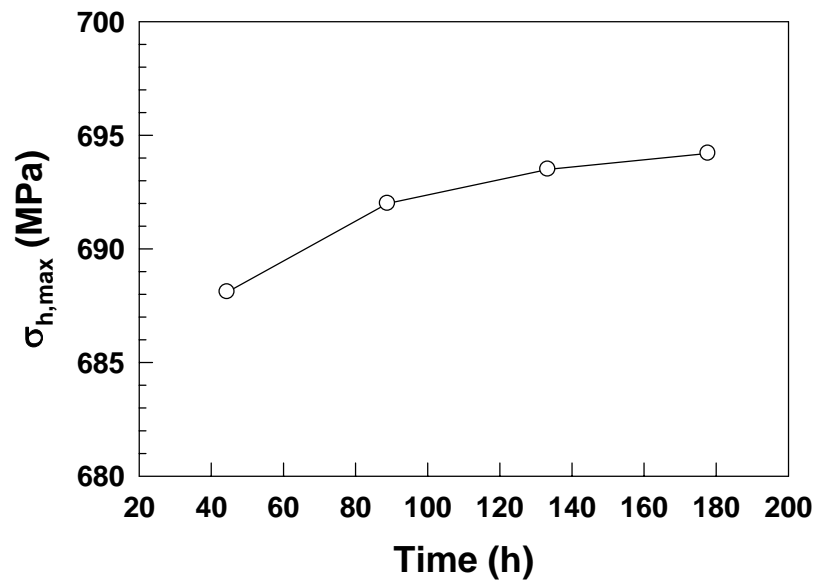


Figure 4.19: Maximum hydrostatic stress evolution in Ni UBM solders with IMC growth at 155°C.

4.4 SUMMARY

This chapter discussed the IMC growth in Pb-free solder joints with and without current stressing. The growth rate was found to follow a parabolic growth law when current stressing was not present. Under high current stressing, a linear growth law was observed for the growth of Cu_6Sn_5 and Ni_3Sn_4 . For Cu UBM solders, the apparent activation energy for the IMC growth was in good agreement with the activation energy for EM obtained in Chapter 3. This indicates the EM voiding mechanism was closely related to the IMC growth driven by interdiffusion. In contrast, the apparent activation energy for the growth of Ni_3Sn_4 was higher than the EM activation energy for Ni UBM solders. It was suggested that the EM failure in the Ni UBM solders could be associated with more than one mass transport mechanism whereas the IMC growth kinetics was controlled by the interdiffusion of Ni and Sn only. It was demonstrated using FEM that EM-enhanced IMC growth led to a large hydrostatic tension in IMC layers. This condition could accelerate the void growth once voids were initiated by EM in that region although the accompanying plastic deformation of solder, UBM, and/or IMC may slow down the stress evolution.

Chapter 5: Effects of Current Crowding on Electromigration Reliability of Solder Joints with Thin Ni UBM

In Chapter 3, electromigration (EM) reliability in solder joints with thin Ni UBM was confirmed to be directly related to the current crowding at the entrance of electron current. To characterize the effect of current crowding on the EM reliability of solder joints quantitatively, EM tests were performed on Pb-free solder joints having different thicknesses of Ni UBM. The UBM thickness dependency of EM lifetime was accounted for by the current crowding effect based on finite element analysis (FEA). Combining results from the experiments and FEA, the maximum current density at the UBM/solder interface was found to be an important parameter controlling EM reliability. Further analyses were conducted by FEA to evaluate the dependency of current density distribution on the design of the metal trace. The results showed that the design optimization for the metal trace was as important as the UBM thickness in controlling EM reliability. To assess the scaling effect on EM reliability of solder joints, the current crowding phenomena with scaling of solder joints are also addressed in this chapter.

5.1 INTRODUCTION

With continuing scaling of device feature sizes, the size and pitch of flip-chip solder joints will continue to decrease. As a result, current density in solder joints will rise to about 10^4 A/cm² when the solder diameter decreases below 100 μ m [5.1]. Together with the implementation of Pb-free solders in flip-chip packages, this raises serious electromigration (EM) reliability concerns. Comparing with high-Pb solders, the

Pb-free solders have inferior current carrying capability and faster intermetallic compound (IMC) growth rate. Both factors can accelerate EM failure.

Significant current crowding can occur in solder joints due to the abrupt change in the cross-sectional area as electron current passes through the thin metallization layer to enter the solder joints. This phenomenon has been known to be a key factor to induce EM failure in solder joints with thin UBM structures [5.1-5.5]. Results from previous simulation studies have reported that a thicker UBM can relieve current crowding effectively [5.3, 5.6]. However, a quantitative correlation between current crowding and experimentally determined EM lifetime, particularly for Pb-free solders with different UBM thicknesses, has not been reported. Of particular concern to this problem are the effects of metal trace (thin metal strip on the die side) design and solder joint scaling on current crowding.

In this study, the effect of these issues on Pb-free solder joints was addressed. First, EM experiments were performed on Sn-2.5Ag solder joints with Ni UBM of 1, 2, and 3 μm in thickness. 3-D finite element analysis (FEA) was employed to obtain the current density distribution in solder joints, and the maximum current density was correlated to the EM lifetime. Second, the effect of metal trace design on the current crowding was investigated. These included different thicknesses (1 and 2 μm), materials (Cu and Al), and geometries (rectangular and dog-bone shape). Simple modifications of the metal trace design were demonstrated to mitigate the current crowding effect. Third, the effects of solder joint scaling on current density distribution were studied using FEA to assess EM reliability issues for next generation fine pitch solder joints.

5.2 EXPERIMENTAL DETAILS

Three EM runs were conducted on Sn-2.5Ag solder joints with Ni UBM in plastic flip chip packages. Each run comprised of testing the structure with UBM thickness of 1, 2, and 3 μm , respectively. Figure 5.1 shows cross-sectional micrographs of pristine solder joints with different UBM thicknesses. About 1 μm of Ni_3Sn_4 layer was formed in as-reflowed solder joints. The diameters of passivation opening, Al pad, and UBM, were 50, 54, and 94 μm , respectively as marked in Fig. 5.1. The nominal diameter of solder bump was 130 μm , and the diameter of substrate pad was 94 μm as shown in Fig. 5.2. The stand-off height of the solder bump was about 53 μm . The metal trace was a rectangular Cu strip of 74 μm in width and 1 μm in thickness.

Two pairs of solder joints, i.e. two cathode and two anode joints, were subject to current stressing of 1.0 A at a chamber temperature of 126.5°C. The test setup was the same as illustrated in Fig. 2.11. Due to the Joule heating effect, the temperature at the Si backside increased to 136°C, which was kept constant throughout the run. A 3-D coupled electro-thermal FEM modeling was performed to determine the temperature of solder joints under current stressing as discussed in Chapter 3. The resulting solder temperature was ~148°C.

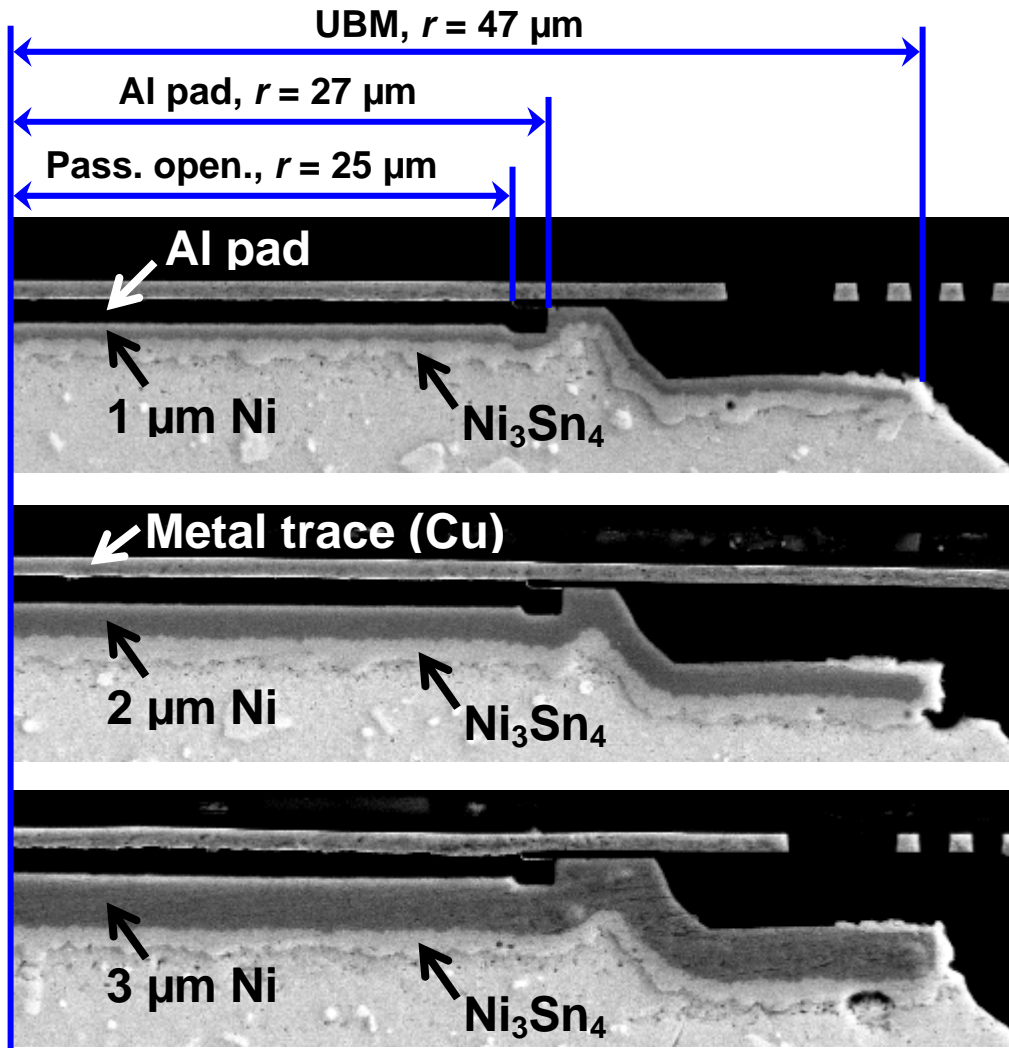


Figure 5.1: SEM images of upper part of pristine solder joints with (a) 1 μm , (b) 2 μm , and (c) 3 μm of Ni UBM. Diameters of passivation opening, Al pad, and UBM are marked.

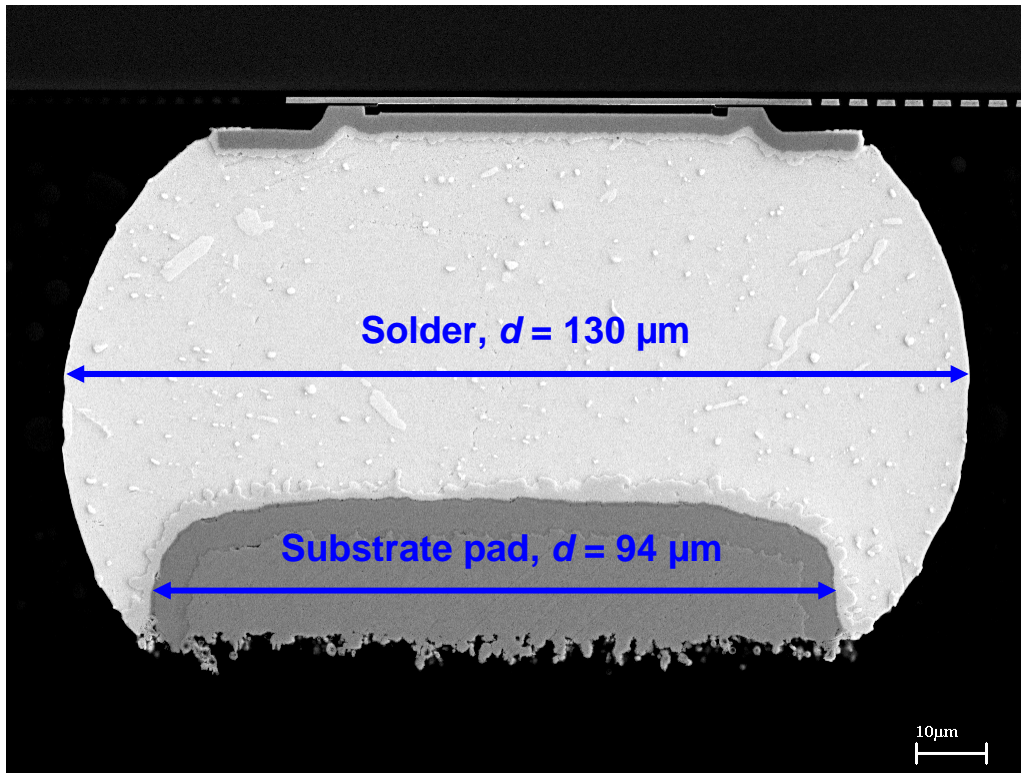


Figure 5.2: Diameters of solder bump and substrate pad.

5.3 FINITE ELEMENT MODELING

Commercial CAD software I-DEAS and FEM software ABAQUS were utilized to characterize the current density distribution in solder joints. Figure 5.3 shows the 3-D FEM model and mesh for a pair of solder joints. The dimensions of the geometry were described in the previous section. The electrical conductivity of each material at the experimental test condition is summarized in Table 5.1. The boundary conditions were based on a surface current density applied at the bottom of one substrate pad based on 1.0 A of applied current and the bottom of the other substrate pad grounded at 0 V.

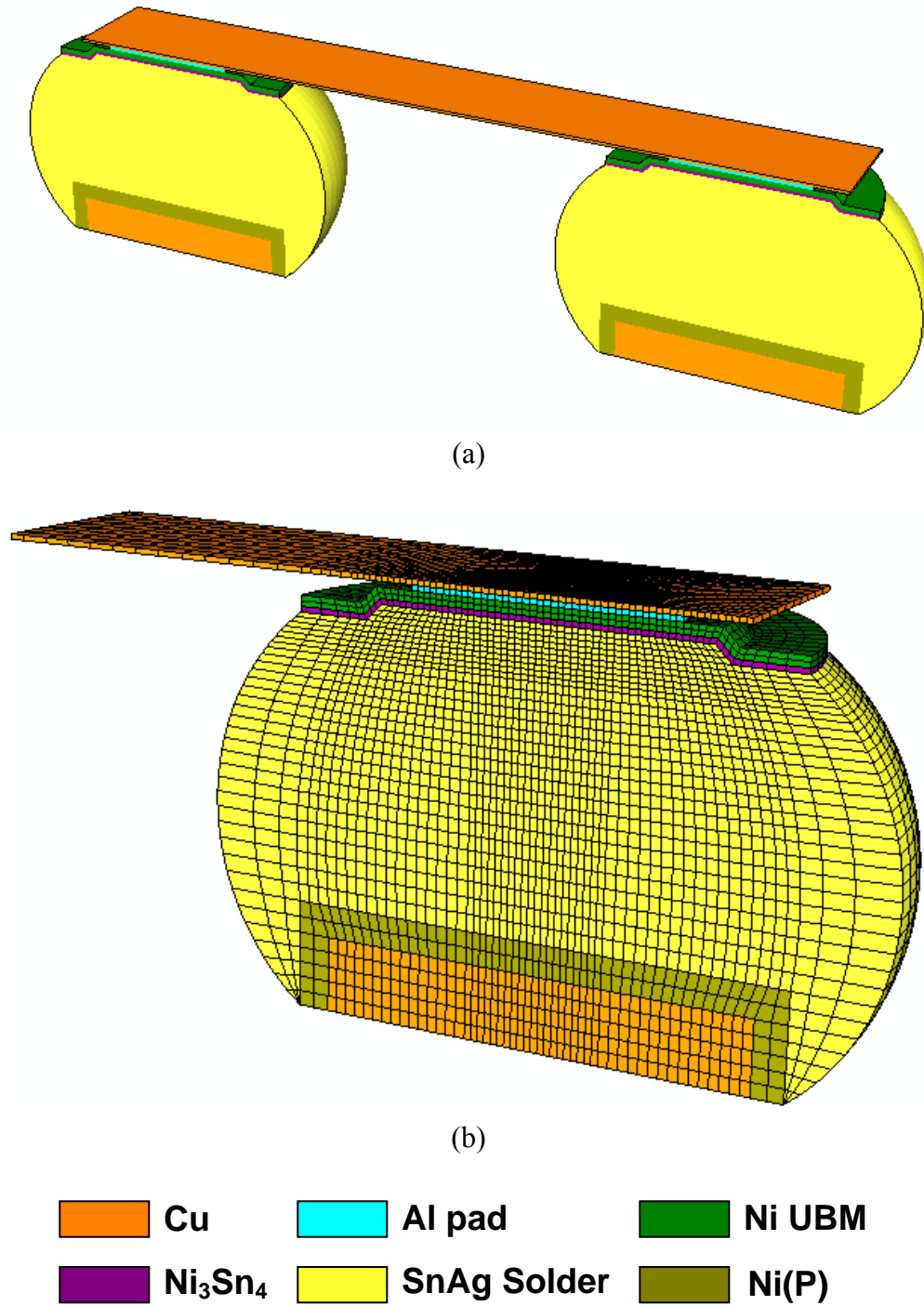


Figure 5.3: (a) Solid model of a pair of solder joint with 2 μm UBM, and (b) finite element mesh. The cross-sectional plane is the symmetry plane.

Table 5.1: Electrical conductivity of the materials used in FEM.

Material	Electrical conductivity ($\Omega^{-1}\text{m}^{-1}$)
Al	3.78×10^7
Cu	5.8×10^7
Ni	1.43×10^7
Ni_3Sn_4	3.5×10^6
Solder	8×10^6

5.4 EXPERIMENTAL RESULTS

Figure 5.4 shows an example of resistance traces of solder joints with different UBM thicknesses. Although it was not always the case, thicker UBM was prone to have a longer resistance jittering period. The onset of jittering occurred at $\sim 40\text{-}50$ mV of V_g (off-balance voltage in the Wheatstone bridge configuration) or ~ 100 m Ω of ΔR (resistance rise) as discussed in Chapter 3. The EM lifetime was determined based on the first resistance jump criterion where the onset of jittering was marked as failure.

The cumulative distribution function (CDF) of EM lifetime for different UBM thicknesses is plotted in Fig. 5.5. The median-time-to-failure (MTTF or t_{50}) was found to be 103, 196, and 232 hours for 1, 2, and 3 μm UBM, respectively. Apparently, no simple linear relation could be established between UBM thickness and the EM lifetime.

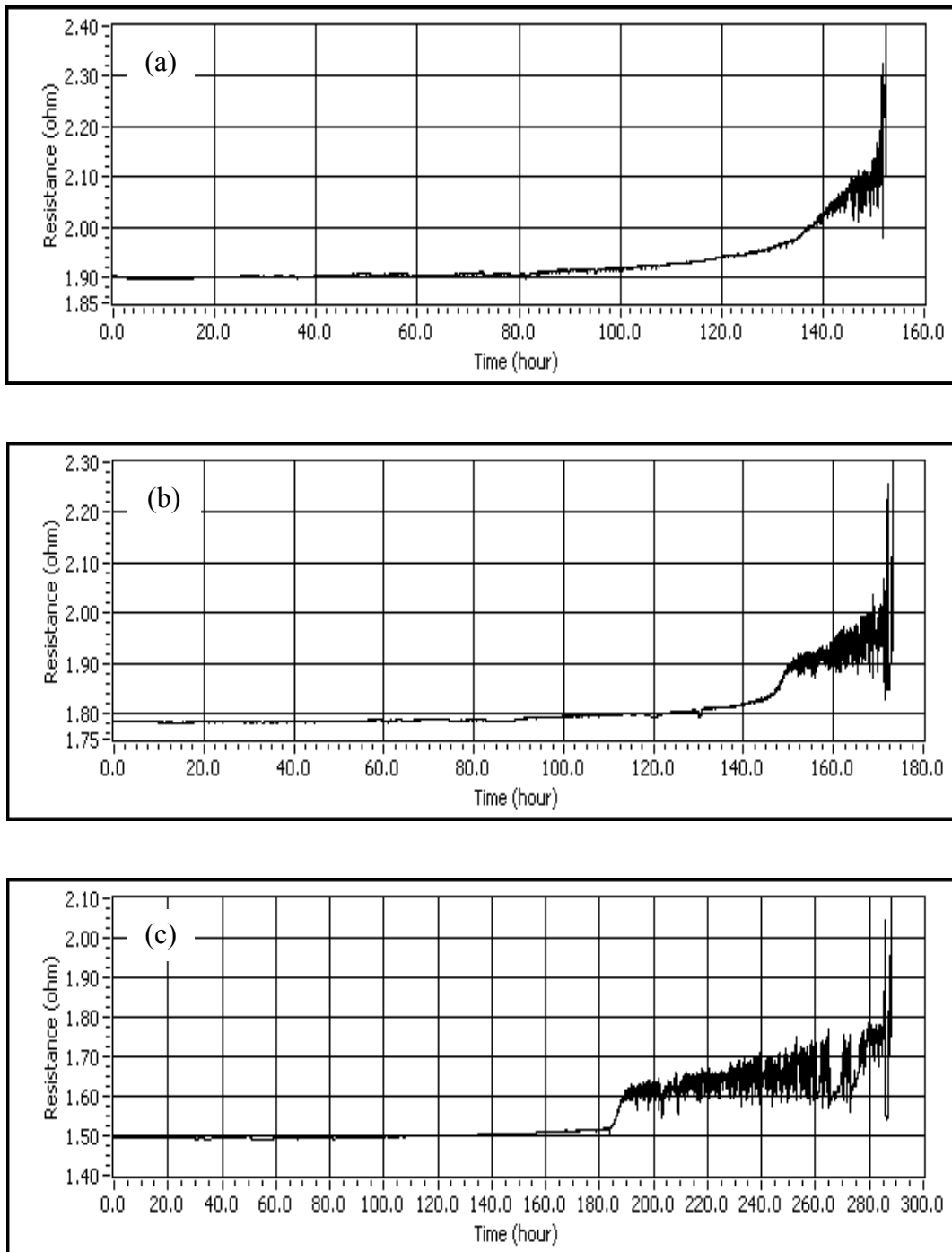


Figure 5.4: Example of resistance traces for (a) 1 μm , (b) 2 μm , and (c) 3 μm of Ni UBM.

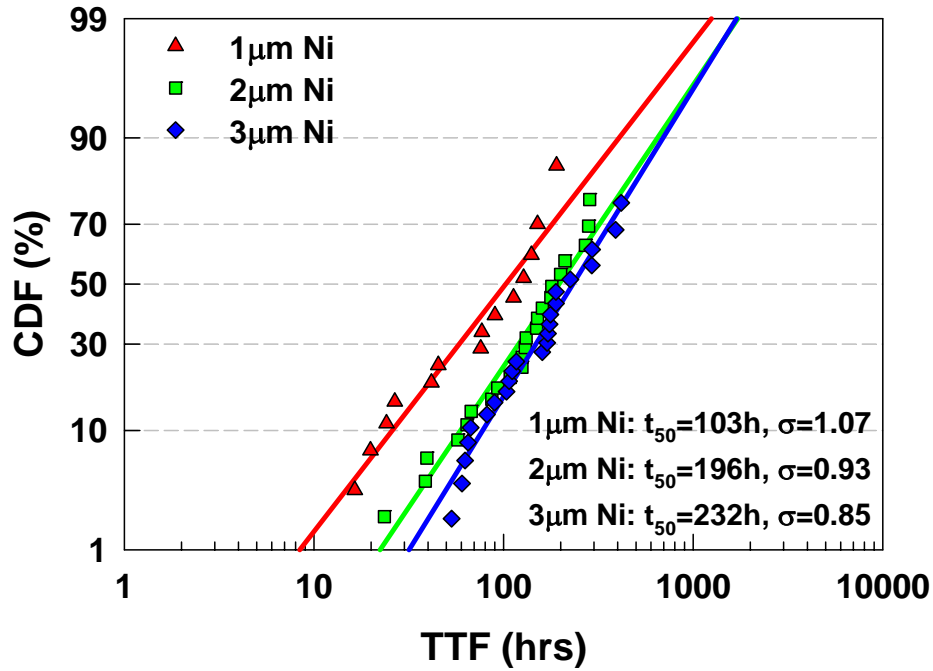


Figure 5.5: Log-normal CDF plot of EM lifetime of solder joints with Ni UBM of 1, 2, and 3 μm in thickness.

Cross-sectional micrographs of solder joints after current stressing are shown in Fig. 5.6. EM voiding was observed at the Ni_3Sn_4 /solder interface preferentially in the current crowding region and propagated through the interface. At the same time, the UBM dissolved into the solder with further growth of Ni_3Sn_4 . While the thickness of UBM shown in Fig. 5.6 is 3 μm , the same failure mode was observed as UBM thickness of 1 and 2 μm . This agrees with other studies with thin UBM structures where initial EM voiding was also observed in the current crowding region followed by void propagation along the UBM/solder interface [5.2, 5.4, 5.7, 5.8].

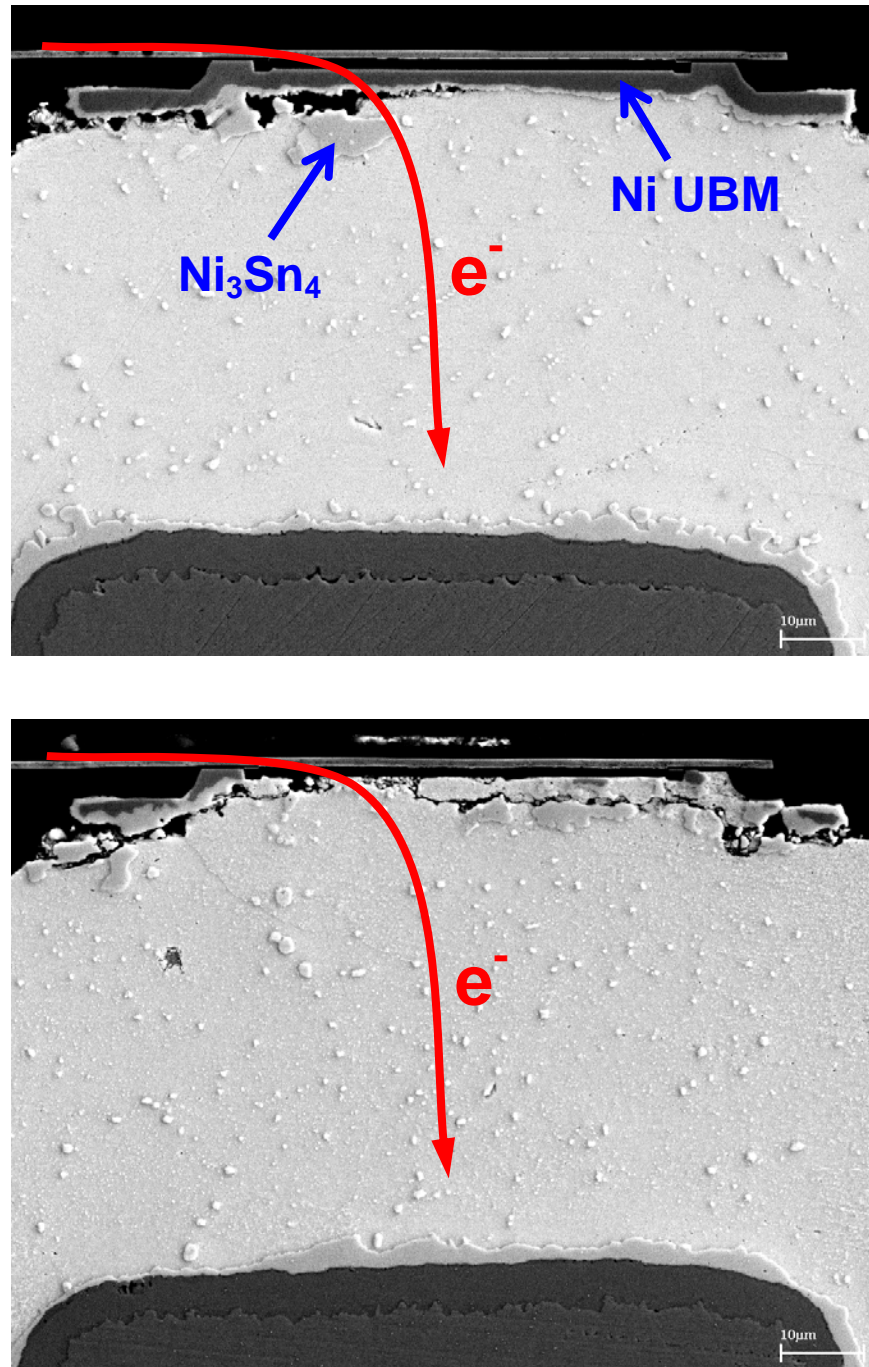


Figure 5.6: SEM images of Sn-2.5Ag solder joints with 3 μm Ni UBM at 1.0 A of current stressing. (a) EM voiding initiated at a current crowding region and propagated through the IMC/solder interface ($\Delta R \sim 10 \text{ m}\Omega$). (b) Failed solder based on the first resistance jump criterion ($\Delta R \sim 160 \text{ m}\Omega$). UBM was almost depleted.

5.5 DISCUSSION

5.5.1 Correlation between Current Crowding and EM Lifetime

In general, EM lifetime is correlated with temperature and current density through Black's equation [5.9]:

$$t_{50} = Aj^{-n} \exp\left(\frac{Q}{kT}\right), \quad (5.1)$$

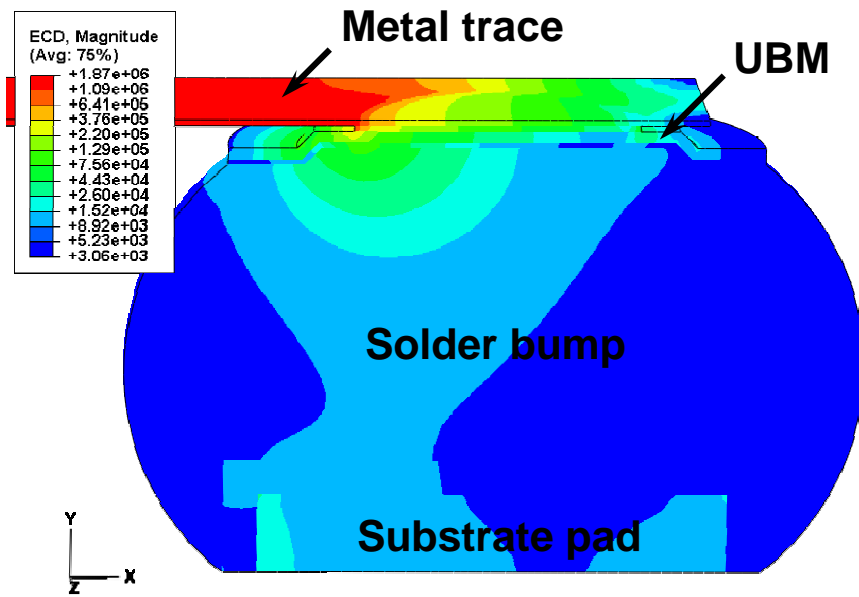
where t_{50} is the median-time-to-failure (MTTF), A is a constant, j is the current density, n is the current density exponent, Q is the EM activation energy, k is the Boltzmann constant, and T is the absolute temperature. When this relationship is applied to EM data for solder joints, the average current density at the passivation opening is usually used for the j term for simplicity [5.7, 5.8, 5.10-5.12]. However, this simple approach does not allow the prediction of EM lifetimes if design parameters other than the passivation opening diameter are changed. To cope with this problem and find a quantitative correlation between UBM thickness and EM lifetime, FEM analyses were performed to examine the current crowding phenomena.

The simulation results for solder joints with 2 μm Ni UBM is shown in Fig. 5.7. Since the cross-section of the metal trace was about 26 times smaller than that of the passivation opening, the maximum current density, j_{max} , was found at the entrance of the passivation opening through which the electron current is passed (Fig. 5.7(a)). As a results, the j_{max} in the solder bump was found right below this entrance of the passivation opening (Fig. 5.5(b)). This is the region where EM voiding usually initiated as shown in Fig. 5.6(a). As electrons traveled away from the metal trace in the solder joint, the current density distribution became more uniform. The j_{max} in each layer shown in Fig. 5.7(a) is

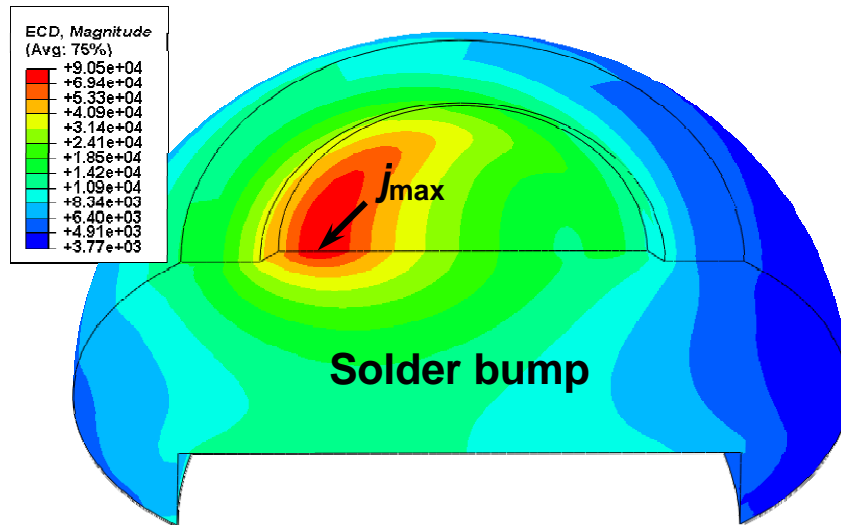
compared with the average current density, j_{avg} , in the layer. The result is summarized in Table 5.2 where the average current density is calculated by dividing the applied current by the cross-sectional area of each layer. The ratio of j_{max} to j_{avg} is also included, which is called “current crowding factor” or “crowding ratio” [5.3, 5.13]. This ratio increases with the non-uniformity of the current density distribution. The current crowding factor was found to be 23 at the top of Al pad (passivation opening), but decreased to 6.5 at the top interface of the solder bump.

Table 5.2: Average and maximum current density and current crowding factor ($j_{\text{max}} / j_{\text{avg}}$) in each layer.

		j_{avg} (10^4 A/cm ²)	j_{max} (10^4 A/cm ²)	$j_{\text{max}} / j_{\text{avg}}$
Metal (Cu) trace		135	187	1.4
Al pad (top)		5.1	117	23.0
Ni UBM	Top	1.4	38.8	27.7
	Bottom		19.0	13.6
Ni ₃ Sn ₄ (top)			10.4	7.4
Solder (top)			9.1	6.5



(a)



(b)

Figure 5.7: Current density contour for a solder joint with 2 μm Ni UBM at an applied current of 1 A. (a) shows the entire solder joint system, and (b) shows the solder bump only (rotated from (a) for better illustration of the area of interest).

Figure 5.8 plots j_{\max} in each layer as a function of UBM thickness. The UBM thickness has little effect on the current density distribution in the metal trace, Al pad, and the top portion of UBM. However, as the UBM thickness increases, the j_{\max} at the bottom portion of UBM decreases substantially. This is because an electric current could spread out more readily throughout the thicker UBM. As a result, the j_{\max} at the top interface of a solder bump, $j_{\max, \text{solder}}$, reduced by 22% and 38% as the UBM thickness increased from 1 μm to 2 and 3 μm , respectively. This can account for the non-linear dependence of EM lifetime with the UBM thickness. A thick Ni UBM is not very practical because the residual stress in thick Ni film is highly concentrated, especially on the Si chip side [5.14].

EM voiding at the IMC/solder interface in Ni UBM solders can be attributed to migration of Sn atoms, especially at an early stage of damage evolution. Thus $j_{\max, \text{solder}}$ can be important in controlling the EM lifetime of Ni UBM solders, which is aggravated by the current crowding effect. Figure 5.9 plots t_{50} with respect to $j_{\max, \text{solder}}$ for different UBM thicknesses in a log scale. The slope from a linear regression was determined to be -1.9 ± 0.5 . In fact, this corresponds to $(-n)$ in Eq. (5.1). This n value is reasonably close to, but a little smaller than $n = 2.2 \pm 0.9$ obtained in Chapter 3. A possible reason is given as follows. In Chapter 3, the average current density based on the passivation opening diameter was used to determine the current density exponent. Although j_{avg} is proportional to the applied current, $j_{\max, \text{solder}}$ may not be so. In fact, it is expected that $dj_{\max}/dj_{\text{avg}} > 1$ as the applied voltage increases. In this scenario, the n value in Chapter 3 would be smaller than 2.2 if $j_{\max, \text{solder}}$ is used. This suggests that $j_{\max, \text{solder}}$ can be a more reasonable representation of the j -term in Eq. (5.1) if the failure mechanism is associated with the migration of Sn atoms under non-uniform current density distribution. Again, the dependence of EM lifetime on UBM thickness or other design parameters cannot be correlated simply with j_{avg} .

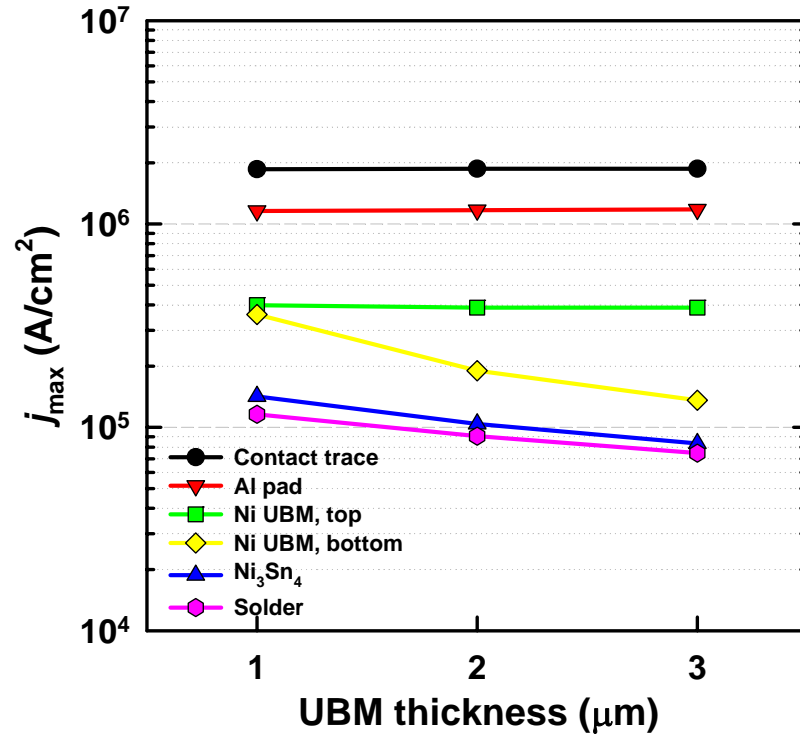


Figure 5.8: Maximum current density in each layer as a function of UBM thickness at an applied current of 1 A.

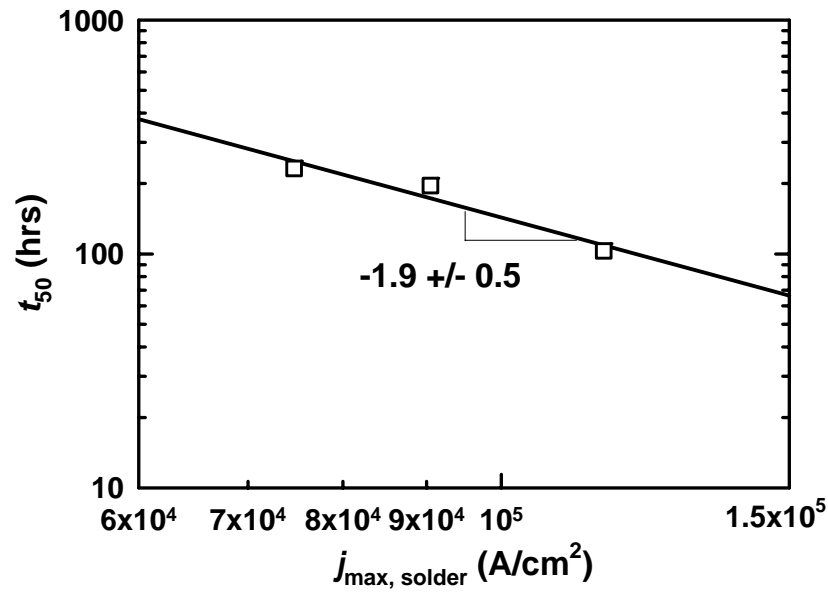


Figure 5.9: Log-log plot of t_{50} vs. $j_{\max, \text{solder}}$ for different UBM thicknesses.

5.5.2 Effects of Metal Trace Design on Current Crowding

Since j_{\max} was shown to be an important factor in controlling EM reliability of solder joints, the effects of various metal trace designs on current crowding were investigated using FEM. The model geometry shown in Fig. 5.3 served as a control model to compare the results. In this model, the metal trace was a rectangular Cu strip of 74 μm in width and 1 μm in thickness. Five different metal trace designs as listed in Table 5.3 were compared with the control. Individual design parameters such as material, thickness, or shape of the metal trace can be changed in each model. Additionally, minor modifications were made on the control in a way that small holes were created in front of the entrance of passivation opening in an attempt to alleviate current crowding (Design D/E).

Table 5.3: Variations in metal trace design simulated by FEM.

Trace design	Material	Thickness	Shape
Control	Cu	1 μm	Rectangle
A	Al	1 μm	Rectangle
B	Cu	2 μm	Rectangle
C	Cu	1 μm	Dog-bone
D	Cu	1 μm	Rectangle w/ six (4 $\mu\text{m} \times 3.7 \mu\text{m}$) holes
E	Cu	1 μm	Rectangle w/ one (6 $\mu\text{m} \times 22 \mu\text{m}$) hole

Current density contours are shown in Fig. 5.10, and j_{\max} for each type of metal trace design is plotted in Fig. 5.11. When Al was used for metal trace (Design A) instead of Cu, the j_{\max} in the Al pad (at spot “1”) increased by 29% compared with the control design. This was because the electrical conductivity of Al was about 37% lower than that

of Cu. Owing to the better conductivity of Cu, electrons can travel farther along the Cu trace than the Al trace before they enter into the Al pad. As a result, the Al trace led to 8% larger $j_{\max, \text{solder}}$.

When the thickness of metal trace increased to 2 μm (Design B), j_{\max} decreased substantially. When j_{avg} in the trace was lowered by half, j_{\max} in the trace and Al pad (at spot “2”) was reduced by 49% and 32%, respectively. Accordingly, $j_{\max, \text{solder}}$ was reduced by 15%.

In Design C, where a dog-bone shape was applied, the width of the trace was narrowed by half between the bump pads. A significant increase in j_{\max} was observed due to the reduction in the cross-section of the metal trace. The $j_{\max, \text{trace}}$ was found at the spot “3” shown in Fig. 5.10(c), which was about twice as large as that in the control design. Also, a local $j_{\max, \text{trace}}$ at the entrance of passivation opening (spot “4”) had a 36% larger value compared with $j_{\max, \text{trace}}$ of the control. Consequently, $j_{\max, \text{solder}}$ increased by 19%. Apparently, this type of trace design will exaggerate the current crowding effect as well as generate more Joule heat.

Design D and E included a minor modification to the control trace design. Design D had six small holes in front of the entrance of passivation opening, while Design E had one larger hole, as shown in Fig. 5.10(d)-(e). In Design D, $j_{\max, \text{trace}}$ was found at the spot “5” shown in Fig. 5.10(d), which showed 31% larger j_{\max} than the control. Except for this, the current density distribution in Design D was very close to the control design. For example, $j_{\max, \text{solder}}$ as well as the local $j_{\max, \text{trace}}$ at the entrance of passivation opening (spot “6”) were found to decrease only by 1%. Thus the Design D offers only negligible advantage in terms of relaxing current crowding.

In contrast, significant differences were observed in the results of Design E. At first, the location of the local $j_{\max, \text{trace}}$ at the entrance of passivation opening (spot “8”)

was displaced from the symmetry plane because the hole in the middle split the current flow. The resulting local $j_{\max, \text{trace}}$ at the spot “8” was found to be 12% lower than the control design. Consequently, $j_{\max, \text{solder}}$ which was also off the symmetry plane, was dropped by 12%. However, $j_{\max, \text{trace}}$ at the spot “7” had an 86% larger value than $j_{\max, \text{trace}}$ of the control, which could create a local hot spot around this region. This may cancel out some gains achieved from the relieved current crowding. All in all, the material selection, geometry, and dimensions for metal traces were found to be important design parameters that should be considered to mitigate the current crowding effect.

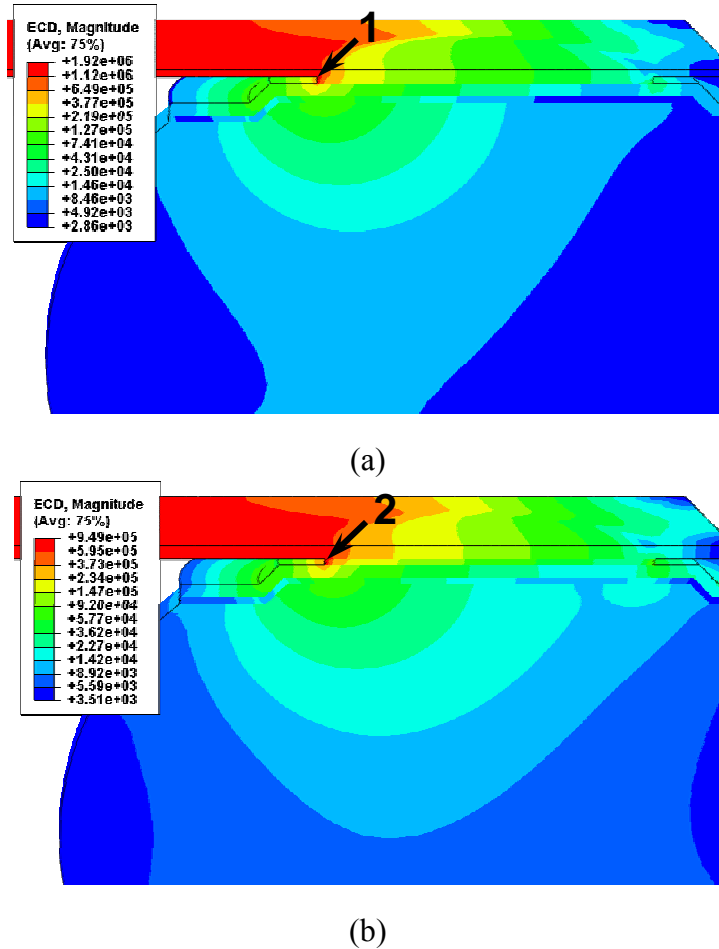
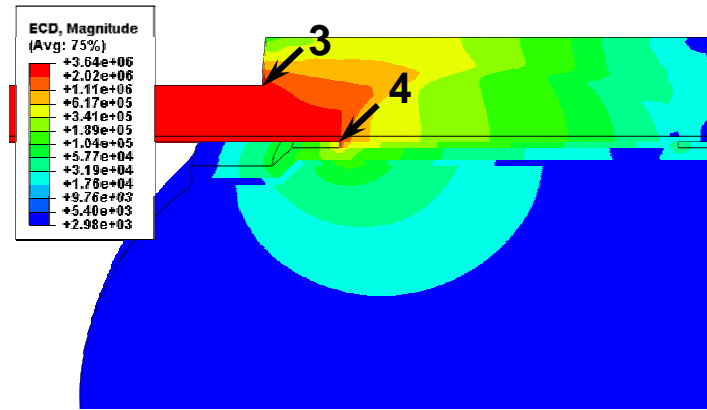
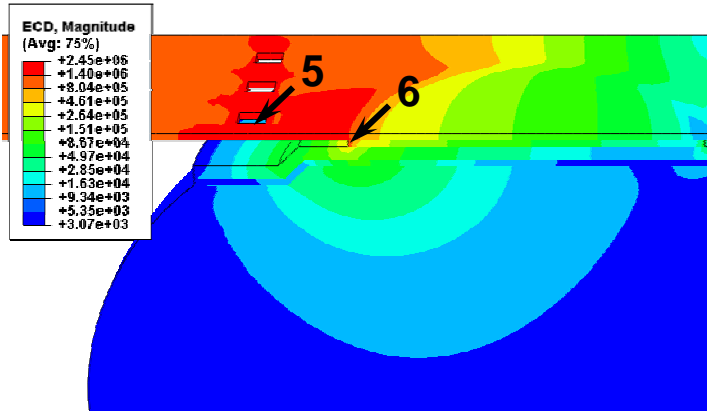


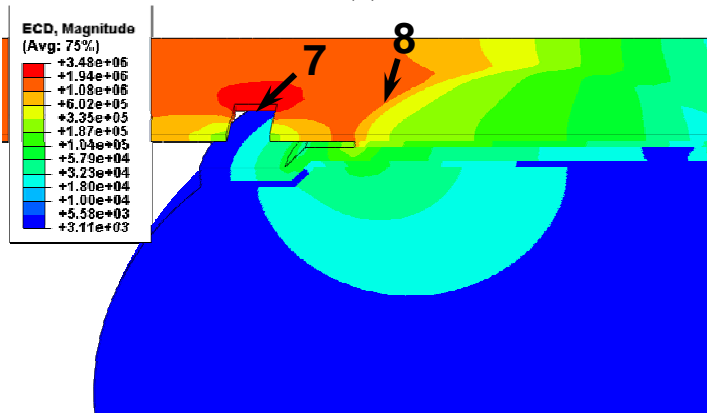
Figure 5.10: Current density distribution for various metal trace designs. (a) Design A, (b) Design B, (c) Design C, (d) Design D, and (e) Design E.



(c)



(d)



(e)

Figure 5.10: (*cont'd*) Current density distribution for various metal trace designs. (a) Design A, (b) Design B, (c) Design C, (d) Design D, and (e) Design E.

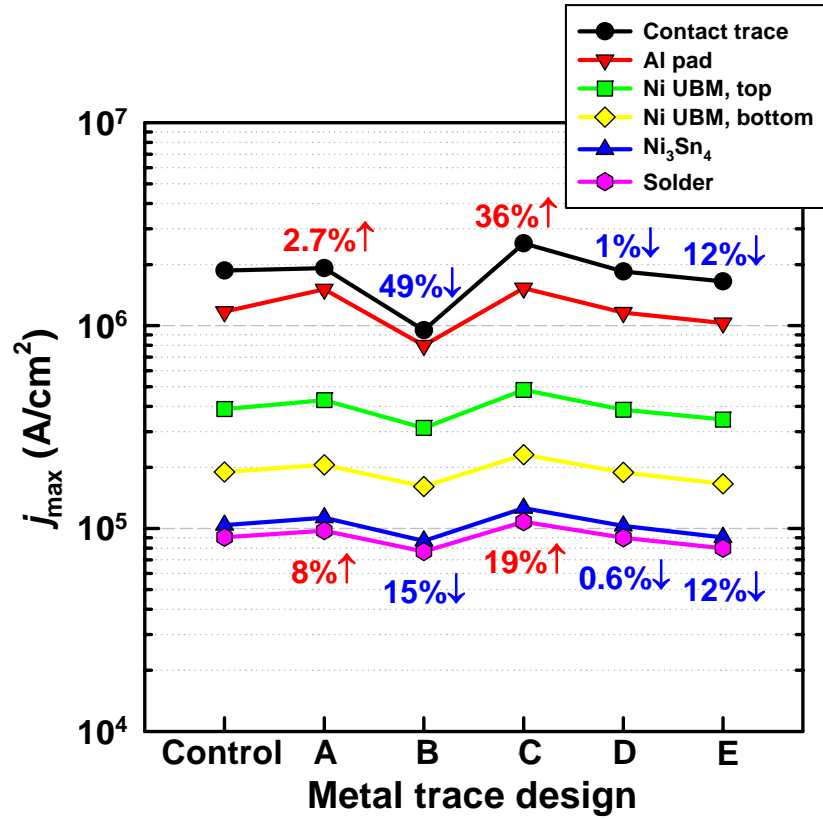


Figure 5.11: Maximum current density in each layer with different metal trace designs at an applied current of 1 A. For Design C, D, and E, the local maximum at the entrance of passivation opening was chosen as j_{\max} in the metal trace.

5.5.3 Effects of Solder Joint Scaling on Current Density Distribution

More FEM was performed to investigate the scaling effect on current density distribution in solder joints. The scaling matrix for this study was based on a 1 A applied current and tabulated in Table 5.4. Again, solder joints with 2 μm Ni UBM shown in Fig. 5.3 was used as a control. In Model I, only the diameter of passivation opening was scaled down by 20% while in Model II, the diameter of UBM was additionally reduced by 21% with other dimensions remaining the same. Approximately uniform down-scaling

of solder joint dimensions was applied in Model III and IV. The scaling factors for Model III and IV were about 20% and 40%, respectively.

Table 5.4: Solder joint scaling matrix for FEM analyses (unit: μm).

Scaling model	Control	Model I	Model II	Model III	Model IV
w_{trace}	74	74	74	64 (-14%)	48 (-35%)
$d_{\text{pass. open.}}$	50	40 (-20%)	40 (-20%)	40 (-20%)	30 (-40%)
d_{UBM}	94	94	74 (-21%)	74 (-21%)	58 (-38%)
d_{solder}	130	130	130	110 (-15%)	92 (-29%)
$d_{\text{sub. pad}}$	94	94	94	74 (-21%)	58 (-38%)

[†] w : width, d : diameter.

Figure 5.12 shows the effects of scaling on j_{max} in each layer of solder joints for the aforementioned models. For Model I, j_{max} in the Al pad rose only by 8%, although the j_{avg} increased by 56% due to the 20% reduction in the diameter of passivation opening. The current crowding factor at the Al pad was determined to be 16, which was smaller than 23 for the control model (see Table 5.2). This indicates that the current density distribution in this layer was more uniform for the smaller passivation opening in spite of the increased j_{avg} , provided that the width of the metal trace remained the same. At the top of the solder bump, however, both j_{max} and the current crowding factor increased by 10%.

For Model II, the reduction in UBM diameter in addition to the passivation opening did not make a large difference compared to Model I. For example, $j_{\text{max, solder}}$ increased by 10.5% compared to the control, which can be considered as a minor difference.

In Model III, solder joints were scaled down by ~20% including the width of metal trace, the nominal diameter of solder bump, and the diameter of substrate pad. The result showed that j_{\max} in the Al pad and on the top of the solder increased by 17% and 18%, respectively. Considering that the diameters of solder bump and substrate pad had little to do with the current density distribution in the upper part of the solder joint, the scaling of the metal trace accounted for an additional 8% rise in j_{\max} . Therefore, the dimensions of metal trace and passivation opening were found to be important in controlling the level of current crowding in solder joints.

The solder joints were further scaled down by ~40% in Model IV compared with the control. This corresponded to 280% increase in j_{avg} in every layer of a solder joint except the metal trace. In contrast, j_{\max} in the Al pad and on the top of a solder increased by 58% and 57%, respectively. The fact that j_{\max} did not scale up at the same rate as j_{avg} indicated the following. First, when solder joints were scaled down, the current crowding factor (j_{\max}/j_{avg}) decreased. In other words, the current density distribution became more uniform although the overall current density level increased. And second, the current density in areas outside of the current crowding region increased at a faster rate than j_{\max} .

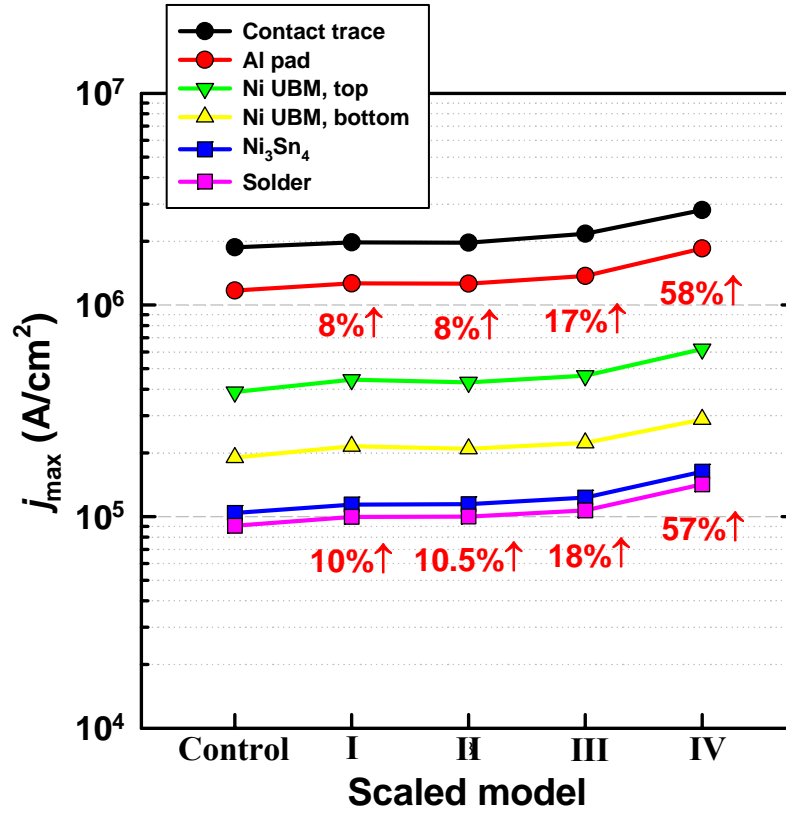


Figure 5.12: Effects of solder joint scaling on maximum current density. The applied current was fixed at 1 A.

5.6 SUMMARY

EM experiments were performed on Pb-free solder joints with different Ni UBM thicknesses and supplemented by FEM to quantitatively determine the correlation between current crowding and EM lifetime. When the UBM thickness increased from 1 μm to 2 and 3 μm , the j_{\max} on the top of a solder decreased by 22% and 38% and led to 90% and 125% longer t_{50} , respectively. The $j_{\max, \text{solder}}$ was found to be a more appropriate parameter than $j_{\text{avg, Al pad}}$ to represent the current density term in Black's equation. Choosing in this way, the current density exponent, n , was determined to be 1.9 ± 0.5 .

The effect of variations of metal trace design was examined by FEM, showing that the metal trace design is an important factor to control the current crowding effect. A rectangular, thick Cu trace might be the best choice without major modifications of the current geometry and process. Placing a small hole in front of the entrance to passivation opening could be an additional option to reduce $j_{\max, \text{solder}}$, providing that a local hot spot near the hole does not significantly increase the solder temperature.

FEM results of solder joint scaling showed that j_{\max} did not increase as much as j_{avg} when solder joints were scaled down. The current crowding became less prominent while j_{avg} increased. It was also found that down-scaling of the diameter of UBM did not have a significant effect on current crowding. Instead, current crowding was mainly controlled by the cross-sectional area of the metal trace and the diameter of the passivation opening.

In summary, UBM thickness, metal trace design, and passivation opening diameter should be optimized to improve EM reliability of solder joints.

Chapter 6: Electromigration versus Thermomigration in Pb-Free Solder Joint Reliability

In previous chapters, the effects of electromigration (EM) on void formation, morphology changes, and intermetallic compound growth in Pb-free solder joints were discussed. Thermomigration (TM), atomic diffusion driven by temperature gradient, is another concern recently raised for solder joint reliability. Nevertheless, the experimental setup used in the previous chapters did not generate large enough thermal gradient to cause noticeable TM in solder joints. In this sense, the results presented previously were exclusively from EM only. In this chapter, the effects of TM on Pb-free solder joint reliability is first evaluated. For this purpose, the experimental setup was modified to create a large temperature gradient in solder joints. Under this condition, evidence of TM was observed but the TM-induced damage looked statistically scattered. The results of EM and TM are compared.

6.1 INTRODUCTION

Thermomigration (TM) is another forced diffusion mechanism analogous to electromigration (EM) except that the driving force is a thermal gradient instead of an electric potential gradient. This phenomenon is also known as the Ludwig-Soret effect. Since first reported for a liquid mixture by Ludwig in 1856 [6.1], critical theoretical and experimental works were established for solid metals by various researchers, especially in 1960's [6.2, 6.3]. The driving forces for EM and TM are given by

$$F_{\text{EM}} = Z^* e \rho j, \quad (6.1)$$

$$F_{\text{TM}} = -(Q^* / T) \nabla T, \quad (6.2)$$

where F is the driving force, Z^* the effective charge number, e the electronic charge, ρ the electric resistivity, j the current density, Q^* the heat of transport per atom, and T the absolute temperature. It was observed that TM was more predominant than EM in refractory and transition metals such as Co and Pt [6.2]. However, for good conductors used as typical interconnect metals, the ratio of the driving forces for TM to EM, $F_{\text{TM}}/F_{\text{EM}}$, was estimated to be of the order of 10^{-3} only [6.4]. Therefore, TM has not been a serious problem compared to EM in back-end-of-line (BEOL) interconnects.

In contrast, the effect of TM can be noticeable in solder joints if the thermal gradient is in the order of 10^3 °C/cm because the current density is about 2 orders of magnitude smaller than BEOL interconnects. Huang *et al.* found phase redistribution in SnPb composite solders (97Pb3Sn with 37Pb63Sn) by TM where Pb moved to the cold end while Sn toward the hot end [6.5]. The estimated temperature gradient for TM to occur was 1000 °C/cm. Chuang and Liu created a temperature gradient of 1010 °C/cm in a bulk sample of eutectic SnPb alloy to observe Pb depletion in the hot side [6.6]. Hsiao and Chen applied an alternating current (AC) to eutectic SnPb solder bumps in which the temperature gradient was measured to be 2143 °C/cm by infrared microscopy [6.7]. Similar to the previous studies, Pb-rich phase migrated toward the cold end (substrate side). This is consistent with observations under EM where Pb was the dominant diffusing species at temperatures above 100°C whereas the dominant diffuser was Sn at room temperature [6.8-6.11]. The heat of transport, Q^* , for eutectic SnPb solders was determined to range from 0.23 eV to 0.28 eV [6.6, 6.7, 6.12]. For Pb-free solders, Chen *et al.* found that the Cu migration from the hot end to the cold end leading to dissolution of the Cu UBM (5 μm) and voids at the UBM/IMC interface [6.13]. The temperature

gradient for TM to overwhelm EM in Cu UBM under the current density of 9.7×10^3 A/cm² was estimated to be 400 °C/cm. A recent study by Hsiao and Chen showed that Sn migrated toward the hot end in Sn-3.5Ag solder bumps under the temperature gradient of 2829 °C/cm generated by AC [6.14]. However, the UBM of 5 µm Cu/3 µm Ni looked intact in this case. Q^* of Sn was calculated to be -0.014 eV from measurements of marker movements. Yet studies on TM in solder joints are still limited. Especially for Pb-free solder joints, the effects of TM on atomic diffusion and intermetallic compound (IMC) formation are not clearly understood. In addition, TM failure mechanisms need to be identified for different UBMs, such as thin Ni and thick Cu.

In this study, the effects of TM on Pb-free solder joints were first investigated. For this purpose, a special setup of experiments was employed to create a large temperature gradient without a current flow. Tested solder joints were Sn-2.5Ag with thin (1 µm) Ni UBM and thick (18 µm) Cu UBM in organic flip chip packages. Then a current was applied to a few bump pairs to generate comparable EM flux. Morphology changes by EM and TM were compared by cross-sectional scanning electron microscopy (SEM).

6.2 EXPERIMENTAL DETAILS

When a current is applied to a test module used in this study, Joule heat is generated not only from the metal trace on the die side but also from the substrate trace because the latter is long (~10 mm) and relatively narrow (~500 µm²). For this reason, applying a current alone cannot produce an enough temperature gradient in solder joints to cause TM. Therefore, a special experimental setup was devised to maximize the temperature difference between the top (backside) of the Si die and the bottom of the substrate as shown in Fig. 6.1. The top of the die was placed on a Cu plate which was laid

on a hot plate. On the other hand, the bottom of the substrate was cooled down by a high-performance CPU cooler. The ambient temperature was room temperature. The maximum temperature difference achieved across the 1.9 mm-thick package was 93 °C as seen in Table 6.1. As a control, a sample was thermally aged but without a CPU cooler. Thermal compound was applied between the Cu plate and the test module and between the test module and the cooler base. Temperatures on the die top and the substrate bottom were monitored by thermocouples.

Three samples of Sn-2.5Ag solder joints with 1 μm -Ni UBM and two samples with 18 μm -Cu UBM were tested. Cross-section of each sample is depicted in Fig. 6.2. The Cu UBM samples did not have an Al pad, unlike Ni UBM samples. The test conditions are summarized in Table 6.1. Due to the use of hot plate, the die top temperatures of the samples were not uniform. Samples B-E were subject to an artificially large temperature gradient by using CPU coolers, while Sample A was used as a control without a large temperature gradient. A current stressing of 0.5 A or 0.8 A was applied to two pairs of solder joints (4th, 5th, 8th, and 9th bumps in the first row) in Samples B-D as shown in Fig. 6.3. Based on the area of the passivation opening, the corresponding average current density was 2.5 or 4.1 in 10^4 A/cm^2 , respectively. Thus these bumps experienced both EM and TM. The other solder joints were under TM only. For all samples, resistance changes were monitored for the above two pairs of solder joints using the Wheatstone bridge system described in Chapter 2. For Samples A and E, a minimal current of ~5 mA was applied for the resistance measurements.

After the tests were finished the samples were cross-sectioned to reveal the first row of the solder array as marked in Fig. 6.3. As such, total 31 solder joints were examined under SEM.

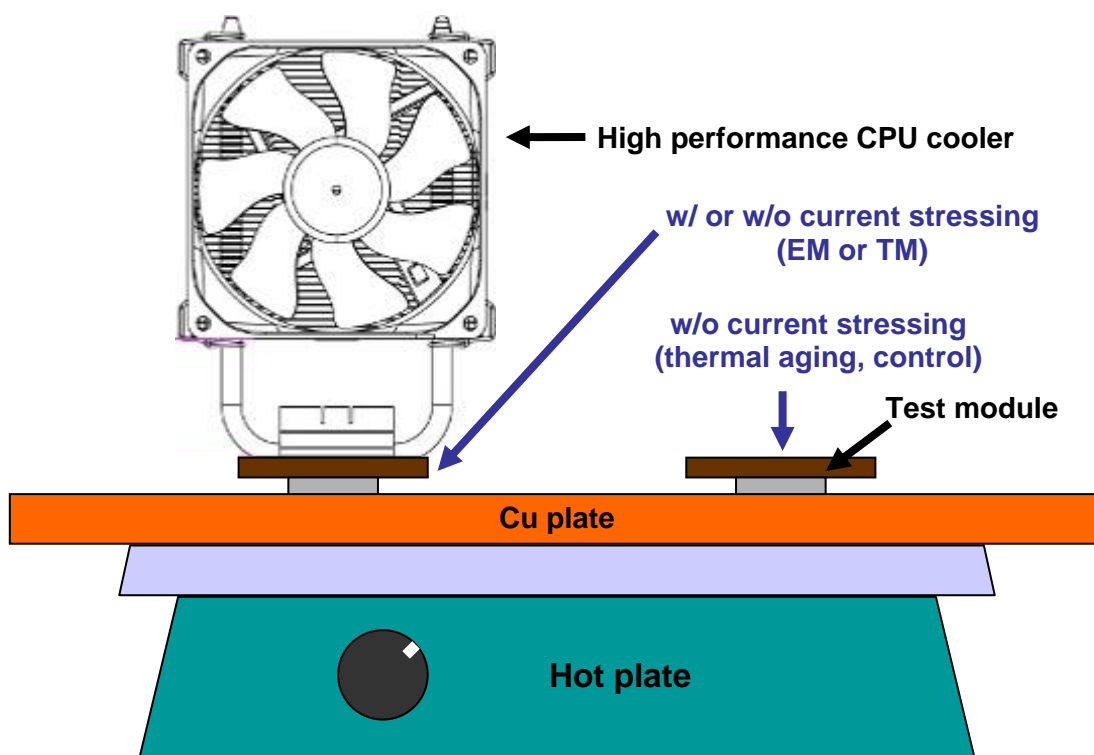


Figure 6.1: Schematic diagram of the experimental setup (not to scale). Thermal compound (not shown) was applied between the Cu plate and the test module and between the test module and the cooler base.

Table 6.1: Summary of TM and EM test conditions.

Sample	UBM	Type of load	Number of bumps	Die top temperature (°C) [†]	Substrate bottom temperature (°C) [†]
A	Ni (1 μm)	Thermal aging	31	163	149
B		EM (0.5A) + TM	4	155	65
		TM	27		
C		EM (0.8A) + TM	4	151	73
		TM	27		
D	Cu (18 μm)	EM (0.8A) + TM	4	154	83
		TM	27		
E		TM	31	170	77

[†]Temperature variation: ±4°C.

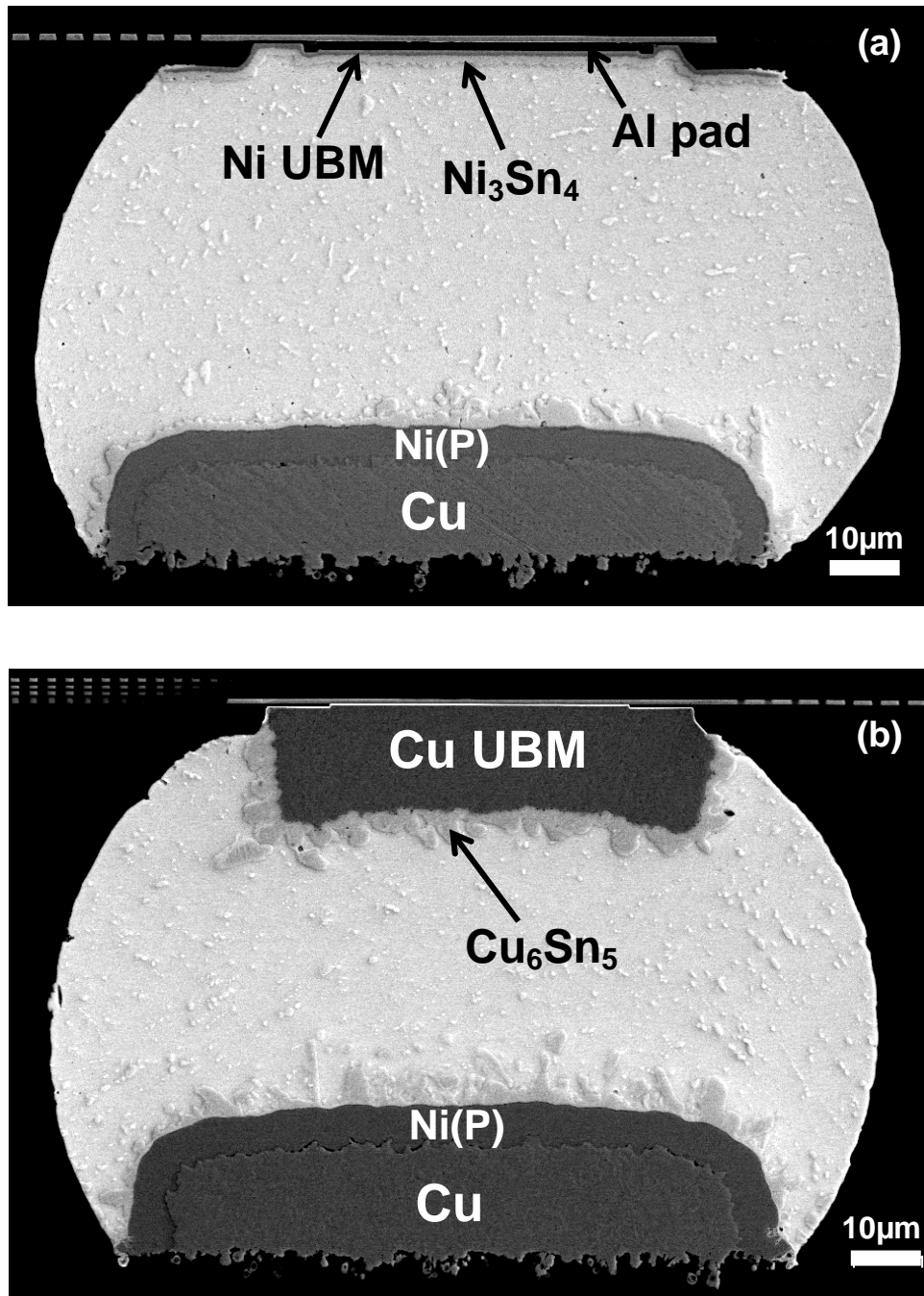


Figure 6.2: Pristine solder joint with (a) Ni UBM (1 µm), and (b) Cu UBM (18 µm).

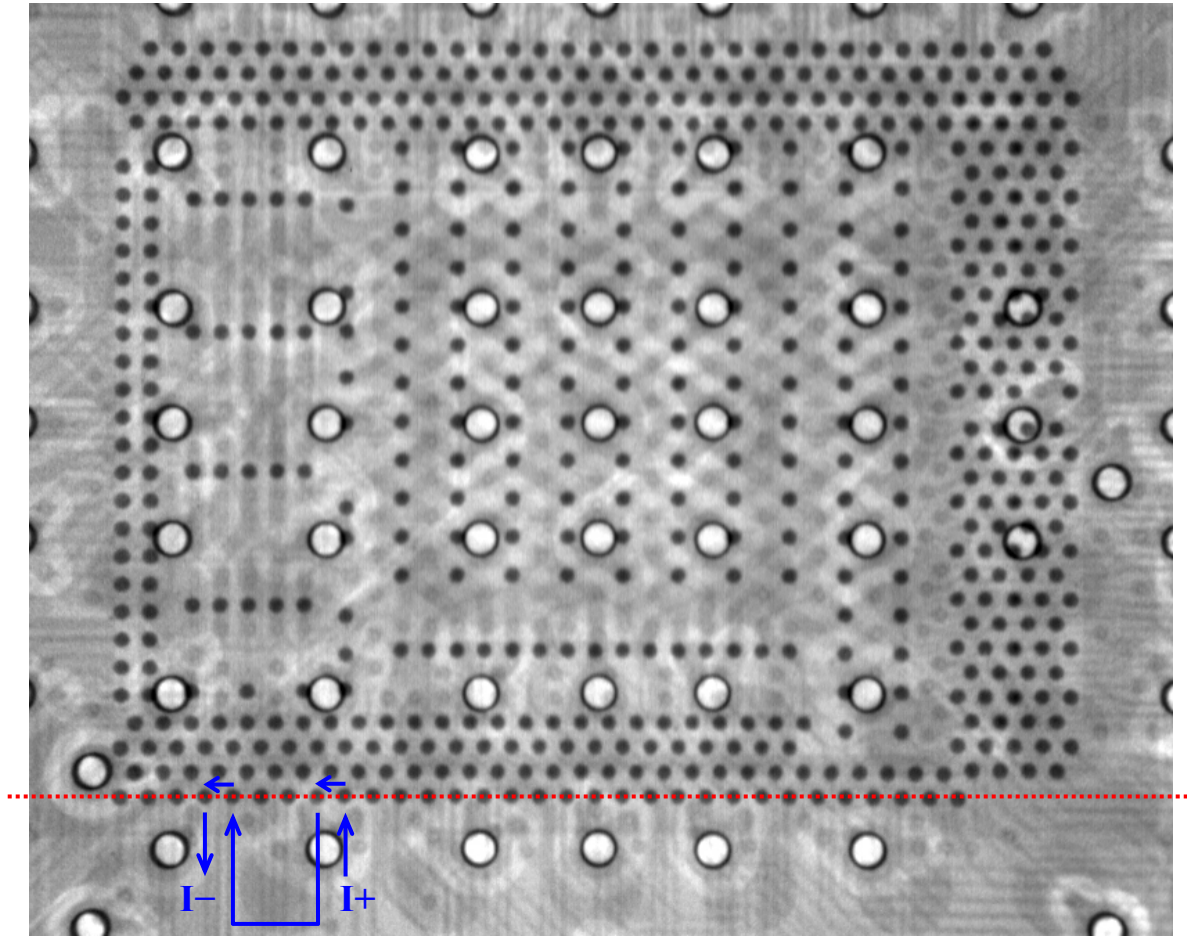


Figure 6.3: X-ray microscope image of solder bump arrays (shown as black solid circles) in a test module. Resistance of two pairs of solder joints (4th, 5th, 8th, and 9th from left in the bottom first row) was monitored during test. 31 solder joints in the bottom first row were cross-sectioned after test. The cross-sectioned plane is marked as a dotted line in red.

6.3 FINITE ELEMENT MODELING

Finite element method (FEM) analyses were performed to determine the temperature distribution in the solder joints. A quarter of a sample was modeled with a 3-D coupled thermal-electric solid element (SOLID69) in ANSYS as shown in Fig. 6.4(a). Figure 6.4(b) shows a solder bump array with substrate traces connected to the 4th, 5th,

8th, and 9th bumps from left in the first row. The die top and the substrate bottom temperatures measured by thermocouples were used as boundary conditions.

To validate the model the resistance of the samples obtained from FEM was compared with that measured by a digital multimeter at the beginning of the test. The resistance was calculated from the voltage drop from the ball-grid-array (BGA) pad connected to the 9th bump to the pad connected to the 4th bump as marked in Fig. 6.4(b). The validation result is depicted in Fig. 6.5. The resistance values determined from measurements and FEM results were in good agreement. The error was less than 7%.

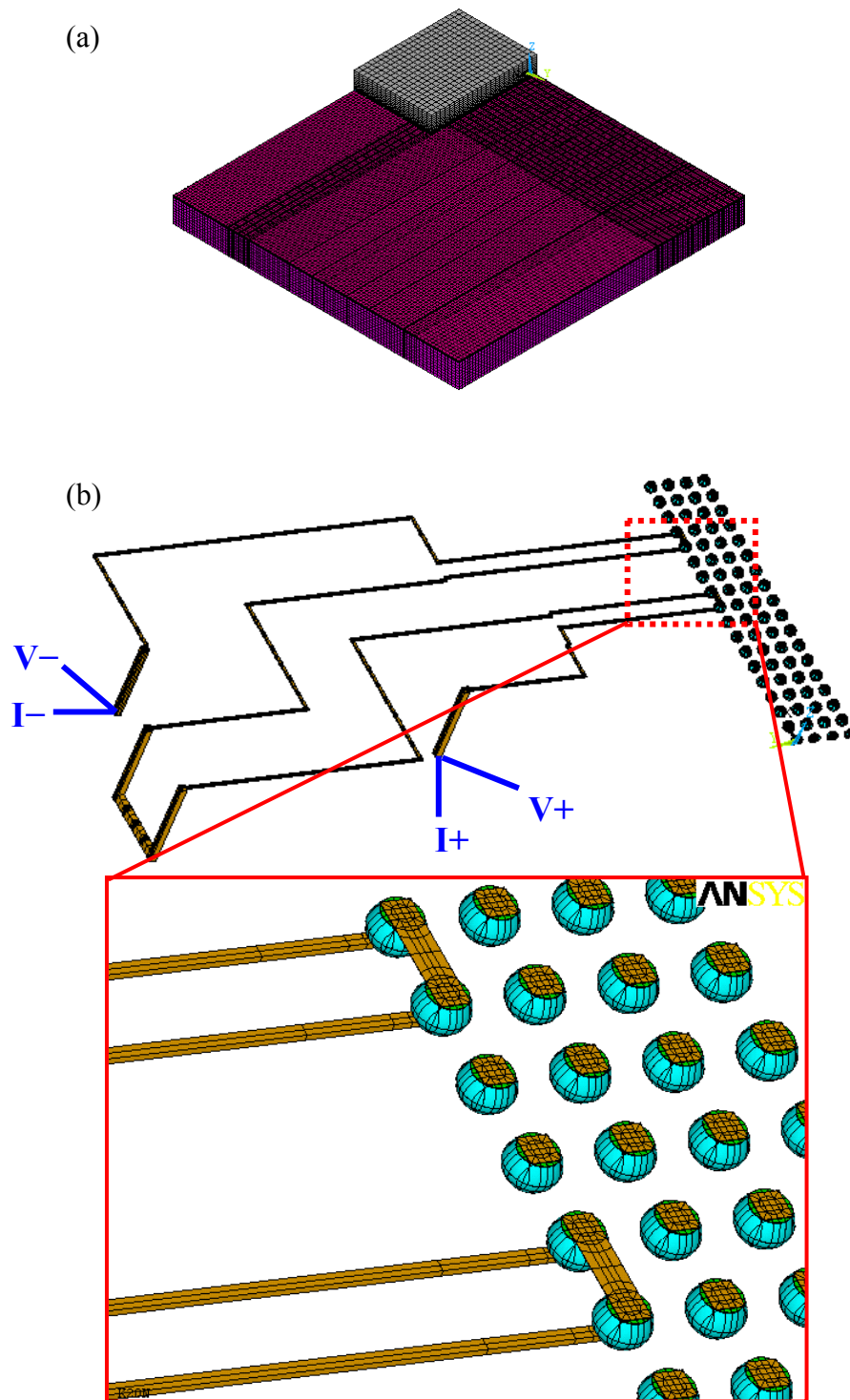


Figure 6.4: Finite element model. (a) Geometry and mesh of test module, and (b) geometry of a bump array and substrate traces.

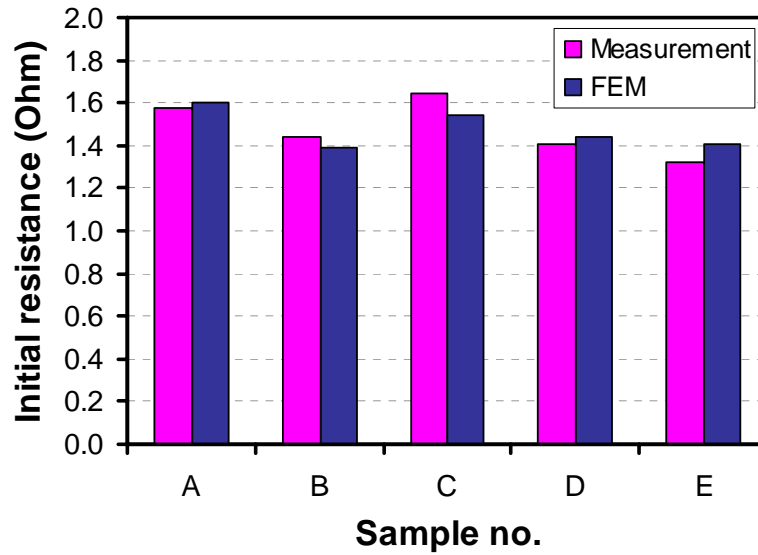


Figure 6.5: Comparison of initial resistances from measurement and FEM as a model validation.

The results of Sample B with two pairs of solder joints subject to a current stressing of 0.5 A are shown in Fig. 6.6. It is seen in Fig. 6.6(a) that the temperature in part of the substrate rose due to the Joule heat generated from the substrate traces. Figure 6.6(b) demonstrates that the metal (Cu) trace was a major source of Joule heat. Yet the trace temperature at the top of the solder joint was much lower than that at the center of the trace. This was because the heat could be dissipated through the solder bump and the substrate trace as the substrate bottom was kept cooled down. Figures 6.6(c) and (d) show contour plots of temperature and temperature gradient in the z -direction in the solder, respectively. Similar to a current density distribution, the temperature gradient was not uniformly distributed, indicating the heat flux crowding at the intersection of the metal trace and the solder joint. As a result, the maximum temperature and temperature gradient were found underneath the inner corner of the contact opening area.

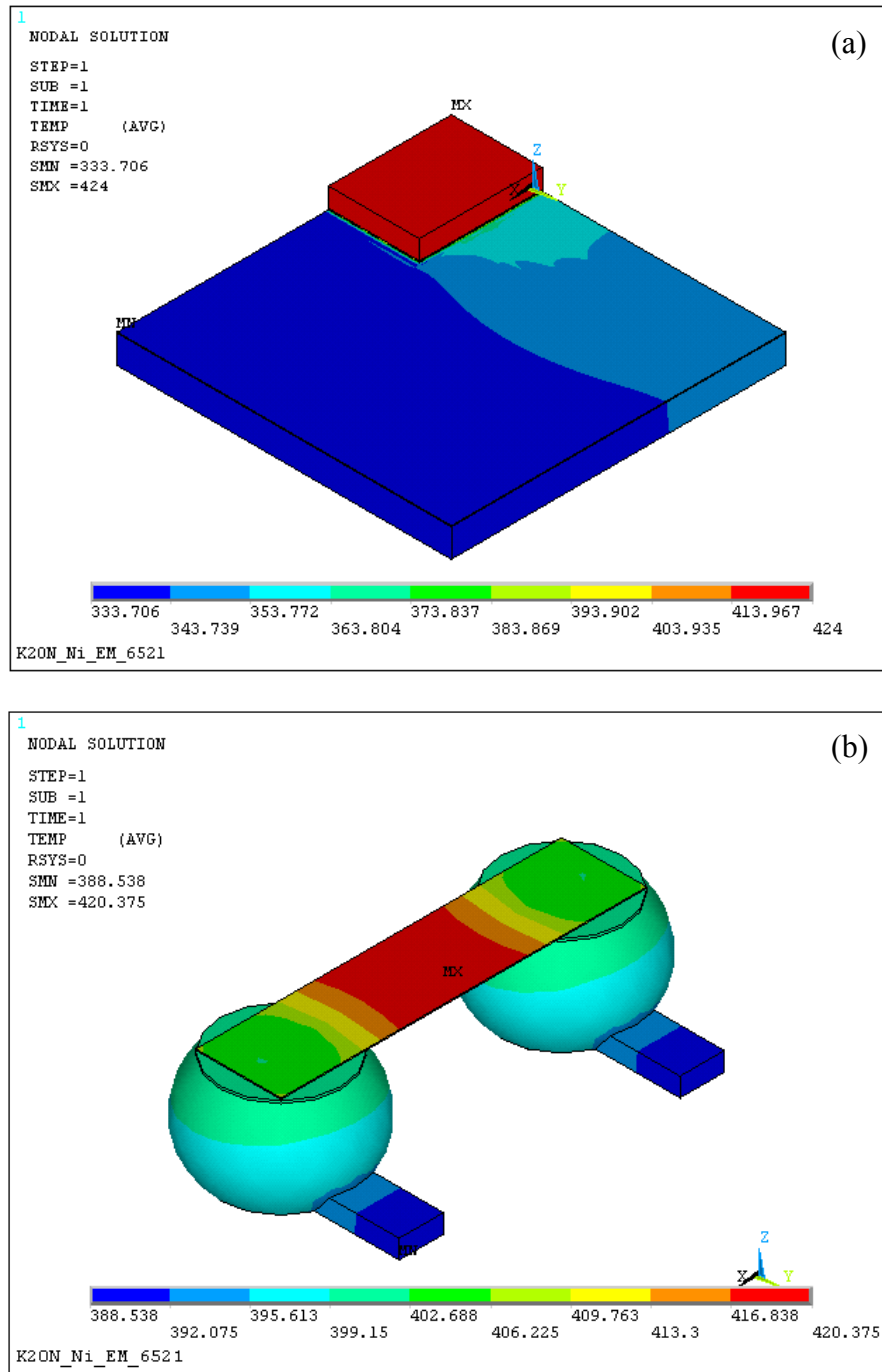


Figure 6.6: Contour plots of Sample B subject to 0.5 A of current stressing. (a)-(c) Temperature contour (in K), and (d) z -component of temperature gradient contour (in K/mm). (a) Package (quarter model), (b) solder joint pair, and (c)-(d) cross-sectioned solder bump pair.

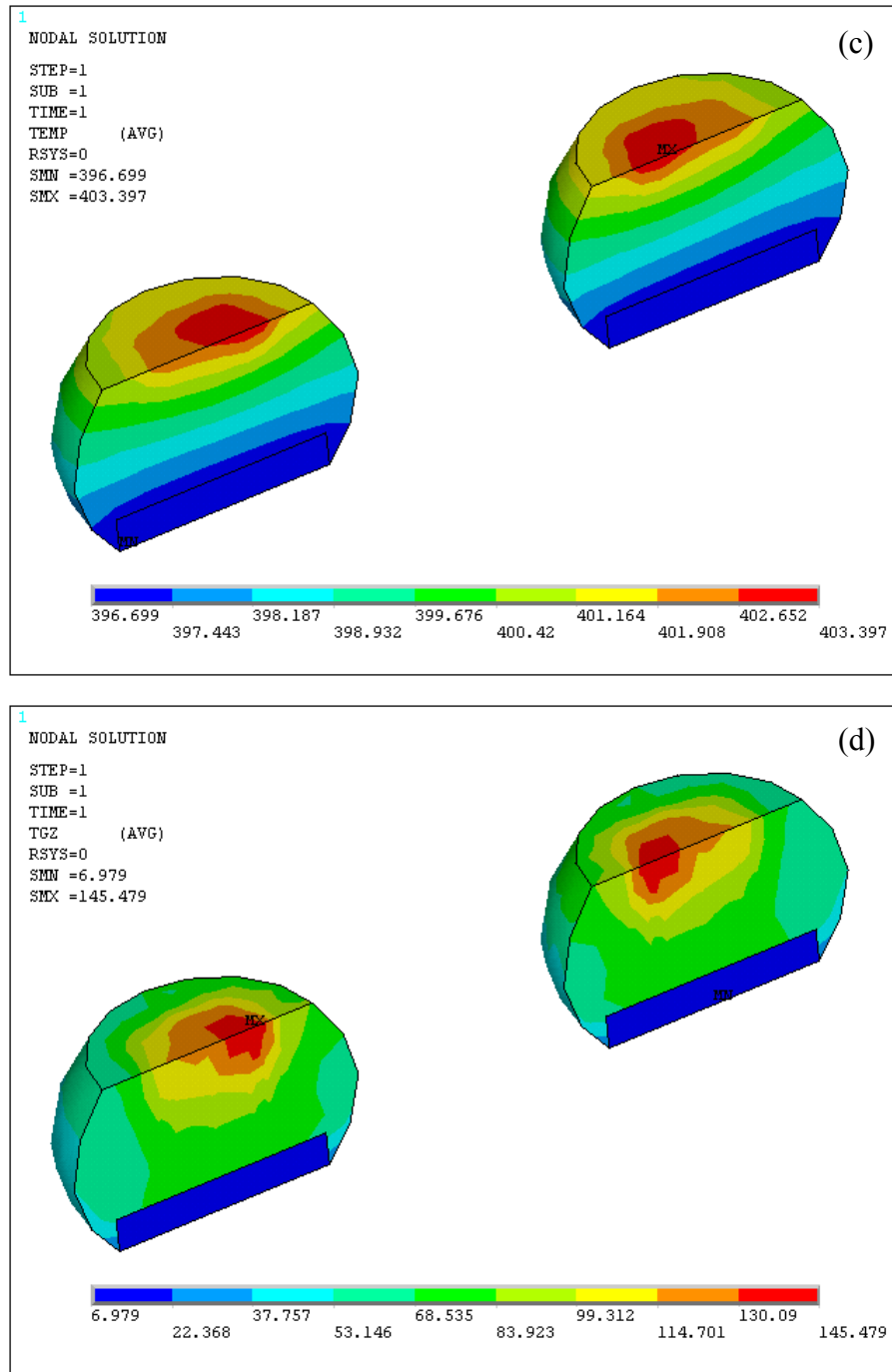


Figure 6.6: (cont'd) Contour plots of Sample B subject to 0.5 A of current stressing. (a)-(c) Temperature contour (in K), and (d) z-component of temperature gradient contour (in K/mm). (a) Package (quarter model), (b) solder joint pair, and (c)-(d) cross-sectioned solder bump pair.

FEM results of all the test conditions are listed in Table 6.2 and plotted in Figs. 6.7 and 6.8. The solder temperature in Sample A was fairly uniform. The temperature of solder joints under current stressing was higher than that without current stressing, due to Joule heating. Nevertheless, the temperature gradients did not differ significantly. Solder joints with thick Cu UBM did not manifest as large of a temperature gradient as those with thin Ni UBM. This is because the height of the solder, which has lower thermal conductivity than Cu, was reduced to accommodate thick Cu in the given space. The temperature gradient in the Ni UBM solders was about 1000 °C/cm, while that in the Cu UBM solders was 700-800 °C/cm.

Table 6.2: Solder joint temperatures determined by FEM.

Sample (UBM)	Type of load	$T_{\text{UBM,top}}$ (°C)	$T_{\text{solder,top}}$ (°C)	$T_{\text{solder,btm}}$ (°C)	$T_{\text{sub,pad,btm}}$ (°C)	$(dT/dz)_{\text{avg,solder}}$ (°C/cm)	$(dT/dz)_{\text{max,solder}}$ (°C/cm)
A (Ni)	Thermal aging	159.5	159.5	158.5	158.5	160	230
B (Ni)	EM (0.5A) + TM	131	130	123.5	123	1070	1530
	TM	129.5	128	121.5	121	1070	1500
C (Ni)	EM (0.8A) + TM	137.5	137	131	131	980	1350
	TM	132.5	131.3	125.5	125.5	950	1310
D (Cu)	EM (0.8A) + TM	140.5	139.5	136.5	136	700	750
	TM	135.5	134.5	131.5	131	700	830
E (Cu)	TM	146	144.5	141	141	810	1080

$T_{\text{UBM,top}}$: temperature at the top of UBM.

$T_{\text{solder,top}}$: temperature at the top of solder bump.

$T_{\text{solder,btm}}$: temperature at the bottom of solder bump.

$T_{\text{sub,pad,btm}}$: temperature at the bottom of substrate pad.

$(dT/dz)_{\text{max,solder}}$: average temperature gradient in solder bump in z (vertical) direction.

$(dT/dz)_{\text{max,solder}}$: maximum temperature gradient in solder bump in z (vertical) direction.

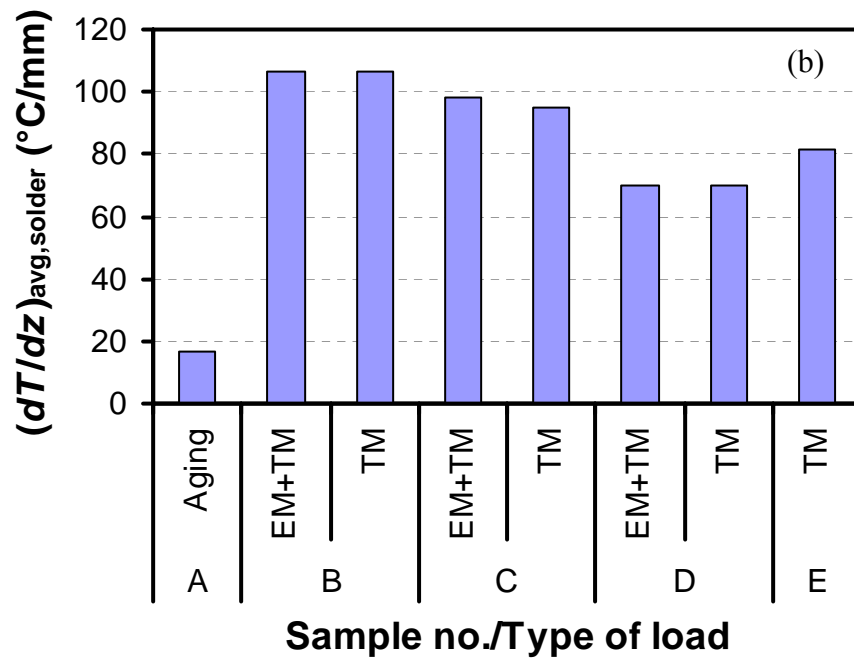
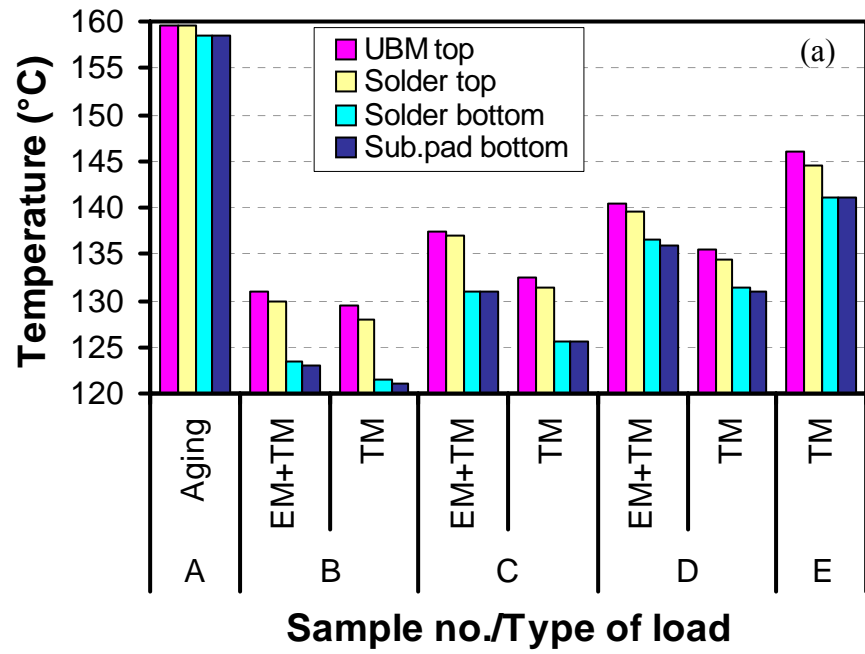


Figure 6.7: FEM results of (a) temperature, and (b) average temperature gradient in a solder bump.

6.4 RESULTS AND DISCUSSION

The test results based on resistance measurements and failure analysis are summarized in Table 6.3. Open failure occurred only in solder joints subject to current stressing. TM load was maintained for a prolonged time after failure of a solder joint under current stressing, because TM-induced damage was not expected to develop as fast as EM damage.

Table 6.3: Summary of TM and EM test results.

Sample	UBM	Type of load	Number of bumps	Result
A	Ni (1 μm)	Thermal aging	31	Not failed until 139 days.
B		EM (0.5A) + TM	4	Open-failed after 116 days.
		TM	27	Not failed until 138 days.
C		EM (0.8A) + TM	4	Open-failed after 6 days.
		TM	27	Not failed until 69 days.
D	Cu (18 μm)	EM (0.8A) + TM	4	Test interrupted after 12 days when V_g reached 20 mV ($\Delta R \sim 50 \text{ m}\Omega$).
		TM	27	Not failed until 48 days.
E		TM	31	Not failed until 48 days.

Figures 6.8-6.14 show backscattered SEM images of cross-sectioned solder joints in the first row of Sample A-E. A solder joint with Ni UBM annealed at 160°C for 139 days is shown in Fig. 6.8. The simulated average temperature gradient was 160 °C/cm. Ni UBM of 1 μm was completely consumed to form Ni_3Sn_4 IMC of $\sim 4 \mu\text{m}$. This was consistent with the fact that when 3 moles of Ni are react with 4 moles of Sn to form 1

mole of Ni_3Sn_4 , the ratio of volume of Ni_3Sn_4 to Ni is approximately 3.8 (see Table 4.1). Still, the resistance increase was not substantial.

Figure 6.9 shows solder joints with 0.5 A of current stressing in Sample B. Figures 6.9(a) and (c) show solder joints in which electrons flowed from the substrate side to the die side, while in Figs. 6.9(b) and (d) electrons flowed from the die side to the substrate side. The 9th joint (Fig. 6.9(d)) has failed by complete dissolution of UBM. In the 5th joint (Fig. 6.9(b)), UBM was depleted leading to a portion of the solder dewet from the Al pad. It is interesting to notice that voids were found in the UBM of the 8th joint (Fig. 6.9(c)). Under a typical EM condition, vacancies move toward the cathode side so voids are not formed at the anode side. Thus, those voids might be induced by TM. However, it could not be confirmed whether those voids were initiated while a current stressing was present or after it was stopped.

Solder joints under TM without current stressing in Sample B are shown in Fig. 6.10. Voiding was observed in 6 solder joints (Figs. 6.10(a)-(f)) out of 27. The average temperature gradient in the solder bump was 1070 °C/cm according to the FEM result as shown in Table 6.2 and Fig. 6.7(b). Ni was found to migrate toward the cold end. The rest of 21 solder joints had no noticeable TM damage as shown in Fig. 6.10(g).

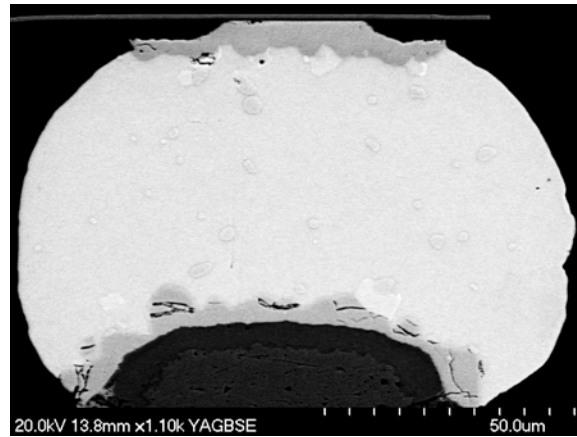


Figure 6.8: Backscattered electron micrograph of a solder joint with Ni UBM in Sample A after 139 days of thermal aging.

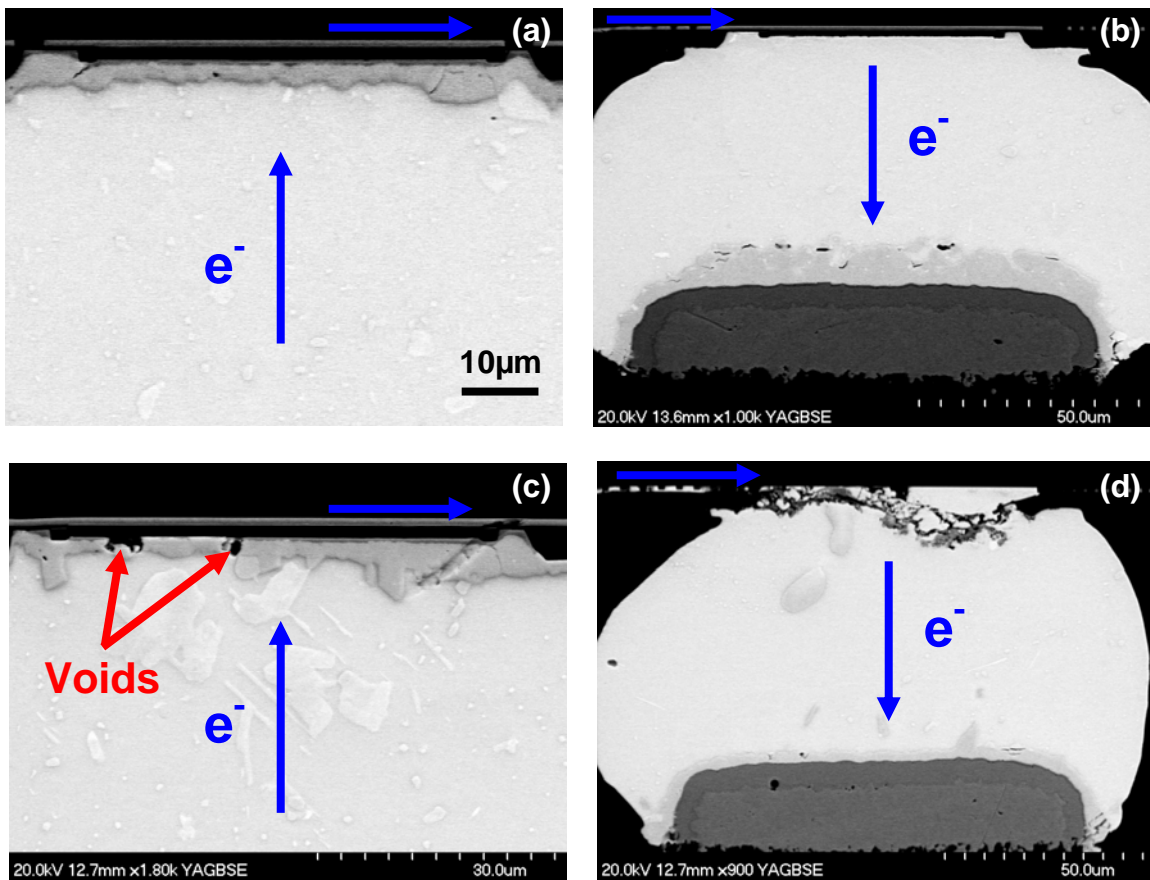


Figure 6.9: Solder joints with Ni UBM subject to a current stressing of 0.5 A in Sample B. (a) 4th, (b) 5th, (c) 8th, and (d) 9th solder joint.

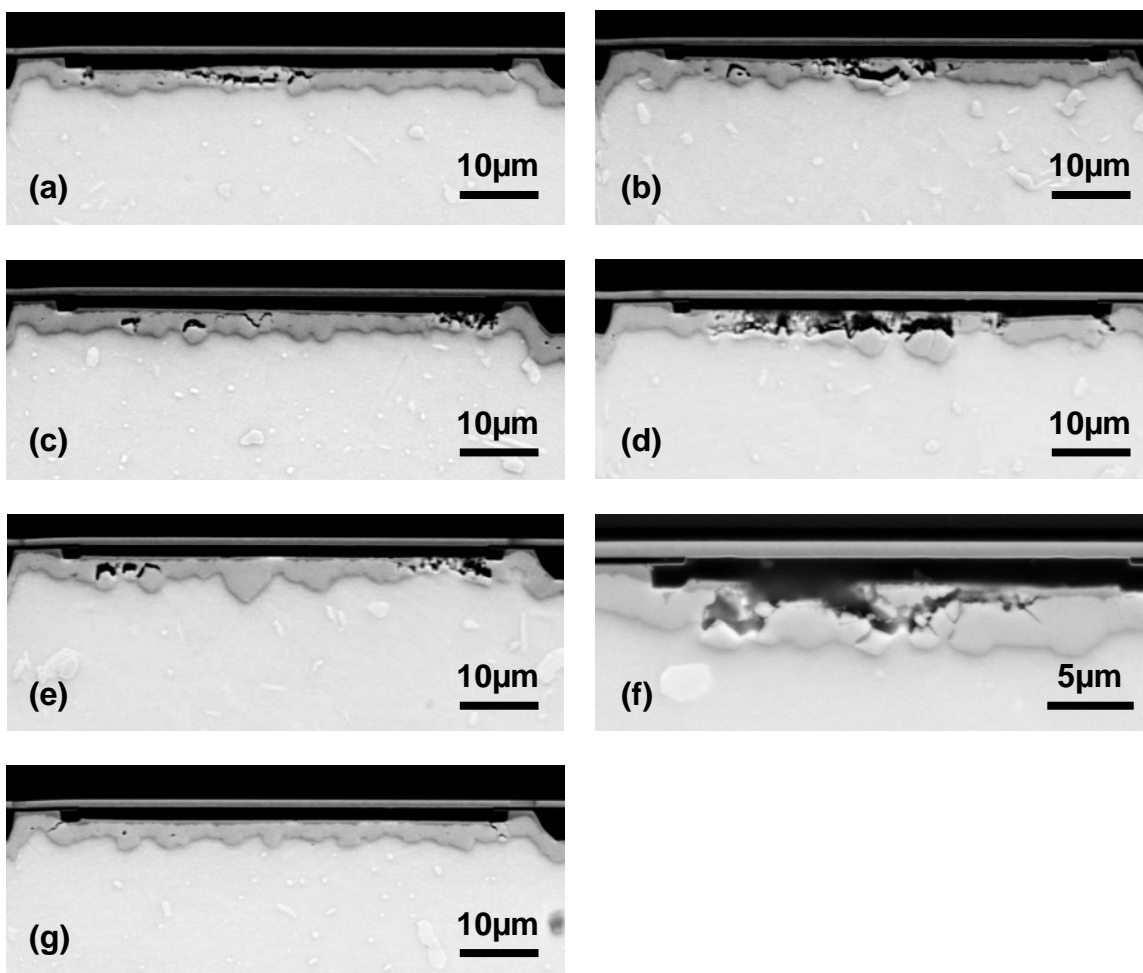


Figure 6.10: Solder joints with Ni UBM in Sample B after 138 days of TM stressing. (a)-(f) show 6 solder joints with voids. The other 21 solder joints under TM stressing only had no voids as shown in (g).

Similar phenomena were observed in Sample C. Figure 6.11 shows 4 solder joints with Ni UBM subjected to a current stressing of 0.8 A. The average temperature gradient in the solder bump was determined to be 980 °C/cm by FEM (Table 6.2 and Fig. 6.7(b)). Similar to the case of Sample B, all the Ni in the UBM was depleted (Fig. 6.11(b)), followed by open failure (Fig. 6.11(d)). Under a large temperature gradient, Ni was thought to be a dominant diffusing species as EM of Sn atoms could be somewhat suppressed by TM because $Q_{\text{Sn}}^* < 0$ [6.14]. In solder joints where electrons traveled to the die side (Figs. 6.11(a) and (c)), no voids were observed although the TM load was kept applied for 63 more days after the current stressing was stopped.

Figure 6.12 shows selected solder joints without current stressing in Sample C. According to the FEM result, the average temperature gradient in the solder bump was 950 °C/cm under this condition for Sample C. 7 solder joints contained voids (Figs. 6.12(a)-(g)), while the other 20 solder joints were not damaged by TM as seen in Fig. 6.12(h). Voiding occurred in UBM and IMC, similar to Sample B.

TM voiding processes were found to be different from EM voiding. EM voids in thin Ni UBM were usually initiated at a current crowding region followed by propagation through the IMC/solder interface as discussed in Chapters 3 and 5. In contrast, the dependence of initial TM voiding location on the heat flux crowding region was not strong. Also, TM voids were observed in UBM and IMC instead of at the IMC/solder interface. This could be related to the different direction in which Sn atoms migrate under EM or TM. Under current stressing, Sn atoms migrate along with electron wind as the effective charge number, Z^* , for Sn is negative. This can cause voiding at the IMC/solder interface. Under TM, however, it was reported that Sn migrated toward the hot end ($Q^* < 0$) in Sn-3.5Ag solder joints [6.14]. Thus voiding at the IMC/solder interface is not expected. Instead, voiding occurs in UBM and IMC as Ni atoms migrate to the cold end.

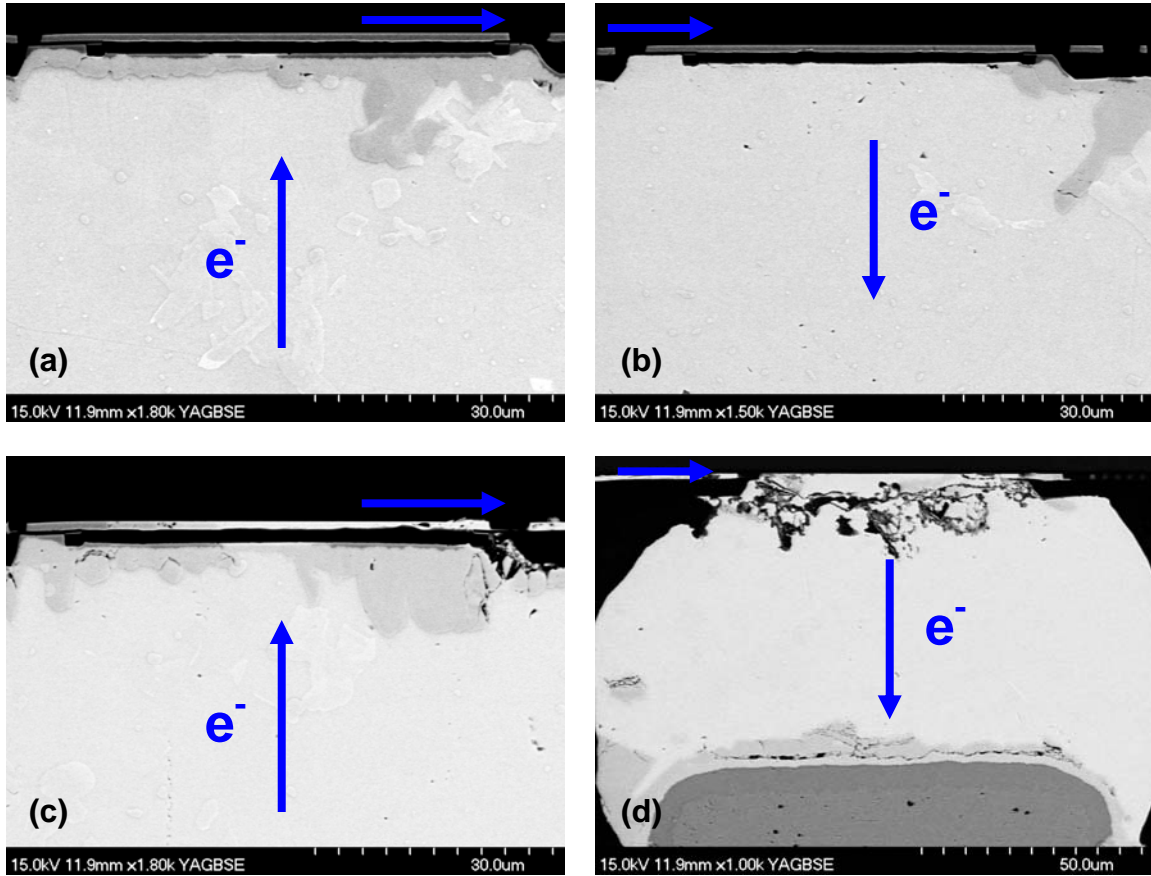


Figure 6.11: Solder joints with Ni UBM under current stressing of 0.8 A in Sample C. (a) 4th, (b) 5th, (c) 8th, and (d) 9th solder joint.

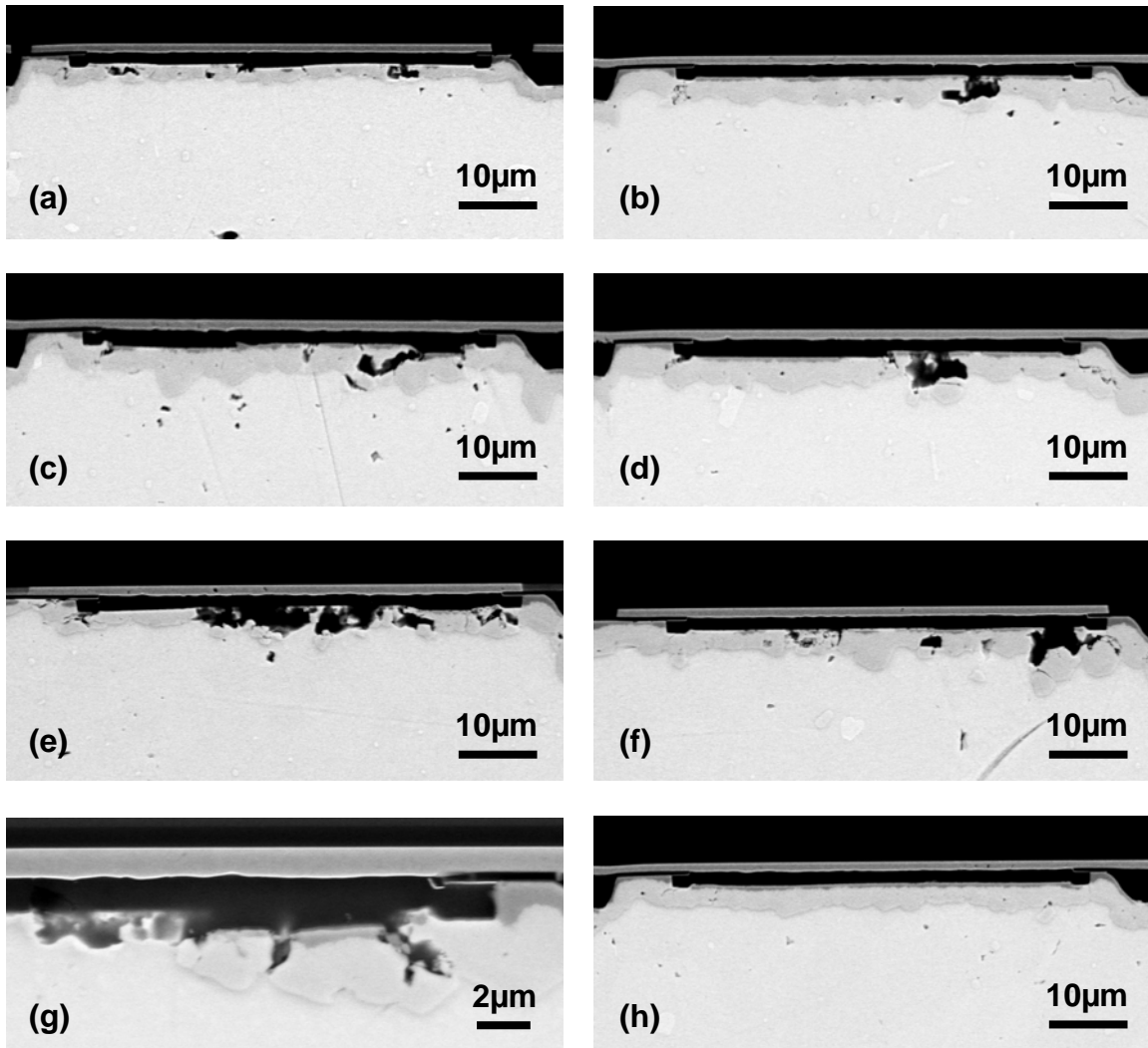


Figure 6.12: Solder joints with Ni UBM in Sample C after 69 days of TM stressing. (a)-(g) show 7 solder joints with voids. The other 20 solder joints without current stressing had no voids as shown in (h).

Solder joints with Cu UBM in Sample D are shown in Fig. 6.13. Figures 6.13(a)-(d) display 4 solder joints which were subject to a current stressing of 0.8 A for 12 days. The applied current was interrupted when ΔR reached $\sim 50 \text{ m}\Omega$ to examine the intermediate stage of damage evolution. The average temperature gradient in the solder bump was obtained to be $700 \text{ }^\circ\text{C}/\text{cm}$ under current stressing by using FEM. The morphology changes indicate that the effect of TM was not significant. When electrons flowed to the die side, IMCs were accumulated on the die side as seen in Fig. 6.13(c). In solder joints in which electrons passed toward the substrate side (Figs. 6.13(b) and (d)), voids were found at the Cu_6Sn_5 /solder interface while Cu_6Sn_5 grew on both die and substrate sides. These phenomena are similar to those in typical EM tests without a large temperature gradient as discussed in Chapter 3. Also in all the other solder joints without current stressing, morphology changes were minimal without significant TM damage, as shown in Fig. 6.13(e).

In contrast, noticeable morphology changes were observed in some of the solder joints in Sample E. All the solder joints in Sample E were subject to TM stressing only. As listed in Table 6.2, the average temperature gradient in the solder bump was $810 \text{ }^\circ\text{C}/\text{cm}$. Also, the solder temperature was about 10°C higher than Sample D. Among 31 solder joints in the first row, the morphology of 27 joints did not change significantly as shown in Fig. 6.14(e). In the other 4 solder joints displayed in Figs. 6.14(a)-(d), irregular UBM dissolution and IMC formation was observed. It is clear that Cu migrated from the hot end (die side) to the cold end (substrate side). Chen *et al.* also observed TM of Cu toward the cold end in Sn-3.5Ag solders, where voids were found between the $5 \text{ }\mu\text{m}$ -Cu UBM and IMC [6.13]. In this study, however, TM-induced voids were not found in solder joints with thick Cu UBM. This could be ascribed to the sufficient amount of Cu in thick UBM as well as the reverse flow of Sn against the temperature gradient. The

irregular morphology of UBM dissolution and IMC formation can be associated with the grain orientation of Sn. Metallic Sn (β -Sn) is highly anisotropic because it has a body centered tetragonal (BCT) structure. For interstitial fast diffusers such as Au, Ag, Cu, and Ni, the diffusivity in the direction parallel to the c -axis, D_{\parallel} , has shown to be much faster than that perpendicular to the c -axis, D_{\perp} [6.15-6.17]. For example, $D_{\parallel, \text{Cu}}$ is about 43 times higher than $D_{\perp, \text{Cu}}$, and $D_{\parallel, \text{Ni}}$ is about 3.0×10^4 times higher than $D_{\perp, \text{Ni}}$ at 150°C. Therefore, if a grain of Sn matrix adjacent to UBM is oriented in a way that the c -axis is aligned parallel to the solder height direction, the UBM component can be dissolved into the solder very fast. This could account for the nonuniform UBM dissolution and the different dissolution rate between solder joints. Recently, Lu *et al.* also reported that when the c -axis was aligned parallel to the electric current direction, Ni/Cu UBM was dissolved quickly into the Sn-based solder leading to early failure [6.18].

To investigate the different effects of TM on Sample D and E, recall the following flux equation for TM:

$$J_{\text{TM}} = -C \frac{D}{kT} \frac{Q^*}{T} \frac{dT}{dx} = -\frac{CD_0 Q^*}{kT^2} \frac{dT}{dx} \exp\left(-\frac{Q}{kT}\right) \quad (6.3)$$

where J is the atomic flux, C the atomic concentration per volume, D the diffusivity, D_0 the pre-factor, k the Boltzmann constant, T the absolute temperature, Q^* the heat of transport, and Q the activation energy for diffusion. Taking $T = T_{\text{solder, top}}$ in Table 6.2 and $Q = 1.0$ eV, the ratio of J_{TM} in Sample E to Sample D was found to be ~ 2.1 . Thus, Sample D would require 48 more days of TM stressing to have equivalent damage to that in Sample E.

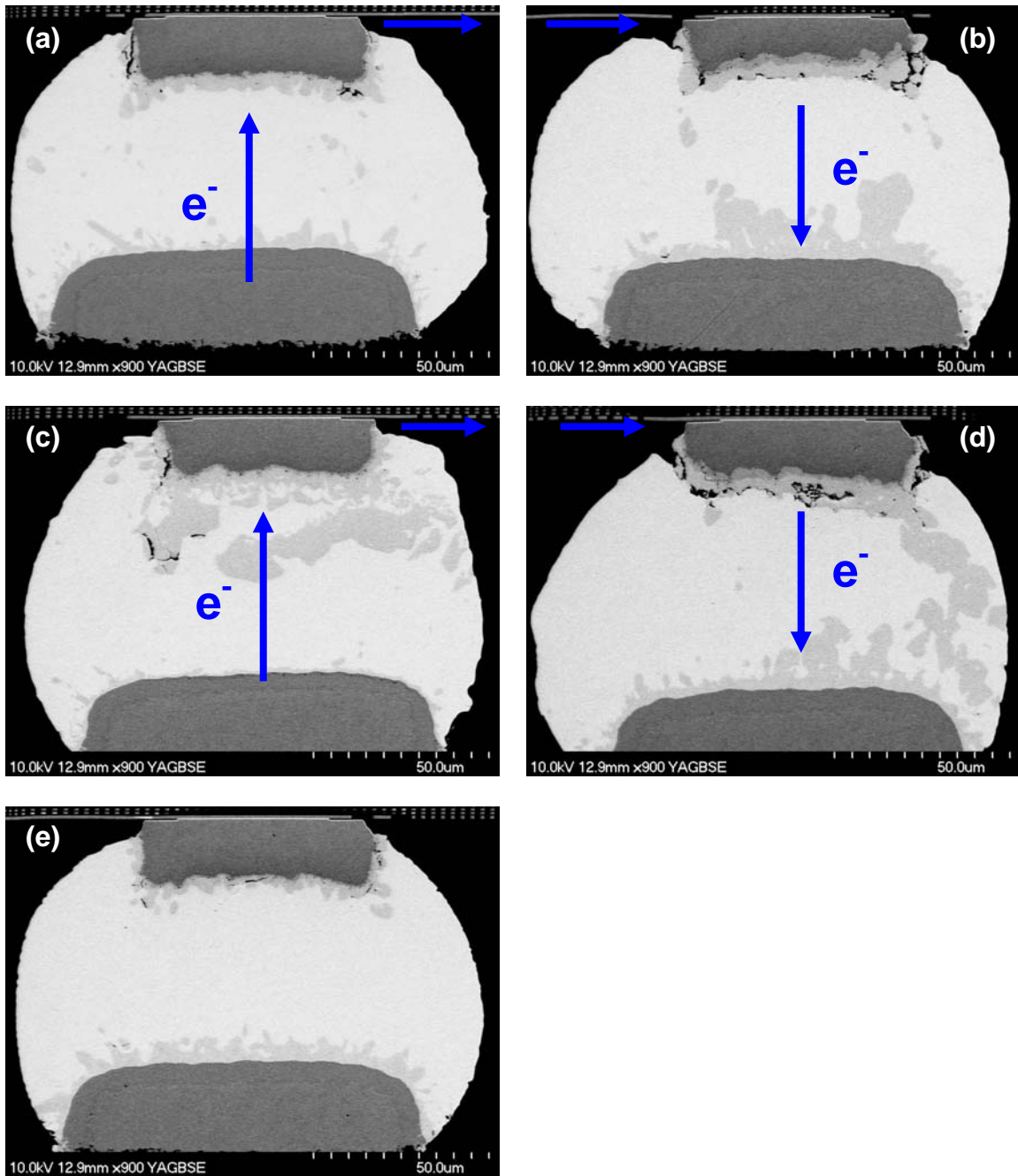


Figure 6.13: Solder joints with Cu UBM (a)-(d) under current stressing of 0.8 A for 12 days, and (e) under TM stressing for 48 days, in Sample D. (a) 4th, (b) 5th, (c) 8th, and (d) 9th solder joint.

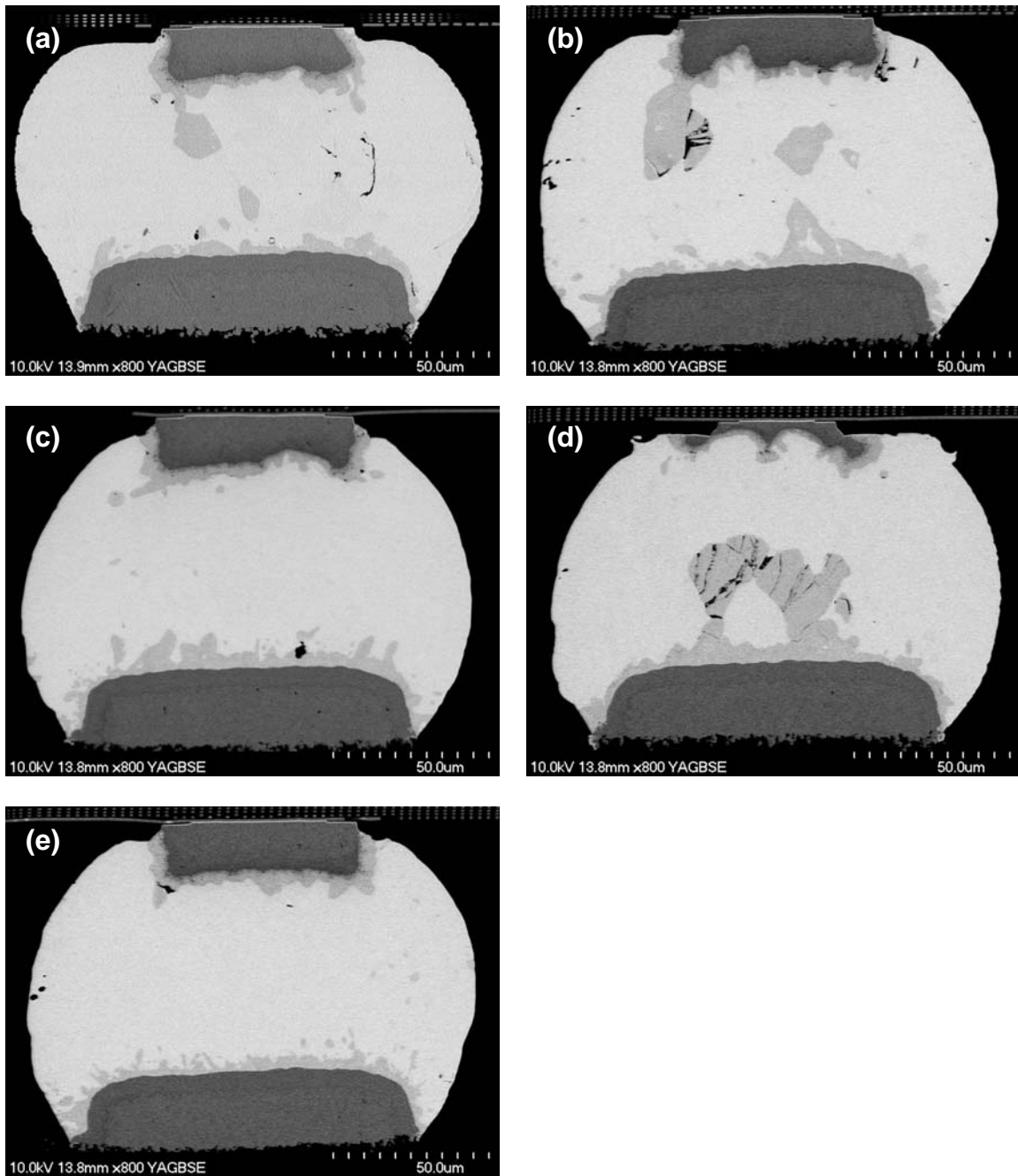


Figure 6.14: Solder joints with Cu UBM in Sample E after TM stressing of 48 days. (a)-(d) show 4 solder joints with UBM dissolution. The other 27 solder joints had no noticeable UBM dissolution as shown in (e).

Because solder joints under current stressing in Sample B, C, and D also experienced a temperature gradient, the effects of EM and TM should coexist. It is important to estimate the relative contribution of TM to the solder joint failure. With the lifetime data for Sample B, C, and D, the cumulative distribution of failure (CDF) or probability of failure can be estimated. The CDF values would be very small if the effect of TM is significant. First, the median-time-to-failure (MTTF or t_{50}) at the test condition of each sample is deduced. From the Black's equation,

$$\frac{t_{50,2}}{t_{50,1}} = \left(\frac{j_1}{j_2} \right)^n \exp \left[\frac{Q}{K} \left(\frac{1}{T_2} - \frac{1}{T_1} \right) \right], \quad (6.4)$$

where A is a constant, j is the current density, n is the current density exponent, Q is the activation energy, k is the Boltzmann constant, and T is the absolute temperature. The subscripts 1 and 2 denote a reference and a different test condition, respectively. Second, the Z -value for the standard log-normal distribution is obtained as

$$Z = \frac{\log TTF - \log t_{50,2}}{\sigma}, \quad (6.5)$$

where TTF is the time-to-failure of a sample, and σ is the standard deviation of the logarithm of TTFs. Accordingly, CDF values are calculated from the Z -value based on the normal distribution statistics.

The TTFs of Sample B, C, and D are 2714 h, 120 h, and 300 h, respectively, based on the first resistance criterion. The TTF of Sample D was estimated from the resistance trace because the applied current was stopped before it failed. The temperature at the top of solder bump was taken as the test temperature. The experimental data

discussed in Chapters 3 and 5 were used as reference test conditions (T and j) and data (t_{50} and σ). Also, the activation energies and current density exponents for Cu and Ni UBM obtained in Chapter 3 were utilized. Accordingly, the CDF values obtained for Sample B, C, and D were 59%, 34%, and 45%. All of them were relatively close to 50% of CDF. This indicates that the effect of TM did not have a significant effect on the EM lifetime even under the very large temperature gradient.

In general, the relative atomic flux by EM and TM can be compared by utilizing the following flux relation:

$$J_{\text{EM}} / (CD_0 / k) = \frac{Z^* e \rho j}{T} \exp\left(-\frac{Q}{kT}\right), \quad (6.6)$$

$$J_{\text{TM}} / (CD_0 / k) = \frac{Q^*}{T^2} \left| \frac{dT}{dx} \right| \exp\left(-\frac{Q}{kT}\right). \quad (6.7)$$

In this study, $j = 4 \times 10^4$ A/cm² and $dT/dx \sim 10^3$ K/cm. For solder joints, it is also reasonable to take $Z^* \sim 10$, $\rho \sim 10^{-7}$ Ω m, and $Q^* \sim 0.25$ eV. Figure 6.15 plots Eqs. (6.6) and (6.7), and $F_{\text{TM}}/F_{\text{EM}}$ ($=J_{\text{TM}}/J_{\text{EM}}$) as a function of temperature using the above parameters. The EM flux was always predominant over the TM flux even with the very large temperature gradient. The relative effect of TM increased with decreasing temperature. Still, the ratio was less than a quarter at 0°C. Since typical current density and temperature gradient for solder joints in a field condition are $\leq 10^4$ A/cm² and ≤ 300 K/cm [6.19], the relative ratio shown in Fig. 6.15 will still hold at the field condition unless the above estimated parameters need to be corrected.

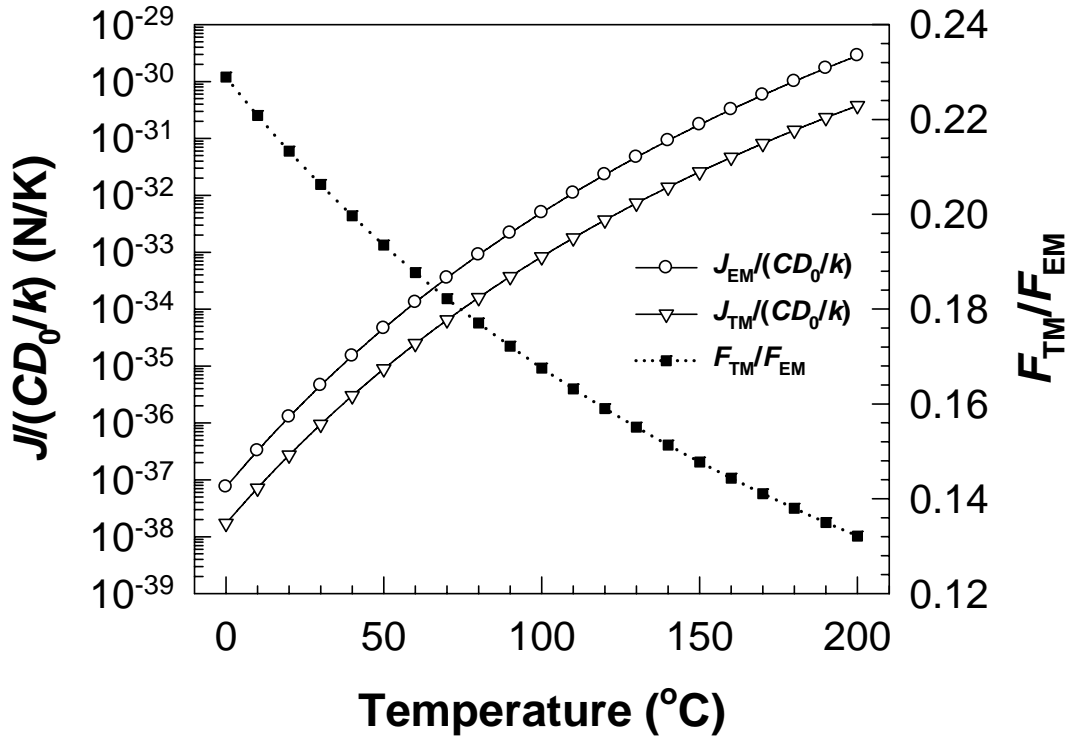


Figure 6.15: Estimated atomic flux driven by EM and TM, and the ratio of corresponding driving forces as a function of temperature for solder joints.

6.5 SUMMARY

Large temperature gradients were created in test modules in order to investigate the TM reliability of Pb-free solder joints. FEM was utilized to estimate the temperature gradient in solder joints with validation against the resistance measurement data. TM damage was observed when the average temperature gradient was larger than 950°C/cm and 810°C/cm in solder bumps with Ni UBM and Cu UBM, respectively, at a given testing time. Voids were found in Ni UBM solders while UBM was dissolved by TM without void formation in Cu UBM solders, although TM damage evolution was

statistically scattered. This indicates that Ni and Cu atoms migrate toward the cold end, i.e. $Q^* > 0$. However, it was found that the rate of TM was several times slower compared to EM, resulting in little impact on EM failure lifetime.

Chapter 7: Conclusions and Future Work

7.1 CONCLUSIONS

Flip chip packages are mainly used for high-end devices such as CPUs, GPUs, and high performance ASICs because of their advantages of high I/O density and superior electrical performance. As recent trends in semiconductor devices and packages are toward multi-functionality, smaller form factor as well as higher performance, the application of flip chip technology has gained momentum. Flip chip solder bumping processes can also be applied in novel packaging concepts including SiP and 3D integration. Therefore, long-term reliability assessment for solder joints such as EM and TM is crucial to ensure the devices to function properly for a desired lifetime. In addition, the recent implementation of Pb-free solders added more reliability concerns due to the insufficient knowledge base.

This study aimed to investigate EM and TM reliability of Pb-free solder joints in flip-chip or advanced packaging applications. Thick Cu UBM and thin Ni UBM structures were adapted in the test vehicle. First, a series of EM tests were performed to obtain essential EM parameters, including activation energy (Q) and current density exponent (n), which are associated with a lifetime prediction model. A failure criterion, named first resistance jump criterion, was newly introduced based on resistance traces and damage evolution, which was found to be more reasonable than an open-failure criterion. Since the direct measurement of solder joint temperature was not possible, FEM was utilized to simulate the temperature of solder joints under current stressing. After the Joule heating effect was taken into account, EM activation energies and current density exponents were determined. For solder joints with Cu UBM, $Q = 1.0$ eV and $n = 1.5$; for

Ni UBM solders, $Q = 0.9$ and $n = 2.2$. Failure analysis of solder joints at different stages of EM voiding revealed that in solder joints with Cu UBM, voids initiated at the Cu_6Sn_5 /solder interface but the voiding location at the later stage moved near the $\text{Cu}_3\text{Sn}/\text{Cu}_6\text{Sn}_5$ interface as IMCs and voids continued to grow. In solder joints with Ni UBM, initial EM voiding was observed at the current crowding location at the Ni_3Sn_4 /solder interface, followed by void propagation along this interface. Important factors in controlling EM reliability of Pb-free solder joints were found to be UBM dissolution with extensive IMC growth for thick Cu UBM solders, and current crowding for thin Ni UBM solders.

IMC growth in Pb-free solder joints with and without current stressing was discussed. The growth rate was found to follow the parabolic growth law when current stressing was not present. Under high current stressing, the linear growth law was observed for the growth of Cu_6Sn_5 and Ni_3Sn_4 . For Cu UBM solders, the apparent activation energy for the IMC growth was in good agreement with the aforementioned activation energy of EM. This supports that the EM voiding mechanism for Cu UBM solders was closely related to the IMC growth driven by interdiffusion. In contrast, the apparent activation energy for the growth of Ni_3Sn_4 was higher than the EM activation energy for Ni UBM solders. It was suggested that the EM failure in the Ni UBM solders could be associated with more than one mass transport mechanism in addition to the interdiffusion of Ni and Sn. It was also demonstrated by using FEM that EM-enhanced IMC growth led to a large hydrostatic tension in IMC layers due to the volumetric shrinkage accompanied by IMC formation. This condition could accelerate the void growth once voids were initiated by EM in that region.

The effect of current crowding on EM reliability of thin Ni UBM solder joints was studied by conducting EM tests on different Ni UBM thicknesses. The current

density distribution was obtained by FEM to supplement the experimental results. The EM lifetime was quantitatively correlated with the maximum current density occurring at the top of solder bump, $j_{\max, \text{solder}}$. Accordingly, $j_{\max, \text{solder}}$ was suggested to be used for the current density term in Black's equation. The current density exponent determined in this manner was 1.9. Effects of metal trace design on the current crowding were also examined by FEM, showing that the metal trace design is an important consideration to control the current crowding effect. Wide and thick traces made of Cu might be the best choice in the absence of major modifications of the current geometry and process. Placing a small hole in front of the entrance to passivation opening could be an additional option to further lower $j_{\max, \text{solder}}$, provided that a local hot spot in the vicinity of the hole did not significantly increase the solder temperature. FEM results of solder joint scaling showed that j_{\max} did not increase as much as j_{avg} when solder joints were scaled down. In other words, the current crowding became less prominent while j_{avg} was increased. It was also found that down-scaling of the diameter of UBM did not have a significant effect on the current crowding. Instead, current crowding was mainly controlled by the cross-sectional area of the metal trace and the diameter of the passivation opening.

During EM tests significant Joule heating can be generated from the metal trace on the die side, which results in temperature gradient in solder joints. If the temperature gradient is large enough to cause substantial TM, the EM reliability data may not be reliable. To examine TM issues in Pb-free solder joints as well as to define relative significance of TM over EM, large temperature gradients were induced in test modules. FEM was performed to estimate the temperature gradient in solder joints. In solder bumps with Ni UBM, TM-induced voids damage was observed in UBM and IMC layers when the average temperature gradient was larger than 950°C. In Cu UBM solders, UBM dissolution and IMC formation were induced by TM with the average temperature

gradient in a bump above 810°C/cm. Voiding by TM was not observed in Cu UBM solders. It was found that in solder joints, the atomic flux by TM was still several times slower compared to EM. This resulted in little impact of TM on EM failure lifetime even under a temperature gradient in solder bumps of the order of 10³°C/cm.

7.2 SUGGESTIONS FOR FUTURE WORK

Although this study tackled various issues associated with EM and TM reliability of Pb-free solder joints, there are still numerous interesting problems to be addressed, which include but not limited to:

- *Revisiting Black's equation:* Although Black's equation was proposed decades ago for EM failure of thin metal lines [7.1], it has been adopted for solder EM failure as well because of its simplicity and flexibility. However, because solder joints are much more complex material system than interconnect metal lines, more comprehensive research needs to be performed for in-depth understanding of void nucleation and growth kinetics. In particular, the physical meaning of the current density exponent in solder EM has not been fully clarified.
- *Interdiffusion model with current stressing:* A multi-phase diffusion model was recently developed by Chao to simulate EM-enhanced IMC growth [7.2]. This model is based on a vacancy diffusion mechanism in all phases. Since Cu and Ni are fast diffusers in solder by an interstitial mechanism, appropriate modification of this model will be invaluable.
- *IMC growth and failure mechanism at low current density:* The kinetic model for EM-enhanced IMC growth showed that IMC growth kinetics will follow t^n ($0.5 < n < 1$) dependence if a current density is low [7.2]. Therefore, damage evolution and failure mechanism need to be examined at this condition to find

out if they are different from those at high current density. Accelerated testing can lead to a wrong reliability prediction if the failure mechanism at an accelerated test condition is different from that at a field condition. A daisy-chain structure can be employed to reduce the testing time.

- *Thermomechanical reliability*: Extensive IMC growth causes solder bumps to be stiffer and more brittle. This could affect the thermomechanical reliability of the solder joints or package. For example, it can intensify chip-package interaction (CPI) when a significant thermal load is present.
- *Systematic study on TM reliability*: Although the contribution of TM to solder joint failure may not be as significant as EM, it will be interesting to study TM reliability systematically as has been conducted for EM reliability. Temperature gradient over 10^3 °C/cm should be necessary to observe failure by TM in a reasonable time frame. A constant temperature control on the die top and the substrate bottom is important. A thermoelectric cooler (TEC) can be employed to accomplish this goal. Not many package samples are necessary to collect lifetime statistics because all the bumps in a package can be used in a test as far as the resistance of each bump can be monitored.
- *Effect of Sn grain size and orientation on EM reliability*: An IBM group reported two failure mechanisms of bulk Pb-free solder joints under current stressing, which depended on the orientation of Sn grains [7.3]. However, a similar study on flip-chip solder joints has not been reported yet. Correlation of EM damage evolution and lifetime with Sn grain size and orientation will be an interesting research topic, which can be studied by utilizing electron backscattered diffraction (EBSD).

Appendix A: Thermal-Electric Analysis Using Finite Element Method

Joule heating analysis in this study was performed using finite element software ANSYS. The basic information on the finite element method (FEM) used for coupled thermal-electric analyses is introduced based on ANSYS help manuals.

A.1 INTRODUCTION

Heating occurs in a resistive conductor carrying an electric current. Joule heating is proportional to the square of the current, and is independent of the current direction. Joule heating is also present and accounted for at the contact interface between bodies in inverse proportion to the contact electric conductance properties.

A.2 GOVERNING EQUATIONS

The electric field in a conducting material is governed by Maxwell's equation of conservation of charge. Assuming steady-state direct current, the equation reduces to

$$\int_S \vec{J} \cdot \vec{n} dS = \int_V r_c dV, \quad (\text{A.1})$$

where V is any control volume whose surface is S , \vec{n} is the outward normal to S , \vec{J} is the electrical current density, and r_c is the internal volumetric current source per unit volume.

The flow of electrical current is described by Ohm's law:

$$\vec{J} = \vec{\sigma}^E \cdot \vec{E} = -\vec{\sigma}^E \cdot \frac{\partial \varphi}{\partial x}, \quad (\text{A.2})$$

where $\vec{E}(x)$ is the electrical field intensity, defined as the negative of the gradient of the electrical potential $\vec{E} = -\partial\varphi/\partial x$, φ is the electrical potential, $\vec{\sigma}^E(\theta, f^\alpha)$ is the electrical conductivity matrix, θ is the temperature, and $f^\alpha (\alpha = 1, 2, \dots)$ are predefined field variables. Ohm's law assumes that the electrical conductivity is independent of the electrical field. The coupled thermal-electric problem is nonlinear when the electrical conductivity depends on temperature.

Using Ohm's law in the conservation equation, written in variational form, provides the governing equation of the finite element model:

$$\int_V \frac{\partial \delta \varphi}{\partial x} \cdot \vec{\sigma}^E \cdot \frac{\partial \varphi}{\partial x} dV = \int_S \delta \varphi J dS + \int_V \delta \varphi r_e dV \quad (\text{A.3})$$

where $J \equiv -\vec{J} \cdot \vec{n}$ is the current density entering the control volume across S .

Joule's law describes the rate of electrical energy, P_{ec} , dissipated by current flowing through a conductor as

$$P_{ec} = \vec{J} \cdot \vec{E} = \frac{\partial \varphi}{\partial x} \cdot \vec{\sigma}^E \cdot \frac{\partial \varphi}{\partial x}. \quad (\text{A.4})$$

The amount of this energy released as internal heat within the body is $\eta_v P_{ec}$, where η_v is an energy conversion factor (default = 1.0).

The matrix equation is given as

$$\begin{bmatrix} [C^t] & [0] \\ [0] & [C^v] \end{bmatrix} \begin{Bmatrix} \{\dot{T}\} \\ \{\dot{V}\} \end{Bmatrix} + \begin{bmatrix} [K^t] & [0] \\ [K^{vt}] & [K^v] \end{bmatrix} \begin{Bmatrix} \{T\} \\ \{V\} \end{Bmatrix} = \begin{Bmatrix} \{Q\} \\ \{I\} \end{Bmatrix}, \quad (\text{A.5})$$

where $[C^t]$ is the thermal specific heat matrix, $[C^v]$ the dielectric permittivity coefficient matrix, $[K^t]$ the thermal conductivity matrix ($[K^t] = [K^{tb}] + [K^{tc}]$), $[K^{tb}]$ the thermal conductivity matrix of material, $[K^{tc}]$ the thermal conductivity matrix of convection surface, $[K^v]$ the electrical conductivity coefficient matrix, $[K^{vt}]$ the Seebeck coefficient coupling matrix, $\{Q\} = \{Q^{nd}\} + \{Q^c\} + \{Q^g\} + \{Q^j\} + \{Q^p\}$, $\{Q^{nd}\}$ the applied nodal heat flow rate vector, $\{Q^c\}$ the convection surface vector, $\{Q^g\}$ the heat generation rate vector for causes other than Joule heating, $\{Q^j\}$ the heat generation rate vector for Joule heating, $\{Q^p\}$ the Peltier heat flux vector, $\{I\} = \{I^{nd}\}$ the applied nodal charge vector, $\{T\}$ the thermal potential (temperature) vector, $\{V\}$ the electrical potential vector, and \cdot denotes the time derivative. $[C^v]$, $[K^{vt}]$, and $\{Q^p\}$ are only for PLANE223, SOLID226, and SOLID227 elements.

A.3 ELEMENT DESCRIPTION

The SOLID69 element in ANSYS was used in this study. SOLID69 has a 3-D thermal and electrical conduction capability. Joule heat generated by the current flow is also included in the heat balance. The element has eight nodes with two degrees of freedom, temperature and voltage, at each node. The thermal-electric solid element is applicable to a 3-D, steady-state or transient thermal analysis, although no transient electrical capacitance or inductance effects are included in the element. The element requires an iterative solution to include the Joule heating effect in the thermal solution.

For Joule heating effects, both electrical resistivity (RSVX, RSVY, RSVZ) and thermal conductivity (KXX, KYY, KZZ) must be defined. Mass density (DENS),

specific heat (C), and enthalpy (ENTH) may be defined to take into account thermal transient effects.

A.4 BOUNDARY CONDITIONS AND LOAD

Since the Si backside (die top) temperature and substrate bottom temperature were maintained constant during the EM tests, constant temperatures were assigned at those surfaces based on thermocouple readings. For other surfaces of the sample convection boundary conditions were applied with an input of the oven temperature.

An applied current was assigned to one of the terminals of the sample, while the other terminal was grounded, i.e. 0 V was applied.

Glossary

ACA	Anisotropic Conductive Adhesive
ASIC	Application-Specific Integrated Circuit
BEOL	Back-End-Of-the-Line
BGA	Ball Grid Array
C4	Controlled Collapse Chip Connection
CDF	Cumulative Distribution Function
CMOS	Complementary Metal-Oxide-Semiconductor
CPU	Central Processing Unit
DMM	Digital MultiMeter
EBS	Electron BackScattered Diffraction
ECA	Electrically Conductive Adhesive
EDS (or EDX)	Energy Dispersive X-ray Spectroscopy
EM	Electromigration
FEM (or FEA)	Finite Element Method (or Analysis)
GPIO	General Purpose Interface Bus (IEEE 488)
GPU	Graphics Processing Unit
IC	Integrated Circuit
ICA	Isotropic Conductive Adhesive
IMC	InterMetallic Compound
I/O	Input/Output
ITRS	International Technology Roadmap for Semiconductors
MPU	MicroProcessor Unit
MTTF	Median Time To Fail (t_{50})

PDF	Probability Density Function
RoHS	Restriction of Hazardous Substances
SEM	Scanning Electron Microscopy
TAB	Tape Automated Bonding
TCR	Temperature Coefficient of Resistance
TM	Thermomigration
TSM	Top Side Metallurgy (Metallization)
TTF	Time To Fail
UBM	Under Bump Metallurgy (Metallization)
WEEE	Waste Electrical and Electronic Equipment

References

Chapter 1

- [1.1] *Transistor count*, Wikipedia. Web. Mar. 2010.
<http://en.wikipedia.org/wiki/Transistor_count>.
- [1.2] International SEMATECH, “Critical Reliability Challenges for The International Technology Roadmap for Semiconductors (ITRS),” Technology Transfer #03024377A-TR, Mar. 2003.
- [1.3] B. S. Landman and R. L. Russo, “On a Pin Versus Block Relationship for Partitions of Logic Graphs,” *IEEE Trans. Comp.* C-20, 1469 (1971).
- [1.4] *International Technology Roadmap for Semiconductors, 2007 Edition, Assembly and Packaging*. <<http://www.itrs.net>>.
- [1.5] L. J. Turbini and D. Bernier, “Environmental Impact of Lead and Alternatives in Electronics,” in *Handbook of Lead-Free Solder Technology for Microelectronic Assemblies*, edited by K. J. Puttlitz and K. A. Stalter (Marcel Dekker, New York, 2004), pp. 83-84.
- [1.6] *RoHS Exemptions*, The National Measurement Office (UK), Oct. 6, 2009. Web. Mar. 2010. <<http://www.rohs.gov.uk/content.aspx?id=15>>.
- [1.7] *RoHS/Lead (Pb) Free Solutions*, Intel. Web. Mar. 2010.
<<http://www.intel.com/technology/silicon/leadfree.htm>>.
- [1.8] R. R. Tummala, *Fundamentals of Microsystems Packaging* (McGraw-Hill, New York, 2001).
- [1.9] H. K. Charles, Jr., “The Wirebonded Interconnect: A Mainstay for Electronics,” in *Micro- and Opto-Electronic Materials and Structures: Physics, Mechanics, Design, Reliability, Packaging*, Vol. 2, edited by E. Sui, Y. C. Lee, C. P. Wong (Springer, New York, 2007), pp. 71-120.
- [1.10] H. J. Kim et al., “Effects of Cu/Al Intermetallic Compound (IMC) Formation on Cu Wire and Al Pad Bondability,” *IEEE Trans. Comp. Packag. Technol.* 26, 367 (2003).
- [1.11] B. Krenik, D. Buss, and P. Rickert, “Choose the best IC integration method when designing a 3G handset.” *CommsDesign*, May 24, 2005. Web. Mar. 2010.
<<http://www.commsdesign.com/showArticle.jhtml?articleID=163700264>>.

- [1.12] A. Edgar, M. MacCallum, *Printed Circuit Board Design, Unit 3: Packaging and manufacturing*, The University of Bolton. Web. Mar. 2010.
<http://www.ami.ac.uk/courses/ami4931_pcd/u03/index.asp>.
- [1.13] *Solder Bump*, Korea International Trade Association. Web. Mar. 2010.
<http://www.tradekorea.com/product-detail/P00032217/Solder_Bump.html>.
- [1.14] Intel Unveils All New 2010 Intel Core Processor Family, Intel Press Releases, Jan. 7, 2010. Web. Mar. 2010.
<http://www.intel.com/pressroom/archive/releases/20100107comp_sm.htm>.
- [1.15] E. M. Davis, W. E. Harding, R. S. Schwartz, J. J. Corning, "Solid State Technology: Versatile, High-Performance Microelectronics," *IBM J. Res. Develop.* 8, 102 (1964).
- [1.16] L. F. Miller, "Controlled Collapse Reflow Chip Joining," *IBM J. Res. Develop.* 13, 239 (1969).
- [1.17] *Tutorials*, FlipChips Dot Com. Web. Mar. 2010. <<http://www.flipchips.com>>.
- [1.18] Dietrich Tönnies, "Overview and Trends in Flip Chip Technology," *The SUSS Report*, 3rd Quarter 2004, p. 22.
- [1.19] George Riley, "Solder Bumping – Mastering Challenges of Lead-free Alloys," *Advanced Packaging*, Nov. 2005. Web. Jul. 2006. <<http://ap.pennet.com>>.
- [1.20] P. A. Gruber, DY. Shih, L. Belanger, G. Brouillette, D. Danovitch, V. Oberson, M. Torgeon and H. Kimura, "C4NP Technology for Pb-free Wafer Bumping," *The SUSS Report*, 3rd Quarter 2004, p. 3.
- [1.21] K. O'Donnell, "Under Bump Metallurgy for Lead-Free Solder," *Advanced Packaging*, Nov. 2004. Web. Mar. 2010.
<<http://www.nexxsystems.com/pdfs/nimbus/AP%20leadfree.pdf>>.
- [1.22] C. Y. Liu and S. J. Wang, "Prevention of Spalling by the Self-Formed Reaction Barrier Layer on Controlled Collapse Chip Connections Under Bump Metallization," *J. Electron. Mater.* 32, L1 (2003).
- [1.23] D. R. Frear, J. W. Jang, J. K. Lin, and C. Zhang, "Pb-Free Solders for Flip-Chip Interconnects," *JOM* 53, 28 (2001).
- [1.24] J. Liang, N. Dariavach, and D. Shangguan, "Metallurgy, Processing and Reliability of Lead-Free Solder Joint Interconnections," in *Micro- and Opto-Electronic Materials and Structures: Physics, Mechanics, Design, Reliability, Packaging*, Vol. 1, edited by E. Sui, Y. C. Lee, C. P. Wong (Springer, New York, 2007), pp. 351-409.

- [1.25] C.-S. Oh, J.-H. Shim, B.-J. Lee, and D. N. Lee, *J. Alloys Compd.* 238, 155 (1996).
- [1.26] K.-N. Tu, *Solder Joint Technology – Materials, Properties, and Reliability* (Springer, New York, 2007).
- [1.27] *ASM Handbooks Online, Vol. 3: Alloy Phase Diagrams*, ASM International, 2010.
Web. Mar. 2010. <<http://products.asminternational.org/hbk/index.jsp>>.
- [1.28] P. T. Vianco, P. F. Hlava, and A. C. Kilgo, “Intermetallic Compound Layer Formation Between Copper and Hot-Dipped 100In, 50In-50Sn, 100Sn and 63Sn37Pb Coatings,” *J. Electron. Mater.* 23, 583 (1994).
- [1.29] Y. G. Lee and J. G. Duh, “Interfacial Morphology and Concentration Profile in the Unleaded Solder/Cu Joint Assembly,” *J. Mater. Sci. - Mater. Electron.* 10, 33 (1999).
- [1.30] K. H. Prakash and T. Sritharan, “Effects of Solid State Annealing on the Interface Intermetallics Between Tin-Lead Solders and Copper,” *J. Electron. Mater.* 32, 939 (2003).
- [1.31] R. Labie, W. Ruythooren, J. V. Humbeeck, “Solid State Diffusion in Cu-Sn and Ni-Sn Diffusion Couples with Flip-Chip Scale Dimensions,” *Intermetallics* 15, 396 (2007).
- [1.32] W. Yang and R. W. Messler, “Microstructure Evolution of Eutectic Sn-Ag Solder Joints,” *J. Electron. Mater.* 23, 765 (1994).
- [1.33] T. Y. Lee et al., “Morphology, Kinetics, and Thermodynamics of Solid-State Aging of Eutectic SnPb and Pb-Free Solders (Sn-3.5Ag, Sn-3.8Ag-0.7Cu and Sn-0.7Cu) on Cu,” *J. Mater. Res.* 17, 291 (2002).
- [1.34] S. Bader, W. Gust, and H. Hieber, “Rapid Formation of Intermetallic Compounds by Interdiffusion in the Cu-Sn and Ni-Sn Systems,” *Acta Metall. Mater.* 43, 329, 1995.
- [1.35] P. G. Kim, J. W. Jang, T. Y. Lee, and K. N. Tu, *J. Appl. Phys.* 86, 6746, 1999.
- [1.36] K. Kulojarvi, V. Vuorinen, and J. Kivilahti, *Microelectronics International* 15, 20, 1998.
- [1.37] H. D. Blair, T. Pan, and J. M. Nicholson, “Intermetallic Compound Growth on Ni, Au/Ni and Pd/Ni Substrates with Sn/Pb, Sn/Ag and Sn Solders,” *Proc. IEEE 48th Electronic Components and Technology Conference*, 1998, pp. 259-67.
- [1.38] G. Ghosh, *J. Appl. Phys.* 88, 6887, 2000.

- [1.39] G. Ghosh, *J. Electron. Mater.* 28, 1238, 1999.
- [1.40] R. Labie, W. Ruythooren, J. V. Humbeeck, "Solid State Diffusion in Cu-Sn and Ni-Sn Diffusion Couples with Flip-Chip Scale Dimensions," *Intermetallics* 15, 396 (2007).
- [1.41] M. O. Alam and Y. C. Chan, "Solid-state growth kinetics of Ni₃Sn₄ at the Sn–3.5Ag solder/Ni interface," *J. Appl. Phys.* 98, 123527 (2005).
- [1.42] T. Laurila, V. Vuorinen, and J. K. Kivilahti, "Interfacial Reactions Between Lead-Free Solders and Common Base Materials," *Mater. Sci. Eng., R* 49,1 (2005).
- [1.43] A. Zribi *et al.*, "The growth of intermetallic compounds at Sn-Ag-Cu solder/Cu and Sn-Ag-Cu solder/Ni interfaces and the associated evolution of the solder microstructure," *J. Electron. Mater.* 30, 1157 (2001).
- [1.44] K. N. Tu, "Recent advances on electromigration in very-large-scale-integration of interconnects," *J. Appl. Phys.* 94, 5451 (2003).
- [1.45] K. N. Tu, "Physics and materials challenges for lead-free solders," *J. Appl. Phys.* 93, 1335 (2003).
- [1.46] G. D. Giacomo and S. Oggioni, "Reliability of Flip Chip Applications with Ceramic and Organic Chip Carriers," *Microelectron. Reliab.* 42, 1541 (2002).
- [1.47] H. Ye, C. Basaran, and D. Hopkins, "Thermomigration in Pb-Sn Solder Joints under Joule Heating during Electric Current Stressing," *Appl. Phys. Lett.* 82, 1045 (2003).
- [1.48] H. B. Huntington and A. R. Grone, "Current-Induced Marker Motion in Gold Wires," *J. Phys. Chem. Solids* 20, 76 (1961).
- [1.49] P. S. Ho and T. Kwok, "Electromigration in Metals," *Rep. Prog. Phys.* 52, 301 (1989).
- [1.50] I. A. Blech and E. S. Meieran, *Appl. Phys. Lett.* 11, 263 (1967).
- [1.51] M. A. Korhonen *et al.*, "Stress Evolution due to Electromigration in Confined Metal Lines," *J. Appl. Phys.* 73, 3790 (1993).
- [1.52] B. F. Dyson, T. Anthony and D. Turnbull, "Interstitial Diffusion of Copper and Silver in Lead," *J. Appl. Phys.* 37, 2370 (1966).
- [1.53] W. K. Warburton and D. Turnbull, in *Diffusion in Solids*, edited by A. S. Nowick and J. J. Burton (Academic, New York, 1975) pp.171-226.

- [1.54] D. L. Decker, C. T. Candland and H. B. Vanfleet, "Diffusion of Pd in Pb at high pressures," *Phys. Rev. B* 11, 2885 (1975).
- [1.55] E. C. C. Yeh, W. J. Choi, K. N. Tu, P. Elenius and H. Balkan, "Current-crowding-induced electromigration failure in flip chip solder joints," *Appl. Phys. Lett.* 80, 580 (2002).
- [1.56] S. W. Liang, Y. W. Chang, and C. Chen, "Effect of Al-Trace Dimension on Joule Heating and Current Crowding in Flip-Chip Solder Joints under Accelerated Electromigration," *Appl. Phys. Lett.* 88, 172108 (2006).
- [1.57] C. T. Liu, C. Chen, and K. N. Tu, "Electromigration in Sn-Pb Solder Strips as a Function of Alloy Composition," *J. Appl. Phys.* 88, 5703 (2000).
- [1.58] S. Brandenburg and S. Yeh, *Proc. Surface Mount International Conference and Exhibition*, San Jose, CA, 1998, pp. 337-344.
- [1.59] Q. T. Huynh, C. Y. Liu, C. Chen, and K. N. Tu, "Electromigration in Eutectic SnPb Solder Lines," *J. Appl. Phys.* 89, 4332 (2000).
- [1.60] T. Y. Lee, K. N. Tu, S. M. Kuo, and D. R. Frear, "Electromigration of Eutectic SnPb Solder Interconnects for Flip Chip Technology," *J. Appl. Phys.* 89, 3189 (2001).
- [1.61] T. Y. Lee, K. N. Tu, and D. R. Frear, "Electromigration of Eutectic SnPb and SnAg_{3.8}Cu_{0.7} Flip Chip Solder Bumps and Under-Bump Metallization," *J. Appl. Phys.* 90, 4502 (2001).
- [1.62] D.-G. Kim, W.-C. Moon, and S.-B. Jung, "Effects of Electromigration on Microstructural Evolution of Eutectic SnPb Flip Chip Solder Bumps," *Microelectron. Reliab.* 83, 2391 (2006).
- [1.63] D. Gupta, K. Vieregge, and W. Gust, "Interface Diffusion in Eutectic Pb-Sn Solder," *Acta Mater.* 47, 5 (1998).
- [1.64] J. R. Lloyd, K.-N. Tu, and J. Jaspal, "The Physics and Materials Science of Electromigration and Thermomigration in Solders," in *Handbook of Lead-Free Solder Technology for Microelectronic Assemblies*, edited by K. J. Puttlitz and K. A. Stalter (Marcel Dekker, New York, 2004), pp. 827-850.
- [1.65] J. W. Nah, K. W. Paik, J. O. Suh, and K. N. Tu, "Mechanism of Electromigration-Induced Failure in the 97Pb-3Sn and 37Pb-63Sn Composite Solder Joints," *J. Appl. Phys.* 94, 7560 (2003).
- [1.66] E. C. C. Yeh et al., "Current-Crowding-Induced Electromigration Failure in Flip Chip Solder Joints," *Appl. Phys. Lett.* 80, 580 (2002).

- [1.67] L. Zhang *et al.*, “Effect of Current Crowding on Void Propagation at the Interface between Intermetallic Compound and Solder in Flip Chip Solder Joints,” *Appl. Phys. Lett.* 88,012106 (2006).
- [1.68] A. T. Huang, K. N. Tu, and Y.-S. Lai, “Effect of the Combination of Electromigration and Thermomigration on Phase Migration and Partial Melting in Flip Chip Composite SnPb Solder Joints,” *J. Appl. Phys.* 100, 033512 (2006).
- [1.69] J. Shi, S. Mei, and H. B. Huntington, “Diffusion and Electromigration in Lead Alloys. II. Ag, Au, and Cu in Lead-Indium,” *J. Appl. Phys.* 62, 451 (1987).
- [1.70] M. Y. Hsieh and H. B. Huntington, “Electromigration of Copper in Lead,” *J. Phys. Chem. Solids* 39, 867 (1978).
- [1.71] D. A. Golopenta and H. B. Huntington, “A Study of Electromigration of Nickel in Lead,” *J. Phys. Chem. Solids* 39, 975 (1978).
- [1.72] J. Shi and H. B. Huntington, “Electromigration of Gold and Silver in Single Crystal Tin,” *J. Phys. Chem. Solids* 48, 693 (1987).
- [1.73] D. C. Yeh and H. B. Huntington, “Extreme Fast-Diffusion System: Nickel in Single-Crystal Tin,” *Phys. Rev. Lett.* 53, 1469 (1984).
- [1.74] H.-L. Chao, “Electromigration Enhanced Kinetics of Cu-Sn Intermetallic Compounds in Pb Free Solder Joints and Cu Low-k Dual Damascene Processing Using Step and Flash Imprint Lithography,” *Ph.D. Dissertation*, The University of Texas at Austin, 2009.
- [1.75] P. S. Ho, “Motion of Inclusion Induced by a Direct Current and a Temperature Gradient,” *J. Appl. Phys.* 41, 64 (1970).
- [1.76] H. Ye, C. Basaran, and D. Hopkins, “Thermomigration in Pb-Sn Solder Joints under Joule Heating during Electric Current Stressing,” *Appl. Phys. Lett.* 82, 1045 (2003).
- [1.77] A. T. Huang, A. M. Gusak and K. N. Tu, “Thermomigration in SnPb composite flip chip solder joints,” *Appl. Phys. Lett.* 88, 141911 (2006).
- [1.78] Y. C. Chuang and C. Y. Liu, “Thermomigration in Eutectic SnPb Alloy,” *Appl. Phys. Lett.* 88, 174105 (2006).
- [1.79] H.-Y. Hsiao and C. Chen, “Thermomigration in Flip-Chip SnPb Solder Joints under Alternating Current Stressing,” *Appl. Phys. Lett.* 90, 152105 (2007).

Chapter 2

- [2.1] M. Ding, "Investigation of Electromigration Reliability of Solder Joint in Flip Chip Packages," *Ph.D. Dissertation*, The University of Texas at Austin, 2007.
- [2.2] M. Gall, "Investigation of Electromigration Reliability in Al(Cu) interconnects," *Ph.D. Dissertation*, The University of Texas at Austin, 1999.
- [2.3] K.-D. Lee, "Electromigration Critical Length Effect and Early Failures in Cu/oxide and Cu/low k Interconnects," *Ph.D. Dissertation*, The University of Texas at Austin, 2003.
- [2.4] J. R. Lloyd and J. Kitchin, "The Electromigration failure distribution: The fine-line case," *J. Appl. Phys.* **69**, 2117 (1991).
- [2.5] P. A. Tobias and D. C. Trindade, *Applied Reliability* (Van Nostrand Reinhold Company, New York, 1986).
- [2.6] http://en.wikipedia.org/wiki/Kaplan-Meier_estimator.
- [2.7] J. R. Black, "Mass Transport of Aluminum by Momentum Exchange with Conducting Electrons," *Proc. 6th International Reliability Physics Symposium*, Los Angeles, CA, 1967, pp. 148-159.

Chapter 3

- [3.1] M. Ding, H. Matsushashi, G. Wang, and P. S. Ho, *Proc. IEEE 54th Electronic Components and Technology Conference*, Las Vegas, NV, June 2004, p. 968.
- [3.2] K. N. Tu, *J. Appl. Phys.* **94**, 5451 (2003).
- [3.3] B. F. Dyson, T. Anthony, and D. Turnbull, "Interstitial Diffusion of Copper in Tin," *J. Appl. Phys.* **38**, 3408 (1967).
- [3.4] W. K. Warburton and D. Turnbull, in *Diffusion in Solids*, edited by A. S. Nowick and J. J. Burton (Academic, New York, 1975) pp. 171-226.
- [3.5] D. L. Decker, C. T. Candland, and H. B. Vanfleet, *Phys. Rev. B* **11**, 4885 (1975).
- [3.6] M. Ding, G. Wang, B. Chao, and P. S. Ho, *Proc. IEEE 43rd Annual International Reliability Physics Symposium*, San Jose, CA, April 2005, p. 518.
- [3.7] Y. C. Hu, Y. H. Lin, C. R. Kao, and K. N. Tu, *J. Mater. Res.* **18**, 2544 (2003).

- [3.8] J. W. Jang, D. R. Frear, T. Y. Lee, and K. N. Tu, *J. Appl. Phys.* 88, 6359 (2000).
- [3.9] J. W. Nah, J. O. Suh, and K. N. Tu, *J. Appl. Phys.* 98, 013715 (2005).
- [3.10] M. Ding, "Investigation of Electromigration Reliability of Solder Joint in Flip-Chip Packages," *Ph.D. Dissertation*, The University of Texas at Austin, 2007.
- [3.11] J. W. Nah, J. O., Suh and K. N. Tu, "Effect of current crowding and Joule heating on electromigration-induced failure in flip chip composite solder joints tested at room temperature," *J. Appl. Phys.* **98**, 013715 (2005).
- [3.12] Y. H. Lin, C. M. Tsai, Y. C. Hu, Y. L. Lin and C. R. Kao, "Electromigration-Induced Failure in Flip-Chip Solder Joints," *J. Electron. Mater.* **34**, 27 (2005).
- [3.13] K.-D. Lee, "Electromigration Critical Length Effect and Early Failures in Cu/oxide and Cu/low k Interconnects," *Ph.D. Dissertation*, The University of Texas at Austin, 2003.
- [3.14] W. Roush and J. Jaspal, *Proc. IEEE 32nd Electronic Components and Technology Conference*, San Diego, CA, May 1982, p. 342.
- [3.15] H. Ye, C. Basaran and D. Hopkins, "Thermomigration in Pb-Sn solder joints under joule heating during electric current stressing," *Appl. Phys. Lett.* **82**, 1045 (2003).
- [3.16] A. T. Huang, A. M. Gusak and K. N. Tu, "Thermomigration in SnPb composite flip chip solder joints," *Appl. Phys. Lett.* **88**, 141911 (2006).
- [3.17] J. R. Black, "Mass Transport of Aluminum by Momentum Exchange with Conducting Electrons," *Proc. 6th International Reliability Physics Symposium*, Los Angeles, CA, 1967, pp. 148-159.
- [3.18] Y. C. Chan, Alex C. K. So and J. K. L. Lai, "Growth kinetic studies of Cu-Sn intermetallic compound and its effect on shear strength of LCCC SMT solder joints," *Mat. Sci. Eng. B* **55**, 5 (1998).
- [3.20] J.-W. Yoon and S.-B. Jung, "Investigation of interfacial reactions between Sn-5Bi solder and Cu substrate," *J. Alloys Compd.* **359**, 202 (2003).
- [3.21] C. N. Liao and C. T. Wei, "Effect of Intermetallic Compound Formation on Electrical Properties of Cu/Sn Interface during Thermal Treatment," *J. Electron. Mater.* **33**, 1137 (2004).
- [3.22] Z. Chen, M. He and G. Qi, "Morphology and Kinetic Study of the Interfacial Reaction between the Sn-3.5Ag Solder and Electroless Ni-P Metallization," *J. Electron. Mater.* **33**, 1465 (2004).

- [3.23] A. S. Oates, "Current density dependence of electromigration failure of submicron width, multilayer Al alloy conductors," *Appl. Phys. Lett.* **66**, 1475 (1995).
- [3.24] M. Ding, G. Wang, B. Chao and P. S. Ho, "Effect of contact metallization on electromigration reliability of Pb-free solder joints," *J. Appl. Phys.* **99**, 094906 (2006).
- [3.25] Y. C. Hu, Y. H. Lin, C. R. Kao and K. N. Tu, "Electromigration failure in flip chip solder joints due to rapid dissolution of copper," *J. Mater. Res.* **18**, 2544 (2003).
- [3.26] K. Zeng, R. Stierman, T.-C. Chiu, D. Edwards, K. Ano and K. N. Tu, "Kirkendall void formation in eutectic SnPb solder joints on bare Cu and its effect on joint reliability," *J. Appl. Phys.* **97**, 024508 (2005).
- [3.27] H.-L. Chao, "Electromigration Enhanced Kinetics of Cu-Sn Intermetallic Compounds in Pb Free Solder Joints and Cu Low-k Dual Damascene Processing Using Step and Flash Imprint Lithography," *Ph.D. Dissertation*, The University of Texas at Austin, 2009.
- [3.28] C. Chen and S. Chen, "Electromigration effect upon the Sn-0.7 wt% Cu/Ni and Sn-3.5 wt% Ag/Ni interfacial reactions," *J. Appl. Phys.* **90**, 1208 (2001).

Chapter 4

- [4.1] L. F. Miller, "Controlled Collapse Reflow Chip Joining," *IBM J. Res. Develop.* **13**, 239 (1969).
- [4.2] D. Tonnie, "Overview and Trends in Flip Chip Technology," *The SUSS Report*, 3rd Quarter 2004, p. 22.
- [4.3] http://ec.europa.eu/environment/waste/weee_index.htm
- [4.4] http://en.wikipedia.org/wiki/Restriction_of_Hazardous_Substances_Directive
- [4.5] K. N. Tu and K. Zeng, "Tin-Lead (SnPb) Solder Reaction in Flip Chip Technology," *Mater. Sci. Eng. R*, Vol. 34, No. 1, pp. 1-58 (2001).
- [4.6] K. N. Tu, A. M. Gusak, and M. Li, "Physics and Materials Challenges for Lead-Free Solders," *J. Appl. Phys.*, Vol. 93, pp. 1335-1353 (2003).
- [4.7] S. Chen and C. Chen, "Electromigration Effects upon Interfacial Reactions," *JOM*, pp. 62-67 (2003).

- [4.8] H. Gan and K. N. Tu, "Polarity Effect of Electromigration on Kinetics of Intermetallic Compound Formation in Pb-Free Solder V-Groove Samples," *J. Appl. Phys.*, Vol. 97, p. 063514 (2005).
- [4.9] S.-H. Chae *et al.*, "Electromigration Statistics and Damage Evolution for Pb-Free Solder Joints with Cu and Ni UBM in Plastic Flip-Chip Packages," *J. Mater. Sci.: Mater. Electron.*, Vol. 18, No. 1-3, pp. 247-258 (2007).
- [4.10] G. T. Galyon *et al.*, *iNEMI Tin Whisker Workshop presented at IEEE Electronic Components & Technology Conference (ECTC)*, Lake Buena Vista, FL, May 2005.
- [4.11] K. Zeng, R. Stierman, T.-C. Chiu, D. Edwards, K. Ano and K. N. Tu, "Kirkendall void formation in eutectic SnPb solder joints on bare Cu and its effect on joint reliability," *J. Appl. Phys.* **97**, 024508 (2005).
- [4.12] M. O. Alam and Y. C. Chan, "Solid-state growth kinetics of Ni₃Sn₄ at the Sn-3.5Ag solder/Ni interface," *J. Appl. Phys.* **98**, 123527 (2005).
- [4.13] C. E. Circhenall, *Physical Metallurgy* (McGraw-Hill, New York, 1959), pp. 216-217.
- [4.14] D. R. Frear, in *Solder Mechanics: A State of the Art Assessment*, edited by D. R. Frear, W. B. Jones and K. R. Kinsman, (TMS, Warrendale, PA, 1991), p. 191.
- [4.15] M. Schaefer, W. Laub, J. M. Sabee, and R. A. Fournelle, *J. Electron. Mater.* **25** (6), 992 (1993).
- [4.16] S. Bader, W. Gust, and H. Hieber, *Acta Met.* **43** (1), 329 (1995).
- [4.17] F. Bartels, J. W. Morris, Jr., G. Dalke and W. Gust, *J. Electron. Mater.* **23** (8), 787 (1994).
- [4.18] H. K. Kim and K. N. Tu, "Kinetic Analysis of the Soldering Reaction Between Eutectic SnPb Alloy and Cu Accompanied by Ripening," *Phys. Rev. B* **53** (23), 16027 (1996).
- [4.19] M. Schaefer, W. Laub, R. A. Fournelle and J. Liang, in *Design & Reliability of Solders and Solder Interconnections*, edited by R. K. Mahidhara, *et al.*, (TMS, Warrendale, PA, 1997), p. 247.
- [4.20] J. London and D. W. Ashall, *Brazing & Soldering* **11**, 49 (1986).
- [4.21] M. Schaefer, R. A. Rournelle, and J. Liang, "Theory for Intermetallic Phase Growth Between Cu and Liquid Sn-Pb Solder Based on Grain Boundary Diffusion Control," *J. Electron. Mater.* **27**, 1167 (1998).

- [4.22] M. Onishi and H. Fujibuchi, "Reaction-diffusion in Cu-Sn system," *Trans. Jpn. Inst. Met.* 16, 539 (1975).
- [4.23] D. R. Flanders, E. G. Jacobs, and R. F. Pinizzotto, "Activation Energies of Intermetallic Growth of Sn-Ag Eutectic Solder on Copper Substrates," *J. Electron. Mater.* 26, 883 (1997).
- [4.24] H. D. Blair, T. Pan, and J. M. Nicholson, "Intermetallic Compound Growth on Ni, Au/Ni and Pd/Ni Substrates with Sn/Pb, Sn/Ag and Sn Solders," *Proc. IEEE 48th Electronic Components and Technology Conference*, 1998, pp. 259-67.
- [4.25] S. Choi, T. R. Bieler, J. P. Lucas, and K. N. Subramanian, "Characterization of the Growth of Intermetallic Interfacial Layers of Sn-Ag and Sn-Pb Eutectic Solders and Their Composite Solders on Cu Substrate During Isothermal Long-Term Aging," *J. Electron. Mater.* 28, 1209 (1999).
- [4.26] G.-W. Xiao *et al.*, "Effect of Cu Stud Microstructure and Electroplating Process on Intermetallic Compounds Growth and Reliability of Flip-Chip Solder Bump," *IEEE Trans. Comp. Packag. Technol.* 24, 682 (2001).
- [4.27] Z. Chen, M. He, and G. Qi, "Morphology and Kinetic Study of the Interfacial Reaction between the Sn-3.5Ag Solder and Electroless Ni-P Metallization," *J. Electron. Mater.* 33, 1465 (2004).
- [4.28] J. W. Yoon and S. B. Jung, "Growth Kinetics of Ni_3Sn_4 and Ni_3P Layer Between Sn-3.5Ag Solder and Electroless Ni-P Substrate," *J. Alloy Compd.* 376, 105 (2004).
- [4.29] D. Q. Yu *et al.*, "Intermetallic Compounds Growth between Sn-3.5Ag Lead-Free Solder and Cu Substrate by Dipping Method," *J. Alloys Compd.* 392, 192 (2005).
- [4.30] R. Labie, W. Ruythooren, J. V. Humbeeck, "Solid State Diffusion in Cu-Sn and Ni-Sn Diffusion Couples with Flip-Chip Scale Dimensions," *Intermetallics* 15, 396 (2007).
- [4.31] G.-T. Lim *et al.*, "Temperature Effect on Intermetallic Compound Growth Kinetics of Cu Pillar/Sn Bumps," *J. Electron. Mater.* 38, 2228 (2009).
- [4.32] Z. Mei, A. J. Sunwoo, and J. W. Morris, Jr., "Analysis of Low-Temperature Intermetallic Growth in Copper-Tin Diffusion Couples," *Metall. Trans. A* 23A, 857 (1992).
- [4.33] A. J. Sunwoo, J. W. Morris, Jr., and G. K. Lucey, Jr., "The Growth of Cu-Sn Intermetallics at a Pretinned Copper-Solder Interface," *Metall. Trans. A* 23A, 1323 (1992).

- [4.34] P. T. Vianco, P. F. Hlava, and A. C. Kilgo, "Intermetallic Compound Layer Formation Between Copper and Hot-Dipped 100In, 50In-50Sn, 100Sn and 63Sn37Pb Coatings," *J. Electron. Mater.* 23, 583 (1994).
- [4.35] K. N. Tu, "Interdiffusion and Reaction in Bimetallic Cu-Sn Thin Films," *Acta Metall.* 21, 317 (1973).
- [4.36] K. N. Tu and R. D. Thompson, "Kinetics of Interfacial Reaction in Bimetallic Cu-Sn Thin Films," *Acta Metall.* 30, 947 (1982).
- [4.37] Y. G. Lee and J. G. Duh, "Interfacial Morphology and Concentration Profile in the Unleaded Solder/Cu Joint Assembly," *J. Mater. Sci. - Mater. Electron.* 10, 33 (1999).
- [4.38] K. H. Prakash and T. Sriharan, "Effects of Solid State Annealing on the Interface Intermetallics Between Tin-Lead Solders and Copper," *J. Electron. Mater.* 32, 939 (2003).
- [4.39] B. F. Dyson, T. Anthony, and D. Turnbull, "Interstitial Diffusion of Copper in Tin," *J. Appl. Phys.* 38, 3408 (1967).
- [4.40] H. Oikawa and A. Hosoi, *Scripta Metall.* 9, 823 (1975).
- [4.41] K. Hoshino, Y. Iijima, and K. Hirano, *Trans. Jpn. Inst. Met.* 21, 674 (1980).
- [4.42] J. H. L. Pang, K. H. Prakash, and T. H. Low, "Isothermal and Thermal Cycling Aging on IMC Growth Rate in Pb-free and Pb-based Solder Interfaces," *Proc. Inter Society Conference on Thermal Phenomena*, 2004, pp. 109-115.
- [4.43] M. R. Harrison, J. H. Vincent, and H. A. H. Steen, "Lead-Free Reflow Soldering for Electronics Assembly," *Sold. & Surf. Mount. Tech.* 13, 21 (2001).
- [4.44] E. Starke and H. Wever, *Z. Metallk.* 55, 107 (1964).
- [4.45] L. Zakraysek, "Intermetallic Growth in Tin-rich Solders," *Welding J.* 51, 536s (1972).
- [4.46] D. A. Unsworth and C. A. Mackay, "Preliminary Report on Growth of Compound Layers on Various Metals Bases Plated with Tin and its Alloys," *Trans. Inst. Met. Finish* 51, 85 (1973).
- [4.47] J. Stephens, in internal memorandum, Sandia National Laboratories, Mar. 2, 1989.

- [4.48] P. J. Kay, C. A. Mackay, "The Growth of Intermetallic Compounds on Common Basis Materials Coated with Tin and Tin-Lead Alloys," *Trans. Inst. Met. Finish.* 54, 68 (1976).
- [4.49] J. Haimovich, "Cu-Sn Intermetallic Compound Growth in Hot-Air-Levelled Tin at and below 100°C," *AMP J. Technol.* 3, 46 (1993).
- [4.50] P. T. Vianco, K. L. Erickson, and P. L. Hopkins, "Solid State Intermetallic Compound Growth between Copper and High Temperature Tin-Rich Solders - Part I: Experimental Analysis," *J. Electron. Mater.* 23, 721 (1994).
- [4.51] Y. C. Chan, A. C. K. So, and J. K. L. Lai, "Growth Kinetic Studies of Cu-Sn Intermetallic Compound and its Effect on Shear Strength of LCCC SMT Solder Joints," *Mater. Sci. Eng.* B55, 5 (1998).
- [4.52] T. Y. Lee *et al.*, "Morphology, Kinetics, and Thermodynamics of Solid-State Aging of Eutectic SnPb and Pb-Free Solders (Sn-3.5Ag, Sn-3.8Ag-0.7Cu and Sn-0.7Cu) on Cu," *J. Mater. Res.* 17, 291 (2002).
- [4.53] T. A. Siewert, J. C. Madeni, and S. Liu, *Proc. APEX94 Conference on Electronics Manufacturing*, Apr. 2003.
- [4.54] C. B. Lee *et al.*, "Intermetallic compound layer formation between Sn-3.5 mass% Ag BGA solder ball and (Cu, immersion Au/electroless Ni-P/Cu) substrate," *J. Mater. Sci. - Mater. Electron.* 14, 487 (2003).
- [4.55] J. W. Yoon, C. B. Lee, and S. B. Jung, "Interfacial reactions between Sn-58 mass% Bi eutectic solder and (Cu, electroless Ni-P/Cu) substrate," *Mater. Trans.* 43, 1821 (2002).
- [4.56] J. W. Yoon and S. B. Jung, "Investigation of Interfacial Reactions between Sn-5Bi Solder and Cu Substrate," *J. Alloys Compd.* 359, 202 (2003).
- [4.57] J. W. Yoon, C. B. Lee, D. U. Kim, and S. B. Jung, "Reaction diffusions of Cu₆Sn₅ and Cu₃Sn intermetallic compound in the couple of Sn-3.5Ag eutectic solder and copper substrate," *Met. Mater. Int.* 9, 193 (2003).
- [4.58] J. W. Yoon and S. B. Jung, "Effect of isothermal aging on intermetallic compound layer growth at the interface between Sn-3.5Ag-0.75Cu solder and Cu substrate," *J. Mater. Sci.* 39, 4211 (2004).
- [4.59] D. Olsen, R. Wright, and H. Berg, "Effects of Intermetallics on the Reliability of Tin Coated Cu, Ag, and Ni Parts," *Proc. Reliability Phys. Symp.*, Las Vegas, NV, 1978, pp. 80-86.

- [4.60] C. Chen *et al.*, “Long-Term Aging Study on the Solid-State Reaction Between 58Bi42Sn Solder and Ni Substrate,” *J. Electron. Mater.* 29, 1200 (2000).
- [4.61] P. L. Tu, Y. C. Chan, K. C. Hung, and J. K. L. Lai, “Growth Kinetics of Intermetallic Compounds in Chip Scale Package Solder Joint,” *Scripta Mater.* 44, 317 (2001).
- [4.62] M. Li *et al.*, “Microstructure, Joint Strength and Failure Mechanisms of SnPb and Pb-Free Solders in BGA Packages,” *IEEE Trans. Electron. Packag.* 25, 185 (2002).
- [4.63] J. W. Yoon, C. B. Lee, and S. B. Jung, “Growth of an intermetallic compound layer with Sn-3.5Ag-5Bi on Cu and Ni-P/Cu during aging treatment,” *J. Electron. Mater.* 32, 1195 (2003).
- [4.64] M. He, Z. Chen, and G. Qi, “Solid State Interfacial Reaction of Sn-37Pb and Sn-3.5Ag Solders with Ni-P Under Bump Metallization,” *Acta Mater.* 52, 2047 (2004).
- [4.65] R. F. Pinizzotto *et al.*, “The Dependence of the Activation Energies of Intermetallic Formation on the Composition of Composite Sn/Pb Solders,” *Proc. IEEE 31st Annual International Reliability Physics Symposium*, 1993, pp. 209-216.
- [4.66] G. Ghosh, “Interfacial Microstructure and the Kinetics of Interfacial Reaction in Diffusion Couples Between Sn-Pb Solder and Cu/Ni/Pd Metallization,” *Acta Mater.* 48, 3719 (2000).
- [4.67] X. Deng, G. Piotrowski, J. J. Williams, and N. Chawla, “Influence of Initial Morphology and Thickness of Cu₆Sn₅ and Cu₃Sn Intermetallics on Growth and Evolution during Thermal Aging of Sn-Ag Solder/Cu Joints,” *J. Electron. Mater.* 32, 1403 (2003).
- [4.68] B. Chao, S.-H. Chae, X. Zhang, K.-H. Lu, J. Im and P. S. Ho, “Electromigration Enhanced Intermetallic Growth and Void Formation in Pb-Free Solder Joints,” *J. Appl. Phys.* 100, 084909 (2006).
- [4.69] B. Chao, S.-H. Chae, X. Zhang, K.-H. Lu, J. Im and P. S. Ho, “Investigation of Diffusion and Electromigration Parameters for Cu-Sn Intermetallic Compounds in Pb-Free Solders Using Simulated Annealing,” *Acta Materialia*, 55, 2805 (2007).
- [4.70] H.-L. Chao, “Electromigration Enhanced Kinetics of Cu-Sn Intermetallic Compounds in Pb Free Solder Joints and Cu Low-k Dual Damascene Processing Using Step and Flash Imprint Lithography,” *Ph.D. Dissertation*, The University of Texas at Austin, 2009.

- [4.71] H. B. Huntington and A. R. Grone, *J. Phys. Chem. Solids*, **20**, 76 (1961).
- [4.72] M. Lu et al., "Effect of Sn Grain Orientation on Electromigration Degradation Mechanism in High Sn-Based Pb-Free Solders," *Appl. Phys. Lett.* 92, 211909 (2008).
- [4.73] Y.-W. Cheng and T. A. Siewert, "Predicting Tensile Properties of the Bulk 96.5Sn-3.5Ag Lead-Free Solder," *J. Electron. Mater.* 32, 535 (2003).
- [4.74] H. D. Merchant, G. Khatibi, and B. Weiss, "Elastic and Elastoplastic Response of Thin Copper Foil," *J. Mater. Sci.* 39, 4157 (2004).
- [4.75] H. S. Cho *et al.*, "Tensile, Creep and Fatigue Properties of LIGA Nickel Structures," *Proc. 15th IEEE International Conf. on Micro Electro Mechanical Systems*, Jan. 2002, pp. 439-442.
- [4.76] R.J. Fields, S. R. Low III, and G.K. Lucey, Jr., in *The Metal Science and Joining*, edited by M. J. Cieslak *et al.* (TMS, Warrendale, PA, May 1991), pp. 165-174.
- [4.77] G. O. Mallory and J. B. Hajdu, *Electroless Plating Fundamentals and Applications* (Amer. Electroplaters & Surface Finishers Soc., New York, 1990), Ch. 1 and 4.
- [4.78] M. S. Islam, J. C. Suhling, and P. Lall, "Measurement of the Temperature Dependent Constitutive Behavior of Underfill Encapsulants," *IEEE Trans. Comp. Packag. Technol.* 28, 467 (2005).
- [4.79] J. Pyland, R. Pucha, and S. Sitaraman, "Effect of Underfill on BGA Reliability," *Proc. IEEE 51st Electronic Components and Technology Conference*, Orlando, FL, May 2001, pp. 85-90.
- [4.80] T. Moore and J. Jarvis, "Failure Analysis and Stress Simulation in Small Multichip BGAs," *Proc. 38th International Reliability Physics Symposium*, Apr. 2000, pp. 217-224.
- [4.81] W. D. Nix and E. Arzt, "On Void Nucleation and Growth in Metal Interconnect Lines under Electromigration Conditions," *Metall. Trans. A* 23A, 2007 (1992).
- [4.82] D. Porter and K. E. Easterling, *Phase Transformation in Metals and Alloys*, 2nd. ed. (CRC Press, 1992).
- [4.83] R. J. Gleixner, B. M. Clemens, and W. D. Nix, "Void nucleation in passivated interconnect lines: Effects of site geometries, interfaces, and interface flaws," *J. Mater. Res.* 12, 2081 (1997).

- [4.84] Z. Suo, "Reliability of interconnect structures," in *Comprehensive Structural Integrity*, Vol. 8: *Interfacial and Nanoscale Failure*, edited by W. Gerberich and W. Yang (Elsevier, Oxford, 2003), pp. 265-324.

Chapter 5

- [5.1] K. N. Tu, "Recent Advances on Electromigration in Very-Large-Scale-Integration of Interconnects," *J. Appl. Phys.* 94, 5451 (2003).
- [5.2] E. C. C. Yeh *et al.*, "Current-Crowding-Induced Electromigration Failure in Flip Chip Solder Joints," *Appl. Phys. Lett.* 80,580 (2002).
- [5.3] T. L. Shao *et al.*, "Three-Dimensional Simulation on Current-Density Distribution in Flip-Chip Solder Joints under Electric Current Stressing," *J. Appl. Phys.* 98,044509 (2005).
- [5.4] L. Zhang *et al.*, "Effect of Current Crowding on Void Propagation at the Interface between Intermetallic Compound and Solder in Flip Chip Solder Joints," *Appl. Phys. Lett.* 88,012106 (2006).
- [5.5] J. W. Nah *et al.*, "Effect of Current Crowding and Joule Heating on Electromigration-Induced Failure in Flip Chip Composite Solder Joints Tested at Room Temperature," *J. Appl. Phys.* 98,013715 (2005).
- [5.6] S. W. Liang *et al.*, "Three-Dimensional Thermoelectrical Simulation in Flip-Chip Solder Joints with Thick Underbump Metallizations during Accelerated Electromigration Testing," *J. Electron. Mater.* 36, 159 (2007).
- [5.7] M. Ding, G. Wang, B. Chao, P. S. Ho, P. Su, and T. Uehling, "Effect of Contact Metallization on Electromigration Reliability of Pb-free Solder Joints," *J. Appl. Phys.* 99, 094906 (2006).
- [5.8] S.-H. Chae *et al.*, "Electromigration Statistics and Damage Evolution for Pb-Free Solder Joints with Cu and Ni UBM in Plastic Flip-Chip Packages," *J. Mater. Sci.: Mater. Electron.* 18, 247 (2007).
- [5.9] J. R. Black, "Mass Transport of Aluminum by Momentum Exchange with Conducting Electrons," *Proc. 6th International Reliability Physics Symposium*, Los Angeles, CA, 1967, pp. 148-159.
- [5.10] J. D. Wu *et al.*, "A Study in Flip-Chip UBM/Bump Reliability with Effects of SnPb Solder Composition," *Proc. 41st International Reliability Physics Symposium*, Dallas, TX, 2003, pp. 132-139.

- [5.11] W. J. Choi *et al.*, “Mean-Time-To-Failure Study of Flip Chip Solder Joints on Cu/Ni(V)/Al Thin-Film Under-Bump-Metallization,” *J. Appl. Phys.* 94, 5665 (2003).
- [5.12] K.-M. Chen *et al.*, “Effects of Pre-Bump Probing and Bumping Processes on Eutectic Solder Bump Electromigration,” *Microelectron. Reliab.* 46, 2104 (2006).
- [5.13] T.-S. Lai *et al.*, “Characteristics of Current Crowding in Flip-Chip Solder Bumps,” *Microelectron. Reliab.* 46, 915 (2006).
- [5.14] C. Y. Liu and S. J. Wang, “Prevention of Spalling by the Self-Formed Reaction Barrier Layer on Controlled Collapse Chip Connections Under Bump Metallization,” *J. Electron. Mater.* 32, L1 (2003).

Chapter 6

- [6.1] C. Ludwig, *Sitzungsber. Akad. Wiss. Wien, Math.-Naturwiss.* K120, 539 (1856).
- [6.2] P. S. Ho, “Electromigration and Soret Effect in Cobalt,” *J. Phys. Chem. Solids* 27, 1331 (1966).
- [6.3] R. A. Oriani, “Thermomigration in Solid Metals,” *J. Phys. Chem. Solids* 30, 339 (1969).
- [6.4] P. S. Ho, “Motion of Inclusion Induced by a Direct Current and a Temperature Gradient,” *J. Appl. Phys.* 41, 64 (1970).
- [6.5] A. T. Huang, A. M. Gusak and K. N. Tu, “Thermomigration in SnPb composite flip chip solder joints,” *Appl. Phys. Lett.* 88, 141911 (2006).
- [6.6] Y. C. Chuang and C. Y. Liu, “Thermomigration in Eutectic SnPb Alloy,” *Appl. Phys. Lett.* 88, 174105 (2006).
- [6.7] H.-Y. Hsiao and C. Chen, “Thermomigration in Flip-Chip SnPb Solder Joints under Alternating Current Stressing,” *Appl. Phys. Lett.* 90, 152105 (2007).
- [6.8] J. R. Lloyd, K.-N. Tu, and J. Jaspal, “The Physics and Materials Science of Electromigration and Thermomigration in Solders,” in *Handbook of Lead-Free Solder Technology for Microelectronic Assemblies*, edited by K. J. Puttlitz and K. A. Stalter (Marcel Dekker, New York, 2004), pp. 827-850.
- [6.9] T. Y. Lee, K. N. Tu, S. M. Kuo, and D. R. Frear, “Electromigration of Eutectic SnPb Solder Interconnects for Flip Chip Technology,” *J. Appl. Phys.* 89, 3189 (2001).

- [6.10] D.-G. Kim, W.-C. Moon, and S.-B. Jung, "Effects of Electromigration on Microstructural Evolution of Eutectic SnPb Flip Chip Solder Bumps," *Microelectron. Reliab.* 83, 2391 (2006).
- [6.11] C. Y. Liu, C. Chen, C. N. Liao, and K. N. Tu, "Microstructure-Electromigration Correlation in a Thin Stripe of Eutectic SnPb Solder Stressed Between Cu Electrodes," *Appl. Phys. Lett.* 75, 58 (1999).
- [6.12] F.-Y. Ouyang, K. N. Tu, Y.-S. Lai, and A. M. Gusak, "Effect of Entropy Production on Microstructure Change in Eutectic SnPb Flip Chip Solder Joints by Thermomigration," *Appl. Phys. Lett.* 89, 221906 (2006).
- [6.13] H.-Y. Chen, C. Chen, and K. N. Tu, "Failure Induced by Thermomigration of Interstitial Cu in Pb-Free Flip Chip Solder Joints," *Appl. Phys. Lett.* 93, 122103 (2008).
- [6.14] H.-Y. Hsiao and C. Chen, "Thermomigration in Pb-Free SnAg Solder Joint under Alternating Current Stressing," *Appl. Phys. Lett.* 94, 092107 (2009).
- [6.15] B. F. Dyson, "Diffusion of Gold and Silver in Tin Single Crystals," *J. Appl. Phys.* 37, 2375 (1966)
- [6.16] B. F. Dyson, T. R. Anthony, and D. Turnbull, "Interstitial Diffusion of Copper in Tin," *J. Appl. Phys.* 37, 3408 (1967)
- [6.17] D. C. Yeh and H. B. Huntington, "Extreme Fast-Diffusion System: Nickel in Single-Crystal Tin," *Phys. Rev. Lett.* 53, 1469 (1984)
- [6.18] M. Lu et al., "Effect of Sn Grain Orientation on Electromigration Degradation Mechanism in High Sn-Based Pb-Free Solders," *Appl. Phys. Lett.* 92, 211909 (2008).
- [6.19] G. D. Giacomo and S. Oggioni, "Reliability of Flip Chip Applications with Ceramic and Organic Chip Carriers," *Microelectron. Reliab.* 42, 1541 (2002).

Chapter 7

- [7.1] J. R. Black, "Mass Transport of Aluminum by Momentum Exchange with Conducting Electrons," *Proc. 6th International Reliability Physics Symposium*, Los Angeles, CA, 1967, pp. 148-159.
- [7.2] H.-L. Chao, "Electromigration Enhanced Kinetics of Cu-Sn Intermetallic Compounds in Pb Free Solder Joints and Cu Low-k Dual Damascene Processing

Using Step and Flash Imprint Lithography,” *Ph.D. Dissertation*, The University of Texas at Austin, 2009.

- [7.3] M. Lu et al., “Effect of Sn Grain Orientation on Electromigration Degradation Mechanism in High Sn-Based Pb-Free Solders,” *Appl. Phys. Lett.* 92, 211909 (2008).

Vita

Seung-Hyun Chae was born in Gunsan-si, Jeollabuk-do, Republic of Korea (South) on February 22, 1977, as the first son of Seok-Jun Chae and Oe-Sun Choi. After graduating from Gunsan High School at the top of his class in 1996, he entered Seoul National University, Korea. He received the degree of Bachelor of Science, cum laude, in Materials Science and Engineering in February 2003. In August 2003, he entered The University of Texas at Austin to pursue a doctoral degree in Materials Science and Engineering. He joined the Laboratory for Interconnect and Packaging in Microelectronics Research Center in June 2004. Under Prof. Ho's supervision, he conducted research in the area of microelectronics packaging reliability. In August 2006, he received the degree of Master of Science in Materials Science and Engineering. He was employed by IBM T. J. Watson Research Center, Yorktown Heights, NY as a Graduate Level Co-op from June to August in 2007. For two years from January 2008 to January 2010, he conducted research on packaging materials and reliability at Texas Instruments, Inc., Dallas, TX as a Graduate Fellowship Intern. He has published over 10 technical papers in journals and conference proceedings. After completing his Ph.D. degree in May 2010, he will be working for Texas Instruments, Inc., Dallas, TX as Advanced SC Packaging Engineer.

Permanent address (or email): 106/1001 Hyundai Apt., 1255-8 Naun3-dong, Gunsan-si,
Jeollabuk-do, 573-776, Republic of Korea (South).

This dissertation was typed by Seung-Hyun Chae.

List of Publications

- [1] S.-H. Chae, J.-H. Zhao, D. R. Edwards, and P. S. Ho, "Characterization of the Viscoelasticity of Molding Compounds in the Time Domain," *J. Electron. Mater.* 39, 419 (2010).
- [2] S.-H. Chae, J.-H. Zhao, D. R. Edwards, and P. S. Ho, "Effect of Dicing Technique on the Fracture Strength of Si Dies with Emphasis on Multimodal Failure Distribution," *IEEE Trans. Dev. Mater. Reliab.* 10, 149 (2010).
- [3] S.-H. Chae, J.-H. Zhao, D. R. Edwards, and P. S. Ho, "Characterization of Viscoelasticity of Molding Compounds in Time Domain," in *Proc. ASME InterPACK*, San Francisco, CA (Jul. 2009).
- [4] S.-H. Chae, J.-H. Zhao, D. R. Edwards, and P. S. Ho, "Effect of Dicing Technique on the Fracture Strength of Si Dies with Emphasis on Multi-Modal Failure Distribution," in *Proc. ASME InterPACK*, San Francisco, CA (Jul. 2009).
- [5] B. Chao, X. Zhang, S.-H. Chae, and P. S. Ho, "Recent Advances on Kinetic Analysis of Electromigration Enhanced Intermetallic Growth and Damage Formation in Pb-Free Solder Joints," *Microelectron. Reliab.* 49, 253 (2009).
- [6] S.-H. Chae, J. Im, T. Uehling, and P. S. Ho, "Effects of UBM Thickness, Contact Trace Structure and Solder Joint Scaling on Electromigration Reliability of Pb-Free Solder Joints," in *Proc. 58th IEEE Electronic Components and Technology Conference (ECTC)*, Orlando, FL (May. 2008), pp. 354-359.
- [7] B. Chao, S.-H. Chae, X. Zhang, and P. S. Ho "Kinetic Analysis of Electromigration Enhanced Intermetallic Growth and Void Formation in Pb-free Solders," in *Proc. 8th International Conference on Thermal, Mechanical and Multi-Physics Simulation and Experiments in Micro-Electronics and Micro-Systems (EuroSimE)*, London, England (Apr. 2007), pp. 746-753.
- [8] L. N. Ramanathan, T.-Y. T. Lee, J. W. Jang, S.-H. Chae, and P. S. Ho, "Current Carrying Capability of Sn0.7Cu Solder Bumps in Flip Chip Modules for High Power Applications," in *Proc. 57th IEEE Electronic Components and Technology Conference (ECTC)*, Reno, NV (May-Jun. 2007), pp. 1456-1461.
- [9] S.-H. Chae, X. Zhang, J. Im, and P. S. Ho, "Investigation of Intermetallic Compound Growth Enhanced by Electromigration in Pb-Free Solder Joints," in *Proc. 57th IEEE Electronic Components and Technology Conference (ECTC)*, Reno, NV (May-Jun. 2007), pp. 1442-1449.

- [10] B. Chao, S.-H. Chae, X. Zhang, K.-H. Lu, J. Im, and P. S. Ho, "Investigation of Diffusion and Electromigration Parameters for Cu-Sn Intermetallic Compounds in Pb-Free Solders Using Simulated Annealing," *Acta Materialia*, 55, 2805 (2007).
- [11] S.-H. Chae, X. Zhang, K.-H. Lu, H.-L. Chao, and P. S. Ho; M. Ding, P. Su, T. Uehling and L. N. Ramanathan, "Electromigration Statistics and Damage Evolution for Pb-Free Solder Joints with Cu and Ni UBM in Plastic Flip-Chip Packages," *J. Mater. Sci. – Mater. Electron.* 18, 247 (2007); also in *Lead-Free Electronic Solders*, edited by K. N. Subramanian (Springer, New York, 2007), pp. 247-258.
- [12] B. Chao, S.-H. Chae, X. Zhang, K.-H. Lu, J. Im, and P. S. Ho, "Electromigration Enhanced Intermetallic Growth and Void Formation in Pb-Free Solder Joints," *J. Appl. Phys.* 100, 084909 (2006).
- [13] S.-H. Chae, X. Zhang, H.-L. Chao, K.-H. Lu, and P. S. Ho; M. Ding, P. Su, T. Uehling, and L. N. Ramanathan, "Electromigration Lifetime Statistics for Pb-Free Solder Joints with Cu and Ni UBM in Plastic Flip-Chip Packages," in *Proc. 56th IEEE Electronic Components and Technology Conference (ECTC)*, San Diego, CA (May-Jun. 2006), pp. 650-656.
- [14] H.-L. Chao, S.-H. Chae, X. Zhang, K.-H. Lu, J. Im, and P. S. Ho, "Kinetic Analysis of Current Enhanced Intermetallic Growth and Its Effect on Electromigration Reliability for Solder Joints," in *Proc. IEEE 44th Annual International Reliability Physics Symposium (IRPS)*, San Jose, CA (Mar. 2006), pp. 250-255.